MANIPULATION OF STRUCTURAL DESIGN PARAMETERS TO MITIGATE THE CONCENTRATION OF INTERSTORY DRIFT RATIOS

A Thesis Submitted to
the Graduate School of Engineering and Sciences of
İzmir Institute of Technology
in Partial Fulfillment of the Requirements for the Degree of

DOCTOR OF PHILOSOPHY

in Civil Engineering

by
Egemen SÖNMEZ

June 2020
İZMİR

ACKNOWLEDGMENTS

First and foremost, I would like to express my sincere gratitude to my advisor, Assoc. Prof. Cemalettin Dönmez, for his guidance and constant motivation throughout this study. I have learned so much from him, both as a person and a researcher.

I also would like to thank the members of my dissertation committee, Prof. Özgür Özçelik and Assoc. Prof. Gürsoy Turan, for their support and guidance at times I lost my way and for their significant contributions to the study.

I also thank the members of my defense jury, Assoc. Prof. Engin Aktaş and Assist. Prof. Ahmet Anıl Dindar, for generously offering their time and valuable comments.

Special thanks go to my colleagues, Baturay Batarlar, Alper Çankaya, Mustafa Vardaroğlu, Mustafa Karaman, and Çağlayan Hızal. We shared the cheerful moments and hard times throughout this journey. I would also like to thank Assoc. Prof. Ali Demir for encouraging me to be a researcher when I was an undergraduate.

My highest appreciation goes to my parents and my beloved sister for their endless support and sacrifice throughout my life. If it weren't for you, I wouldn't be where and who I am today.

And for my wife Hande, thank you for being endlessly patient and believing in me, even when I could not believe in myself. You gave me the greatest PhD graduation gift ever: our daughter, Umay. I love both of you with all my heart and soul.

ABSTRACT

MANIPULATION OF STRUCTURAL DESIGN PARAMETERS TO MITIGATE THE CONCENTRATION OF INTERSTORY DRIFT RATIOS

Although the interstory drift ratio is used as a limiting factor for specific performance levels by the structural engineering profession, its distribution among the stories is generally disregarded. Observations and analytical studies have shown that even the structures are designed to conform seismic design codes, interstory drifts tend to concentrate at certain regions of the frame structures. In other words, the seismic demand the earthquake imposes is attempted to be provided from a limited part of the structure. As a result, the damage concentrates, and the stiffness of the corresponding stories decreases significantly. Locally, the story drifts become larger. Soft-story mechanisms and abrupt failures may occur under such conditions. In this study, a seismic design method was developed to control the distribution of interstory drifts in a frame structure during the nonlinear seismic response. This method is based on two observations: (i) in the inelastic range, the drift distribution is highly dependent on the yield strengths of the members; (ii) there is a strong correlation between the interstory drift distribution and the plastic rotation distribution at member-ends. Thus, an iterative design procedure is developed to control the distribution of the interstory drifts by adjusting the member yield strengths. Plastic rotations are used as a tool for estimating the required yield strengths. The efficiency of the proposed method was tested using nonlinear time-history analyses. The results demonstrated that the frames designed using the proposed method had well-distributed interstory drift and story damage patterns compared to those of the conventionally designed frames. Furthermore, the overall damage of frames was reduced remarkably.

Keywords: Interstory drift ratio; seismic design; structural dynamics; reinforced concrete structures; design optimization; earthquake engineering.

ÖZET

GÖRELİ KAT ÖTELEMESİ YOĞUNLAŞMALARININ YÖNLENDİRİLMİŞ YAPISAL TASARIM İLE AZALTILMASI

Deprem tasarımında göreli kat öteleme oranı, belirli performans seviyeleri için sınır değer olarak kullanılmasına rağmen, ötelenme oranlarının yapı yüksekliği boyunca gösterdikleri dağılım genellikle göz ardı edilmektedir. Yapılan gözlemler ve analitik çalışmalar, yapıların güncel yönetmeliklere göre tasarlanması durumunda dahi katarası ötelenmelerin yapıların belirli bölgelerinde yoğunlaştıklarını göstermektedir. Diğer bir deyişle deprem talebi, yapının sınırlı bir bölgesi tarafından karşılanmak zorunda kalmakta ve yerel olarak yüksek hasarlar gözlenmektedir. Bu şartlar altında yumuşak kat mekanizmaları ve ani göçmelerin oluşması ihtimali yüksektir. Bu çalışmada doğrusal olmayan deprem davranışı sırasında gerçekleşen katarası ötelenmeleri kontrol etmek amacıyla bir deprem tasarımı yöntemi geliştirilmiştir. Bu yöntem iki gözleme dayanmaktadır: (i) Doğrusal olmayan deprem davranışı sırasındaki ötelenme dağılımı, büyük oranda elemanların akma dayanımlarına bağlıdır; (ii) eleman uçlarındaki plastik dönmelerin dağılımı ile katarası ötelenme dağılımları arasında güçlü bir ilişki vardır. Bu gözlemlere dayanarak, elemanların akma dayanımlarını kurgulamak üzerine kurulu katarası ötelenme dağılımlarını kontrol edecek iteratif bir yöntem geliştirilmiştir. Bu yöntemde, gerekli akma dayanımlarını belirlemek amacıyla plastik dönmeler birer araç olarak kullanılmaktadır. Geliştirilen yöntemin başarısı, doğrusal olmayan dinamik analizler aracılığıyla sınanmıştır. Sonuçlar, önerilen yöntemle tasarlanan çerçevelerin katarası ötelenme ve hasarlarının, geleneksel yöntemlere uygun olarak tasarlanan çerçevelerinkilere oranla çok daha düzgün dağıldığını göstermiştir. Ayrıca, yapı genel hasarı da belirgin ölçüde düşük gerçekleşmiştir.

Anahtar Kelimeler: Göreli kat ötelemesi; depreme dayanıklı yapı tasarımı; yapı dinamiği; betonarme yapılar; tasarım optimizasyonu; deprem mühendisliği.

To the women who shaped me with their presence:

my mother, Halime,

my sister, Ezgi,

my grandmothers, Elmas and Havva,

my wife Hande,

and my daughter Umay.

TABLE OF CONTENTS

LIST OF FIGURES

Figure **Page**

Figure **Page**

Figure **Page**

Figure **Page**

Figure **Page**

Figure **Page**

Figure **Page**

Figure **Page**

LIST OF TABLES

Table **Page**

CHAPTER 1

INTRODUCTION

1.1. Statement of the Problem

The seismic design of structures has progressed substantially since the 1908 Messina Earthquake. Attempts to comprehend and quantify the seismic response of structures from different perspectives have led to the development of various design methods. The accumulated experience and knowledge have shown that the traditional force-based design approach is not sufficient to satisfy the demands of the modern buildings (Moehle, 1992; Priestley, 2000). Therefore, the contemporary approach is shifting to displacement-based design.

The current state of practice, on the other hand, first considers the effects of ground motions by means of equivalent lateral loads for the design of regular structures. Then, proportions and details the structural members based on these demands along with other loads expected to act on the structure (TEC2018, 2018). The displacement sufficiency is checked afterward.

During the evolution of the seismic-resistant design, lateral drift began to be used as a design criterion rather than an optional check (Sozen, 2003). This change happened as the interstory drift ratio (relative lateral displacement of a floor level with respect to the lower floor level divided by the story height) began to be regarded as a measure of structural and non-structural seismic damage. However, most of the contemporary seismic design approaches relate the damage with the ductility ratio (the ratio of the maximum deformation to the yield deformation). Some methods use arbitrary factors to account for the expected ductility during the design calculations, while others use it as a performance criterion (Miranda & Bertero, 1994). Estimating the displacement ductility, specifically in reinforced concrete structures, is not an easy task since it is very difficult to quantize the yield displacement. In addition, the ductility ratio may not always be associated with non-structural damage (Algan, 1982). On the other hand, the interstory drift ratio emerges as a convenient tool to be used in the design process − both as a performance criterion and as a guide for proportioning and detailing. It was confirmed that there is a satisfactory correlation between the interstory

drift and the seismic damage. Furthermore, interstory drift ratio is relatively easier to determine and to interpret. The contemporary seismic codes attempt to control the structural performance based on the predefined limits of the interstory drift ratio.

Although the interstory drift ratio is used as a limiting factor for certain performance levels by the profession, its distribution among the stories is disregarded. Observations and analytical studies have shown that, during seismic motions, interstory drifts tend to concentrate at certain regions of the frame structures (Miranda, 1999; Haselton et al., 2011). Even when the structures are designed to conform seismic design codes. In other words, seismic damage is likely to concentrate at certain stories. As a result, the stiffnesses of the corresponding stories decrease significantly and story drifts become larger. Soft-story mechanisms and abrupt failures may occur under such conditions.

Considering that if the distribution of the expected interstory drifts could be controlled during the design process, it could be a key for avoiding damage concentrations and premature failures. Therefore, it is believed that there is potential to exploit the distribution of interstory drift ratio as a tool for controlling the distribution of damage throughout the height of the structures during seismic motions.

1.2. Objective and Scope

The main objective of this study is to develop a practical seismic design procedure that prevents the concentration of interstory drifts at certain regions of the structures during the seismic response.

Several studies that address similar issues from different perspectives, exist in the literature (Zou, 2002; Hajirasouliha et al., 2012; Bai et al., 2016). However, most of them treat the seismic design as an optimization problem. Design requirements and constraints, as well as seismic response and capacities of the members are expressed in the form of mathematical expressions and solved in an iterative manner. Such methods generally oversimplify the design and/or the analysis phases to reduce the amount of constraint equations and the number of iteration steps. Reducing the seismic design to a sole optimization problem may result in bypassing the application of precious engineering judgment to the design process.

This study aims to set forth a design methodology, which leads to better seismic behavior in terms of drift and damage distribution without ruling out the engineering judgment. Initially, a procedure to proportion the member cross-sections for optimum drift behavior in the elastic range was developed. This procedure is based on calculating an optimum heightwise stiffness distribution based on prescribed modal vectors and fundamental period. Then, the member cross-sections are proportioned in a way that each story satisfies the required stiffness. The frames designed using this procedure are expected to exhibit well-distributed interstory drift ratios within the linear range of response and until the inelastic deformations become prevalent. However, as the intensity of ground motions increase, inelastic actions become more pronounced. In this case, the elastic modal properties are no longer constant and cannot be used to control the drift behavior. Therefore, another procedure was developed to control the distribution of interstory drifts in the inelastic range of response. This procedure is based on two observations: (i) in the inelastic range, the drift distribution is highly dependent on the yield strengths of the members; (ii) there is a strong correlation between the interstory drift distribution and the plastic rotation distribution at member-ends. Thus, an iterative procedure is developed to control the distribution of the interstory drifts by adjusting the member yield strengths. Plastic rotations are used as a tool for estimating the required yield strengths.

The type of structures considered in the study includes low- and mid-rise reinforced concrete moment frames. The mass distribution and the framing were assumed to be regular. Planar frames were used to develop and validate the proposed design approach. Therefore, torsional effects and structural irregularities are not addressed. The deformations of the members were assumed to be governed by the flexural actions. Also, the members were assumed to adequately detailed to prevent brittle shear and bond failures.

The effectiveness of the proposed design procedure was validated by means of nonlinear time-history analyses. The ground motion sets used for this purpose included acceleration time-histories recorded at sites that are at a moderate distance from the epicenter. Therefore, near-fault effects are not considered in the study.

The methods proposed herein have the potential to be expanded to cover moment frames built with different construction materials.

1.3. Outline of the Thesis

Chapter 2 gives an overview of the studies in the literature that aim to develop alternative design procedures to be used for improving the seismic response of the buildings. The shortcomings of the summarized work are pointed out in this chapter.

Chapter 3 presents a method to determine the optimum stiffness distribution along the height of the frames considered in the study. The aim of the targeted optimum stiffness distribution is to obtain prescribed modal vector properties. The method is based on manipulating the governing modal vectors to enhance the seismic behavior in terms of interstory drift ratios. The chapter also includes a proposed method that is used for the proportioning of the member cross-sections so as to obtain the determined stiffness distribution. The applicability of the proposed method was evaluated on shear-beam models, as well as on reinforced concrete frames with various heights. The method presented in this chapter mostly targets the linear response range.

The purpose of Chapter 4 is to determine the adequate material and element models to be used for modeling the reinforced concrete frames for the study. The effect of different numerical material and element modeling methods on the seismic response of reinforced concrete members was investigated.

Chapter 5 presents a design methodology for inelastic seismic response of low- to mid-rise reinforced concrete moment frame structures. It is an iterative methodology, which is based on the relationship between the plastic rotations and interstory drift ratios. In each iterative step, reinforcement ratios of the members are revised to obtain a uniform plastic rotation distribution. The theoretical background of the revision procedure is described within this chapter. In addition, an illustrative example is included to demonstrate the application of the procedure.

Chapter 6 consists of three case studies in which both the modal vector proportioning and reinforcement allocation procedures of the proposed design procedures in Chapters 3 and 5 are applied. The frames were designed such that the displacement demand is higher than expected in order to test the ability of the proposed procedure to reduce interstory drift concentrations. The results obtained using the proposed procedures are compared with the results of the frames that are designed using conventional seismic design methods.

In Chapter 7, a ten-story reinforced concrete frame was designed with a prescribed drift target using the proposed procedures. This frame has a shorter fundamental period compared to the ten-story frame designed in Chapter 6. The results are compared to those of a conventionally designed frame. In addition, the effect of the primary proportioning to the effectiveness of the proposed iterative procedure was investigated.

The summary of the study and the conclusions inferred are presented in Chapter 8.

CHAPTER 2

LITERATURE REVIEW

2.1. Introduction

The endeavor to develop an efficient seismic design procedure constituted a popular research field within earthquake engineering. Researchers have been trying to optimize various elements of the seismic design to reach different targets that are believed to improve the seismic performance of the structure in one way or another. The purpose of this chapter is not to present a thorough history of seismic design improvements. Since the object of the presented thesis is to obtain uniform story drifts, which in turn expected to result in evenly distributed damage over the height of the structures, only the selected research related to drift and damage optimization will be covered.

2.2. Selected Literature

Zou (2002) developed a two-stage seismic design optimization method for reinforced concrete frames. The method aims to obtain uniform interstory drifts for the response to linear and non-linear pushover analyses. The principle of virtual work and Taylor Series approximation method are implemented to express the seismic design problem in terms of the selected design variables. The reinforcement ratios of the members are selected as variables in the proposed method. The so-called optimality criteria technique is used for solving the optimization problem. The interstory drifts are shown to be distributed evenly after the application of the proposed procedure. However, this method is effective only for the pushover response of the reinforced concrete frames. Therefore, it does not consider the dynamic effect of the earthquakes and the effects of the higher modes.

Estes (2003) proposed an energy-based seismic design procedure for steel moment frames. The amount and the distribution of demanded hysteretic energy from the structure during the design-basis earthquake are estimated, initially. The required

moment capacities of the members are formulated using plastic analysis by assuming various types of failure mechanisms. The energy dissipation capacity of a section is assumed as the energy dissipated in a single excursion to its ultimate deformation limits in both directions. Some design constraints including lateral drift and plastic rotations are also expressed. An optimization algorithm is implemented to obtain the member moment capacities that will meet the hysteretic energy demand and satisfy the design constraints. The results of the study show that the proposed method is effective at keeping the response parameters within the targeted limits. However, no information is provided regarding the resulting interstory drift distributions.

Moghaddam and Hajirasouliha (2004) proposed an optimization algorithm to obtain uniform ductility demands along the height of shear-type buildings. The essence of the method depends on modifying the strength and the stiffness of the stories in an iterative manner until the target ductility demands is reached at each story. The proposed method is effective at obtaining a uniform ductility demand over the height. However, it is not applicable to moment frames.

Medina (2004) investigated the dependence of the size and the distribution of story ductility demands along the height of regular frames on the shear design strength distribution. A wide range of regular frame structures are designed as per seismic design codes and analyzed using 40 ground motion records in the study. The results show that the ductility demand distribution of code-conforming frames is not uniform. Based on the relations obtained from the performed analyses, story shear design strength patterns are proposed which are functions of the ground motion and structural characteristics, as well as the performance level. It is stated that the proposed patterns lead to more balanced ductility demands over the height. However, it is noted that the proposed patterns do not necessarily lead to uniform interstory drift distribution.

Mohammadi et al. (2004) pointed out that the equivalent lateral load distribution suggested by design codes does not lead to equal displacement and optimum ductility demands in frame structures during earthquakes. A lateral design load pattern for shear-beam buildings is proposed which is a function of the fundamental period and the target ductility. Also, an iterative procedure to determine the optimum strength distribution for achieving prescribed ductility demand distribution throughout the buildings is proposed. The optimum strength distribution is observed to depend on the ground motion characteristics. The results indicate that the target ductility demands are reached for the considered frames. However, information regarding the distribution of damage and

interstory drifts is not included in the study. In addition, the study considers only the shear-beam systems. Therefore, it does not present a practicable method to be applied in the design of moment frames.

Bertero and Bertero (2004) proposed a comprehensive performance-based seismic design approach for reinforced concrete frames. In this design approach, the aim is to obtain minimum strength and stiffness for controlling the design demands, elastic and inelastic deformations while satisfying the selected performance criteria. For preliminary design, member sizes are determined such that the first mode has a linear shape while satisfying the target period. Initially, a linear optimization algorithm is used to determine the reinforcement ratios for beams and columns based on the elastic analysis. Subsequently, the detailing requirements are expressed using mathematical expressions that relate the demand to the capacity using the plastic design procedures. Various design requirements such as demand-to-capacity ratios, interstory drift index, damage index are checked. Design is revised where deemed necessary. The application of the proposed procedure is illustrated using a ten-story frame. The results show that the proposed methodology is effective at satisfying the performance objectives while resulting in a balanced damage distribution.

Park and Medina (2007) developed new design lateral load patterns using the same systems and ground motion records as in Medina (2004). The proposed load patterns are calculated based on the expected ductility ratio of the structure for a prescribed hazard level, properties of the ground motions, as well as the period and the height of the structure. The distribution of the calculated design load pattern is expected to produce a balanced damage distribution throughout the structure while satisfying the selected performance objective. The results showed that the frames designed based on the proposed lateral load patterns had more balanced damage and interstory drift distributions compared to those designed based on the code-based lateral load patterns.

Terapathana (2012) expanded the seismic design procedure proposed in Estes (2003) to reinforced concrete frames. Interstory drift is used as a limiting parameter during the optimization process. Results show that the interstory drifts and the damage indices are within the prescribed limits. However, the damage and interstory drift distributions are not uniform although the target plastic rotations used in the plastic design process are the same for all plastic hinges. The reason for this lies in the fact that the assumed energy dissipation capacity of the sections is oversimplified and may not

represent the actual case in every condition. In addition, the interstory drift is used as a limiting parameter rather than a design target.

Hajirasouliha et al. (2012) extended the design method proposed in Moghaddam and Hajirasouliha (2004) to reinforced concrete frames. The proposed procedure depends on revising the reinforcement ratio of the members to reach uniform damage index distribution through the height of the frame structures. Once the structure is proportioned initially, the longitudinal reinforcement is shifted from members with lower damage to those experience higher damage after time-history analyses using a set of equations. This procedure is repeated until the damage index distribution becomes uniform. Interstory drift ratio is used as a limiting parameter in this study. However, as the damage indices become uniform, the interstory drift distribution becomes more balanced consequently.

Bai et al. (2016) developed an optimization method for the seismic design of reinforced concrete frame structures. The method targets uniform interstory drifts along the height of the frames. Consecutive modal pushover method is utilized to derive the seismic demands. Based on the derived demands, the reinforcement ratios are distributed among the stories using the proposed optimization formulations and design constraints that utilize interstory drifts and plastic rotations together. The efficiency of the proposed procedure was tested using nonlinear time-history analyses. The results show that the proposed procedure reduces the amount of interstory drift compared to the code-based frame results. In addition, the interstory drifts are more balanced.

Bai et al. (2020) proposed another method to improve the seismic resistance of reinforced concrete structures. The proposed method implements the so-called optimality criteria method in an iterative manner. In this method, the behavior of the structure is related to the target criterion using a series of equations, which also include design constraints. The proposed optimization procedure was tested on five- and ten-story moment frames. It is observed that the proposed method is effective at reducing the maximum interstory drifts while distributing the drifts and the damage evenly throughout the elevation. The proposed method requires ten to twenty iteration steps to reach the target optimized solution.

As it can be implied from the literature summarized, there exist numerous attempts that seek ways to enhance the response of the structures to seismic demands. Pursuit of the optimum solution leads to fully automated procedures at some of the studies, due to its appeal in the face of the computational capacities that are advancing

exponentially. However, engineering, as a term, involves not only understanding the nature of the problems, but also creating practical solutions to the problems, which could be understood and implemented by the engineer. Therefore, the methods that are to be developed should satisfy the requirements of the term “engineering” if they are aimed to be expanded for the use of the engineers.

CHAPTER 3

ELASTIC DESIGN PROCEDURE

3.1. Introduction

Preliminary sizing of the structural members is generally based on the gravity-load demands and/or the engineering judgment in the conventional force-based design approaches. This approach is likely to require iterations for modifying member sizes after seismic analyses. The proportioning of the members also determines the stiffness distribution over the height of the structures. This distribution directly affects the elastic dynamic properties of the structures, such as mode shapes and periods. These parameters not only dictate the dynamic response of the structures until structural damage becomes significant but also the global seismic response of the structures. The so-called “equal displacement rule” depends on the observation that the maximum seismic drift demand of an elastic system and that of the associated inelastic system are approximately the same. Therefore, it is of major importance to proportion members adequately for controlling the seismic demand levels and also the proper seismic behavior for the ground motions up to the elastic limit of the structures.

This chapter presents a simple primary design procedure. The proposed procedure aims to proportion frame members such that the frames exhibit uniform interstory drift values until the damage becomes prevalent.

The outline of the proposed procedure is presented in the following section. Then, the effects of the proposed optimum stiffness distribution on the linear seismic behavior of the lumped-mass shear-beam models are evaluated. Next, the same evaluation is presented for reinforced concrete frames of different heights.

3.2. Outline of the Procedure

In case of an ideal seismic behavior, which targets the distribution of the demand through the structure, each story of the building should undergo equal amount of interstory drift values. Hence, not only the damage of non-structural and structural

elements would be roughly uniform along the height of the structure, but also an early failure of a region of the structure could be avoided. However, modern seismic design procedures disregard the distribution of interstory drifts. Instead, they establish maximum drift limits for the individual stories of the structure. Therefore, the concentration of the drifts at particular parts of the code-conforming frame structures is a common practical result. Studies and observations confirmed that interstory drifts and damage are likely to concentrate at these parts of this type of structures.

The proposed procedure is based on the assumption that a combination of the governing modes determines the drift response of frame structures. Therefore, a linear combined modal pattern is targeted to achieve a uniform interstory drift demand. Considering the difficulty to modify the mass distribution in a structure, optimum stiffness distribution, which will yield a linear combined modal pattern for a selected fundamental period, is sought. Subsequently, frame members are proportioned so as to obtain the required stiffness at each story. A simple tool that approximates the story stiffness is used for this purpose. Figure 1 shows the flowchart of the proposed preliminary design procedure.

3.3. Procedure to Determine Required Stiffness Distribution to Satisfy Target Fundamental Mode and Period

As it is stated above, mode shapes and periods of a structure governs the dynamic response under seismic demands. Quantifying the stiffness distribution over the height of the structure for a prescribed mode shape and a corresponding target period is an alternative approach for preliminary sizing of the frame members. If the target mode shape and the target period are selected properly, the preliminary design will satisfy the design requirements and will not require iterations during the seismic design.

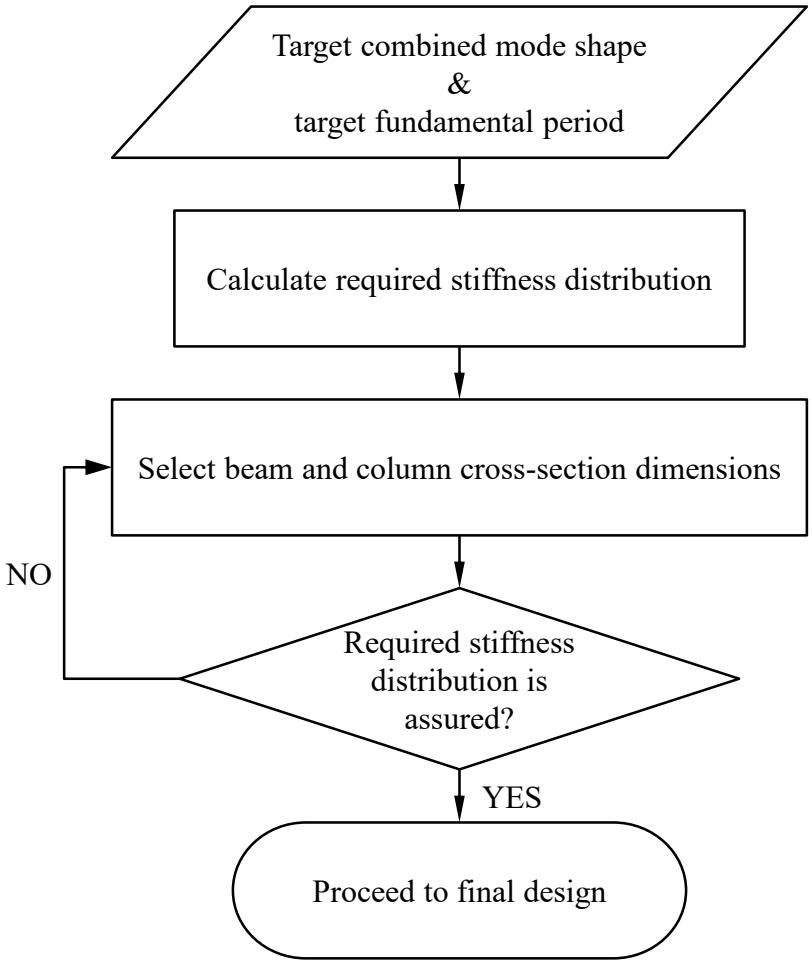

Figure 1. Flowchart for the proposed elastic design procedure

3.3.1. Formulation of the Required Stiffness for a Given Mode Shape

In structural dynamics problems, generally, the external forces and the system properties (mass and stiffness) are the known variables. The equation of motion is solved for the unknown displacements. However, in the proposed procedure, stiffness is the unknown variable. Therefore, the equation of motion should be solved to find the stiffness matrix of the system. The formulation to calculate the required stiffness distribution for a prescribed mode shape and target period can be obtained by implementing modal analysis and using the equilibrium of inertia and elastic forces at each story of a lumped-mass shear beam model (Figure 2).

The equation of motion which governs the free vibration of linear multi-degree-of-freedom systems without damping is

$$\mathbf{m}\ddot{\mathbf{u}} + \mathbf{k}\mathbf{u} = 0 \tag{3.1}$$

where **m** is the mass matrix, **k** is the stiffness matrix, **u** is the displacement vector, $\ddot{\mathbf{u}}$ is the acceleration vector.

The displacement vector can be expanded in terms of modal contributions as in (3.2).

$$\mathbf{u}(t) = \sum_{n=1}^{N} q_n(t)\phi_n \tag{3.2}$$

where N is the total number of modes, ϕ_n is the n^{th} mode shape vector, and $q_n(t)$ is the time variation of the modal displacements which is described by

$$q_n(t) = A_n \cos\omega_n t + B_n \sin\omega_n t \tag{3.3}$$

Therefore,

$$\mathbf{u}(t) = \sum_{n=1}^{N} \phi_n \left(A_n \cos\omega_n t + B_n \sin\omega_n t\right) \tag{3.4}$$

Substituting this form of $\mathbf{u}(t)$ into (3.1) gives

$$\left(-\omega_n^2 \mathbf{m}\phi_n + \mathbf{k}\phi_n\right) q_n(t) = 0 \tag{3.5}$$

In case of motion, this equation can only be satisfied if the expression in parentheses is equal to zero. Therefore,

$$\mathbf{k}\phi_n = \omega_n^2 \mathbf{m}\phi_n \tag{3.6}$$

In the static case, the set of equilibrium equations that relate the nodal forces and nodal displacements for an N-story shear-beam model with lumped story masses (Figure 2) is

$$\begin{Bmatrix} p_1 \\ p_2 \\ . \\ . \\ . \\ p_N \end{Bmatrix} = \begin{bmatrix} k_1 + k_2 & -k_2 & \dots & 0 \\ -k_2 & k_2 + k_3 & \dots & 0 \\ . & . & & . \\ . & . & . & . \\ . & . & & . \\ 0 & 0 & \dots & k_N \end{bmatrix} \begin{Bmatrix} u_1 \\ u_2 \\ . \\ . \\ . \\ u_N \end{Bmatrix} \tag{3.7}$$

In matrix form:

$$\mathbf{P} = \mathbf{K}\,\mathbf{U} \tag{3.8}$$

For the proposed procedure, **P** and **U** are the prescribed matrices, and **K** is the unknown stiffness matrix. To find the required stiffness distribution, an unknown stiffness column vector, $\hat{\mathbf{K}}$, is defined:

$$\hat{\mathbf{K}} = \begin{Bmatrix} k_1 \\ k_2 \\ . \\ . \\ . \\ k_N \end{Bmatrix} \tag{3.9}$$

The unknown stiffness vector must satisfy (3.10):

$$\mathbf{D}\hat{\mathbf{K}} = \mathbf{P} \tag{3.10}$$

where **D** is a matrix which relates known displacements with the required story stiffness values. **D** matrix can be derived for the dynamic case using the dynamic equilibrium.

In the dynamic case, the equilibrium equation of the kinetic diagram seen in Figure 2 gives

$$p_i = m_i \ddot{u}_i + V_i - V_{i+1} \tag{3.11}$$

where V_i is the shear force of the i^{th} story and expressed as

$$V_i = k_i\left(u_i - u_{i-1}\right) \tag{3.12}$$

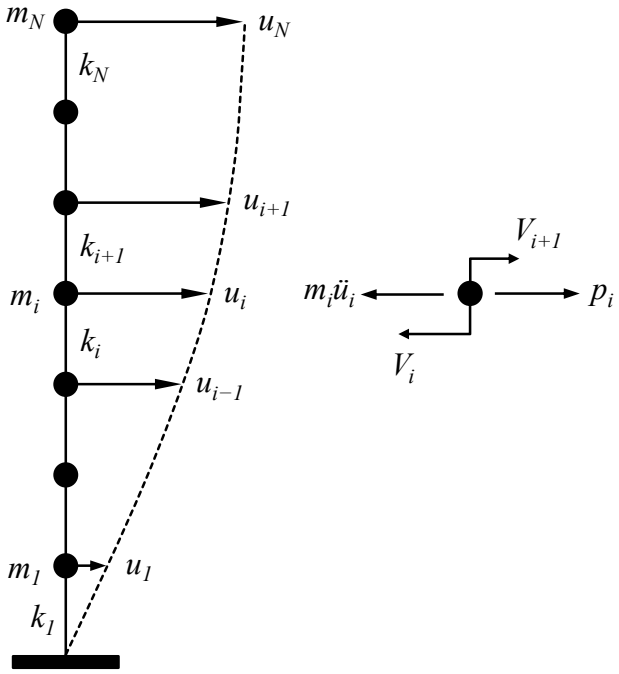

Figure 2. Lumped-mass shear beam model

Substituting (3.12) into (3.11),

$$p_i = m_i\ddot{u}_i + k_i\left(u_i - u_{i-1}\right) - k_{i+1}\left(u_{i+1} - u_i\right) \tag{3.13}$$

To enforce the equilibrium at any time instant of free vibration, p_i must be zero. Thus, (3.13) can be rewritten as:

$$m_i\ddot{u}_i = k_{i+1}\left(u_{i+1} - u_i\right) - k_i\left(u_i - u_{i-1}\right) \tag{3.14}$$

Expressing (3.14) in modal domain using (3.4) leads to (3.17):

$$\omega_n^2 m_i \phi_{n_i} = k_{i+1}\left(\phi_{n_{i+1}} - \phi_{n_i}\right) - k_i\left(\phi_{n_i} - \phi_{n_{i-1}}\right) \tag{3.15}$$

By expressing (3.15) in matrix form for the whole system, one can assemble the *D* matrix for the modal analysis of the system shown in Figure 2 as:

$$\mathbf{D} = \begin{bmatrix} \phi_{n_1} - \phi_{n_0} & \phi_{n_1} - \phi_{n_2} & 0 & \dots & 0 \\ 0 & \phi_{n_2} - \phi_{n_1} & \phi_{n_2} - \phi_{n_3} & \dots & 0 \\ . & . & . & . & . \\ . & . & . & . & . \\ . & . & . & . & \phi_{n_{N-1}} - \phi_{n_N} \\ 0 & \dots & \dots & 0 & \phi_{n_N} - \phi_{n_{N-1}} \end{bmatrix} \tag{3.16}$$

For a prescribed mode shape, ϕ_n, and a corresponding target period, ω_n, the required stiffness distribution can be calculated using (3.17):

$$\hat{\mathbf{K}} = \mathbf{D}^{-1}\,\mathbf{P} \tag{3.17}$$

where **P** corresponds to $\omega_n^2 \mathbf{m}\phi_n$ for the modal case, as shown above.

3.3.2. Iterative Algorithm to Obtain the Optimum Stiffness Distribution in Shear-Beam Models

The required stiffness distribution for a prescribed mode shape and the corresponding target period can be calculated using the formulation presented above. However, the dynamic response of the systems considered in this study is composed of more than one modal shape. In this study, it is assumed that first *n* modes of the system which have a minimum cumulative sum of the effective modal masses 90% of the total mass of the system is sufficient for representing the dynamic response of the system. With this approach, the contribution of the upper modes to the dynamic behavior in addition to that of the first mode is also considered. Therefore, the target modal deflected shape in this study corresponds to a combination of several modal vectors which has a linear shape.

An iterative procedure is developed to reach the target combined mode shape (ϕ_{target}) and the corresponding stiffness distribution for a target fundamental period (T_1). The procedure is based on updating the first mode shape after checking the convergence of the combined mode shape to the target shape after each step.

The iterative procedure starts with a linear first mode shape (ϕ_1). Based on the known mass matrix and the target fundamental period, the required stiffness distribution

is calculated. Then, all mode shapes and effective modal masses of each mode are computed. The number of the modes to be considered is found using the expression in (3.18).

$$\sum_{n=1}^{Y} M_n^* \geq 0.90 \sum_{i=1}^{N} m_i \tag{3.18}$$

where Y is the number of the considered modes, M_n^* is the effective modal mass, N is the number of the stories, m_i is the story mass.

Then, the contribution of each considered mode is obtained by multiplying each modal vector by their effective modal mass ratios. The combined shape (ϕ_c) is obtained by combining the contribution of the considered modes using the square-root-of-sum-of-squares (SRSS) rule.

Afterward, the difference between the target and the combined shape is calculated for each story. This difference is then algebraically added to the current first modal vector proportional to the effective modal mass ratio of the first mode (R_1). Therefore, the first mode shape to be used in the next step is obtained. The whole procedure is repeated until the difference between the target combined modal vector and the current combined modal vector is negligibly small. A flowchart of the iterative algorithm is given in Figure 3.

Figure 4 shows the interstory drifts of the combined mode shape and the required stiffness distribution after each iteration step for a 20-story system in a qualitative manner.

It can be seen from Figure 4 that the linear combined shape mode (i.e. uniform modal interstory drift distribution) and the required stiffness distribution were reached after four iterations for the considered case. It was observed that the required stiffness distribution that yields constant interstory drift for every story has a parabolic shape which is not too different than a line.

Figure 5 presents a comparison between a 20-story system with the optimum stiffness distribution as defined above and with a uniform stiffness distribution. The latter could be accepted to represent a frame designed using conventional approaches.

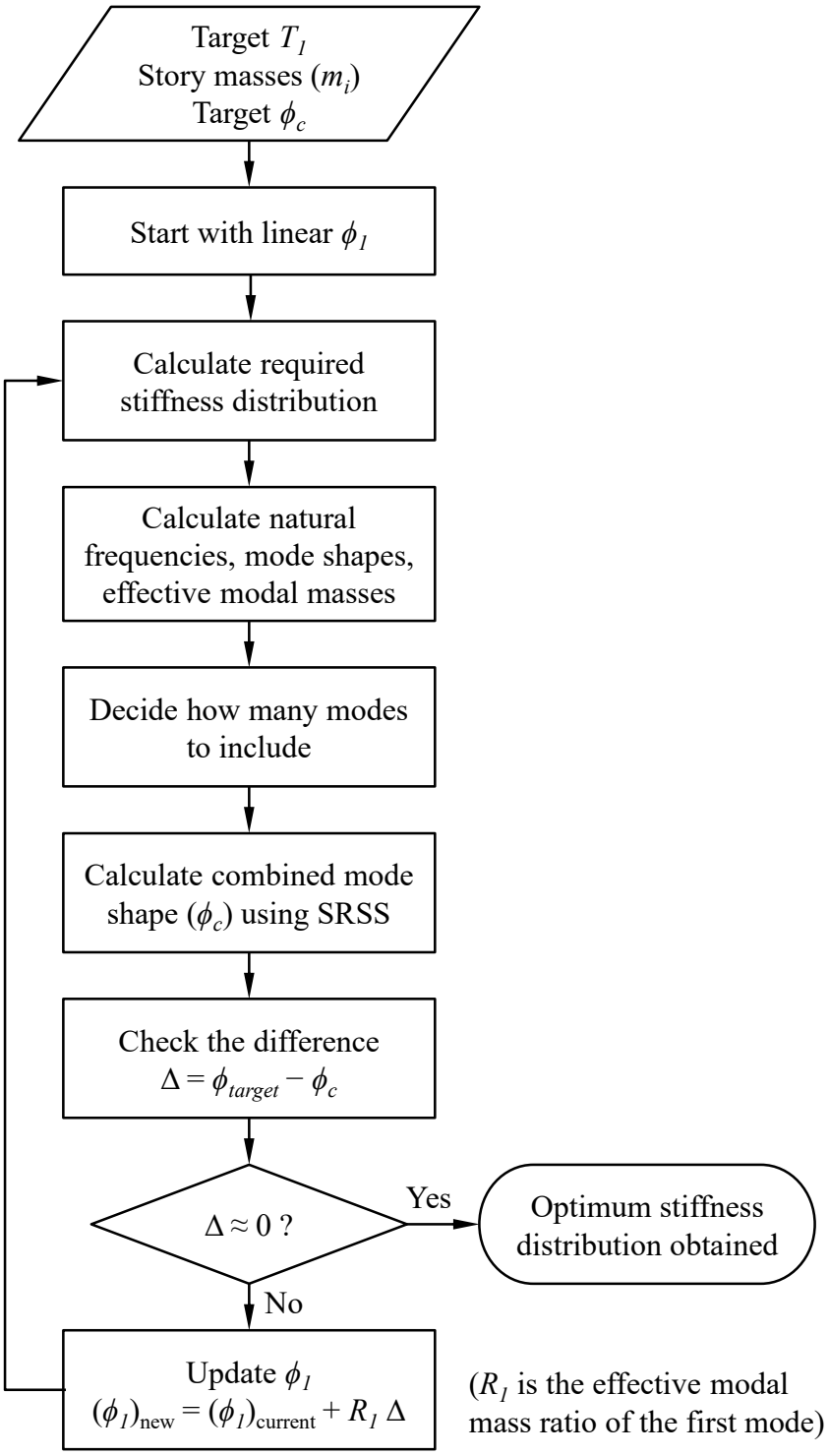

Figure 3. Flowchart of the iterative procedure

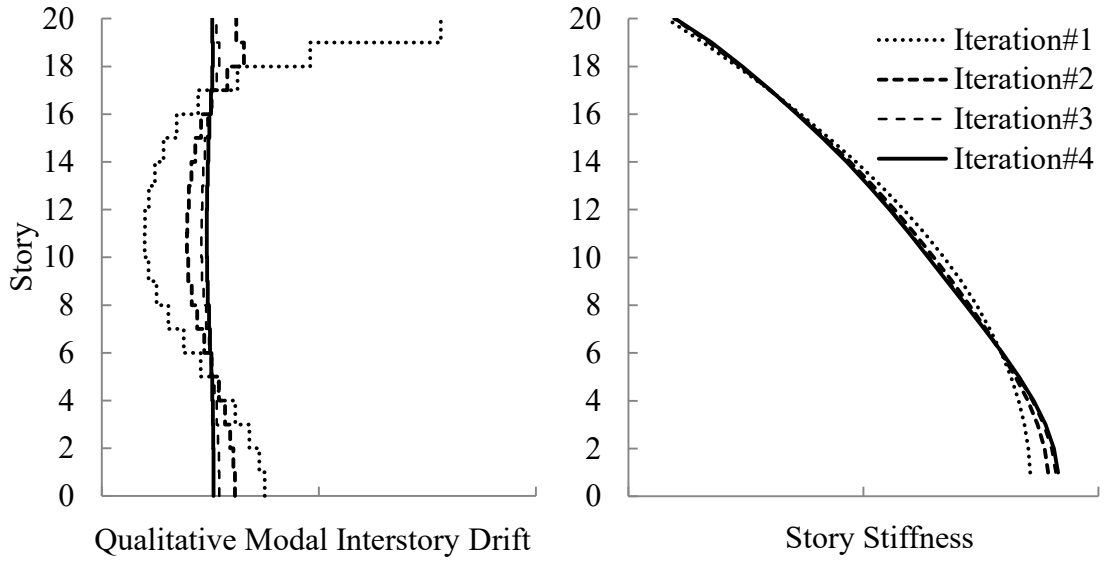

Figure 4. (a) Qualitative modal interstory drift distribution of combined mode shape after each step; (b) Qualitative stiffness distribution after each step

It can be observed from Figure 5 that combined modal interstory drifts increase towards the base in the conventionally designed frame as a result of a uniform stiffness distribution. However, in the proposed system, as a result of the parabolic stiffness distribution, a uniform combined modal interstory drift distribution is obtained.

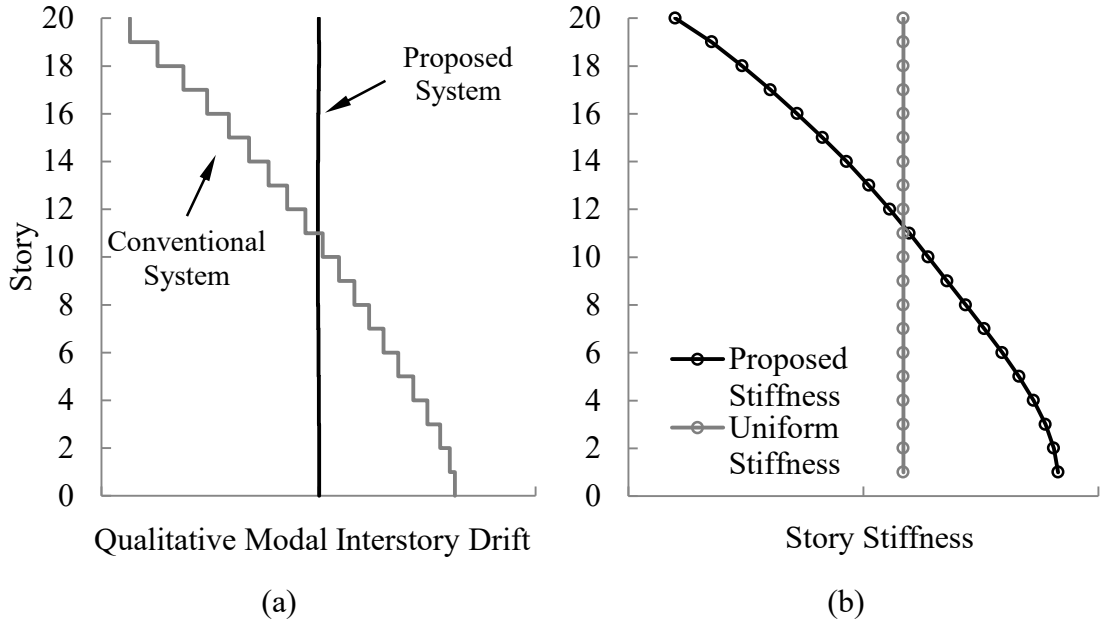

Figure 5. (a) Comparison of qualitative modal interstory drift distribution; (b) Comparison of stiffness distributions

3.4. Linear Dynamic Analyses of Shear-Beam Models

Initially, the effects of the optimum stiffness distribution will be evaluated using multi-degree-of-freedom lumped-mass shear-beam models. Interstory drift distributions will be observed after performing linear time-history analyses using a set of ground motion records. The results will be compared to those of the conventional systems (i.e. systems with uniform stiffness distribution).

3.4.1. Properties of the Shear-Beam Models

Two sets of shear-beam models used for the evaluation. The first set consists of 10-, 20-, and 30-story systems with optimum stiffness distributions. The second set includes systems with the same number of stories with a uniform stiffness distribution. This set represents buildings designed using conventional methods in which the member sizes do not change notably through the elevation. The shear-beam models used in the analyses are shown in Figure 6.

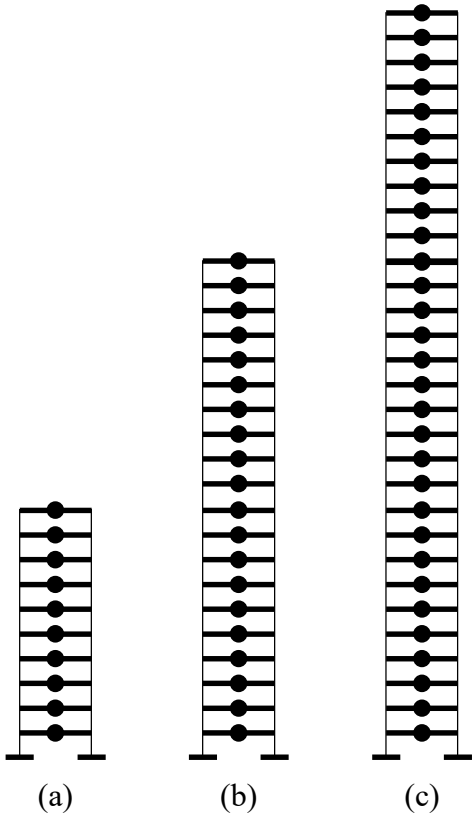

Figure 6. Lumped-mass shear-beam models: (a) 10-story; (b) 20-story; (c) 30-story

The pairs with the same number of stories were tuned to have the same fundamental periods to be able to have comparable responses. The same amount of mass was assigned to the story levels in all systems. The first mode periods are 0.67, 1.33, and 2.00 seconds for the 10-, 20-, and 30-story systems, respectively. The modal vectors for the first three modes of the proposed and the conventional systems are presented from Figure 7 to Figure 9. The modal vectors in these plots are normalized with respect to the modal deflection at the top story where it is taken as unity.

The combined mode shapes and the stiffness distributions of the proposed and the conventional systems are given in Figure 10 to Figure 12. The modal vectors of the combined mode shapes are normalized with respect to the modal deflection at the top story where it is taken as unity.

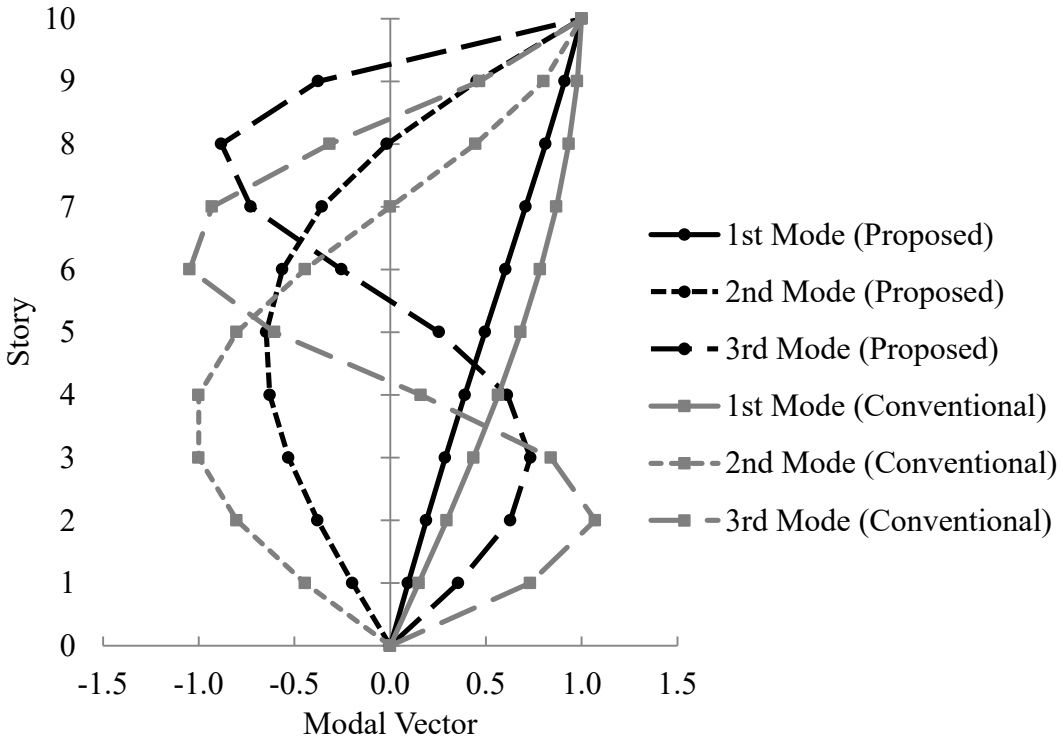

Figure 7. First three mode shapes of 10-story shear-beam model

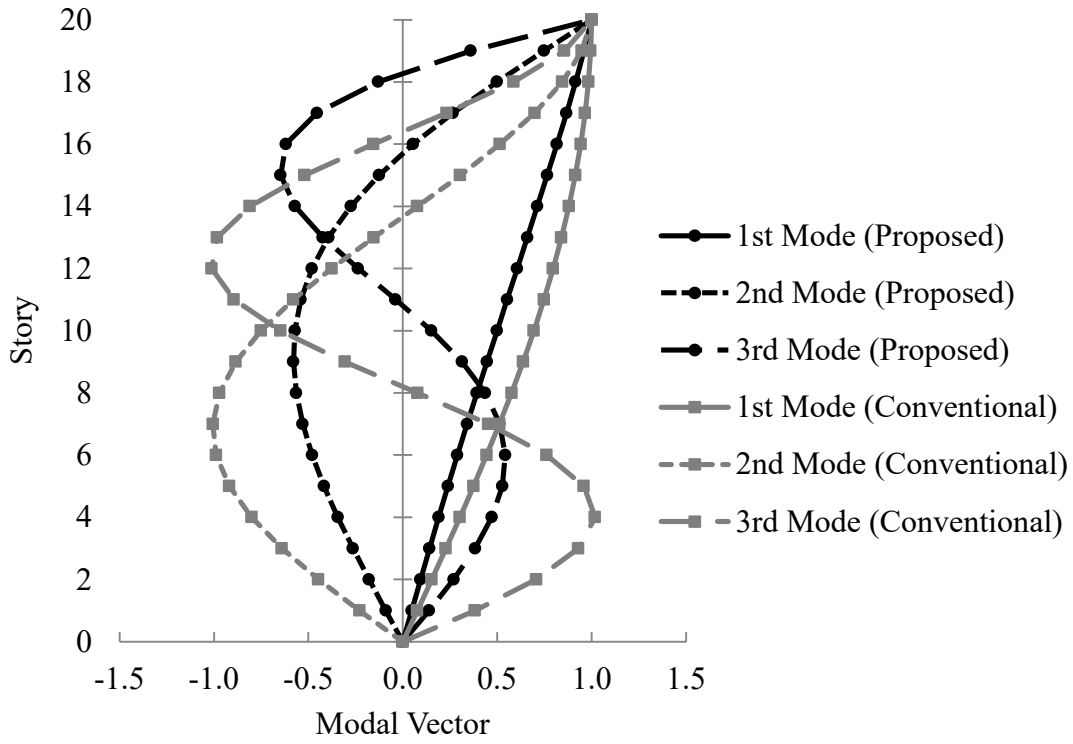

Figure 8. First three mode shapes of 20-story shear-beam model

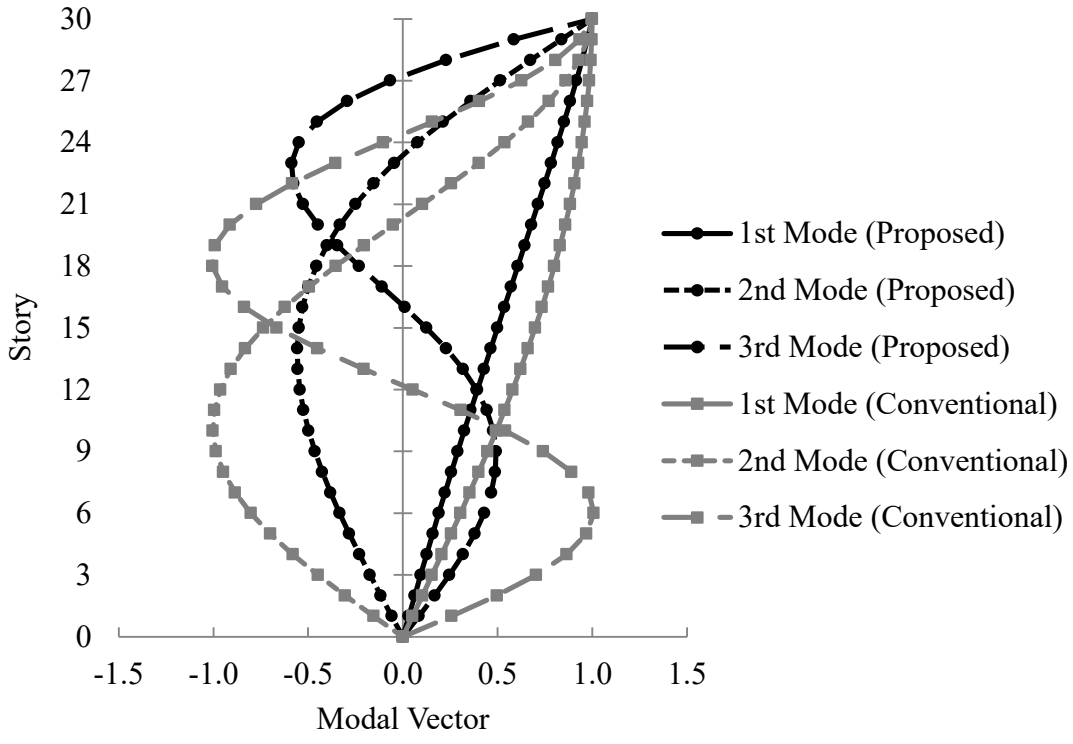

Figure 9. First three mode shapes of 30-story shear-beam model

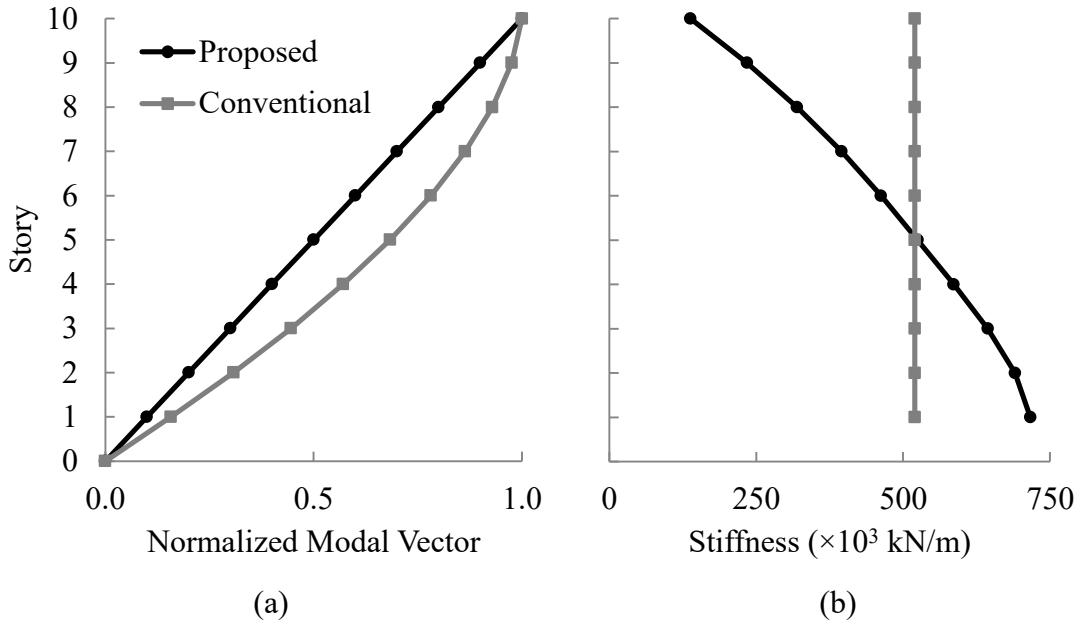

Figure 10. (a) Combined mode shapes; (b) Stiffness distributions of 10-story shear-beam model

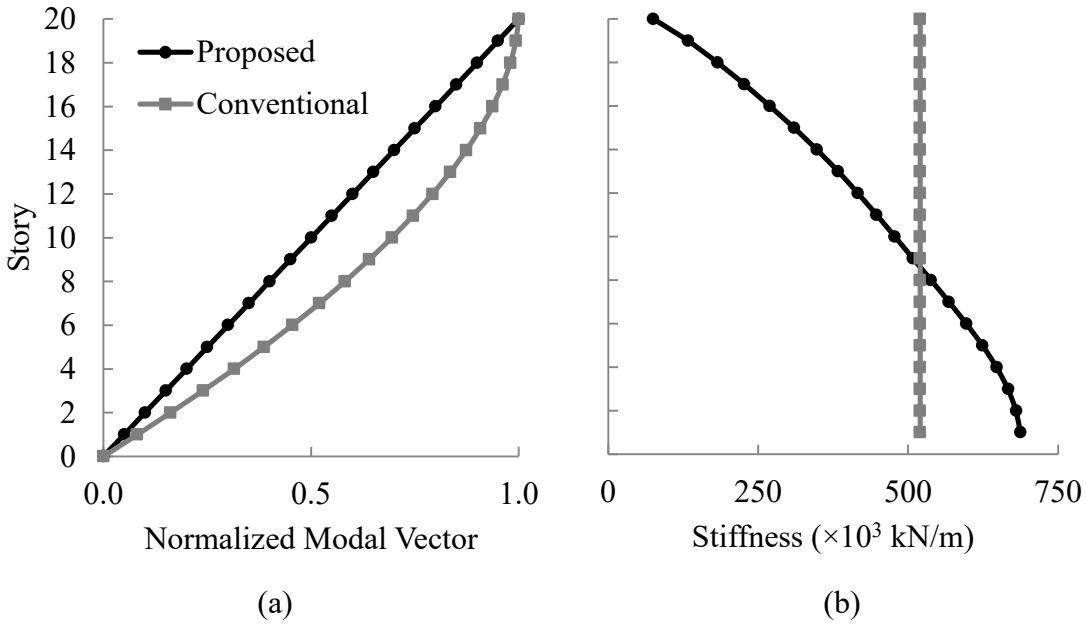

Figure 11. (a) Combined mode shapes; (b) Stiffness distributions of 20-story shear-beam model

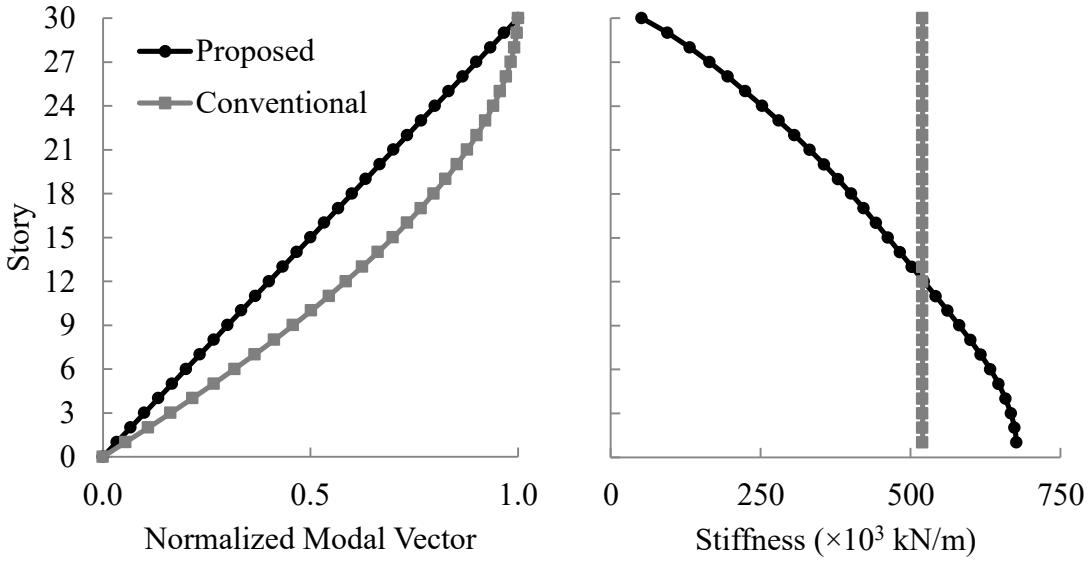

(a) (b)

Figure 12. (a) Combined mode shapes; (b) Stiffness distributions of 30-story shear-beam model

3.4.2. Properties and Scaling of the Ground Motion Records

In order to evaluate the effects of the proposed stiffness distribution on the drift behavior of the shear-beam models, linear time-history analyses were performed. A suite of ten ground motion records were adopted from Lepage (1997) for this purpose. These ground motions were selected so as to represent the typical ground motion demand used in contemporary seismic design codes after the scaling. Information about the ground motions are given in Table 1. The table includes the location and the date of the earthquake, the station name, the characteristic period (T_g, period at which the nearly constant acceleration region ends), the record duration, and the recorded peak ground acceleration (PGA). The characteristic periods of the records range from 0.35 seconds to 1.14 seconds. Therefore, the adopted records refer to a wide range of site conditions. Acceleration time histories of the ground motion records are given in Appendix A.

Additionally, the adopted records were scaled to normalize the spectral drift demands of each ground motion as prescribed by Lepage (1997). The normalization procedure proposed by Lepage depends on a simplified method for estimating the drift response of buildings for a given damping factor (Shimazaki & Sozen, 1984). Using this procedure, a reasonable upper bound for the spectral response can be obtained for

systems with an initial period of up to 3.0 seconds. This upper bound for any given period and ground motion record can be estimated using the expression in (3.19) for spectral acceleration and the expression in (3.20) for spectral displacement for the systems with a 2% damping factor. Thus, envelope acceleration, S_a, and displacement, S_d, response spectra can be obtained by combining the calculated values for a selected period range using the given equations.

$$S_a = \begin{cases} F_a \cdot \alpha \cdot g & \text{for } T < T_g \\ F_a \cdot \alpha \cdot g \cdot \dfrac{T_g}{T} & \text{for } T \geq T_g \end{cases} \tag{3.19}$$

$$S_d = \begin{cases} \dfrac{F_a \cdot \alpha \cdot g}{(2\pi)^2} \cdot T^2 & \text{for } T < T_g \\ \dfrac{F_a \cdot \alpha \cdot g \cdot T_g}{(2\pi)^2} \cdot T & \text{for } T \geq T_g \end{cases} \tag{3.20}$$

where,

F_a = Acceleration amplification factor. A value of 3.75 for oscillators, with 2% damping ratio, is representative of a wide range of earthquakes (Shibata & Sozen, 1976);

g = Acceleration of gravity;

α = Peak ground acceleration expressed as a coefficient of the acceleration of gravity;

T_g = Characteristic period for ground motion. Period at which the nearly constant acceleration region ends.

Equations (3.19) and (3.20) are based on the assumption that for periods lower than T_g, the acceleration response of the structures is nearly constant; and for periods higher than T_g, velocity response is nearly insensitive to period variation.

Table 1. Ground motion records

Earthquake	Station	Component	Peak Ground Acceleration (g)	Record Duration (sec)	Characteristic Period, T_g (sec)
San Fernando 09/02/1971	Castaic Old Ridge Route, California	N21E	0.32	30	0.35
Northridge 17/01/1994	Tarzana Cedar Hill Nursery, California	NS	0.99	30	0.44
Chile 03/03/1985	Llolleo D.I.C., Chile	N10E	0.71	50	0.50
Imperial Valley 18/05/1940	El Centro Irrigation District, California	NS	0.35	30	0.55
Hyogo-Ken-Nanbu 17/01/1995	Kobe KMMO, Japan	NS	0.83	30	0.70
Kern County 21/07/1952	Taft Lincoln School Tunnel, California	N21E	0.16	30	0.72
Western Washington 13/04/1949	Seattle Army Base, Washington	S02W	0.07	50	0.89
Miyagi-Ken-Oki 12/06/1978	Sendai Tohoku University, Japan	NS	0.26	40	0.95
Kern County 21/07/1952	Santa Barbara Corthouse, California	S48E	0.13	40	1.03
Tokachi-Oki 16/05/1968	Hachinohe Harbor, Japan	EW	0.19	40	1.14

In this study, the envelope displacement response spectrum obtained for El Centro record scaled to 0.4*g* peak ground acceleration used for scaling other ground motion records. Substituting 0.4 for α in (3.20) gives the envelope drift response as

$$S_d = \begin{cases} 373\,T^2\,(\text{mm}) \\ 205\,T\,(\text{mm}) \end{cases} \quad \text{for} \quad \begin{matrix} T < T_g \\ T \geq T_g \end{matrix} \tag{3.21}$$

Each record was then linearly scaled in a way that its peak ground acceleration coefficient, α, yields a similar S_d when substituted into (3.20). The peak ground accelerations used to normalize each record and the corresponding scale factors are presented in Table 2. It can be observed from the table that lower values of peak ground acceleration correspond to higher values of characteristic periods for ground motions. Therefore, the product of α times T_g is constant for all ground motions.

The displacement response spectra of the scaled ground motion records are shown in Figure 13 with the envelope spectrum obtained using the expressions in (3.21).

Table 2. Properties of the scaled ground motion records

Record Name	**Characteristic Period, T_g (sec)**	**Original PGA (g)**	**Scaled PGA (g)**	**Scale Factor**
Castaic 1971 N21E	0.35	0.32	0.63	1.97
Tarzana 1994 NS	0.44	0.99	0.50	0.51
Llolleo 1985 N10E	0.50	0.71	0.44	0.62
El Centro 1940 NS	0.55	0.35	0.40	1.14
Kobe 1995 NS	0.70	0.83	0.31	0.37
Taft 1952 N21E	0.72	0.16	0.31	1.94
Seattle 1949 S02W	0.89	0.07	0.25	3.57
Sendai 1978 NS	0.95	0.26	0.23	0.88
Santa Barbara 1952 S48E	1.03	0.13	0.21	1.62
Hachinohe 1968 EW	1.14	0.19	0.19	1.00

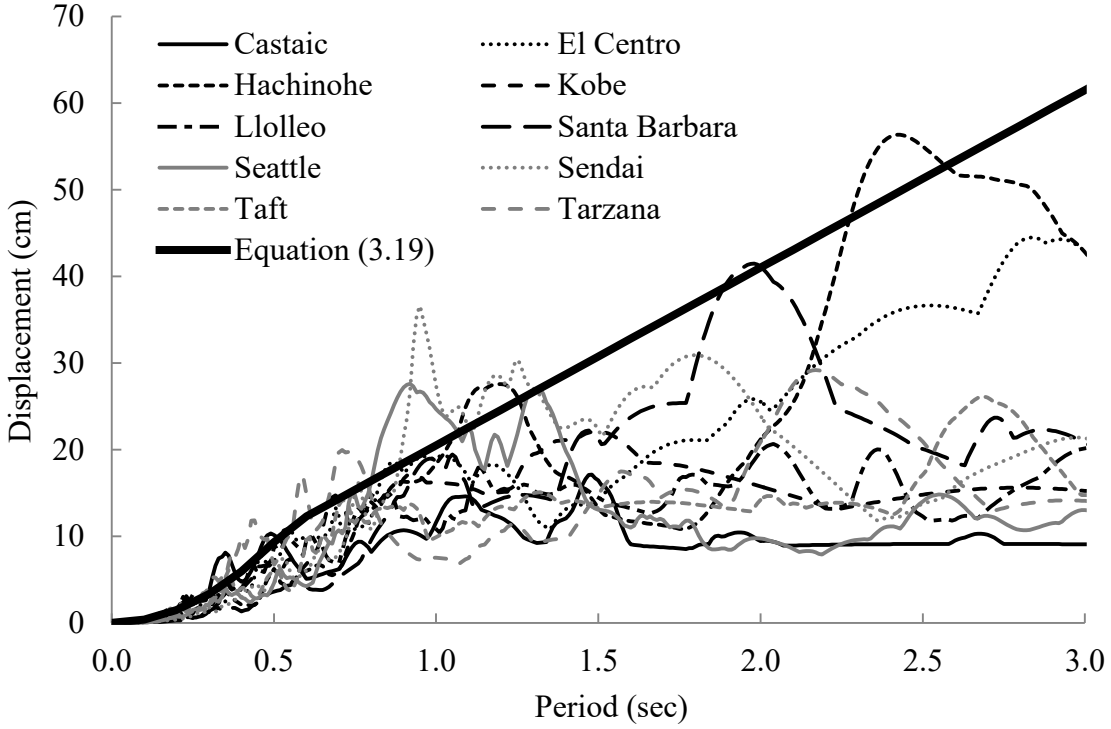

Figure 13. Displacement response spectra of the scaled ground motion records

3.4.3. Analysis Results

The results of the linear time-history analyses of the shear-beam systems are presented for two extreme conditions. First, the interstory drift distributions are presented for the step at which the maximum roof displacement was attained. Second, the envelope interstory drifts reached at each floor is presented. This case is actually a composite representation of different instants during the ground motions. Moreover, the mean (μ), mean plus one standard deviation ($\mu+\sigma$), and mean minus one standard deviation ($\mu-\sigma$) of the results are also given.

3.4.3.1. 10-Story Shear-Beam Models

The interstory drift distributions of the 10-story shear-beam models at the moment when the peak roof displacements were attained are given in Figure 14 and Figure 15 for each ground motion. Figure 14 shows the results of the shear-beam

models with the conventional stiffness distribution. Figure 15 shows the results for the systems with the proposed stiffness distribution. Additionally, the averages of the results are presented together with plus and minus one standard deviation.

Figure 16 and Figure 17 show the envelope interstory drifts observed at each floor for each ground motion. The mean envelopes are also given along with plus and minus one standard deviation.

In Figure 18 and Figure 19, a comparison of mean interstory drift distributions with plus and minus one standard deviations is presented together for the conventional and the proposed systems. Figure 18 is the comparison for the step of maximum roof drift. Figure 19 is the comparison for envelope interstory drift ratios.

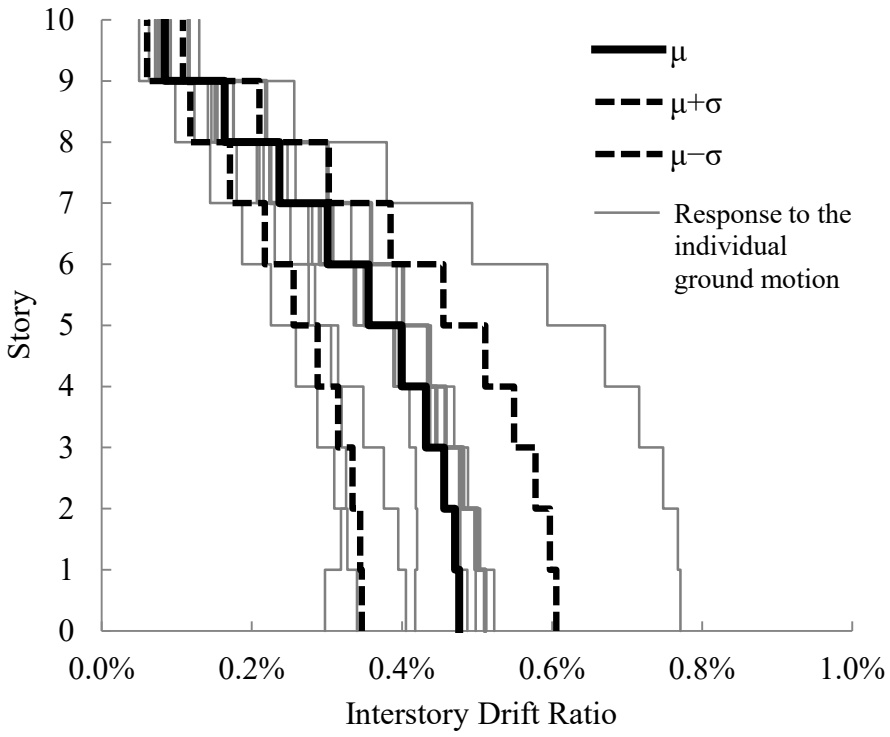

Figure 14. Interstory drift distribution of conventional 10-story shear-beam models at maximum roof displacement

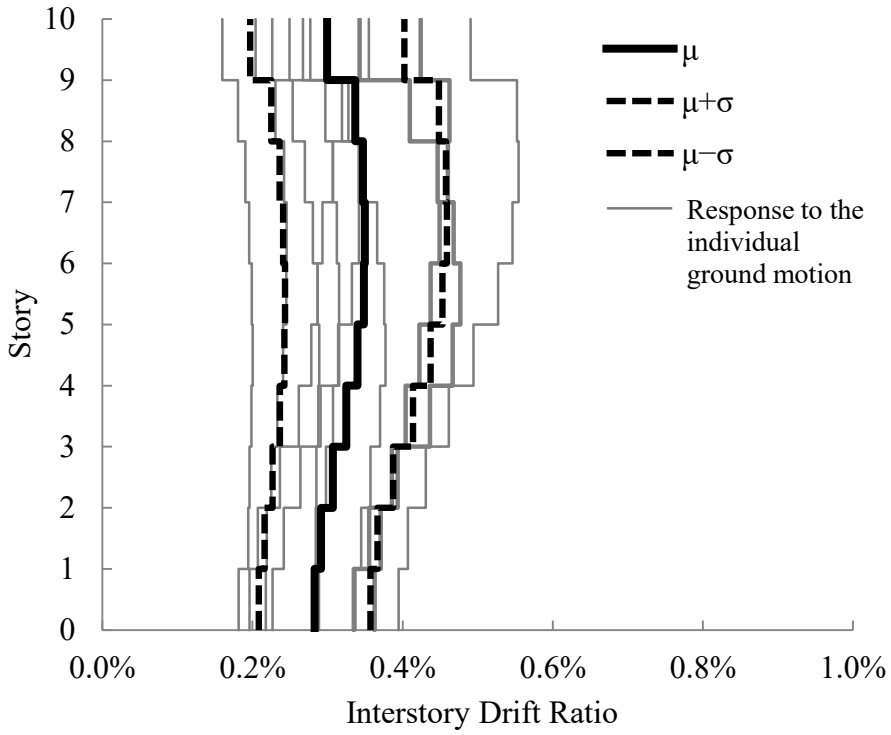

Figure 15. Interstory drift distribution of proposed 10-story shear-beam models at maximum roof displacement

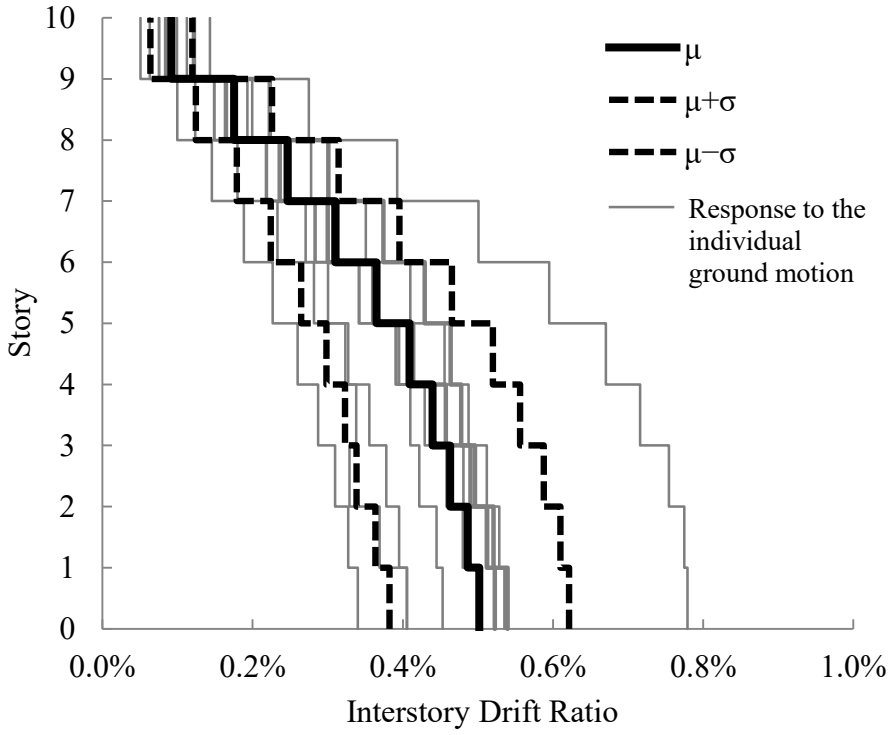

Figure 16. Envelope interstory drifts of conventional 10-story shear-beam models

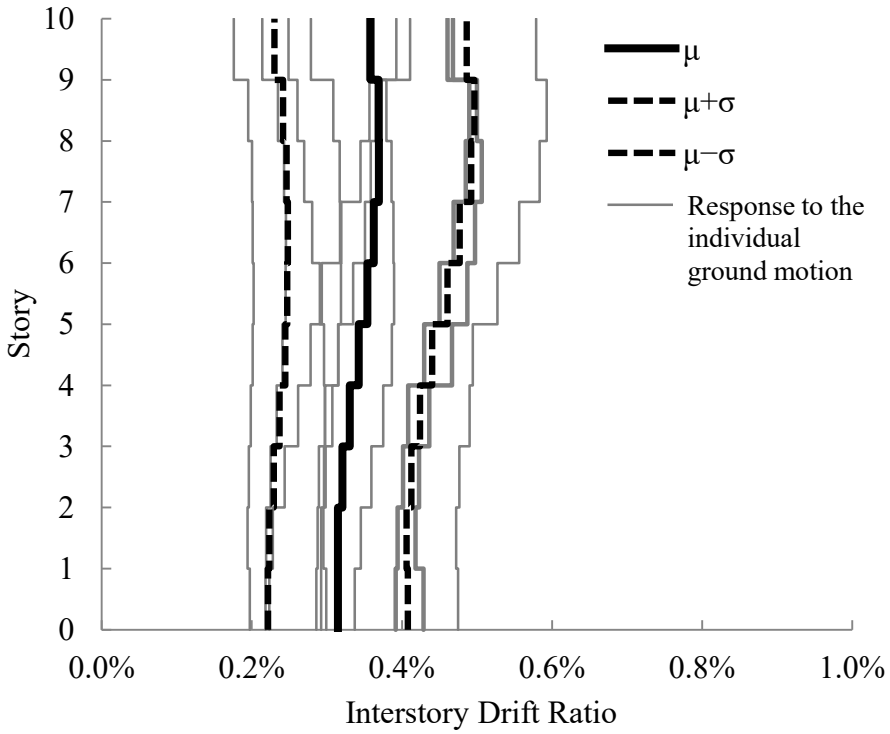

Figure 17. Envelope interstory drifts of proposed 10-story shear-beam models

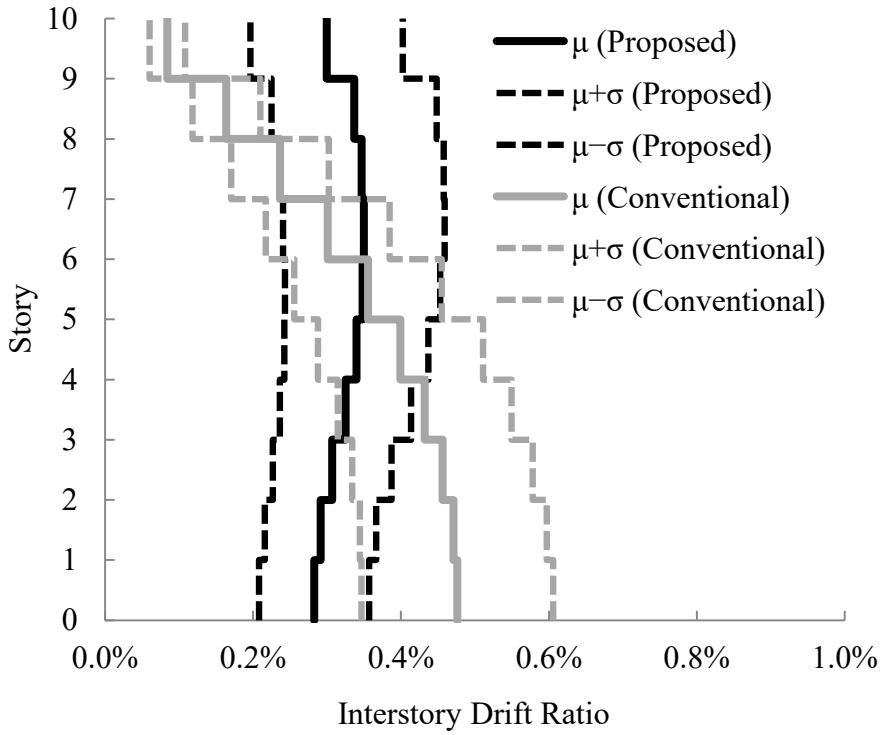

Figure 18. Comparison of mean interstory drift distributions of 10-story shear-beam models at maximum roof displacement

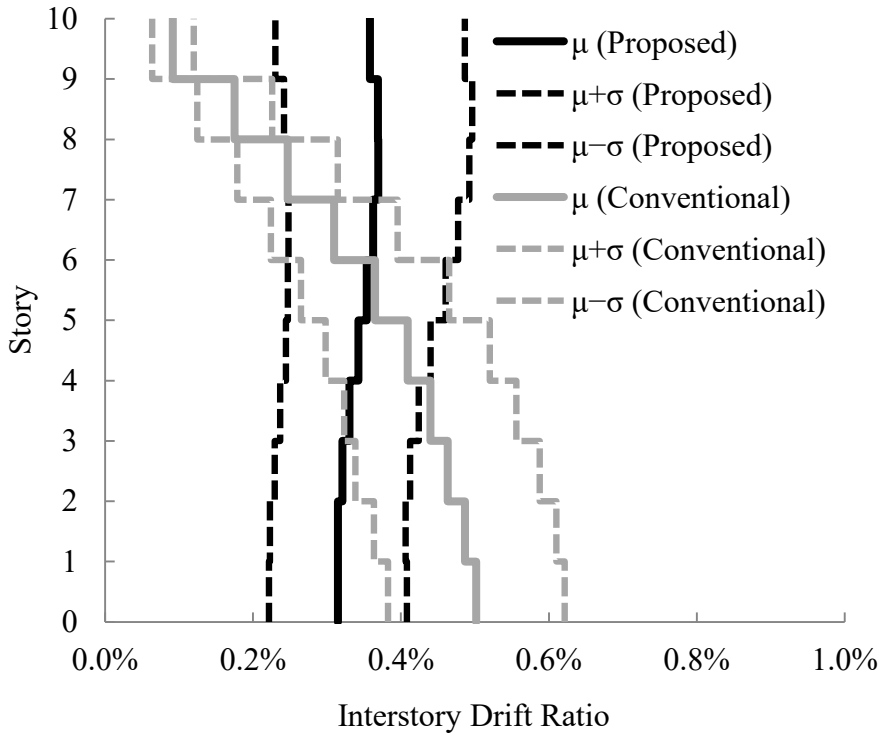

Figure 19. Comparison of mean envelope interstory drifts of 10-story shear-beam models

It can be observed from the figures that, for both systems, the distribution patterns of the interstory drifts are similar for the maximum roof displacement and the envelope cases. Therefore, evaluating the results for the envelope case is sufficient. For the conventional system, the interstory drift ratios increase towards the lower stories. In average, the maximum envelope interstory drift (observed at the first story) is 5.6 times greater than the minimum envelope interstory drift (observed at the tenth story). The coefficient of variation (COV) of mean envelope interstory drifts of the conventional system is 0.40. This parameter represents the amount of deviation of interstory drift distribution from a uniform pattern. On the other hand, the optimum stiffness distribution yielded nearly uniform interstory drift distributions, as intended. The COV of mean envelope drifts for this system is 0.06.

3.4.3.2. 20-Story Shear-Beam Models

The interstory drift distributions of the 20-story shear-beam models for the analysis step at which the peak roof displacements were attained are given in Figure 20

and Figure 21 for each ground motion. Figure 20 shows the results of the systems with the conventional stiffness distribution. Figure 21 shows the results for the systems with the optimum stiffness distribution. Additionally, the averages of the results are presented together with plus and minus one standard deviation.

Figure 22 and Figure 23 shows the envelope interstory drifts observed at each story for each ground motion. The mean envelopes are also given along with plus and minus one standard deviation.

In Figure 24 and Figure 25, a comparison of mean interstory drift distributions with plus and minus one standard deviations is presented in the same plot for the conventional and the proposed systems. Figure 24 is the comparison for the step of maximum roof drift. Figure 25 is the comparison for envelope interstory drift ratios.

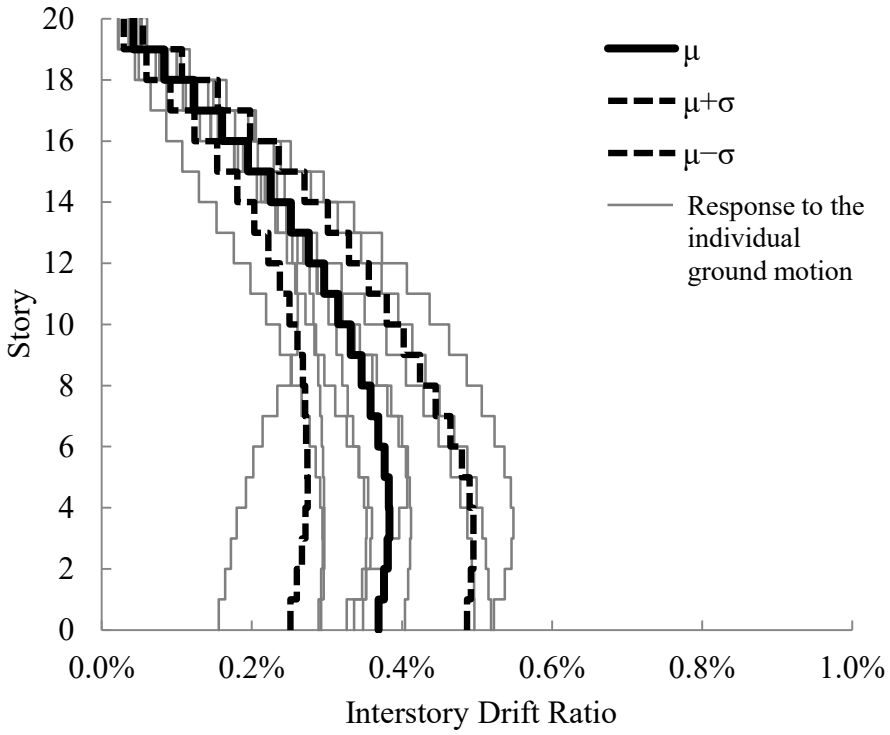

Figure 20. Interstory drift distribution of conventional 20-story shear-beam models at maximum roof displacement

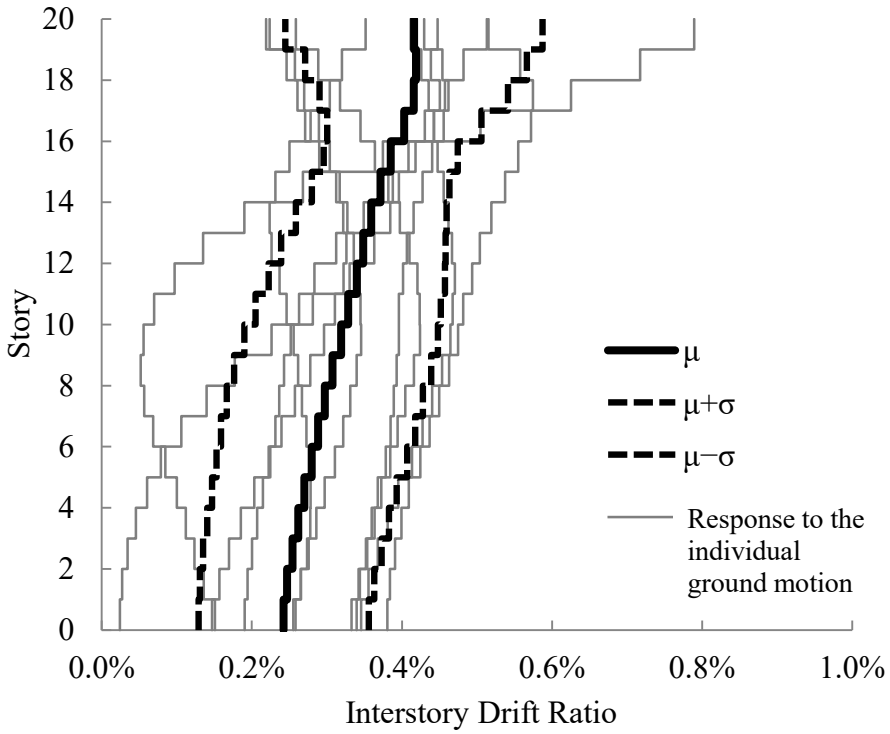

Figure 21. Interstory drift distribution of proposed 20-story shear-beam models at maximum roof displacement

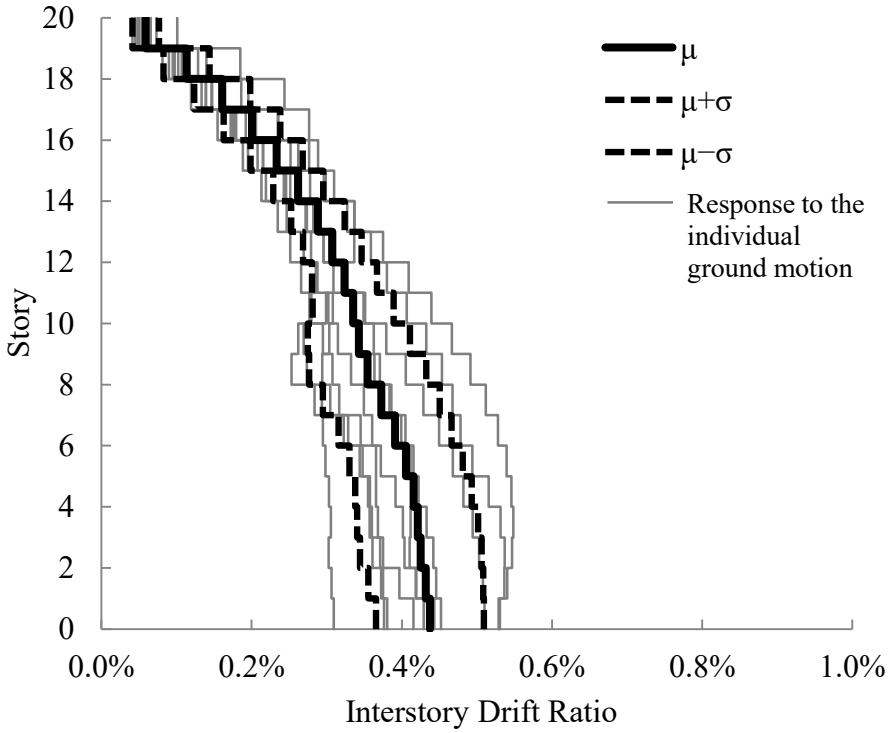

Figure 22. Envelope interstory drifts of conventional 20-story shear-beam models

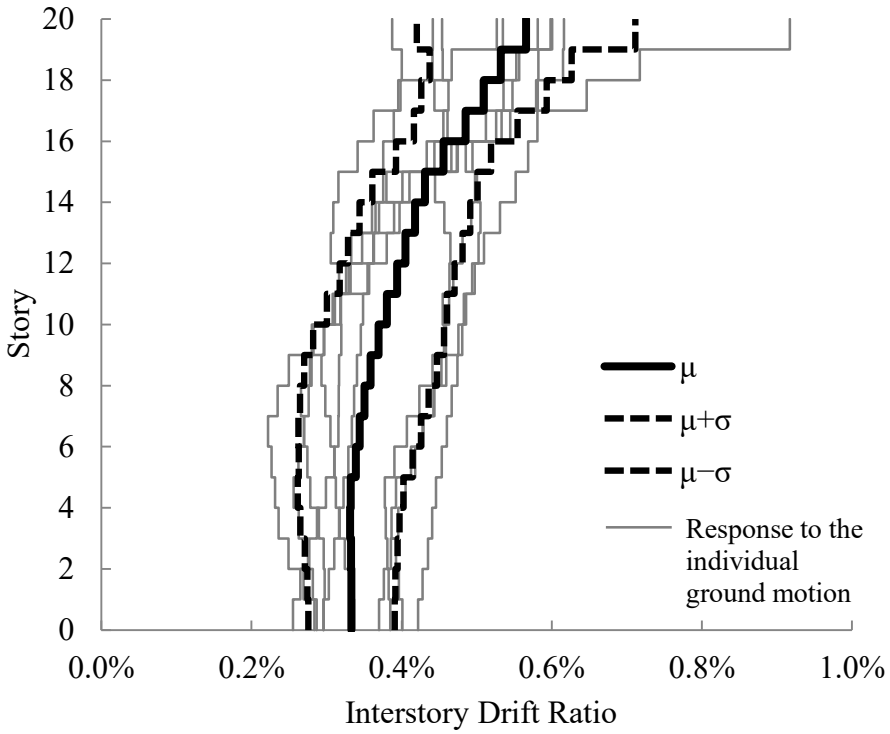

Figure 23. Envelope interstory drifts of proposed 20-story shear-beam models

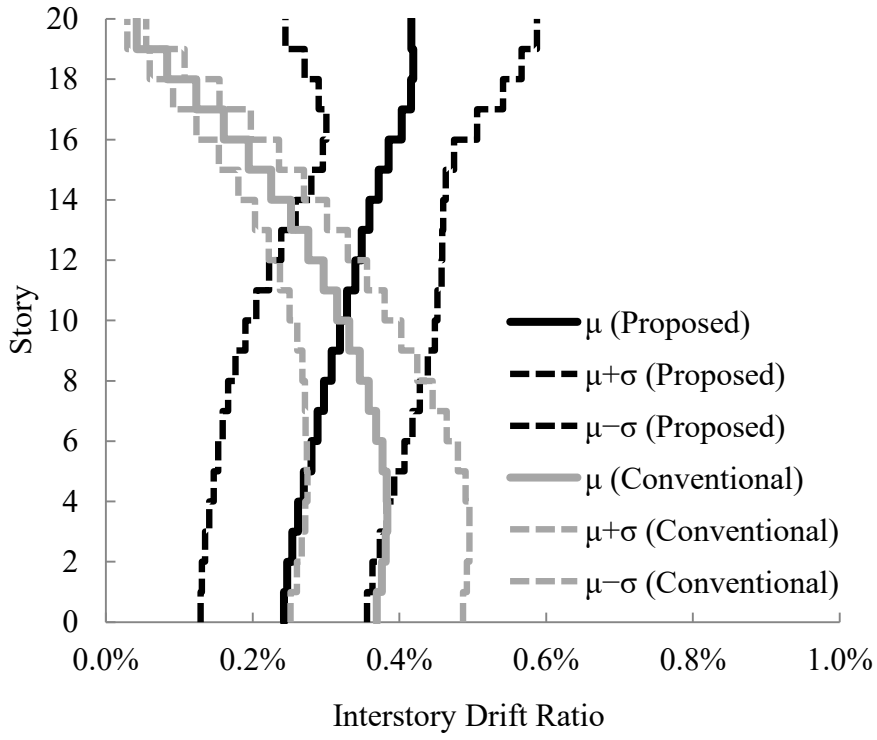

Figure 24. Comparison of mean interstory drift distributions of 20-story shear-beam models at maximum roof displacement

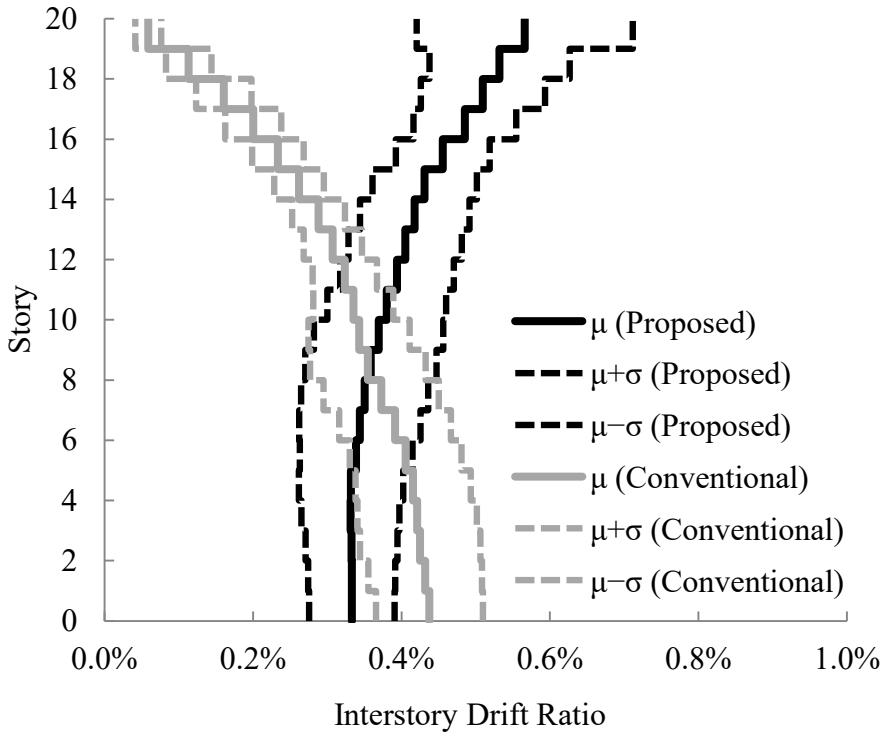

Figure 25. Comparison of mean envelope interstory drifts of 20-story shear-beam models

From the figures, it can be observed that, for both systems, the distribution patterns of the interstory drifts are similar for the maximum roof displacement and the envelope cases. Therefore, the results are evaluated for the envelope case. The interstory drift ratios increase towards the lower stories at the conventional system. In average, the maximum envelope interstory drift (observed at the first story) is 11 times greater than the minimum envelope interstory drift (observed at the top story). The COV of mean envelope interstory drifts of the conventional system is 0.36. On the other hand, the optimum stiffness distribution yielded more balanced interstory drift distributions, as intended. However, the drifts increased towards the upper stories. The interstory drift ratio of the top story is dramatically higher than that of the other stories in the Castaic ground motion. Interstory drift distributions of other ground motions are similar to that of the mean pattern. In average, the maximum envelope interstory drift (observed at the top story) is 1.7 times greater than the minimum envelope interstory drift (observed at the first story). The COV of mean envelope drifts for this system is 0.19.

3.4.3.3. 30-Story Shear-Beam Models

The interstory drift distributions of the 30-story shear-beam models for the analysis step at which the peak roof displacements were attained are given in Figure 26 and Figure 27 for each ground motion. Figure 26 shows the interstory drift results of the systems with the conventional stiffness distribution. Figure 27 shows the results for the systems with the optimum stiffness distribution. Additionally, the averages of the results are presented together with plus and minus one standard deviation.

Figure 28 and Figure 29 shows the envelope interstory drifts observed at each story for each ground motion. The mean envelopes are also given along with plus and minus one standard deviation.

In Figure 30 and Figure 31, a comparison of mean interstory drift distributions with plus and minus one standard deviations is presented in the same plot for conventional and proposed systems. Figure 30 is the comparison for the step of maximum roof drift. Figure 31 is the comparison for envelope interstory drift ratios.

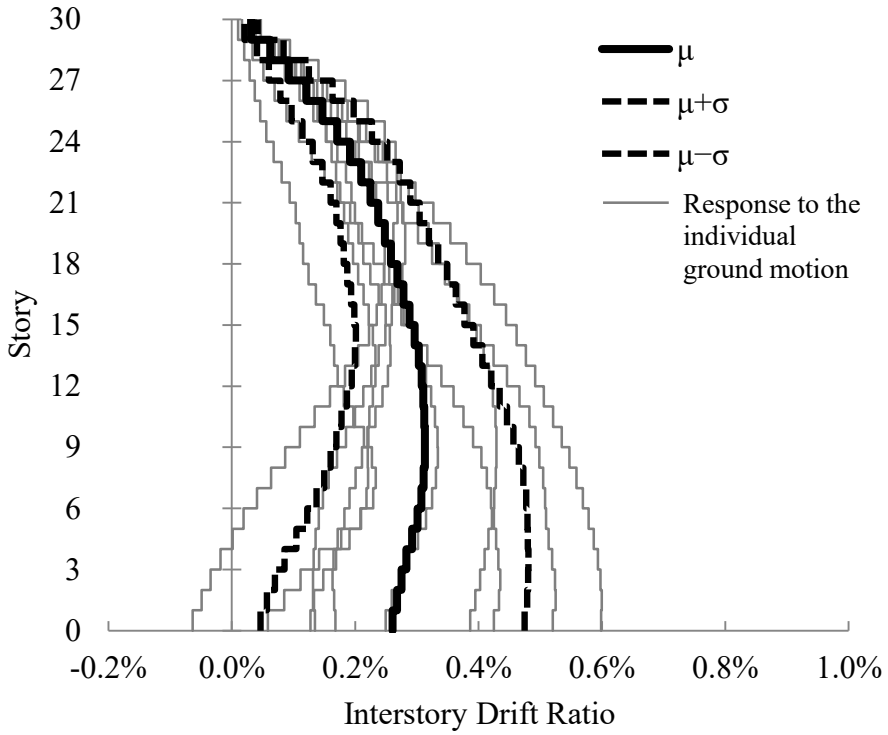

Figure 26. Interstory drift distribution of conventional 30-story shear-beam models at maximum roof displacement

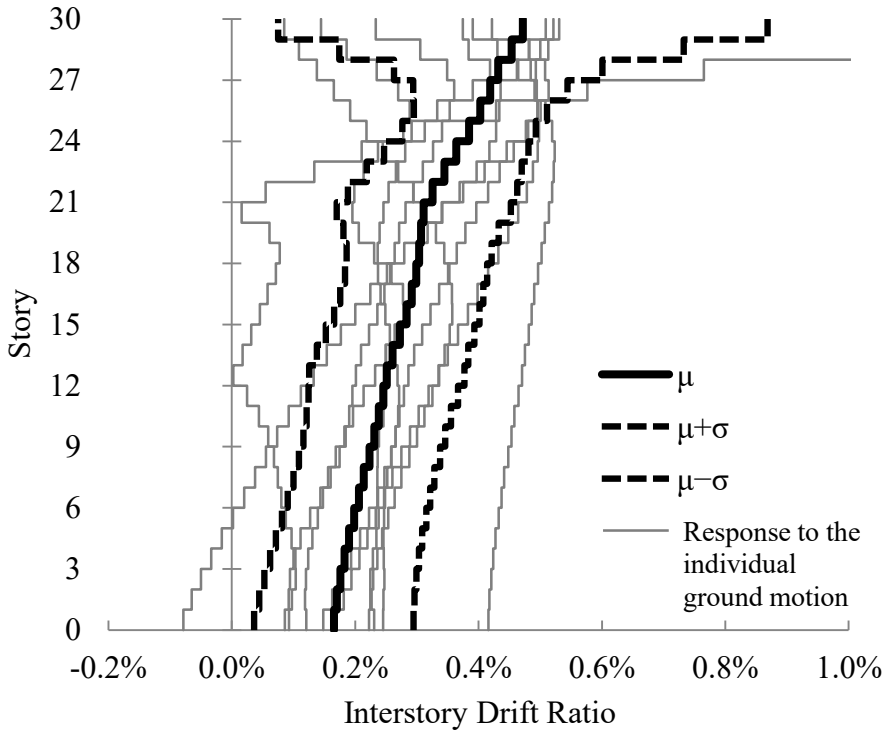

Figure 27. Interstory drift distribution of proposed 30-story shear-beam models at maximum roof displacement

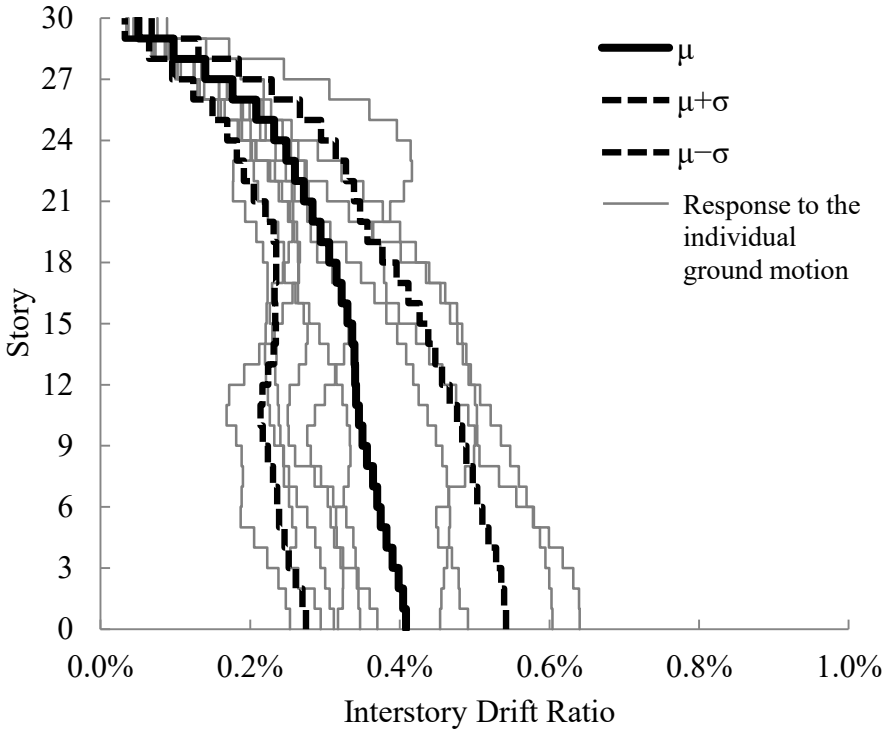

Figure 28. Envelope interstory drifts of conventional 30-story shear-beam models

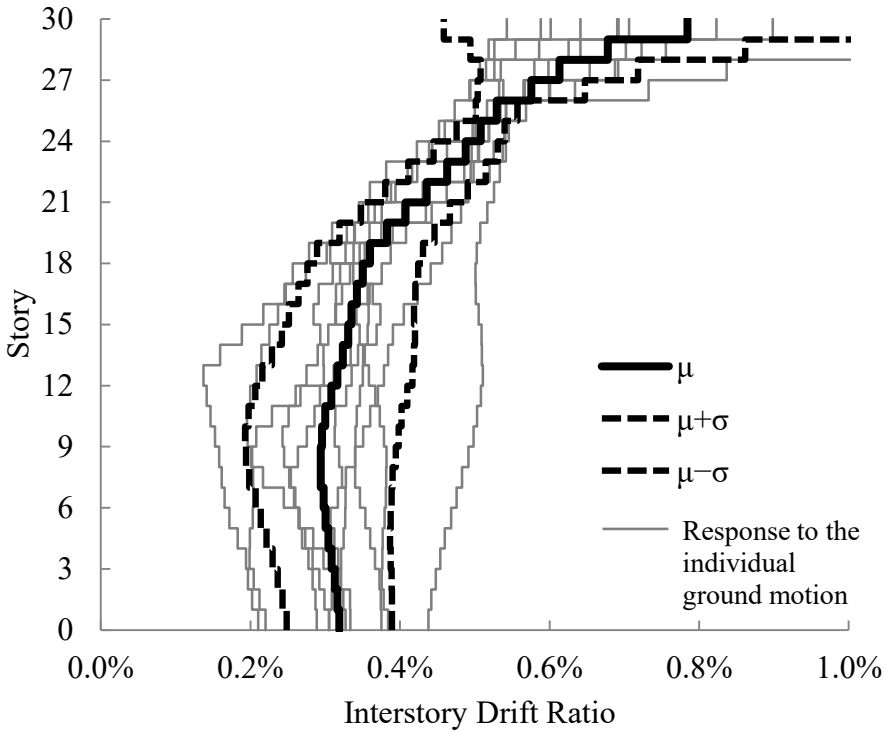

Figure 29. Envelope interstory drifts of proposed 30-story shear-beam models

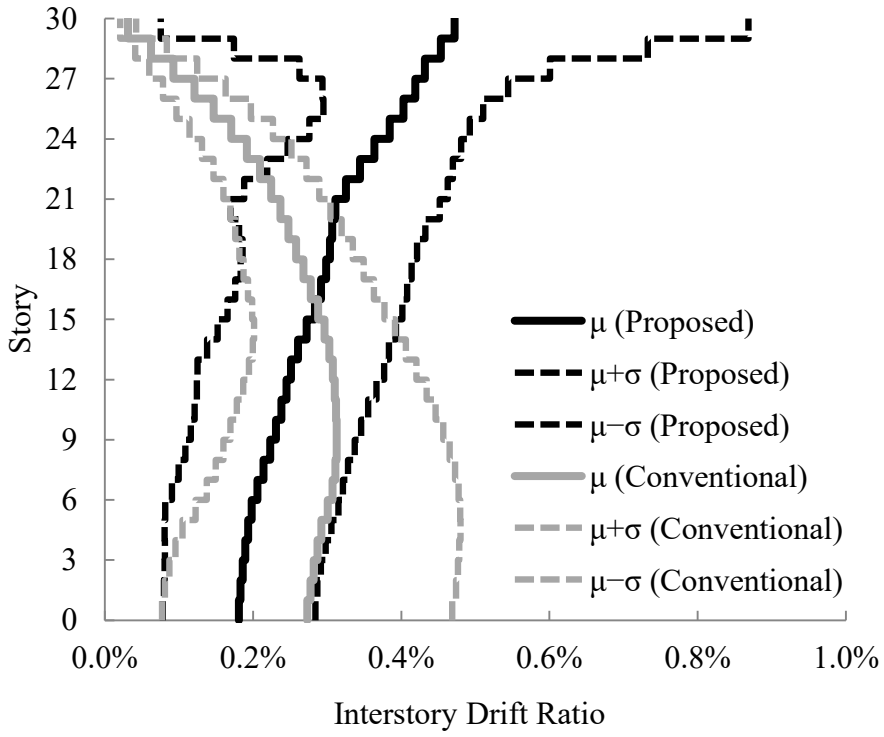

Figure 30. Comparison of mean interstory drift distributions of 30-story shear-beam models at maximum roof displacement

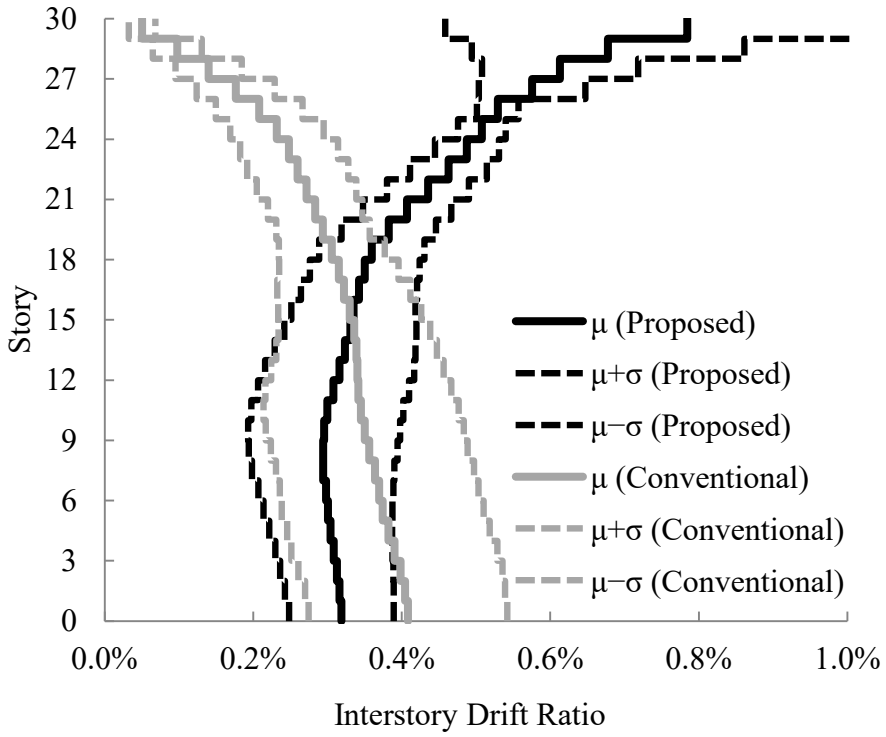

Figure 31. Comparison of mean envelope interstory drifts of 30-story shear-beam models

It can be observed from the figures that, unlike 10- and 20-story systems, the difference between the interstory drift distribution patterns become significant between the maximum roof displacement and the envelope cases. In the former case, the interstory drift ratios increase towards the lower stories at the conventional system. In average, the maximum envelope interstory drift (observed between the 6th and 13th story) is 7.8 times greater than the minimum envelope interstory drift (observed at the top story). The COV of mean envelope interstory drifts of the conventional system is 0.33. On the other hand, interstory drifts concentrated at the upper parts of the proposed system, while they are lower at the bottom parts. The COV of mean envelope interstory drifts of the proposed system is 0.30.

For the envelope case, the concentration of drifts at the upper stories of the proposed system is more significant. Again, the Castaic ground motion yielded the greatest interstory drift demand (1.8%) at the top story of the proposed system. In average, the maximum envelope interstory drift (observed at the top story) is 2.7 times greater than the minimum envelope interstory drift (observed between the 7th and the 10th stories). The COV of mean envelope interstory drifts of the proposed system is 0.33.

3.4.4. Discussion of the Results

The results showed that the interstory drifts concentrated towards the lower parts at the conventional systems. The upper parts did not contribute significantly to the overall drift behavior. On the other hand, the proposed stiffness distribution managed to reduce the interstory drifts at the lower floors up to 40% at the 10-story systems, up to 30% at the 20-story systems, and up to 20% at the 30-story systems. The interstory drifts at the upper parts of the proposed systems were greater than those of the conventional system. A combination of these two effects led to a nearly uniform interstory drift distribution at the 10-story systems. However, as the number of stories increase, the interstory drifts at the upper parts became excessive. As a result, the interstory drifts concentrated at the upper parts – especially at the 30-story systems. The COV of the interstory drifts are given in Table 3 for all systems. The COV of the interstory drifts at the proposed system is lower than that of the conventional system at the 10- and 20-story systems. However, they are approximately equal to each other at the 30-story system. The lowest COV was observed at the proposed 10-story system. These observations imply that the effectiveness of the proposed stiffness distribution decrease as the number of stories increases.

Table 3. Coefficient of variations of mean envelope interstory drift distributions

System	COV of Interstory Drift Distributions	
	Conventional	Proposed
10-Story	0.40	0.06
20-Story	0.36	0.19
30-Story	0.33	0.30

The excessive interstory drifts at the uppermost parts of the taller systems may be attributed to the so-called “whiplash effect” (Clough & Benuska, 1965; Goel, 1967). The whiplash effect was observed to take place especially at the slender buildings. This type of structures generally has stories with lower mass and/or stiffness at the upmost parts compared to those of the lower parts. As a result, these stories deflect dramatically higher during the earthquakes. Likewise, the stiffness of the upper parts is lower than that of the lower parts as a result of the proposed design procedure. The ratio of the story stiffness of the top and the first stories are 0.20, 0.10, and 0.07 for the 10-, 20-,

and 30-story systems, respectively. The upper parts of the systems get weaker as the number of stories increase. Consequently, the whiplash effect becomes significant.

Furthermore, the contribution of the higher modes to the overall response is another source for the whiplash effect. As the systems get higher, spectral demands corresponding to the periods of the higher modes become larger at some ground motion records (e.g. Castaic ground motion). Therefore, the envelope interstory drifts may become accentuated if the maximum drift responses of more than a single mode are combined at a certain moment during the earthquake (French, 1971). Figure 32 shows the contribution of the first three modes to the overall displacement of the proposed system at the time instant of the maximum roof displacement. The upper stories experienced envelope interstory drifts at this step. It can be observed that, in addition to the first mode, the displacement amplitudes of the second and the third modes are also very significant at that time instant. Also, all three modes had the same sign at the top three stories of the system. Thus, the drifts at upper stories were amplified.

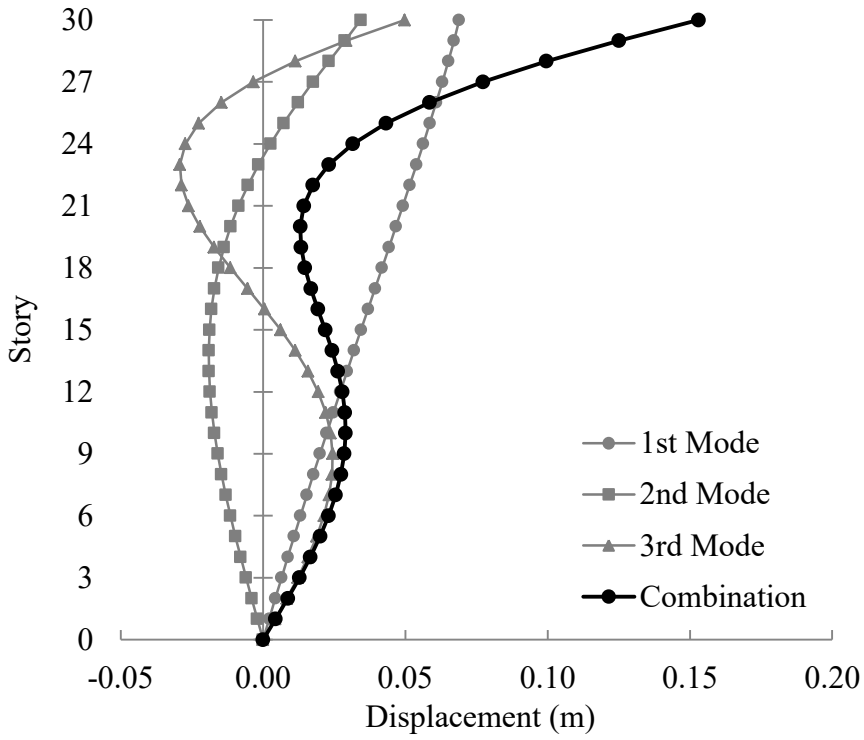

Figure 32. Contribution of first three modes to overall deflection at time step of maximum roof displacement

3.5. Proportioning the Members to Satisfy the Required Stiffness Distribution in Reinforced Concrete Frames

The proposed elastic design procedure yields a unique stiffness distribution for the selected targets. Considering that the lateral stiffness is provided by beams and columns at the frame structures, a simple tool is required to calculate story stiffnesses based on the beam and column cross-sectional dimensions. Thus, the members may be proportioned to achieve the required stiffness distribution throughout the building. A simple and effective method for approximating the lateral stiffness of stories in frame structures, which was proposed by Schultz (1992), was implemented for this purpose.

In this method, an intermediate story is idealized as isolated from the rest of the frame, as shown in Figure 33. This story includes all columns at the story and half of the beam inertias at floor levels above and below. Also, the point of inflection is assumed to be at the mid-lengths of the members.

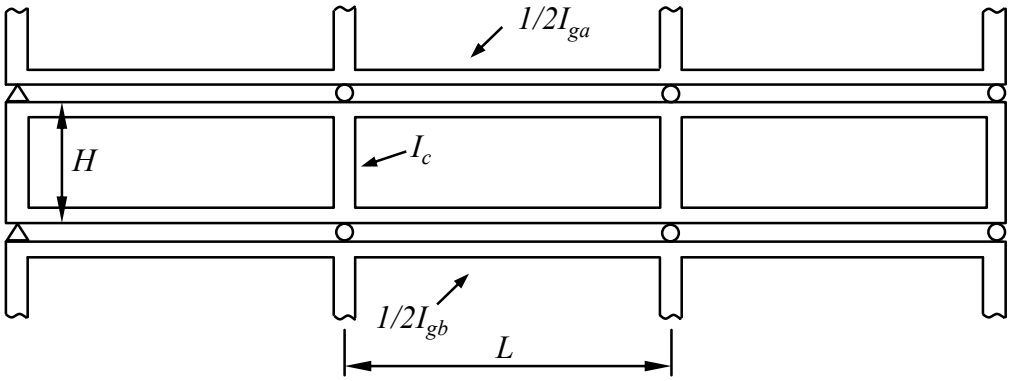

Figure 33. Idealization of an intermediate story (Source: Schultz, 1992)

Then, the equation for the lateral drift is obtained from the equilibrium equations. If this equation is solved for the ratio of story shear to lateral displacement, a closed-form expression for story stiffness is obtained, (3.22).

$$K_s = \left(\frac{24}{H^2}\right)\left(\frac{1+C_s}{\frac{2}{\sum k_c}+\frac{1}{\sum k_{ga}}+\frac{1}{\sum k_{gb}}}\right) \tag{3.22}$$

where,

K_s = Lateral story stiffness;

H = Story height;

C_s = Correction term for the effect of boundaries;

k_c = Flexural stiffness of column;

k_{ga} = Flexural stiffness of the beam above the story;

k_{gb} = Flexural stiffness of the beam below the story;

However, isolating the story for the calculations and the assumption made for the inflection points are not valid for boundary stories (i.e. first and top stories). Correction factors, C_1 and C_t, for these stories were obtained after the comparison of the results obtained by the proposed expression with those of the exact solution. Schultz (1992) observed that the stiffening effect of the fixed-base propagated to the second story, as well. Thus, a correction factor for the second story, C_2, was also proposed. Equations from (3.23) to (3.25) show the proposed expressions for the correction factors.

$$C_1 = \frac{\sum k_c}{22\sum k_{ga}} \tag{3.23}$$

$$C_2 = \frac{\sum k_c}{32\sum k_{gb}} \tag{3.24}$$

$$C_t = \frac{-\sum k_c}{55\sum k_{ga}} \tag{3.25}$$

Schultz also observed that as the number of stories decreases, the effect of the fixed-base influences the stories beyond the second story. Based on this observation, he proposed a correction factor, ξ_s, for low-rise frames, (3.26). This multiplicative factor is calculated for each story and used to modify the story stiffness calculated by (3.22) as $\xi_s K_s$.

$$\xi_s = 1 + \frac{2\sum k_c}{5n^2\left(\sum k_{ga} + \sum k_{gb}\right)} \tag{3.26}$$

The frame members can be proportioned interactively to satisfy the required stiffness distribution using a spreadsheet based on these formulae and this scheme could be applied through a trial-and-error procedure to obtain the intended distribution.

3.6. Linear Dynamic Analyses of Reinforced Concrete Frames

The effects of the proposed stiffness distribution were further evaluated using 10-, 20-, and 30-story elastic reinforced concrete frames. The frames were proportioned so as to satisfy the required stiffness distribution. Interstory drift distributions were observed after conducting linear time-history analyses. The results were compared with the results of the conventional counterpart of each frame.

3.6.1. Properties of the Frames

Two sets of planar reinforced concrete frames were used in this part of the study. The first set includes 10-, 20-, and 30-story linear reinforced concrete frames. These frames were proportioned so as to have the stiffness distribution calculated using the proposed method. The second set consists of the conventional counterparts of the frames in the first set. The frames have five bays and the span length is 5.0 meters at all bays. The story height is 3.0 meters at all floors. A story mass of 1.10 tons/m^2 was assumed per floor area. The model frames were assumed to be located on the interior of a 3-D frame structure. The tributary length in the transverse direction was assumed as 2.5 meters in both directions. Therefore, 125 m^2 of floor area was used for the calculation of the total story mass and gravity load. General configuration of the model frames is presented in Figure 34.

The target fundamental periods are selected as 1.0, 2.0, and 3.0 seconds for the frames with ten, twenty, and thirty stories, respectively. Then, the required stiffness distributions that will yield the target fundamental periods and the intended combined mode shape with a linear drift profile were determined using the proposed method. The members of the proposed frame were proportioned using a spreadsheet that implements the formulae proposed by Schultz (1992). Thus, the cross-sectional dimensions at each story to satisfy the required story stiffness were determined. While determining the member sizes, the following design constraints were considered:

- Columns will have sizes changing in 5 or 10 cm increments.
- Colum sizes will remain constant for at least three stories, where possible.
- The cross-sectional area of a column will not be less than that of the upper story.
- It is preferred to vary the beam depth rather than the beam width, where possible.
- Beam depth will vary in 2-3 cm increments.
- The minimum beam width is 20 cm; the minimum beam depth is 40 cm.

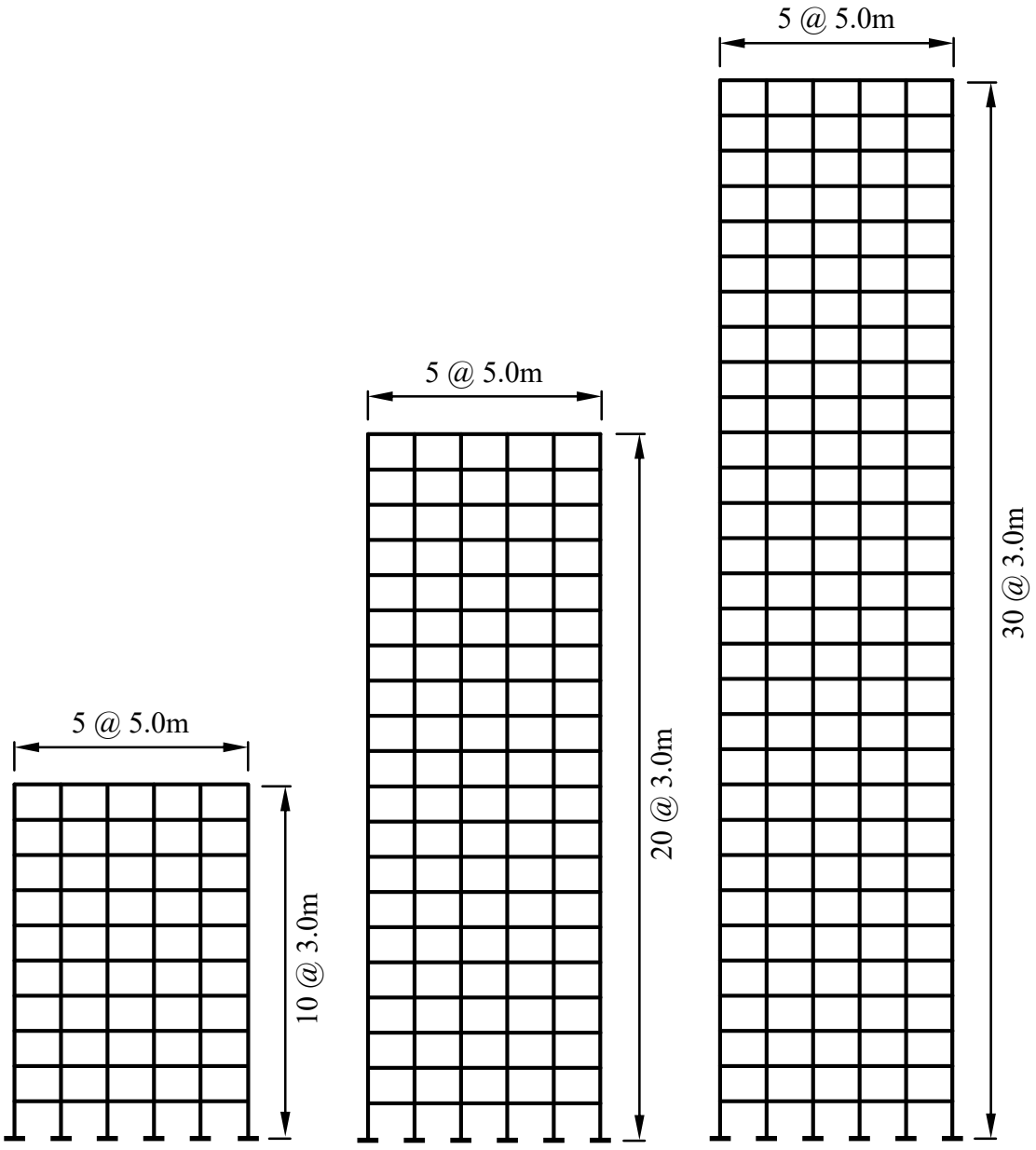

Figure 34. General configuration of the model frames

Table 4. Member cross-section dimensions (in centimeters)

Story	10-Story				20-Story				30-Story			
	Proposed		Uniform		Proposed		Uniform		Proposed		Uniform	
	Column	Beam	Column	Beam	Column	Beam	Column	Beam	Column	Beam	Column	Beam
30									60×60	30×45	75×75	40×65
29									60×60	30×45	75×75	40×65
28									70×70	30×50	75×75	40×65
27									70×70	30×53	75×75	40×65
26									70×70	30×55	75×75	40×65
25									70×70	30×58	75×75	40×65
24									75×75	30×60	75×75	40×65
23									75×75	30×63	80×80	40×65
22									75×75	30×65	80×80	40×65
21									75×75	35×65	80×80	40×65
20					60×60	25×50	75×75	40×65	75×75	35×65	80×80	40×65
19					60×60	30×50	75×75	40×65	75×75	35×68	80×80	40×65
18					70×70	30×55	75×75	40×65	80×80	40×65	80×80	40×65
17					70×70	30×60	75×75	40×65	80×80	40×65	80×80	40×65
16					75×75	30×63	75×75	40×65	80×80	40×68	80×80	40×65
15					75×75	30×65	80×80	40×65	80×80	40×68	85×85	40×65
14					75×75	35×65	80×80	40×65	90×90	40×68	85×85	40×65
13					80×80	35×67	80×80	40×65	90×90	40×68	85×85	40×65
12					80×80	35×70	80×80	40×65	90×90	40×70	85×85	40×65
11					80×80	35×70	80×80	40×65	90×90	40×70	85×85	40×65
10	60×60	30×55	75×75	45×65	80×80	40×70	85×85	40×65	90×90	40×70	85×85	40×65
9	70×70	30×60	75×75	45×65	85×85	40×70	85×85	40×65	95×95	40×73	85×85	40×65
8	75×75	30×67	75×75	45×65	85×85	40×70	85×85	40×65	95×95	40×73	95×95	40×65
7	75×75	35×67	80×80	45×65	85×85	40×73	85×85	40×65	95×95	40×73	95×95	40×65
6	80×80	35×70	80×80	45×65	90×90	40×73	85×85	40×65	95×95	40×73	95×95	40×65
5	80×80	40×70	80×80	45×65	90×90	40×73	95×95	40×65	100×100	40×75	95×95	40×65
4	80×80	40×75	85×85	45×65	90×90	40×75	95×95	40×65	100×100	40×75	95×95	40×65
3	90×90	40×75	85×85	45×65	100×100	40×75	95×95	40×65	100×100	40×75	95×95	40×65
2	90×90	35×65	85×85	45×65	100×100	25×55	95×95	40×65	100×100	30×50	95×95	40×65
1	90×90	25×40	85×85	45×65	100×100	25×40	95×95	40×65	100×100	25×40	95×95	40×65

The concrete compressive strength was assumed to be 25 MPa. Based on this, the modulus of elasticity of the concrete was taken as 30 000 MPa for the stiffness calculations. The cross-sectional dimensions of the proportioned frame members are shown in Table 4. Note that, the conventional frames were proportioned such that they have approximately the same fundamental period as the proposed frames. The beam cross-sections do not change throughout the elevation in the conventional frames. The column sizes were decreased in proportion with the axial load levels as done in general practice.

Figure 35, Figure 36, and Figure 37 show the required stiffness distribution together with the provided stiffness at the proposed frames and the stiffness distribution of the conventional frames.

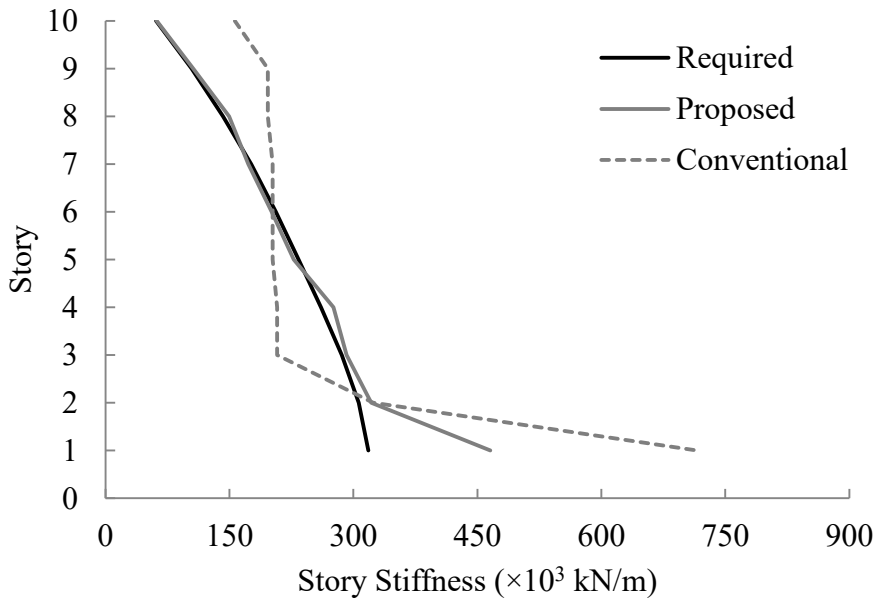

Figure 35. Required and provided stiffness distributions at 10-story frames

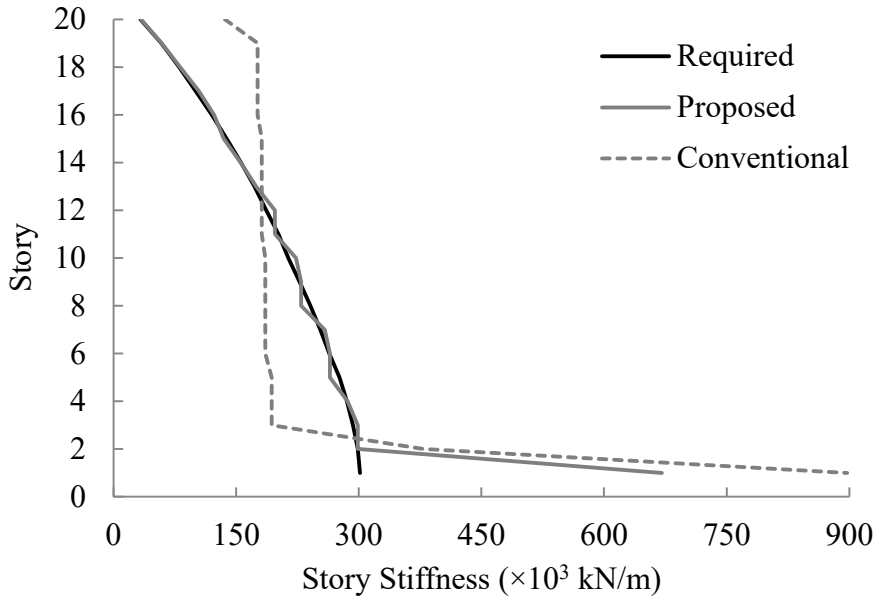

Figure 36. Required and provided stiffness distributions at 20-story frames

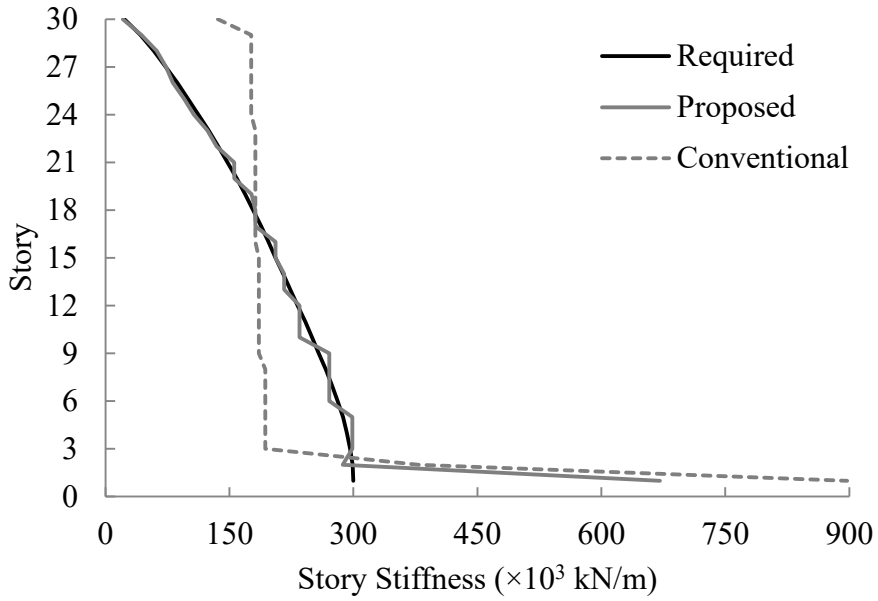

Figure 37. Required and provided stiffness distributions at 30-story frames

As seen from the figures, the required stiffness was satisfied in all stories except the first two stories. The provided stiffness values at the first two stories are significantly higher than the required. The stiffening effect of base-fixity requires smaller columns at the first and the second floors than those in the upper floors to provide the required stiffness. However, this requirement was ignored due to the design constraints. The columns in the first and the second stories were kept the same with those in the third story. As a result, the stiffness values of the first two stories are

significantly higher than the required. Except for these stories, the required stiffness was provided satisfactorily at all frames. The ratio of the provided to the required story stiffness stays between 0.90 and 1.10 for all stories except the first two.

The proportioned frames were numerically modeled in SAP2000 (CSI, 2016) software. Modal analyses were performed to determine the dynamic properties of the frames. Figure 38 shows the combined mode shapes of the proposed and conventional frames along with the target combined mode shapes. The modal vectors are normalized such that the modal deflection at the top story is equal to unity in the plots. The y-axis of the plots shows the normalized frame height where the total height is represented by unity.

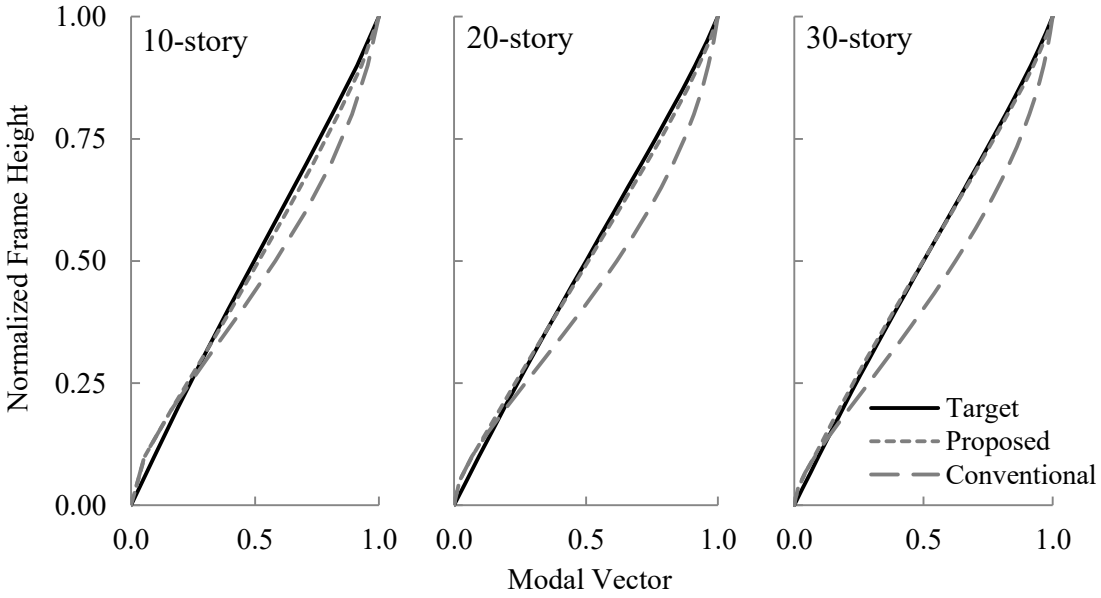

Figure 38. Target combined mode shape and combined mode shapes of proposed and conventional mode shapes

It can be seen from the plots that the target mode shapes are obtained with sufficient accuracy at the proposed frames. Also, it can be observed that the first mode shapes of the conventional frames are quite different from the target mode shapes at the upper two-thirds of the frames. The first mode periods obtained in SAP2000 are presented in Table 5 along with the target fundamental periods for each frame.

Table 5. Fundamental periods of conventional and proposed frames

Frame	Fundamental Period (sec)		
	Target	Conventional	Proposed
10-Story	1.00	1.07	1.09
20-Story	2.00	2.33	2.24
30-Story	3.00	3.65	3.51

The fundamental periods of the modeled frames are approximately 8%, 14%, and 19% higher than the targeted periods for the 10-, 20-, and 30-story frames, respectively.

3.6.2. Ground Motion Set

The same ground motion set as which was used for the analyses of shear-beam systems was used for the linear time history analyses of the model frames, as well. Detailed information on the properties and the scaling of the ground motions can be found in Section 3.4.2.

3.6.3. Analysis Results

The results of the linear time-history analyses of the frames are presented for two cases. First, the interstory drift distributions are presented for the time instant of the maximum roof displacement. Second, the envelope interstory drifts reached at each floor is presented. Moreover, the mean (μ), mean plus one standard deviation ($\mu+\sigma$), and mean minus one standard deviation ($\mu-\sigma$) of the results are also given.

3.6.3.1. 10-Story Frames

The interstory drift distributions of the 10-story frames at the time step when the peak roof displacements were attained are given in Figure 39 and Figure 40 for each ground motion. Figure 39 shows the results for the conventional frame. Figure 40 displays the results of the frame proportioned using the proposed approach.

Additionally, the averages of the results are presented together with plus and minus one standard deviation on the same plots.

Figure 41 and Figure 42 shows the envelope interstory drifts observed at each floor for each ground motion for the conventional and proposed frames, respectively. The mean envelopes are also given along with plus and minus one standard deviation.

In Figure 43 and Figure 44, a comparison of mean interstory drift distributions with plus and minus one standard deviations is presented together for conventional and proposed frames. Figure 43 shows the comparison for the time step of maximum roof drift. Figure 44 shows the comparison for envelope interstory drift ratios.

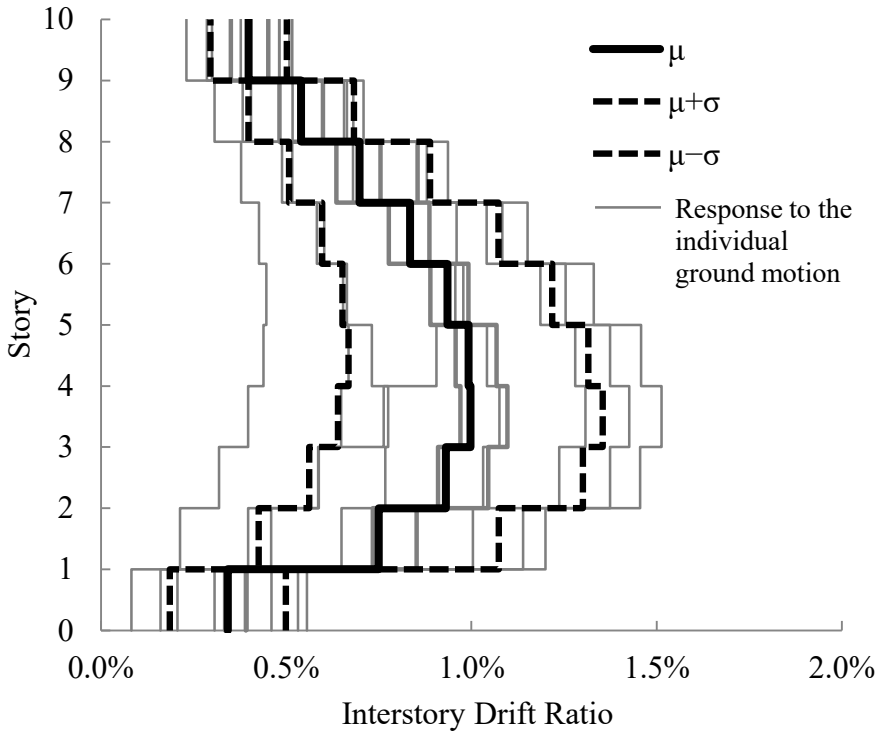

Figure 39. Interstory drift distribution of conventional 10-story frames at maximum roof displacement

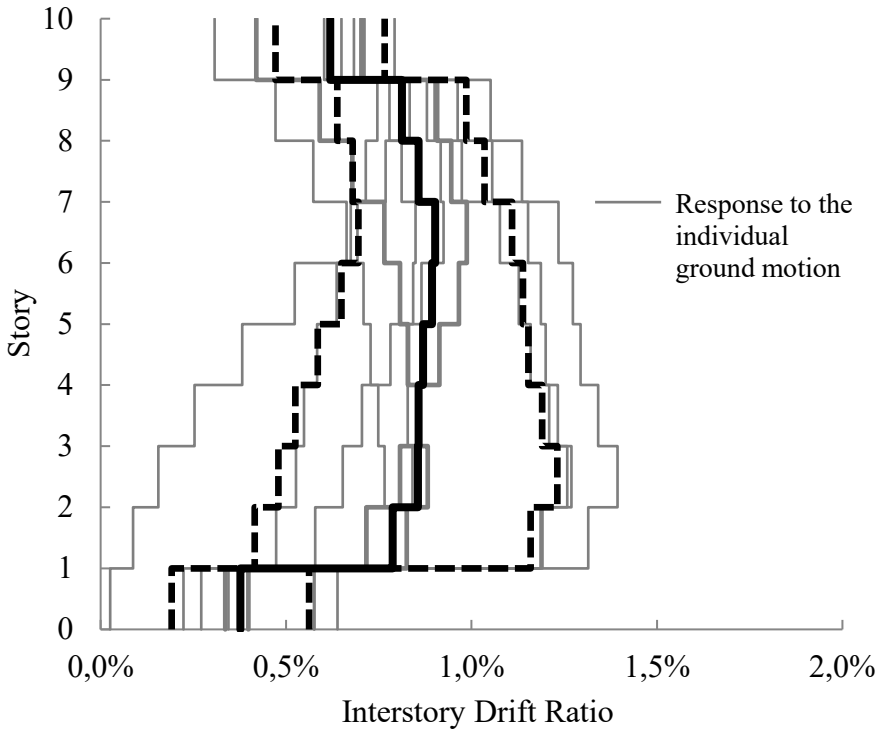

Figure 40. Interstory drift distribution of proposed 10-story frames at maximum roof displacement

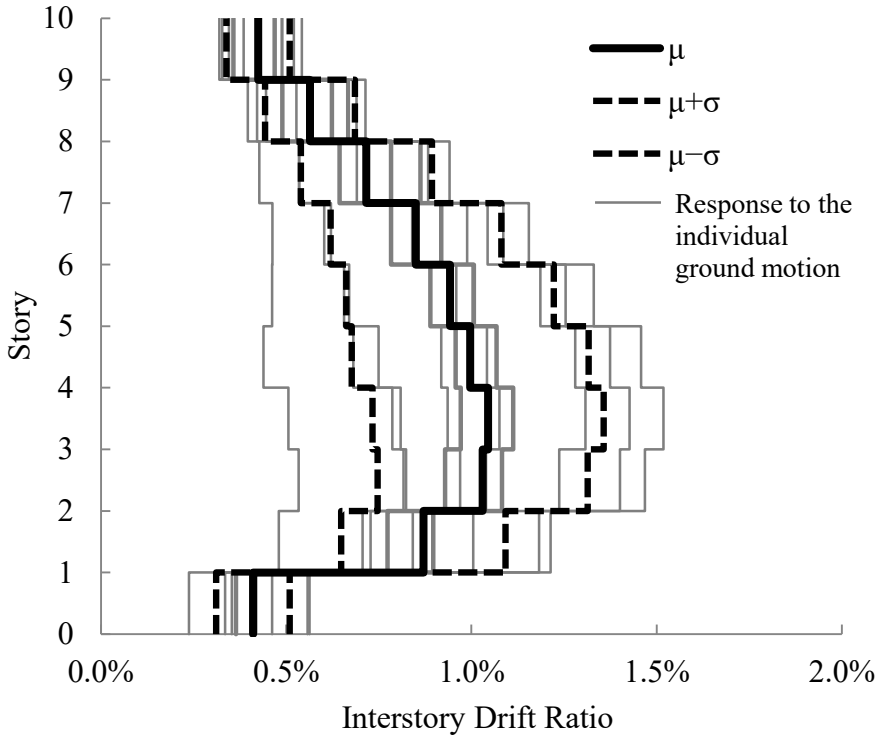

Figure 41. Envelope interstory drifts of conventional 10-story frames

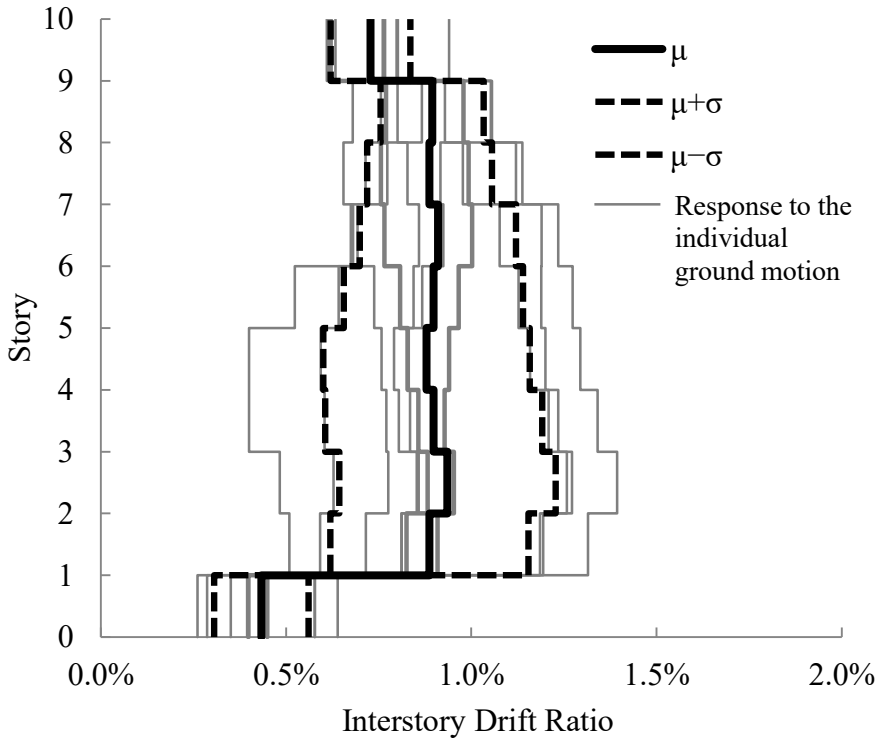

Figure 42. Envelope interstory drifts of proposed 10-story frames

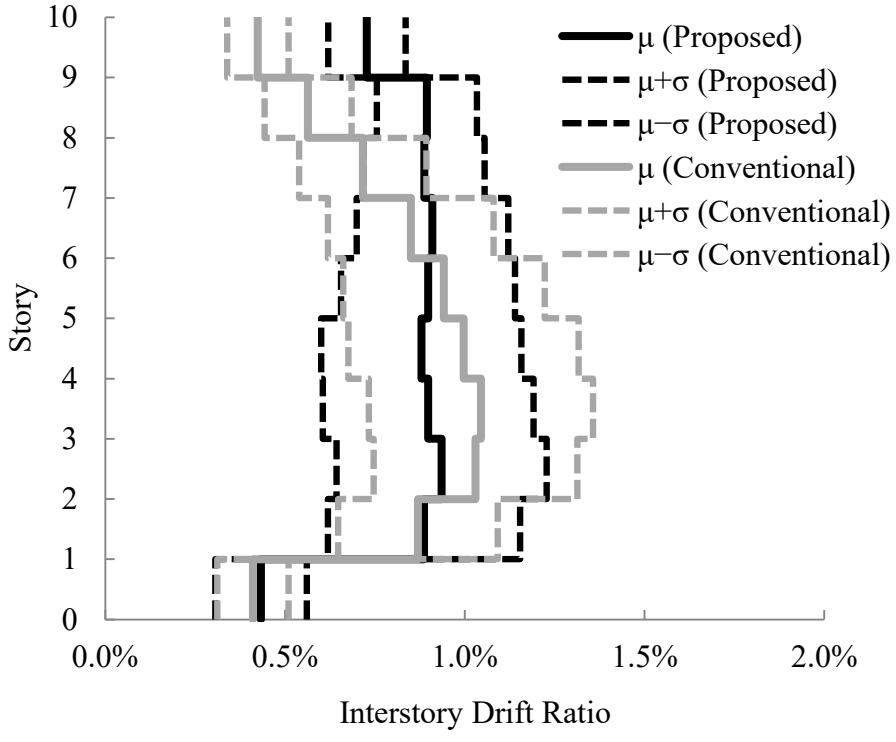

Figure 43. Comparison of mean interstory drift distributions of 10-story frames at maximum roof displacement

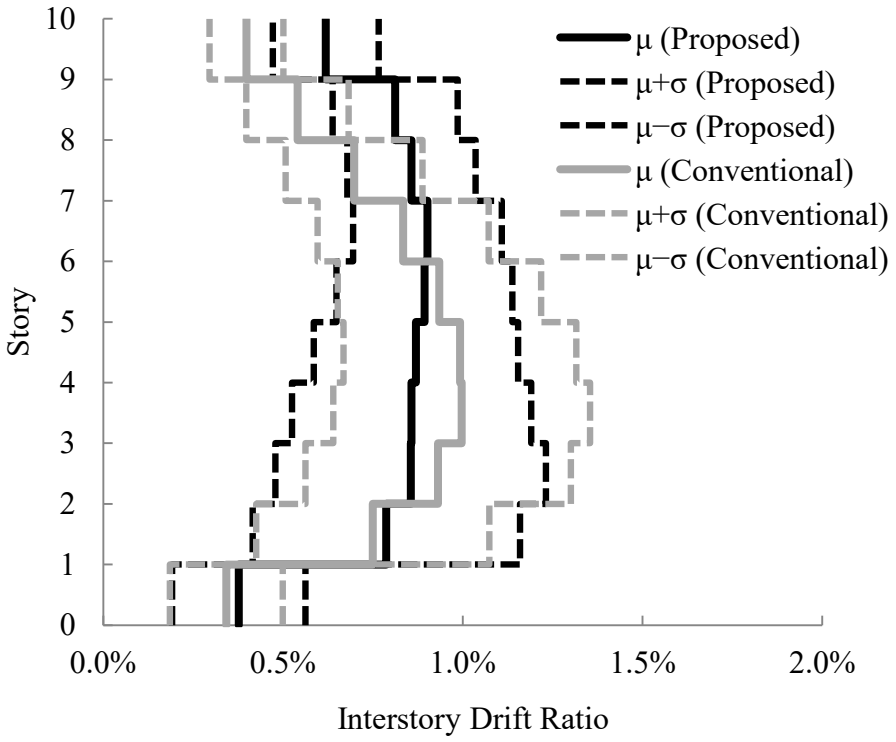

Figure 44. Comparison of mean envelope interstory drifts of 10-story frames

It can be observed from the figures that, for both types of frames, the distribution patterns of the interstory drifts are similar for the maximum roof displacement and the envelope cases. Therefore, the results were evaluated for the envelope case only. The interstory drifts of the first stories are limited due to the stiffening effect of the fixed-base. Therefore, the stories above the first story will be considered while evaluating the interstory drift distributions. For the conventional frame, the interstory drifts concentrated at the lower half. In average, the maximum envelope interstory drift (observed at the fourth story) is 2.5 times greater than the minimum envelope interstory drift (observed at the top story). The COV of mean envelope interstory drifts of the conventional frame is 0.26. On the other hand, the optimum stiffness distribution yielded nearly uniform interstory drift distributions, as intended. The COV of mean envelope drifts for this system is 0.07.

3.6.3.2. 20-Story Frames

The interstory drift distributions of the 20-story model frames for the analysis step at which the peak roof displacements were attained are given in Figure 45 and

Figure 46 for each ground motion. Figure 45 shows the results of the frames with the conventional stiffness distribution. Figure 46 shows the results for the frames with the proposed stiffness distribution. Additionally, the averages of the results are presented together with plus and minus one standard deviation.

Figure 47 and Figure 48 shows the envelope interstory drifts observed at each story for each ground motion. The mean envelopes are also given along with plus and minus one standard deviation.

In Figure 49 and Figure 50, a comparison of mean interstory drift distributions with plus and minus one standard deviations is presented in the same plot for the conventional and the proposed systems. Figure 49 is the comparison for the step of maximum roof drift. Figure 50 is the comparison for envelope interstory drift ratios.

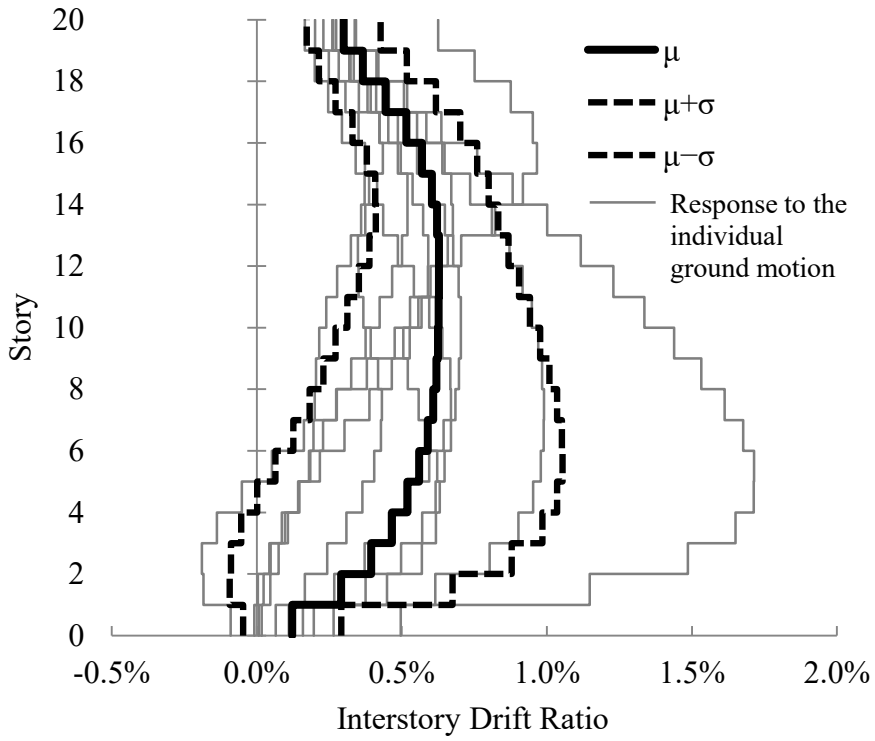

Figure 45. Interstory drift distribution of conventional 20-story frames at maximum roof displacement

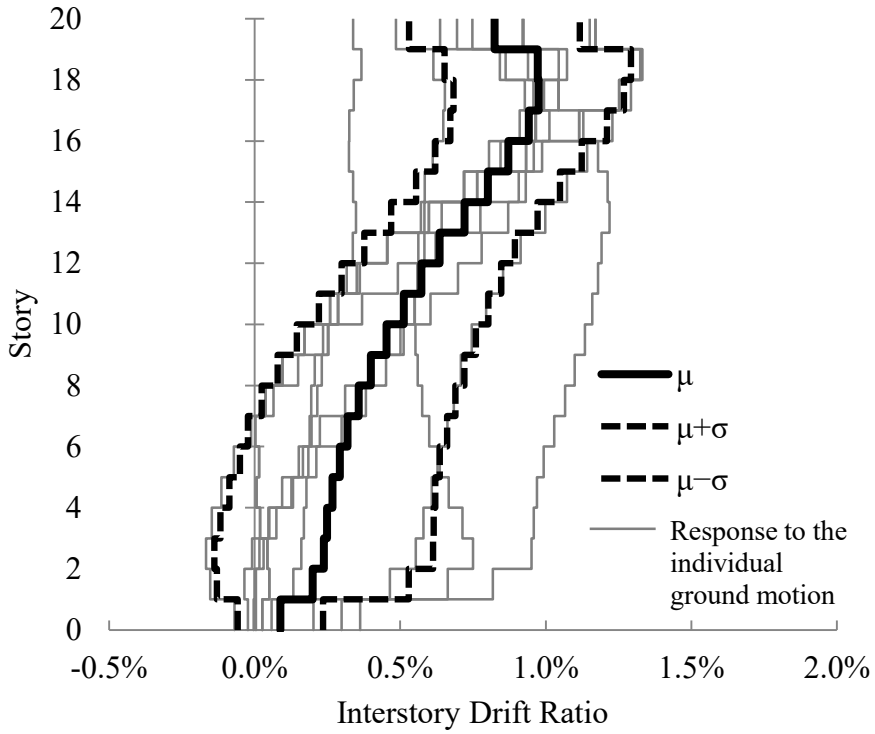

Figure 46. Interstory drift distribution of proposed 20-story frames at maximum roof displacement

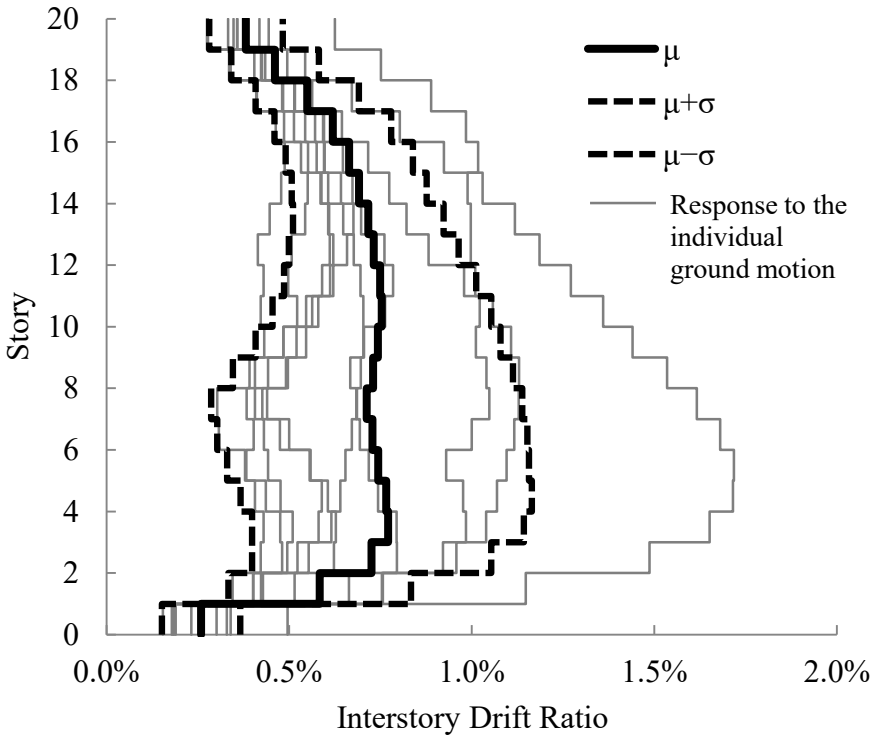

Figure 47. Envelope interstory drifts of conventional 20-story frames

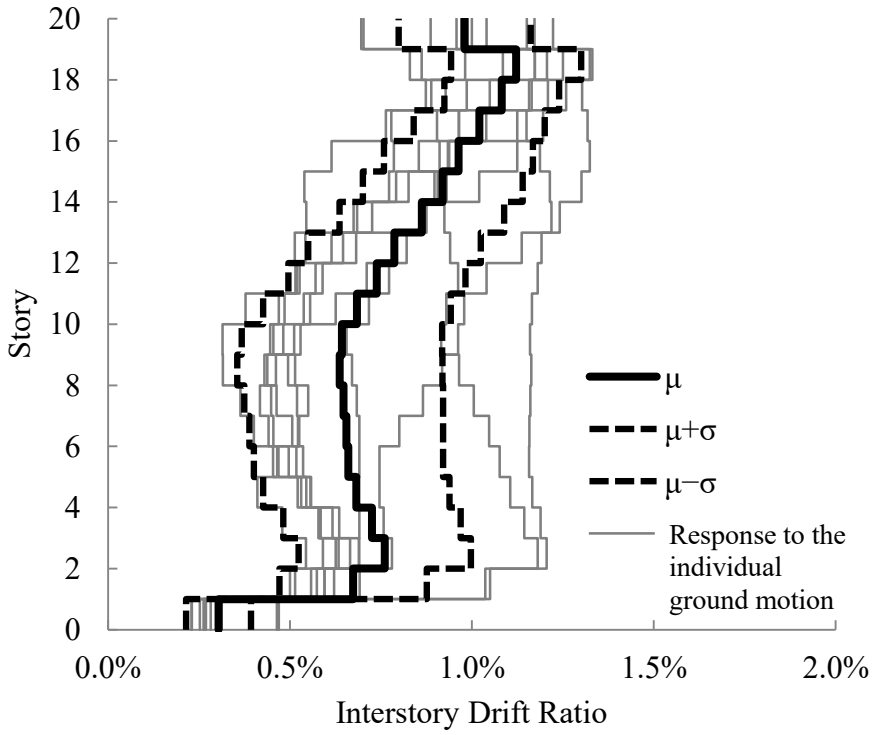

Figure 48. Envelope interstory drifts of proposed 20-story frames

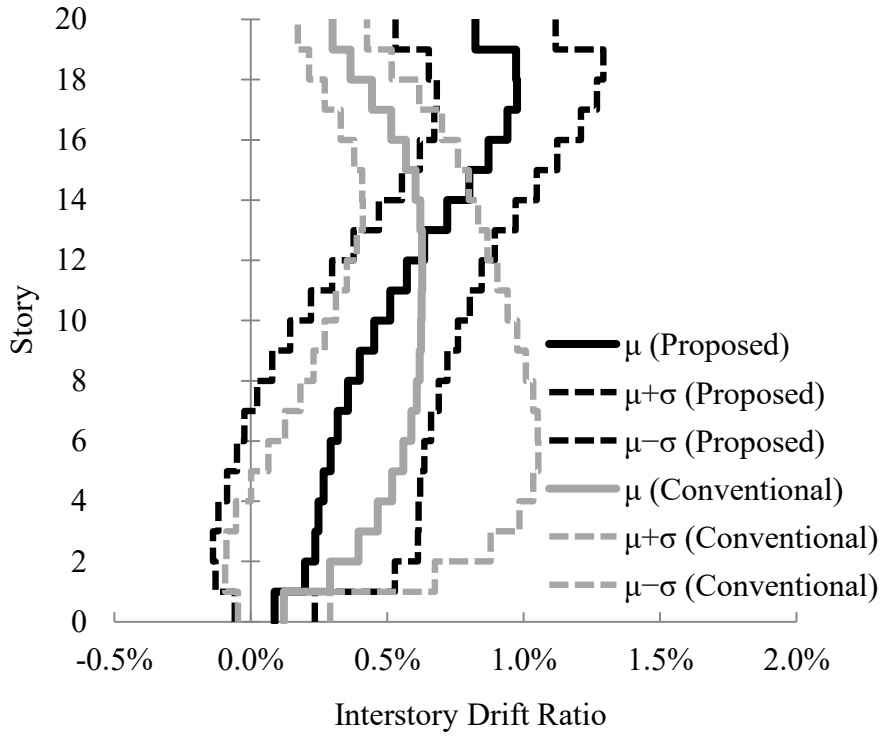

Figure 49. Comparison of mean interstory drift distributions of 20-story frames at maximum roof displacement

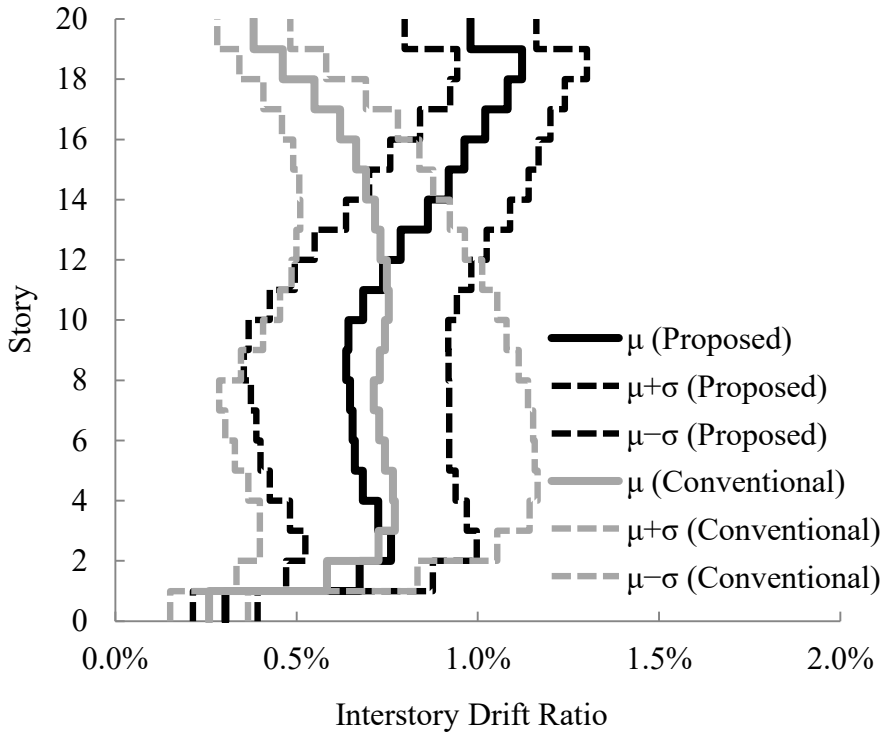

Figure 50. Comparison of mean envelope interstory drifts of 20-story frames

It can be observed from the figures that, for the time step of maximum roof displacement, the interstory drifts at the conventional frame tend to concentrate at the lower and middle parts. The interstory drifts at the proposed frames are lower than those of the conventional frame at the lower half of the building. However, interstory drifts concentrated towards the roof. The results are nearly the same for the envelope case. When compared to the 10-story frames, the proposed stiffness distribution is not effective at preventing the interstory drift concentrations. The COV of mean envelope interstory drifts of the conventional frame is 0.16. On the other hand, the COV of mean envelope drifts of the proposed frames is 0.20. Note that, the interstory drift of the first story was omitted due to the effect of the base-fixity.

3.6.3.3. 30-Story Frames

The interstory drift distributions of the 30-story frames for the time instant at which the peak roof displacements were attained are given in Figure 51 and Figure 52 for each ground motion. Figure 51 shows the interstory drift results of the frames with the conventional stiffness distribution. Figure 52 shows the results for the frames with

the optimum stiffness distribution. Additionally, the averages of the results are presented together with plus and minus one standard deviation.

Figure 53 and Figure 54 shows the envelope interstory drifts observed at each story for each ground motion. The mean envelopes are also given along with plus and minus one standard deviation.

In Figure 55 and Figure 56, a comparison of mean interstory drift distributions with plus and minus one standard deviations is presented in the same plot for the conventional and the proposed systems. Figure 55 is the comparison for the step of maximum roof drift. Figure 56 is the comparison for envelope interstory drift ratios.

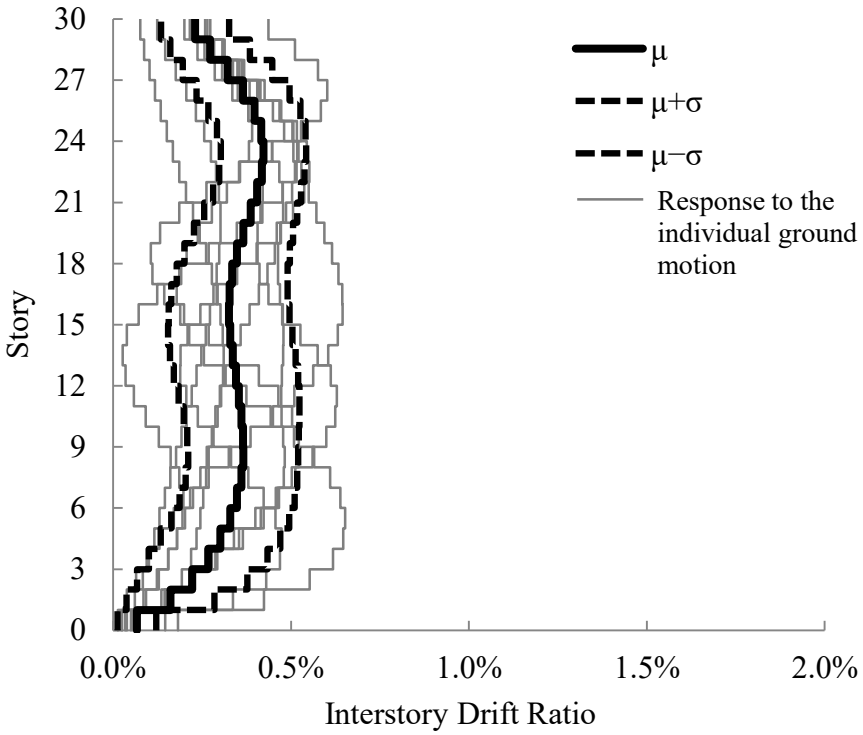

Figure 51. Interstory drift distribution of conventional 30-story frames at maximum roof displacement

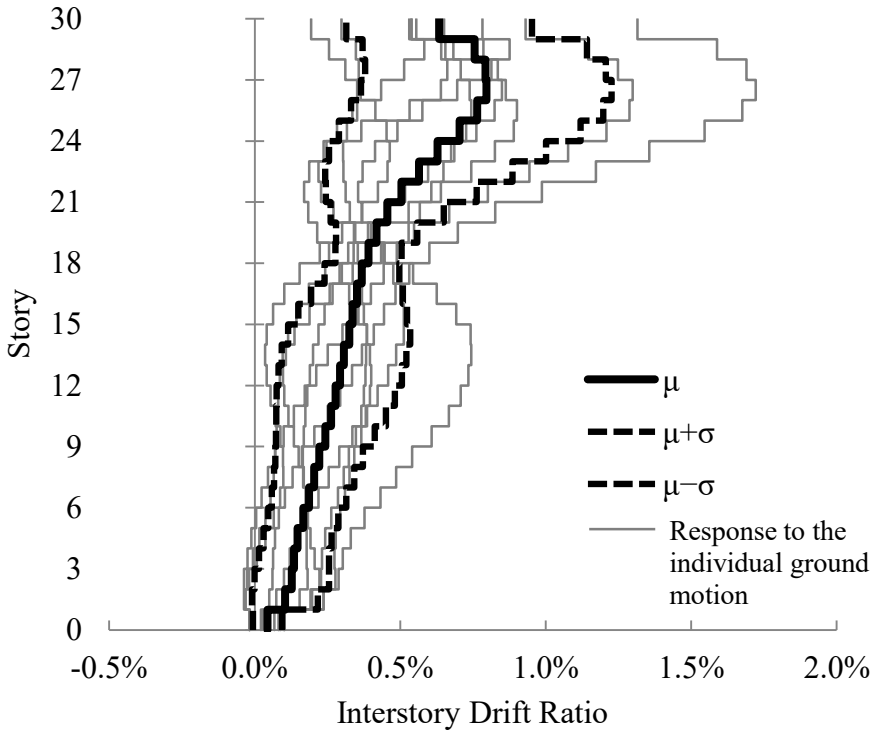

Figure 52. Interstory drift distribution of proposed 30-story frames at maximum roof displacement

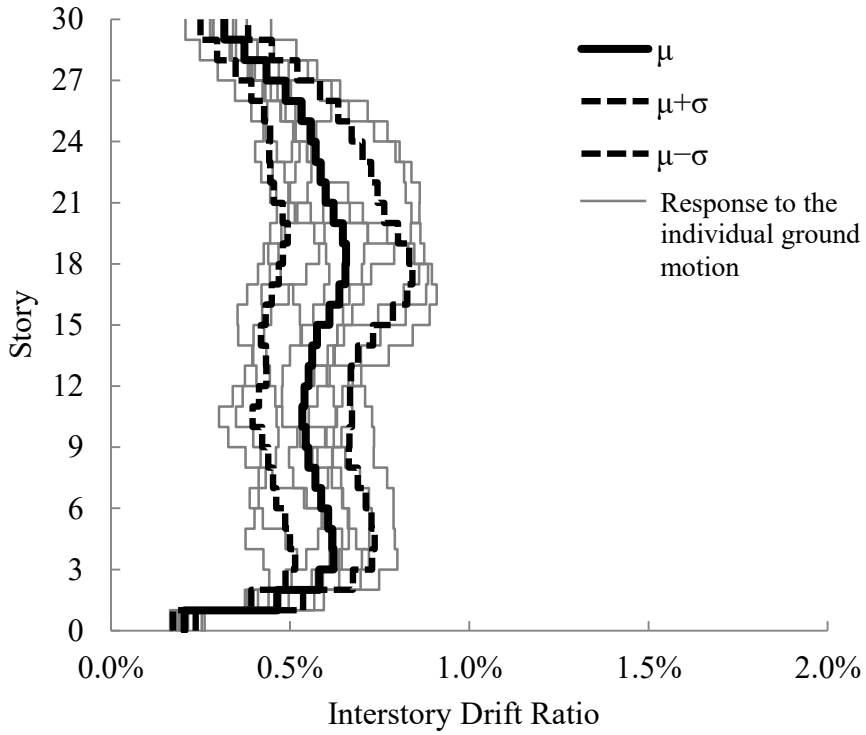

Figure 53. Envelope interstory drifts of conventional 30-story frames

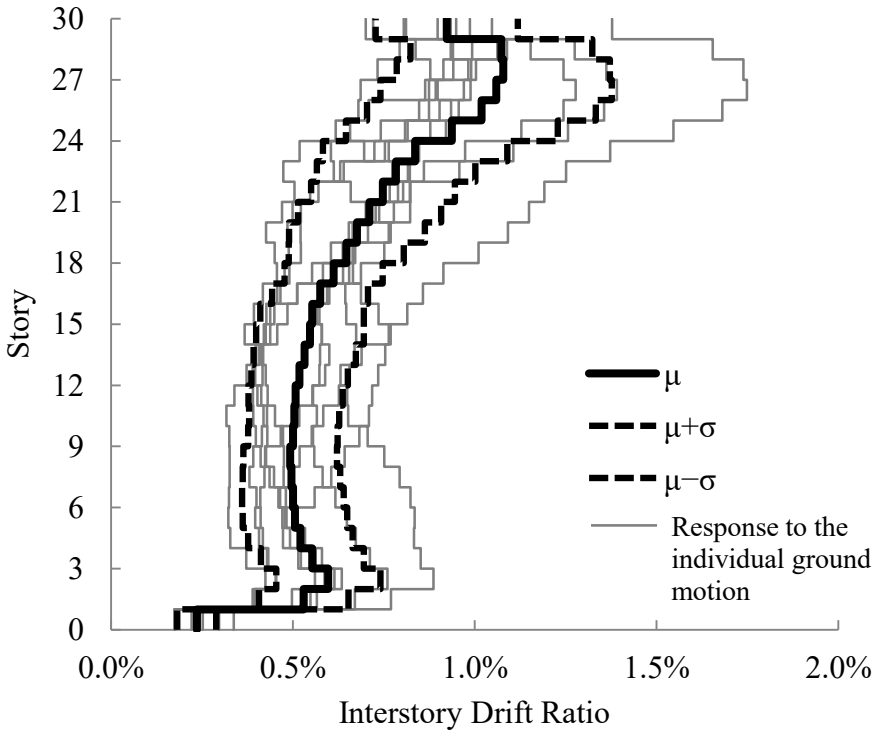

Figure 54. Envelope interstory drifts of proposed 30-story frames

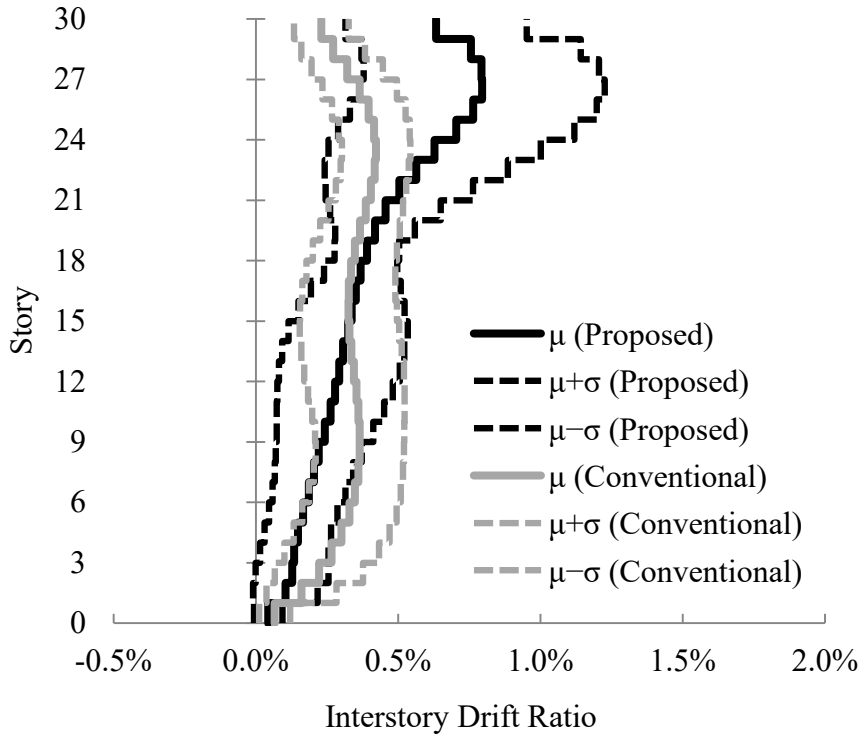

Figure 55. Comparison of mean interstory drift distributions of 30-story frames at maximum roof displacement

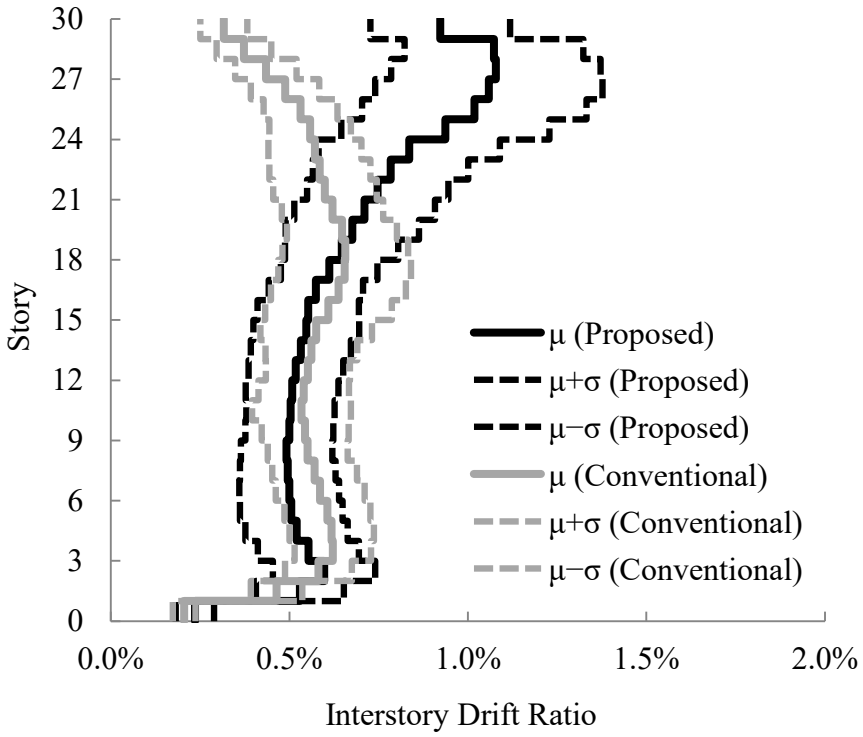

Figure 56. Comparison of mean envelope interstory drifts of 30-story frames

It can be observed from the figures that, for the time instant of maximum roof displacement, the interstory drifts at the lower parts of the proposed frame are lower than those of the conventional frame. However, at the proposed frames, the interstory drifts became excessive at the upper parts. These results are practically the same for the envelope case. Thus, the proposed stiffness distribution is not effective at yielding uniform interstory drift demands. The COV of mean envelope interstory drifts of the conventional frame is 0.14. On the other hand, the COV of mean envelope drifts for the proposed frame is 0.30. Note that, the interstory drift of the first story was omitted due to the effect of the base-fixity.

3.6.4. Discussion of the Results

The results of the linear time history analyses showed that the interstory drift concentrations become less significant at the conventional frames as the height increases. Additionally, the effectiveness of proposed stiffness distribution diminishes as the height of the frames increase. As the number of stories increased, the interstory drifts at the upper parts became excessive due to the whiplash effect and higher

contribution of the upper modes to the drift response as in shear-beam models. The COV of the mean envelope interstory drifts, given in Table 6, supports these observations.

Table 6. Coefficient of variations of mean envelope interstory drift distributions

Frame	COV of Interstory Drift Distributions	
	Conventional	Proposed
10-Story	0.26	0.07
20-Story	0.16	0.20
30-Story	0.14	0.30

The COV values of the conventional frames decrease with the height from 0.26 to 0.14. On the contrary, the COV values of the proposed frames increase with height from 0.07 to 0.30. A value of 0.10 or less may be regarded as a nearly uniform interstory drift distribution. Therefore, two implications can be made from these observations. Firstly, the elastic drift response at tall frames is not necessarily a combination of the dominant modes. Secondly, interstory drift concentrations may not be a major issue at regular tall frames in the elastic range.

3.7. Summary and Concluding Remarks

An elastic primary design procedure for proportioning the frame structures was proposed in this chapter. This procedure aims at a uniform interstory drift demand throughout the designed frames until the damage occurs. The assumption of the proposed procedure is that a combination of the governing modes determines the drift response of the frame structures in the elastic range. Therefore, it is intended to obtain a uniform modal pattern when the governing modes are combined.

Initially, the formulation for obtaining the required stiffness distribution for a prescribed mode shape and period was derived. Then, an iterative procedure is developed to obtain the stiffness distribution that will produce the targeted combined mode shape for a selected fundamental period. The proportioning of the frames is based on providing this stiffness distribution over the height, rather than the conventional design procedure.

The success of the proposed stiffness distribution was initially evaluated at the shear-beam models by performing linear time history analyses. Those were 10-, 20, and 30-story systems. The outcomes of the proposed stiffness distribution were compared to those of a uniform stiffness distribution. The shear-beam models with the uniform stiffness distribution were used for representing the conventional frame structures.

In the following section, a simple method for proportioning the beams and columns at each story to satisfy the required stiffness distribution was described. Then, 10-, 20-, and 30-story planar reinforced concrete frames were proportioned using the proposed procedure. Also, frames with the same number of stories were designed as in the general practice to compare the results of the proposed frames. The effectiveness of the proposed stiffness distribution was investigated by comparing the linear time history results. The conclusions referred from the evaluations are summarized below:

- The proposed iterative algorithm is very effective for obtaining the required stiffness distribution for a linear combined mode shape and selected fundamental period.
- The proposed stiffness distribution is very effective at preventing interstory drift distributions at 10-story frames.
- The effectiveness of the proposed stiffness distribution decreases as the height of the frames increase.
- The assumption made for the proposed preliminary design procedure is not necessarily valid for tall frames.
- The interstory drift concentration may not be a major issue at tall frames.

Based on the conclusions, the context of the thesis was limited to low- to mid-rise frame structures. Note that, most of the high-rise buildings in general practice are designed to have shear walls as lateral load-resisting systems. The combination of the lateral behavior of shear walls and frame systems restrict the interstory drift concentrations in this type of buildings. Therefore, developing a seismic design method to mitigate interstory drift concentrations at mid- to low-rise frames is a more essential task.

CHAPTER 4

EFFECT OF NUMERICAL ELEMENT AND MATERIAL MODELS ON THE SEISMIC BEHAVIOR OF REINFORCED CONCRETE MEMBERS

4.1. Introduction

As stated before, the main purpose of the presented study is to develop an effective inelastic design procedure that prevents interstory drift concentrations during strong ground motions. It is required to have a reliable numerical model for the development and evaluation of the proposed procedure. There are numerous numerical element and material modeling methods developed by researchers to increase the accuracy and efficiency of the analyses. The developments in computational capabilities have enabled the use of sophisticated numerical modeling methods. These numerical models are typically based on various theories and assumptions. Hence, their accuracy and applicability, as well as the computational efficiency, may differ. Therefore, prior to the study on the inelastic design procedure, the effects of different element and material models on the seismic behavior of reinforced concrete members were investigated. The attempt is presented in this chapter. The results of a set of column experiments were adopted for this purpose. The experiments were simulated using the OpenSees platform (McKenna et al., 2010). The results obtained using the selected models were compared with the experimental results. Based on the outcomes, the selection of the numerical element and material models to be implemented for the nonlinear analyses was done.

This chapter begins with a summary of the selected literature on the effects of the numerical modeling methods. Then, brief descriptions of the selected element and material models investigated in this chapter are presented. The properties of the adopted column tests, the numerical model, and the evaluation parameters follow. Next, the results of the study are presented and discussed.

4.2. Background for Numerical Models

Various numerical models for modeling the behavior of both the elements and the materials are available in the literature. All numerical models are based on different assumptions and/or simplifications. Therefore, their accuracy and effectiveness are likely to vary for different conditions. This led researchers to study the effects and issues of different numerical models and their parameters.

Neuenhofer and Filippou (1997) evaluated the effectiveness of force- and displacement-based formulations used for numerical element models. The authors modeled a steel beam with 1, 2, 4, 8, 16 elements, as well as with 3, 5, and 7 integration points using both formulations. It is stated that the forced-based formulations involve a numerical integration error while displacement-based formulations include a discretization error. Based on these, it is concluded that the accuracy of the solution can be enhanced by whether increasing the number of elements or the number of integration points (IPs) for force-based elements. Both approaches improve the solution equally; however, the latter is computationally more effective. On the other hand, the success of the displacement-based elements can only be improved by increasing the number of elements. The convergence rate of the displacement-based formulations was shown to be lower than that of the force-based formulations.

Coleman and Spacone (2001) addressed the loss of objectivity observed in force-based elements. The effect of changing the number of integration points, while modeling various types of reinforced concrete members, is evaluated. The study showed that softening post-peak responses show a great scatter (non-objective response) as the number of integration points is increased. It is argued that the material or the model should be calibrated to obtain an objective response. The authors proposed two regularization methods for this purpose.

Calabrese et al. (2010) investigated the effects of element formulation types, number of integration points, and integration methods used in distributed plasticity elements. The numerical issues encountered while modeling different post-yield behaviors were identified. A cantilever column experiment was simulated using the considered numerical modeling parameters. It is shown that displacement-based elements have a slower convergence compared to the force-based elements. However, both element formulation types had objectivity issues when modeling the post-peak

softening behavior as the number of elements/IPs increased. A material regularization method is proposed to overcome the listed issues.

Rodrigues et al. (2012) simulated 24 column experiments using force and displacement-based distributed plasticity elements, as well as a lumped plasticity approach. The study indicates that the distributed plasticity approach yields the closest agreement with the experiments. However, all modeling approaches were observed to fail to model the strength deterioration which takes place at higher drifts. Depending on that, the dissipated energy amounts were calculated 25% to %50 larger compared to those of the experiments.

Huang and Kwon (2015) modeled 320 column tests using distributed and lumped plasticity approaches, as well as a finite element mesh discretization approach. The study showed that the success of both the distributed and the lumped plasticity approaches decreases as the shear governs the behavior of the specimens. On the other hand, it was observed that the finite element models showed a good agreement with the experiments. However, the computational time required by these models is 150 to 200 times than that of the other modeling approaches.

Gharakhanloo (2014) compared different distributed and lumped plasticity approaches using the test results of a single-story reinforced concrete moment frame. It was observed that the force-based element formulation is more efficient than the displacement-based element formulation in terms of computational time. It is also stated that the use of the lumped plasticity element models is appropriate in cases where plastic behavior is not expected to occur at the mid-span of the elements. This type of elements was observed to perform better in simulations.

Zhao et al. (2017) compared six concrete material models of OpenSees material library using three column tests. It is observed that the Concrete06 model failed to model the tests accurately. Other models were reported to yield similar results to each other.

4.3. Numerical Modeling Methods

Various numerical modeling methods are available to simulate the load-deformation response of structural members. These methods implement different types of nonlinear beam-column finite elements to perform numerical analyses. Numerical

modeling methods may be divided into three main categories in terms of complexity and refinement: (i) global models, (ii) microscopic finite element models, (iii) discrete finite element models. Each method has a trade-off between accuracy and computational efficiency.

Global models represent the structure with lumped masses and limited degrees-of-freedom to estimate the global behavior in an approximate manner with low computational effort. On the other hand, microscopic finite element models adopt sophisticated models to consider the local effects such as cracking, strain penetration, and bond. However, this method is unbearably complex for evaluating the global response of large-scale structures due to its high computational cost.

Discrete finite element models provide a computationally efficient and sufficiently accurate alternative for predicting the global behavior. This method is also very flexible. It is possible to aggregate shear, torsional, rotational and/or axial force-deformation behavior at the same section, if necessary. In this study, discrete finite element models were used to model the reinforced concrete members.

4.3.1. Discrete Finite Element Models

Conceptually, discrete finite element models are based on modeling the inelastic force-deformation behavior using nonlinear springs. These springs are used at the designated parts of an element to represent the sectional behavior, as well as the material behavior. Discrete finite element models may be divided into two categories based on the implementation type of nonlinear springs: (i) distributed plasticity models, (ii) lumped plasticity models.

4.3.1.1. Distributed Plasticity Models

Distributed plasticity models allow plasticity to spread over the entire length of the element. One of the widely used distributed plasticity models is the fiber-based element models. These models have become increasingly popular due to their improved accuracy over the last decades. In this approach, the behavior of an element is calculated at designated integration points where the location and weight are prescribed by an integration rule. These integration points consist of discretized cross-sections of the

modeled member. This discretization divides a cross-section into a number of so-called fibers. A constitutive material stress-strain relationship is assigned at each fiber. The response of a section is obtained by integrating the response of each fiber at the time steps of the analysis. The inelastic response of the element is then obtained by integrating the cross-sectional response using either force-based or displacement-based formulations. Figure 57 shows a fiber discretization of a typical confined reinforced concrete member modeled using force-based element with five integration points. As seen in the figure, the fibers corresponding to the concrete cover are assigned as plain concrete material model. On the other hand, the fibers within the core area are assigned as confined concrete material model. The rebars are represented with fibers that use a steel material model.

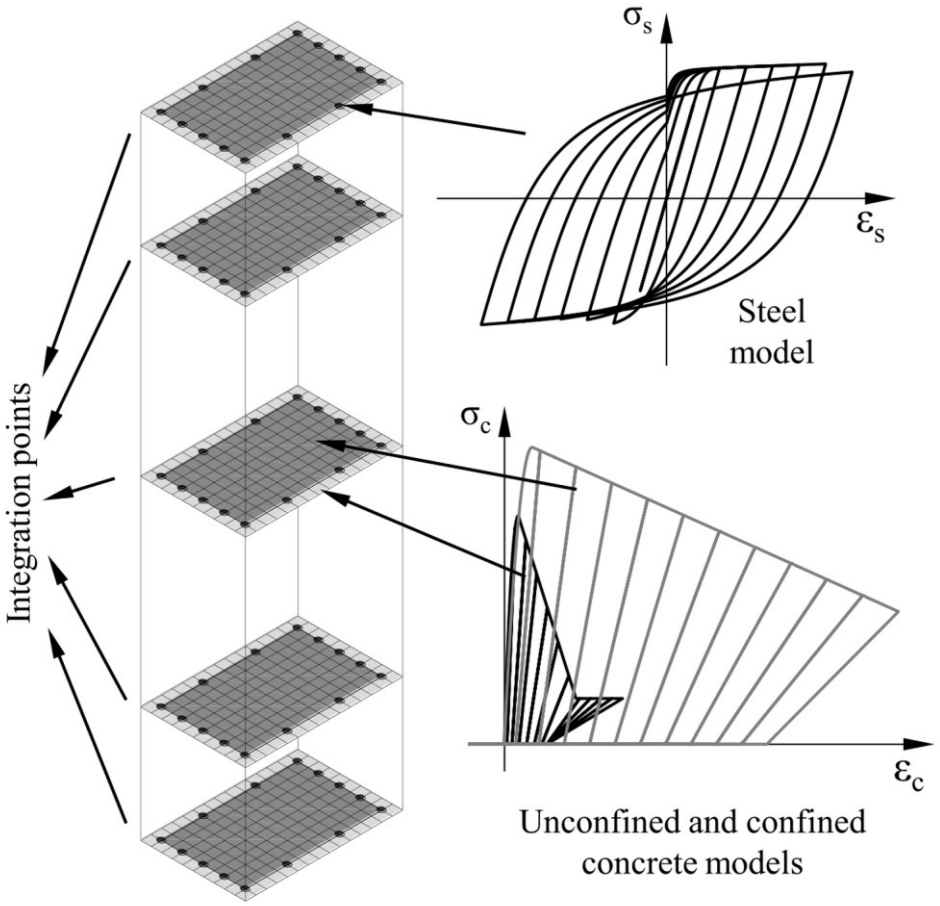

Figure 57. Fiber discretization of a typical confined reinforced concrete member

There are multiple advantages of the fiber-based approach. Most importantly, it does not require a prior moment-curvature analysis of the critical sections. In addition, since the cyclic behavior is directly accounted for from the cyclic material models used

at the fibers, there is no need to associate any hysteretic rule to the section. Furthermore, it can directly account for axial load-moment interaction. However, a major drawback of this approach is that it ignores cyclic shear-flexure interaction and consequent degradations since it neglects shear deformations. It is possible to take the shear behavior into account by aggregating lumped shear springs at the sections deemed critical in terms of shear deformations. However, such approaches currently increase the numerical divergence risk during the analyses. Also, defining the nonlinear shear behavior for each section is not an easy task. Therefore, implementing shear springs is an impractical approach to be used in the design process.

Distributed plasticity elements can be implemented with either the displacement-based (DB) formulation (stiffness formulation) or the force-based (FB) formulation (flexibility formulation). DB formulation implements the standard finite element approach, in which a prescribed displacement field (e.g. linear variation of curvature along the element) is imposed and the element forces are found by using the principle of virtual displacements. The displacement field is approximate, and it becomes highly nonlinear as the material plasticity increases. In this case, DB formulations fail to capture the real deformations with their imposed displacement field. Therefore, this formulation requires a refined discretization of the element so that the linear curvature distribution can be valid within the plastic hinge regions. The element can be densely meshed at the plastic hinge locations, but this approach requires the prediction of the plastic hinge lengths and a separate discretization job. Alternatively, the entire element can be discretized densely. In this case, the runtime of the analyses is likely to increase substantially.

The FB approach, on the other hand, imposes a prescribed force field (e.g. linear variation of forces along the element) and the element deformations are obtained by the principle of virtual work. In the case of high nonlinearity, the FB formulation always satisfies the equilibrium in contrast to the DB formulation (Spacone et al., 1996). The only approximation is the number of integration points (IPs). Therefore, using only a single element to represent a member is sufficient in this approach.

While modeling the nonlinear behavior of reinforced concrete members, the strain-softening behavior of concrete may cause stresses or deformations to localize into a limited region of the beam-column element. The strain-softening behavior is prominent particularly at reinforced concrete members that carry relatively high axial loads. In the DB approach, the response is localized over a single beam-column

element. Larger stresses are required inside this particular element to produce the same amount of displacement, as the mesh gets finer. Therefore, the response becomes dependent on the length of this element, thus leading to non-objectivity.

On the other hand, deformations localize at the most strained IP in the FB elements. The deformation in the element is sampled over the tributary length of the critical IP. This deformation must always be the same to satisfy the equilibrium imposed in the FB formulation. The tributary length of the IP shortens when the number of IPs increase. Thus, increasing curvature values are required in the IPs to achieve the prescribed displacement. This leads to a loss of objectivity since the response varies as a function of the number of IPs. In order to overcome the localization issues, several regularization procedures have been proposed in the literature (e.g. Coleman & Spacone, 2001; Scott & Fenves, 2006; Scott & Hamutçuoğlu, 2008; Lee & Filippou, 2009).

FB element (FBE) model was adopted as the distributed plasticity element model for this study due to its one-on-one element representation. Thus, the number of degrees of freedom is kept at a minimum. Besides, the FB formulation is based on exact force interpolation functions. Therefore, the solution only involves a numerical integration error that can be reduced in most cases by increasing the number of IPs along the element. For a thorough comparison of FB and DB elements see Neuenhofer & Filippou (1997).

4.3.1.2. Lumped Plasticity Models

In reinforced concrete frames, inelastic behavior generally concentrates at specific regions of the members. These regions are commonly referred to as plastic hinges. Lumped plasticity models assign inelastic behavior to these regions using either some sort of rotational springs or fiber-based sections while the remainder of the members generally assumed elastic. The use of rotational springs requires a prior moment-curvature analysis for the sections at the plastic hinge regions. Then, the moment-curvature response needs to be simplified and defined in the numerical model for each plastic hinge.

An alternative lumped plasticity approach was proposed by Scott and Fenves (2006). It is based on a novel integration method (modified Gauss-Radau) which

overcomes the previously mentioned non-objectivity problems of the distributed plasticity elements. The element using this approach is called as beamWithHinges (BWH) in OpenSees. It is somewhat a hybrid approach between the lumped and distributed plasticity approaches. This element model can be used as a conventional lumped plasticity element as described above. However, it is also possible to use FB distributed plasticity using fiber-based sections within the plastic hinge regions as seen in Figure 58. In this case, the inelastic response of the element is a function of the plastic hinge length (L_p) and properties of the fiber-section within the defined plastic hinge region. The remaining part of the element is assumed to be linear elastic. This approach has an additional option which could be an advantage for modeling. Modification of the stiffness of the member in the elastic zone could be a tool for considering the factors that reduce the stiffness such as shear and bar slip. Besides, it demands less computational effort compared to the distributed plasticity models. This element adopted as the lumped plasticity element for this study.

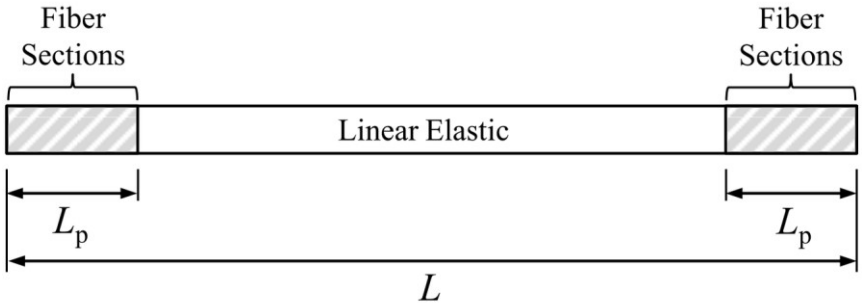

Figure 58. Schematic view of beamWithHinges (BWH) element

4.4. Material Models

The material models used in numerical analysis is expected to represent the real material behavior. As stated earlier, the fiber approach uses the constitutive material models to obtain the sectional and element response. Therefore, these models are required to define not only the monotonic but also the hysteretic behavior of the materials accurately. This part of the study focuses on the selected material models in OpenSees.

Considering the confinement effects, in the current approach, a typical reinforced concrete column is discretized into two concrete regions when implementing

the fiber discretization. The concrete outside the transverse reinforcement could be regarded as the unconfined concrete and expected to exhibit the typical behavior of the plain concrete. On the other hand, the confined concrete zone within transverse reinforcement has increased stress and strain capacities compared to the unconfined concrete zone. The increase in the stress and strain depends on the arrangement of the confinement and the properties of the confining steel material. There are alternative models to simulate this behavior. As one of these models, Mander et al. (1988) defined a theoretical stress-strain relationship for confined concrete as seen in Figure 59. This model also considers the effects of strain rate and cyclic loading. The proposed relationship was built on the one presented by Popovics (1973) and gained a large acceptance. This model was adopted to model the concrete stress-strain relations for the confined concrete in this study.

Four commonly used concrete models from OpenSees library were selected for evaluation. These are Concrete01, Concrete02, Concrete04, and Concrete07 models whose representative hysteretic behaviors are shown in Figure 60. Since these models do not have separate input parameters for the confined region, the peak compressive strength and the corresponding compressive strain, as well as the ultimate strain for the confined regions are calculated based on the relationship proposed by Mander et al. (1988).

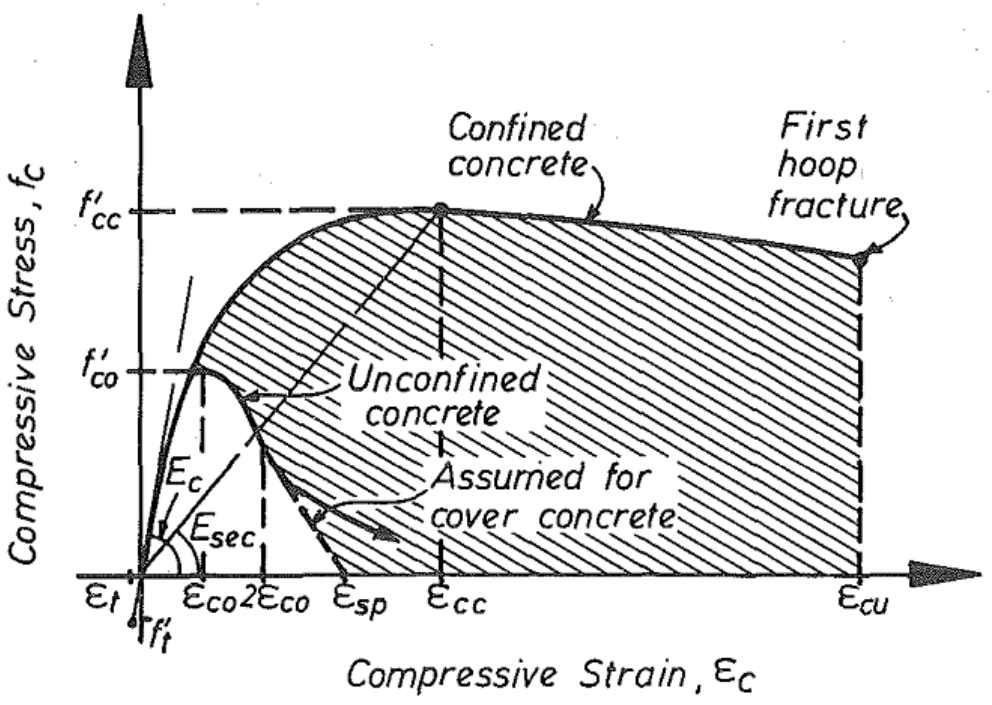

Figure 59. Stress-strain model proposed for monotonic loading of confined and unconfined concrete (Source: Mander et al., 1988)

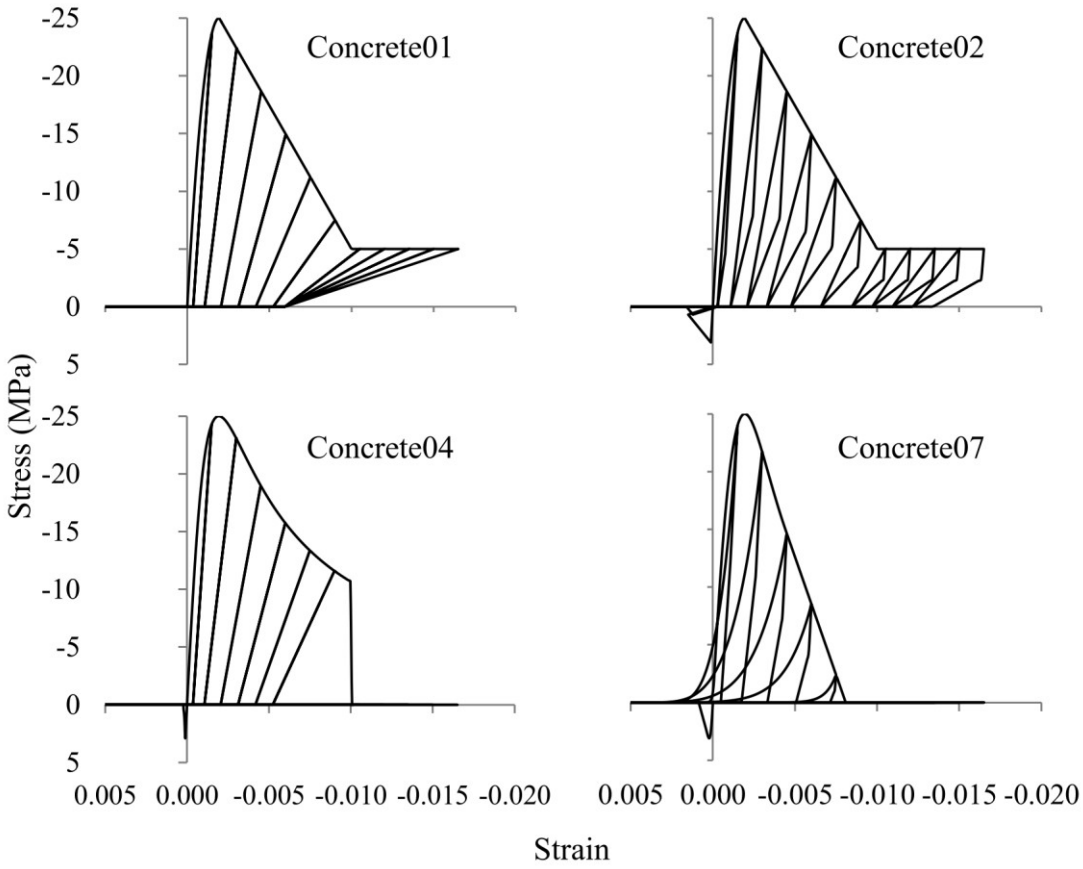

Figure 60. Representative hysteretic responses of the selected concrete material models

4.4.1. Concrete01 Material

Concrete01 is a uniaxial material model that has degraded linear unloading and reloading stiffness defined by Karsan and Jirsa (1969). However, in this model, the loading and unloading lines are simplified to coincide. The monotonic stress-strain relationship is based on Kent-Park concrete model (Kent & Park, 1971) which was modified by Scott (1980). The tensile strength of the concrete is ignored in this model. Stress-strain relationship and an example of the hysteretic behavior of Concrete01 are shown in Figure 61 and Figure 62, respectively.

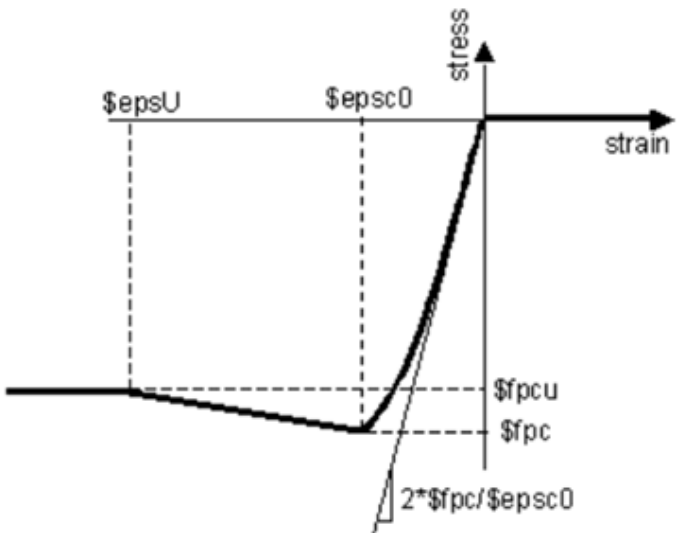

Figure 61. Stress-strain relationship of Concrete01 (Source: Mazzoni et al., 2006)

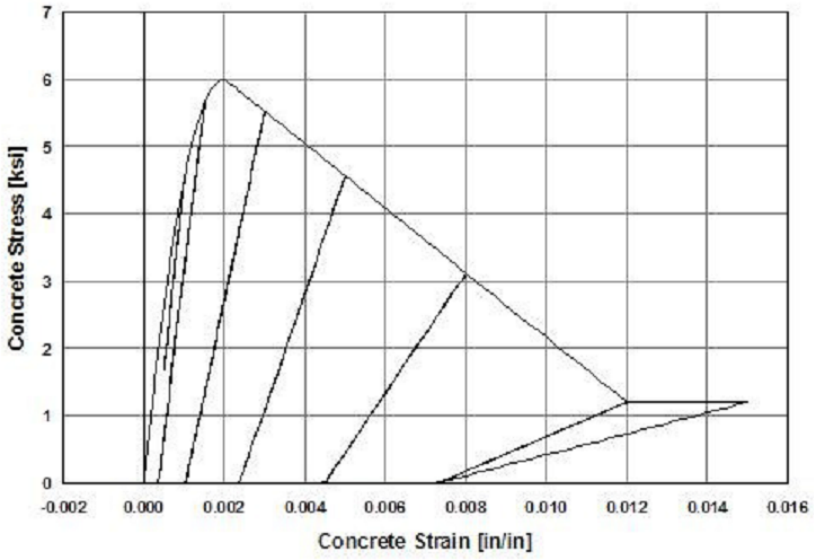

Figure 62. Example hysteretic behavior of Concrete01 (Source: Mazzoni et al., 2006)

4.4.2. Concrete02 Material

Concrete02 is based on the same monotonic model as Concrete01. However, it accounts for the tensile strength and the tension softening behavior of the concrete. The hysteretic stress-strain relationship of this model is shown in Figure 63. This model uses the hysteretic model proposed by Yassin (1994). The model has loading and unloading lines that are straight and intersect at the same point as shown in Figure 64. A comparison of the hysteretic response of Concrete01 and Concrete02 models is shown in Figure 65.

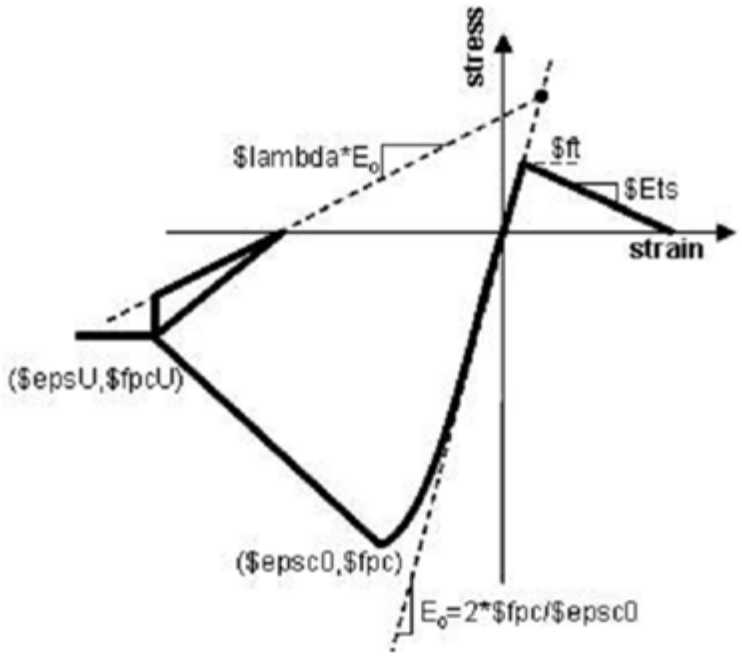

Figure 63. Stress-strain relationship of Concrete02 (Source: Mazzoni et al., 2006)

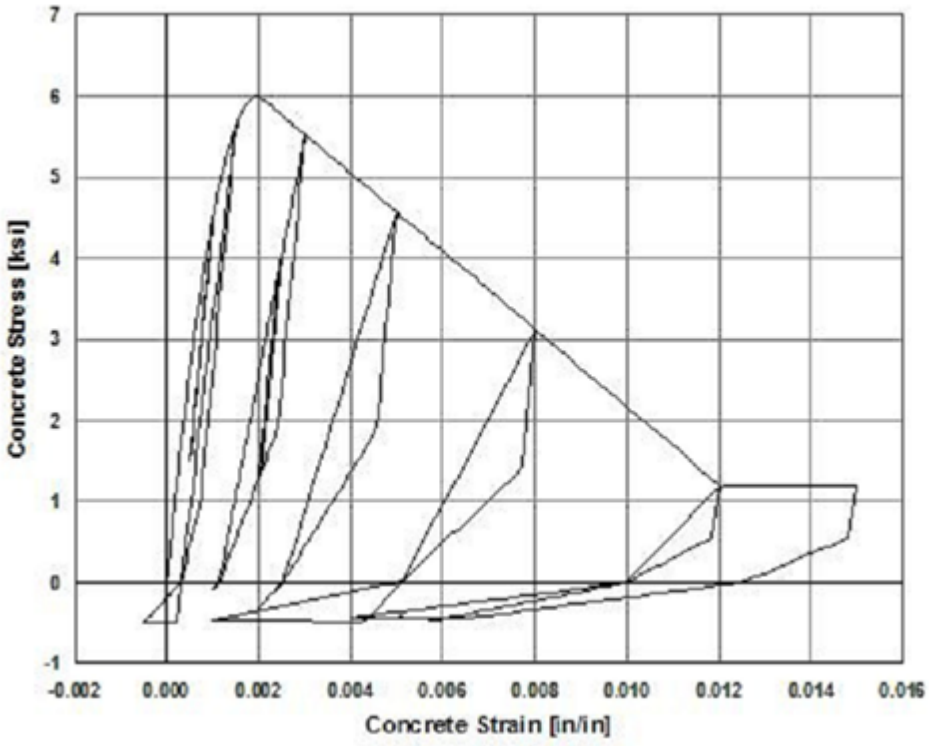

Figure 64. Example hysteretic behavior of Concrete02 (Source: Mazzoni et al., 2006)

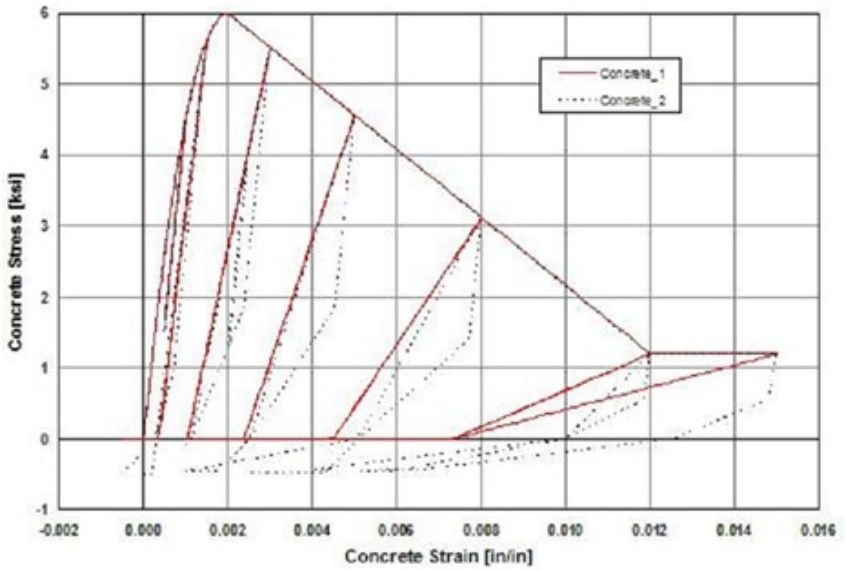

Figure 65. Comparison of hysteretic response of Concrete01 and Concrete02 (Source: Mazzoni et al., 2006)

4.4.3. Concrete04 Material

Concrete04 is based on Popovics (1973) concrete model. It has a degraded linear unloading and reloading stiffness defined by Karsan and Jirsa (1969) as in the Concrete01 model. However, it has a tensile strength with exponential decay. An example of the hysteretic response of this model is shown in Figure 10.

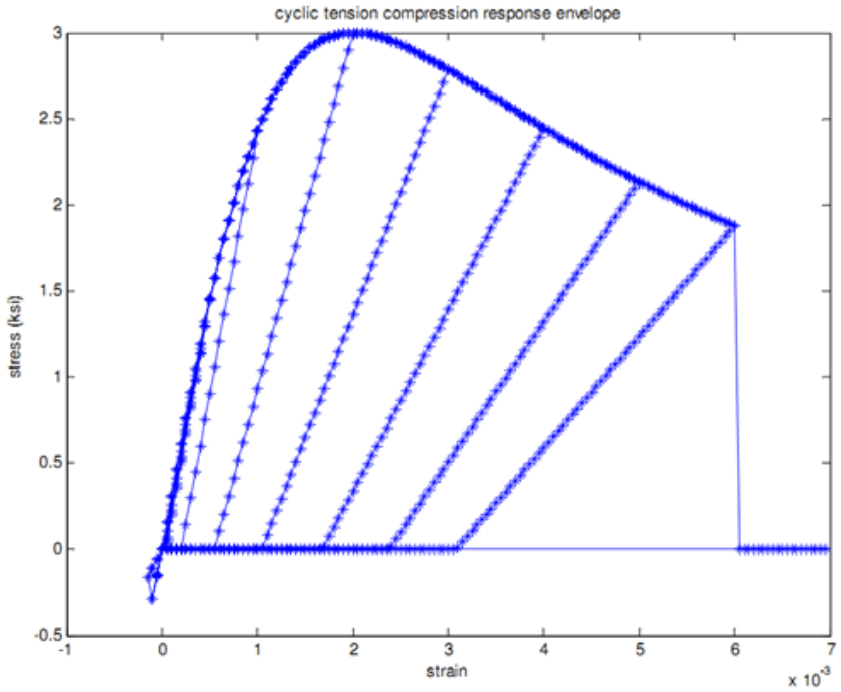

Figure 66. Example hysteretic behavior of Concrete04 (Source: Mazzoni et al., 2006)

4.4.4. Concrete07 Material

Concrete07 is an implementation of Chang and Mander (1994) concrete model. However, unloading and reloading curves of this model were simplified. Also, the tension envelope shift with respect to the origin has been removed. The reason for these modifications is to reduce the computational effort and increase the numerical stability. A full description of this model can be found in Waugh (2009). The stress-strain relationship and the hysteretic behavior of Concrete07 are shown in Figure 67 and Figure 68, respectively.

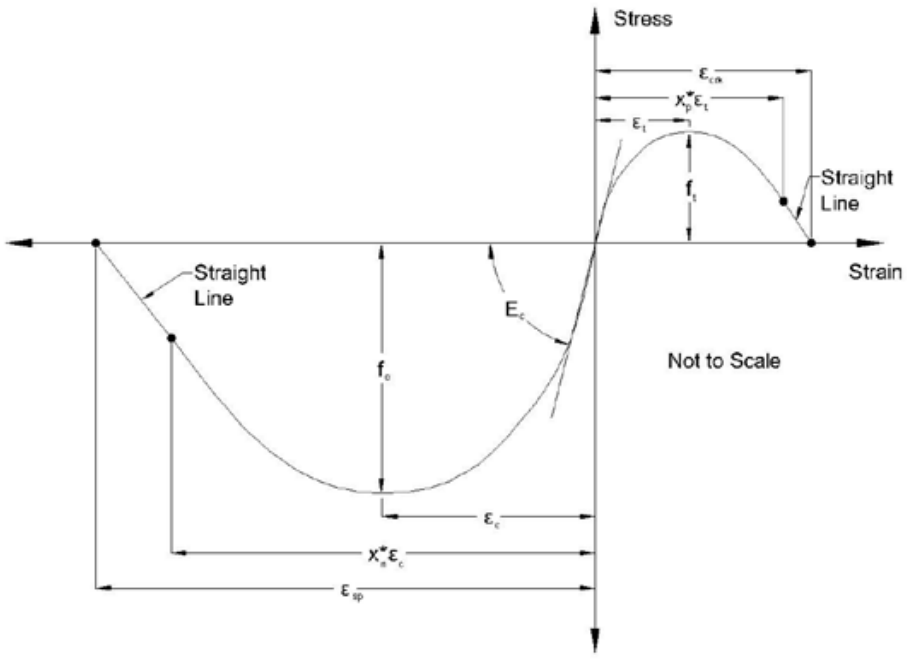

Figure 67. Stress-strain relationship of Concrete07 (Source: Mazzoni et al., 2006)

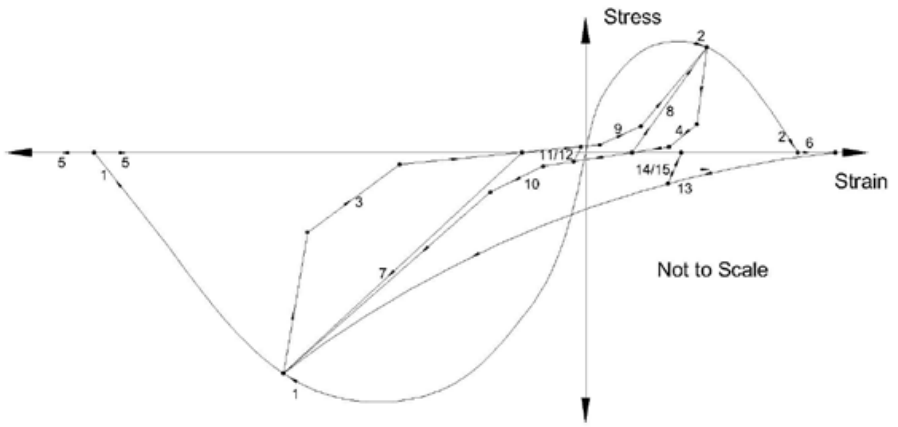

Figure 68. Hysteretic behavior of Concrete07 (Source: Mazzoni et al., 2006)

4.4.5. Steel Material Model

Steel02 material model in OpenSees was implemented in this study to model the behavior of rebars. This model implements Giuffré-Menegotto-Pinto (Giuffrè, 1970; Menegotto & Pinto, 1973) steel model which accounts for the strain hardening. The strain hardening ratio was taken as 1% in this study while other parameters were taken as software defaults.

4.5. Simulated Experiments

Twenty-three cantilever column specimens were selected from PEER Structural Performance Database (Berry et al., 2004). As stated above, the specimens that satisfy the seismic-resistant design requirements were selected. All specimens had sufficient longitudinal and transverse reinforcement to exhibit flexural failure and reported to perform so. The properties of the selected specimens are given in Table 7. Note that, the specimens were named after the name of the first authors along with the specimen codes.

Depending on the type of the vertical actuator used in the experiments, the lateral component of the vertical load may increase or decrease the measured lateral force. This effect must be eliminated to obtain the net lateral force. Therefore, the net lateral forces in the considered experiments were obtained according to the recommended procedures in PEER Structural Performance Database User's Manual to eliminate the horizontal component of the vertical actuators when necessary.

Table 7. Properties of the adopted column specimens

Experiment Name	**#**	***b* (mm)**	***h* (mm)**	***L*/*h***	$P/A_g.f_c$ **(%)**	f_c **(MPa)**	f_y **(MPa)**	ρ_s **(%)**	ρ_{sh} **(%)**	**Max. Drift (%)**
Tanaka No5	1	550	550	3.0	10	32.0	511	1.3	1.7	4.6
Tanaka No9	2	400	600	3.0	10	26.9	380	1.9	2.2	5.9
Ohno L2	3	400	400	4.0	3	24.8	362	1.4	0.3	6.1
Bechtoula D1N30	4	250	250	2.5	30	37.6	461	2.4	5.9	4.0
Bechtoula D1N60	5	250	250	2.5	60	37.6	461	2.4	5.9	3.0
Takemura JSCE-5	6	400	400	3.1	3	35.7	363	1.6	0.2	6.4
Kanda STC-1	7	250	250	3.0	11	27.9	374	1.6	0.4	7.0
Ang No3	8	400	400	4.0	38	23.6	427	1.5	2.8	3.1
Ang No4	9	400	400	4.0	21	25.0	427	1.5	2.2	3.6
Gill No1	10	550	550	2.2	26	23.1	375	1.8	1.5	2.8
Gill No3	11	550	550	2.2	42	21.4	375	1.8	2.0	1.7
Atalay 1S1	12	305	305	5.5	10	29.1	367	1.6	1.5	2.5
Atalay 3S1	13	305	305	5.5	10	29.2	367	1.6	1.5	3.1
Atalay 5S1	14	305	305	5.5	20	29.4	429	1.6	1.5	3.1
Saatcioglu & Ozcebe U4	15	350	350	2.9	15	32.0	438	3.3	2.5	10.2
Saatcioglu & Ozcebe U6	16	350	350	2.9	13	37.3	437	3.3	3.2	8.8
Saatcioglu & Ozcebe U7	17	350	350	2.9	13	39.0	437	3.3	2.0	8.8
Saatcioglu & Grira BG-2	18	350	350	4.7	43	34.0	455	2.0	2.0	5.3
Saatcioglu & Grira BG-3	19	350	350	4.7	20	34.0	455	2.0	2.0	7.0
Saatcioglu & Grira BG-5	20	350	350	4.7	46	34.0	455	2.9	2.7	5.0
Saatcioglu & Grira BG-6	21	350	350	4.7	46	34.0	478	2.3	2.7	7.1
Saatcioglu & Grira BG-8	22	350	350	4.7	23	34.0	455	2.9	1.3	7.1
Saatcioglu & Grira BG-10	23	350	350	4.7	46	34.0	428	3.3	2.7	7.1

4.6. Numerical Models

The selected columns were modeled in OpenSees platform using single FBEs with 3, 5, and 7 IPs. The columns were also modeled using the BWH element to compare the accuracy of two different modeling methods. For these comparisons, the Concrete07 concrete material model was used. The schematic view of the test specimens and the different modeling approaches used is given in Figure 69. Furthermore, all columns were modeled using different concrete material models to compare their effects. FBEs with 5 IPs were used for these comparisons. The sections in both approaches were modeled using the fiber discretization. Each region of the section was divided into 20 by 20 meshes.

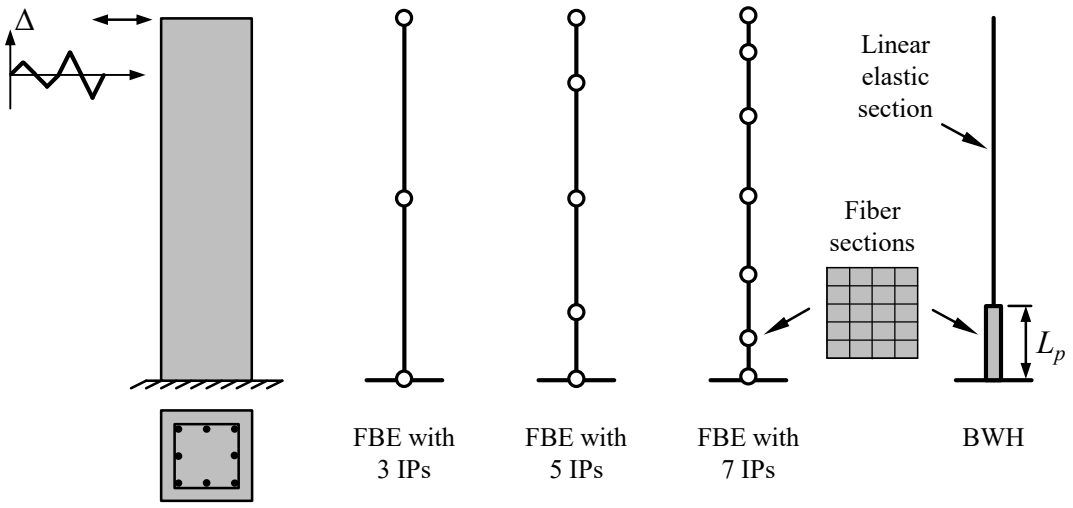

Figure 69. Schematic view of test specimens and implemented element modeling approaches

As stated earlier, it is possible to define an effective stiffness for the linear elastic zone of the BWH elements. This provides an opportunity to modify the gross stiffness of the member to take into account the effect of unconsidered factors implicitly. Empirical formulas denoted by (4.1), (4.2), and (4.3) proposed by Elwood and Eberhard (2009) were used in this study to estimate the effective stiffness of the modeled specimens. These formulations are based on statistical analyses performed on the experiment results available in PEER Structural Performance Database. Also, ASCE 41-13 (2013) recommends using these formulations to account for the effective stiffness of the reinforced concrete columns.

$$EI_{eff} \Big/ EI_g = 0.2 \qquad \text{if} \qquad \frac{P}{A_g f_c^{'}} \le 0.2 \tag{4.1}$$

$$EI_{eff} \Big/ EI_g = \frac{5}{3}\frac{P}{A_g f_c^{'}} - \frac{4}{30} \qquad \text{if} \qquad 0.2 < \frac{P}{A_g f_c^{'}} \le 0.5 \tag{4.2}$$

$$EI_{eff} \Big/ EI_g = 0.7 \qquad \text{if} \qquad 0.5 < \frac{P}{A_g f_c^{'}} \tag{4.3}$$

where EI_{eff} is the effective flexural stiffness, EI_g is the gross flexural stiffness, P is the axial load, A_g is the gross cross-sectional area of the member, f_c' is the peak compressive strength of the concrete.

The plastic hinge length for BWH elements was taken as half of the section depth since this is the common approach in contemporary seismic design codes. P-Δ effects are considered throughout the analyses. The analyses are performed by applying tip deflection history at the top node of the modeled cantilever members.

4.7. Analysis Results

Hysteretic responses obtained from the numerical analyses were compared with the experimental results of the corresponding columns. In order to quantify the hysteretic response, the results were evaluated in terms of initial stiffness (K_0), peak strength ($V_{\max}$), and dissipated energy (E). The evaluation parameters are shown in Figure 70. The comparisons were made by means of normalization of the simulation results with respect to the experimental results, i.e. $\beta_K = (K_0)_{sim} / (K_0)_{exp}$, $\beta_{V+} = (V_{max}+)_{sim} / (V_{max}+)_{exp}$, $\beta_{V-} = (V_{max}-)_{sim} / (V_{max}-)_{exp}$, $\beta_E = E_{sim} / E_{exp}$.

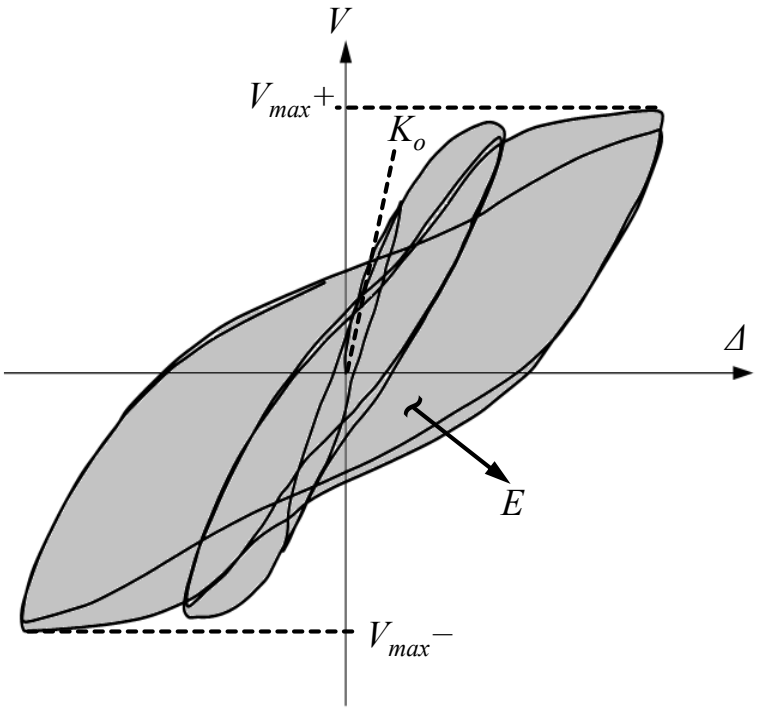

Figure 70. Illustration of evaluation parameters for hysteretic response

It was observed that calculating the initial tangent stiffness from experimental results may lead to incorrect stiffness values since the data at the initial stage of the tests are not reliable in most of the cases. Therefore, the secant stiffness at 0.1% drift was used as the initial stiffness for both the experimental and the numerical results for comparison purposes. The peak strength values were obtained for the positive and the negative directions of the loading and denoted as $V_{max}+$ and $V_{max}-$, respectively. The results show that the modeling approaches are not very effective to model the strength and stiffness degradations specifically at the large displacement levels. It should be noted that shear distortions become effective at high displacement values. However, the numerical model is not sensitive to shear distortions. This leads to overestimation of strength and stiffness, which in turn, yields an overestimation of the dissipated energy for high plastic excursions. Therefore, the comparisons were limited to approximately 2% drift levels for each test. Note that, 2% drift of a cantilever column corresponds to 4% story drift for a column located in a moment frame. As an example, Figure 71 shows the hysteretic response obtained for the Takemura JSCE-5 at full drift (6%) versus at 2% drift. This specimen is one of the specimens which exhibited severe strength degradation during the tests. As can be seen from the first plot, the strength degradation starts at 3% drift ratio. However, the numerical models fail to capture this

behavior. Nevertheless, the calculated response at 2% drift is satisfactory in terms of strength predictions.

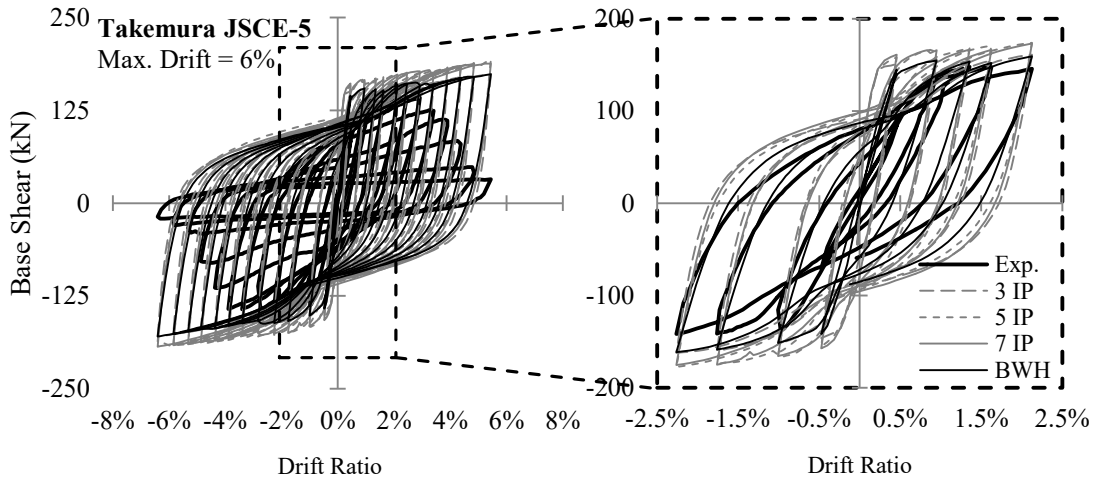

Figure 71. Comparison of analytical results with experimental results at full drift vs. 2% drift ratio for Takemura JSCE-5 specimen

4.7.1. Effect of Element Types and Number of Integration Points

Four representative column tests (Saatcioglu & Grira BG-2, Atalay 3S1, Tanaka No9, Bechtoula D1N30) are selected to provide insight into the results of the analyses. Figure 72 shows the comparison of the hysteretic responses of the selected specimens. The axial load ratio of each specimen is given at the upper left corner of the plots. Also, the effective stiffness values used for the BWH models are shown below the axial load ratios.

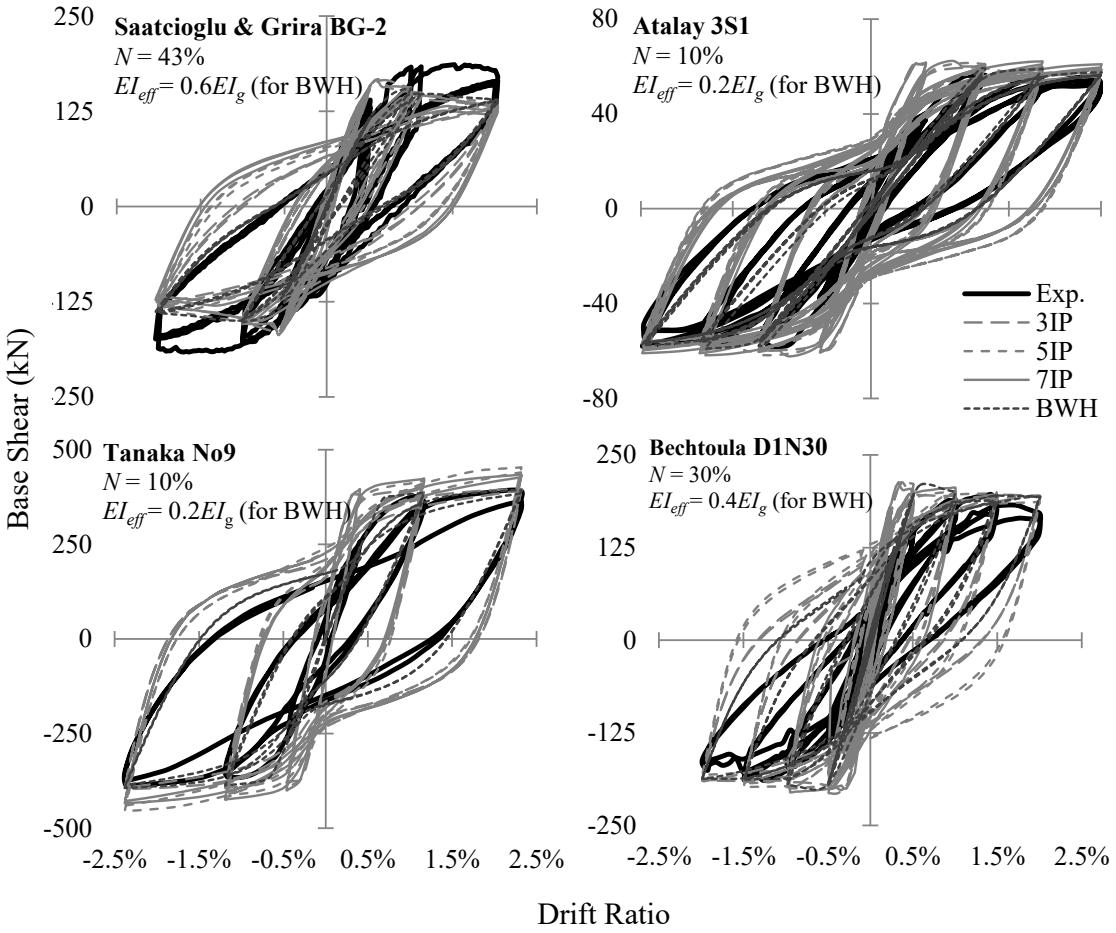

Figure 72. Sample comparisons of experimental and numerical hysteretic responses for FBE (3, 5, 7 IPs) and BWH

The comparison parameters, β_K, β_{V+}, β_{V-}, and β_E, for each simulation are presented separately in Figure 73. The solid black lines correspond to the exact match (i.e. $\beta = 1.0$). Table 8 consists of the means (μ), standard deviations (σ), and coefficient of variations (COV) for each numerical model.

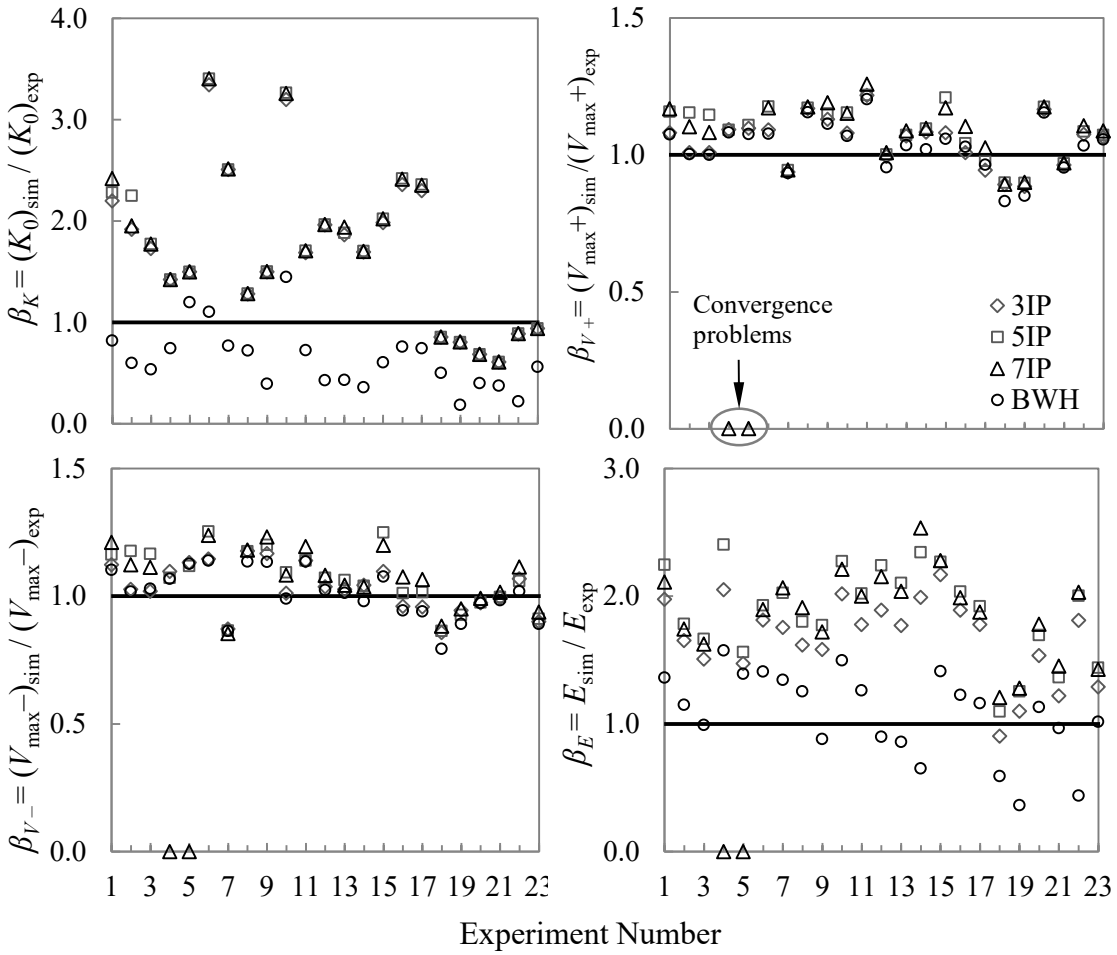

Figure 73. Comparison parameters of different element models for each specimen

Table 8. Mean (μ), standard deviation (σ) and COV values for the selected comparison parameters

Element Type	β_K			β_{Vmax+}			β_{Vmax-}			β_E		
	μ	σ	COV	μ	σ	COV	μ	σ	COV	μ	σ	COV
FBE (3 IP)	1.7	0.7	0.4	1.0	0.1	0.1	1.0	0.1	0.1	1.7	0.3	0.2
FBE (5 IP)	1.7	0.8	0.4	1.1	0.1	0.1	1.1	0.1	0.1	1.9	0.4	0.2
FBE (7 IP)	1.7	0.8	0.4	1.1	0.1	0.1	1.1	0.1	0.1	1.9	0.3	0.2
BWH	0.6	0.3	0.5	1.0	0.1	0.1	1.0	0.1	0.1	1.1	0.3	0.3

It was observed that the numerical models using FBEs generally overestimated the initial stiffness of the specimens up to 3.5 times. The averages of the initial stiffnesses obtained using different number of IPs are very close to each other. It is

about 1.8 times greater than the experimental results. Note that, the initial stiffness was underestimated by FBEs only for the specimens of Saatcioglu and Grira, which may be attributed to an unknown factor of the experiments. On the other hand, numerical models using BWH yielded closer initial stiffness values to those calculated from the experimental results. However, they are generally lower than those of the experiments.

In terms of the peak strengths, all element types and the number of IPs yielded very similar results. The peak strengths in both directions were estimated successfully except for the FBEs with 7 IPs in two of the analyses. Convergence issues were encountered during those simulations and the analyses could not be completed. It was seen that the number of IPs does not have a significant effect on the peak strength estimates. Strength deterioration occurring at higher deflections under relatively higher axial loads is simulated satisfactorily using the fiber approach for all element types.

As mentioned earlier, the fiber approach alone fails to capture stiffness and strength degradations that occur after yielding. Depending on that, the overestimation of those quantities leads to the overestimation of dissipated energies. Therefore, models using FBEs dissipated significantly greater amounts of energy compared to the experiments for they overestimated the stiffness of the specimens up to 80%. There was no significant difference between the results of the models with different number of IPs. On the other hand, by using the effective stiffness to implicitly account for the stiffness degrading factors, models with BWH yielded a better average in terms of the dissipated energy. The mean of the results of BWH models is 1.08 times that of the experiments in terms of energy dissipation with a standard deviation of 0.34. The relationship between the effective stiffness and the dissipated energy will be discussed in the coming sections.

4.7.2. Effect of Concrete Material Models

For the concrete model comparison, all cases yielded similar results. The parameters compared for each simulation are presented separately in Figure 74. It should be reminded that FBEs with 5 IPs were used in the numerical models.

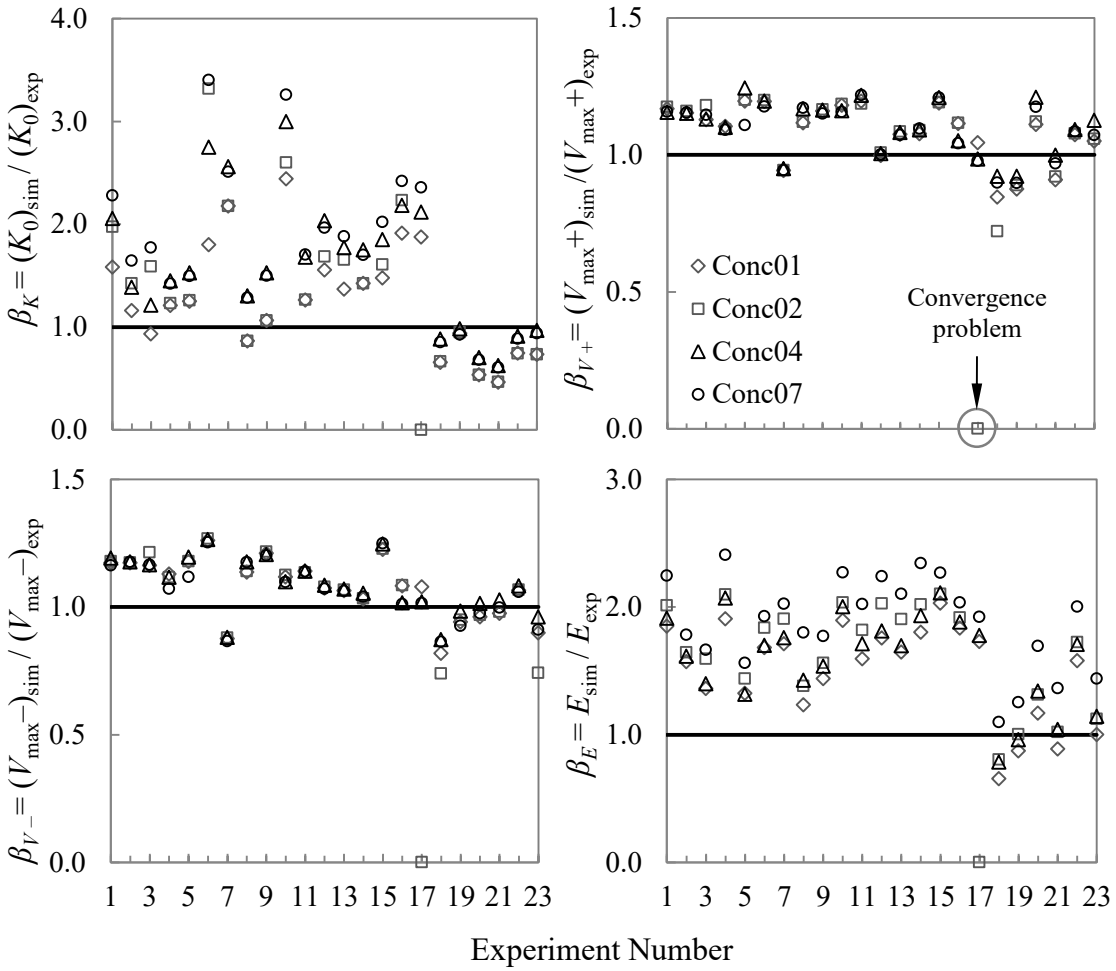

Figure 74. Comparison parameters of different concrete models for each specimen

It can be implied from the analysis results that in terms of the global response, the numerical model is not sensitive to the concrete modeling approaches in OpenSees. There are minor differences among different concrete models in terms of the calculated initial stiffness values. The difference emerges from different Young's modulus values of different models. Concrete01 and Concrete02 models assume $2f_c'/\varepsilon_c$ as the elastic modulus, while Concrete04 and Concrete07 require this value to be defined by the user. For the latter, the Young's modulus was calculated based on the expression proposed by Chang and Mander (1994). The major difference for concrete models occurred at the numerical analysis part. Concrete02 and Concrete04 models caused convergence problems in some of the cases. Those were overcome by changing the solution algorithm or convergence tolerance except for one case. Furthermore, Concrete07 had a longer runtime compared to the other models being approximately twice the time required by other models.

4.8. Discussion of the Results

The discussion is divided into two sections. The first section discusses the effects of the used element and material models. In the following section, the relationship between the effective stiffness and the predicted energy dissipation is discussed.

4.8.1. Element Modeling Methods and Concrete Models

The results of the study indicated that both the numerical modeling method and the number of IPs at FBEs have significant effects on modeling the cyclic behavior of the reinforced concrete members. Using FBEs generally leads to overestimated initial stiffness values. The unloading stiffness was also observed to depend on the initial stiffness. Therefore, using FBEs result in fatter hysteresis loops, which lead to the overestimation of the dissipated hysteretic energy. The amount of dissipated energy is the main design parameter of energy-based design approaches. Therefore, it is of major importance that this quantity is accurately predicted. On the other hand, the use of BWH generally underestimates the initial stiffness. However, in terms of the dissipated energy, this element type results in an average β_E ratio being 1.08 with a standard deviation of 0.34. The number of IPs did not cause any variation on the averages of the selected evaluation parameters. However, increasing the number of IPs may lead to convergence issues – particularly in the cases where a post-peak softening response is present due to relatively higher axial loads. These issues are related to the localization phenomenon which was addressed in depth by Calabrese et al. (2010). BWH model brings a solution to this problem while allowing the use of effective stiffness definitions for compensating unconsidered effects such as slip of the bars.

All models predicted the peak strength of the specimens quite accurately. However, it is worth to remind that all analyses were limited to a cantilever drift of 2% for this study. Beyond that stage, the strengths decrease dramatically at some tests. The element models used in OpenSees are not able to represent the strength degradations except the ones caused by the level of the axial loads. Therefore, these element models should be used cautiously when it is desired to model the behavior and failure at higher drifts.

The study showed that the choice of concrete material model in OpenSees is not as critical as the selection of the element models and number of IPs while modeling the global behavior of the reinforced concrete members. However, Concrete02 and Concrete04 models seemed prone to convergence problems. Moreover, Concrete07 model has a longer runtime compared to the other concrete materials due to its more sophisticated hysteretic model. This property is likely to increase the analysis time while dealing with larger structures.

4.8.2. Effective Stiffness and Energy Dissipation

Most damage indices, as well as the energy-based design methods, use the dissipated hysteretic energy as a measure of the cumulative damage of the structures. Therefore, this quantity should be accurately predicted. As mentioned above, using the BWH element yielded better estimates in terms of the dissipated energy. However, β_E ratio varies between 0.36 and 1.57 as seen in Figure 73. Within this study, possible factors influencing the energy dissipation estimates, such as axial load level, plastic hinge length, and effective stiffness, were investigated. It is found that axial load level and plastic hinge length had no significant effect on the energy dissipation estimates of BWH elements. However, the effective stiffness was observed to have a substantial effect on the energy dissipation mechanism of the numerical models. The stiffness modification factors ($\eta = EI_{eff} / EI_g$) used in numerical modeling were calculated based on the proposed expressions by Elwood and Eberhard (2009), as mentioned earlier. These expressions are based on the averages of data with scatter. Therefore, they give rough estimates of the stiffness modification factors. In order to observe whether the scatter observed in the energy estimation is comparable to scatter in effective stiffness estimation, the stiffness modification factors of the specimens which would yield the exact dissipated energy (i.e. $\beta_E = 1.0$ for all specimens) were found by trial and error. The aim was to observe if these factors are within the range of the scatter used by Elwood and Eberhard (2009). Figure 75 shows the stiffness modification factors that yield the exact energy dissipations together with the plot given by Elwood and Eberhard (2009). It can be observed that the factors yield the best fit are well within the scatter, except for the Saatcioglu & Grira BG-2 and Bechtoula D1N60 specimens.

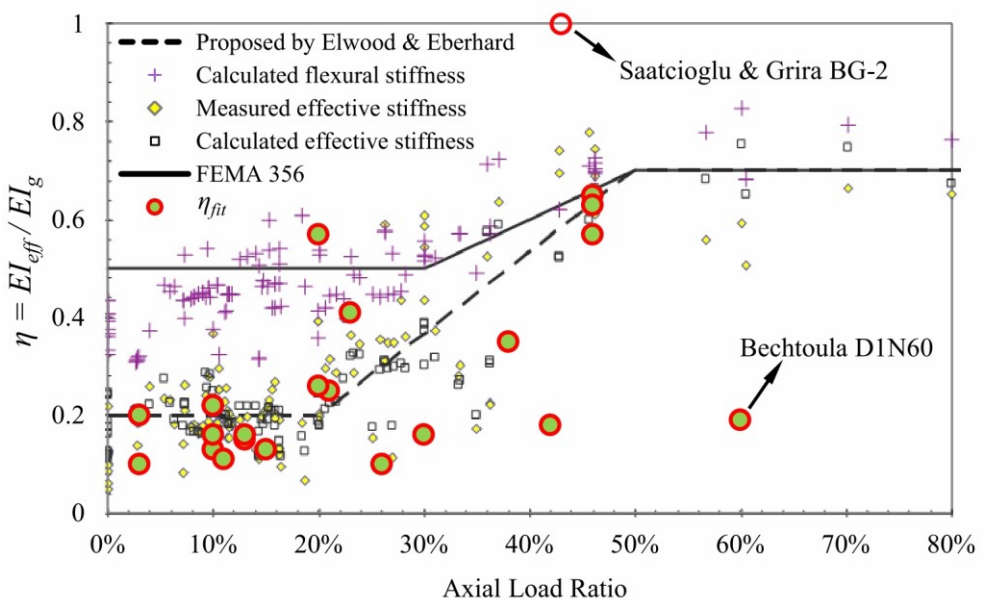

Figure 75. Comparison of effective stiffness values used by Elwood & Eberhard (2009) and those yield the best fit in terms of dissipated energy vs. the axial load ratio

The ratio of the stiffness modification factors that gave the best fit in terms of energy dissipation to those calculated using the equations proposed by Elwood and Eberhard (2009), η_{fit}/η_{calc}, were calculated for each specimen. The mean of the η_{fit}/η_{calc} values is 0.94 while the standard deviation is 0.57. For the specimen Saatcioglu & Grira BG-2, even the gross stiffness yielded lower energy dissipation compared to the experiments. One reason for this is that the peak strength is calculated to be 20% lower for this specimen in both loading directions. The other reason is that this specimen has one of the highest yield drift values compared to the other specimens. As for the Bechtoula D1N60 specimen (60% axial load ratio), the unloading stiffness shows an abrupt degradation at a certain moment of the unloading at each cycle. The reason for this cannot be found in the experiment reports. The numerical models did not exhibit a similar behavior. Therefore, the energy dissipation could be captured only using a very low effective stiffness, $EI_{eff} = 0.19EI_g$.

At this point, it was observed that as the calculated yield drift gets higher, the η_{fit}/η_{calc} ratio tends to get higher as well, i.e. higher effective stiffness than the proposed one should be used. The use of overall effective stiffness decreases the initial stiffness of the specimen. Therefore, the specimen with a relatively higher calculated yield drift ratio dissipates less hysteretic energy compared to a specimen with a lower calculated

yield drift ratio. Since the simulations are performed until a constant drift ratio, the specimens with a higher calculated yield drift ratio could reach the yield only in the last cycles. Upon these observations, a relationship between η_{fit} / η_{calc} and the calculated yield drift ratio was sought. Figure 76 shows this relationship and a trendline. The trend supports the observation about the effect of modeling on the energy dissipation of elements with high yield drift values.

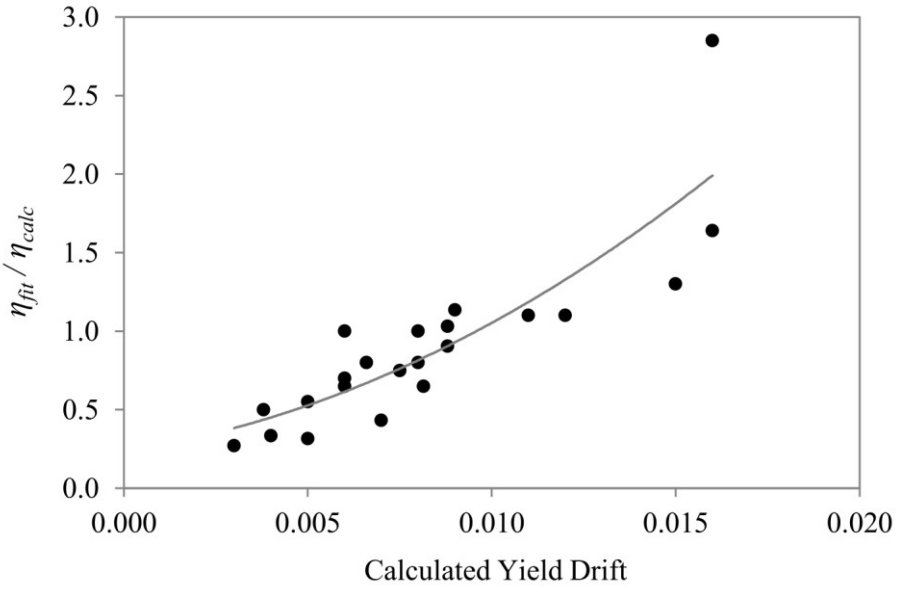

Figure 76. Relationship between calculated yield drift and η_{fit} / η_{calc}

4.9. Concluding Remarks

The accuracy and success of different element and material models on simulating reinforced concrete member behavior were investigated through comparisons with 23 experimental results adopted from PEER Structural Performance Database. OpenSees platform was used for the implementation. Since the study aims to compare the flexure-dominant numerical modeling procedures for the moment frame design purposes, each specimen was selected to have flexure-dominated ductile behavior and represented with only a single FBE or BWH element. Furthermore, the effect of various concrete material models was also investigated. Initial stiffness, peak strength, and dissipated energy were selected as comparison parameters to quantify the global hysteretic response of the specimens. The conclusions referred from the study are summarized below:

- The study showed that using FBEs leads to overestimation of the stiffness values, which in turn, resulted in overestimated energy dissipations. It happened even when the peak strengths were estimated properly.
- Increasing the number of IPs did not have any significant effect on the results. However, it is observed that this may cause convergence problems particularly for the specimens with relatively higher axial loads. Therefore, if FBEs are going to be used, 5 IPs per element can be recommended for an effective analysis.
- BWH element type had some advantages over FBE such as having the option to modify the gross stiffness and demanding less computational effort. It also resulted in better estimates in terms of the parameters considered.
- A further evaluation showed that the effective stiffness has significant effects on the energy dissipation of the numerical model. A relationship between the calculated yield drift and the effective stiffness was observed. However, further research is required to establish a strong correlation between the yield drift and effective stiffness.
- The choice of concrete models does not significantly affect the analysis results. However, Concrete02 and Concrete04 models caused convergence problems in some cases. On the other hand, the Concrete07 model demands more computational time. Therefore, it is recommended to use the Concrete01 model unless a specific case necessitates the use of other concrete models.

Based on the conclusions, the BWH element type and Concrete01 concrete model were selected to be used for the nonlinear numerical modeling of the reinforced concrete frames in the OpenSees platform.

CHAPTER 5

INELASTIC DESIGN PROCEDURE

5.1. Introduction

Interstory drift has been deemed and used as a measure of structural and non-structural damage for multistory buildings subjected to seismic motions (Sozen, 2003). As performance-based seismic design gained traction, the importance of interstory drift as a main design consideration crystallized. However, seismic design codes generally employ interstory drift as a limiting value for certain performance levels. The maximum interstory drift ratio wherever happening within the structure is defined as a precursor parameter of the performance. However, it is believed that there is more potential to exploit the use of drift ratio for design purposes. If it is possible to control its distribution throughout the height, it will provide an opportunity to control the damage throughout the height of the structure.

In the conventional seismic design, low- to mid-rise frame structures are often designed using the equivalent lateral load approach. The heightwise distribution of the lateral loads in this approach is determined based on the linear dynamic properties of the structure. However, this may lead to unpredictable distribution of seismic demands when the structure experience inelastic deformations under severe ground motions. Consequently, the displacement demand of code-complying structures is not expected to be uniform along the height during severe earthquakes. This may lead to interstory drift – and therefore, damage concentrations at particular parts of the structures. Total collapse is likely to occur as a result of these concentrations.

Numerous optimization methods that aim to reach uniform displacement demands under seismic actions are available in the literature (e.g. Zou & Chan, 2005; Bai et al., 2016). The methods used in these studies are generally based on expressing the seismic design in the form of mathematical expressions and solving them in an iterative manner until the results converge to the target criteria. However, obtaining accurate yet simplified mathematical expressions for the optimization process and solving sets of equations at each step is an impractical and cumbersome approach for seismic design. Furthermore, a nonlinear time-history (NLTHA) or pushover analysis is

required between each step to check the convergence. In this type of methods, the design and/or the analysis phases are often oversimplified to reduce the number of constraint equations and the number of the steps to reach the convergence within a reasonable time. Most importantly, reducing the seismic design to a sole optimization problem may result in bypassing the engineering judgment, which is a must in the face of the existing uncertainties of the seismic design.

Some researchers take a different approach and aim to determine the optimum distribution of equivalent design lateral loads that would result in a structure which has uniform drift or ductility demands over its height (e.g. Medina, 2004; Moghaddam & Hajirasouliha, 2006; Park & Medina, 2007; Hajirasouliha & Moghaddam, 2009). These studies showed that the optimum design lateral load distribution is sensitive to the site soil conditions, the properties of the ground motions, the level of inelastic deformation, and the structural characteristics of the building. Therefore, this type of approaches requires a sound prediction of these parameters, which is not straightforward to establish.

This study proposes a two-step seismic design procedure, which optimizes the seismic behavior without ruling out the engineering judgment. The first step is based on aiming a combined modal pattern and a fundamental period (Chapter 3). These targets are of major importance since the global drift response of the structure is imposed at this step. However, the preliminary studies showed that as the seismic response goes into the inelastic range, elastic modal properties change. The yield strength distribution throughout the structure becomes the main parameter that controls the average stiffness and the drift distribution in the inelastic range (Leelataviwat et al., 2002; Hajirasouliha et al., 2012). Therefore, the second step of the proposed procedure attempts to modify the member yield strengths in an iterative manner after the initial proportioning as per the contemporary seismic design codes. This sort of procedure gives the engineer full control over the design while maintaining the code requirements.

This chapter presents the basis of the iterative inelastic design procedure, which aims to mitigate the interstory drift concentrations under the design-basis earthquake. In addition, an illustrative example is presented to demonstrate the application and the success of the proposed procedure.

5.2. Basis of the Procedure

Drift in a moment-resisting frame may be separated into individual deformations of structural members. Flexural actions at the ends of beams and columns constitute a significant portion of the drift. However, as the aspect ratio (height/width) of the frame increases, the axial deformations of the columns (cantilever or chord action) contribute more to the drift (Naeim, 2001). On the other hand, the contribution of shear deformations of beams, columns, and joints remains at negligible levels (Broderick, 1994). Since the context of this study is limited to low- to mid-rise moment-resisting frames, drift may completely be associated to the end rotations of beams and columns.

To avoid the interstory drift concentrations during earthquakes, the maximum interstory drifts attained at all stories should be controlled. However, as mentioned above, the drift itself is a consequence of individual member deformations − particularly the end rotations. Thus, the end rotations of the members can be used as a tool for controlling the drift at low- to mid-rise frame structures. End rotations can be decomposed into two parts: elastic and plastic rotations. The first step of the proposed design procedure controls the elastic part by adjusting the member cross-sectional dimensions (i.e. by altering the flexural stiffness of the members) throughout the structure (procedure defined in Chapter 3). The plastic part of the end rotations may be used to control the drifts in the inelastic range. Note that, damage in a section could be accepted as a function of the maximum plastic deformation and the dissipated hysteretic energy during seismic actions. Therefore, controlling the plastic rotations also helps to control the damage to a great extent.

In the proposed design procedure, the initial proportioning of the reinforcement is performed as per a selected seismic design code after the primary sizing of the members. This ensures that the strong column-weak beam condition is satisfied at the joints. Consequently, plastic actions are expected to take place at the beam-ends, and the lower ends of the first story columns. Literature (Mayengbam & Choudhury, 2014; Bai et al., 2020) and the preliminary studies show that plastic rotations at the beam-ends can be used as a parameter to control the drift throughout the structure in the inelastic range, if the beam-failure mechanism is assured. Beam failure mechanism of moment frames contains plastic hinges at the column-footing interface in addition to the plastic hinges at the beam-ends. Therefore, an additional constraint for the plastic rotation at

columns could be set in addition to those of the beams. In various studies, an almost linear correlation between the drift and the plastic rotation distribution is confirmed to exist for code-conforming frame structures (Mayengbam & Choudhury, 2014; Bai et al., 2020).

The primary purpose of the study is to reach uniform maximum envelope interstory drift ratios during the seismic action. To fulfill this purpose, all beams throughout the considered frames should be "forced" to attain the same amount of maximum plastic rotation during the seismic response while the columns remain elastic except at the base. The target maximum plastic rotation at the beam-ends can be selected according to the required performance level of the structure. For instance, ASCE 41-13 (2013) correlates the performance levels (i.e. immediate occupation, life safety, collapse prevention) with the maximum plastic rotations attained at member-ends. These limits can be used as target maximum plastic rotations. If plastic action in some columns is inevitable, an additional plastic rotation limit could be set for the columns, as well as for the beams.

In nonlinear stages of seismic response, the plastic moment-rotation response of a member is not only controlled by the initial flexural stiffness, but also by the yield moment. This case can be explained on a lumped-mass single-degree-of-freedom system using the equal displacement rule. The equal displacement rule suggests that the spectral deformation demand of a system is independent of its yield strength. It rather depends on the initial stiffness of the system (Veletsos & Newmark, 1960). Therefore, changing the yield strength does not significantly affect the maximum deformation of the system attained during seismic motions provided that the initial period remains constant. However, the extent of the plastic deformation (i.e. displacement ductility demand) changes with the yield strength of the system. The equal displacement rule expresses the maximum response of the system experienced during seismic excitations using a monotonic pushover analogy. Figure 77 illustrates the equal displacement rule for systems having the same initial period but different yield strengths. As seen from the figure, the extent of the plastic deformation is inversely proportional to the yield strength. Therefore, the amount of plastic deformation may be controlled by modifying the yield strength of the system.

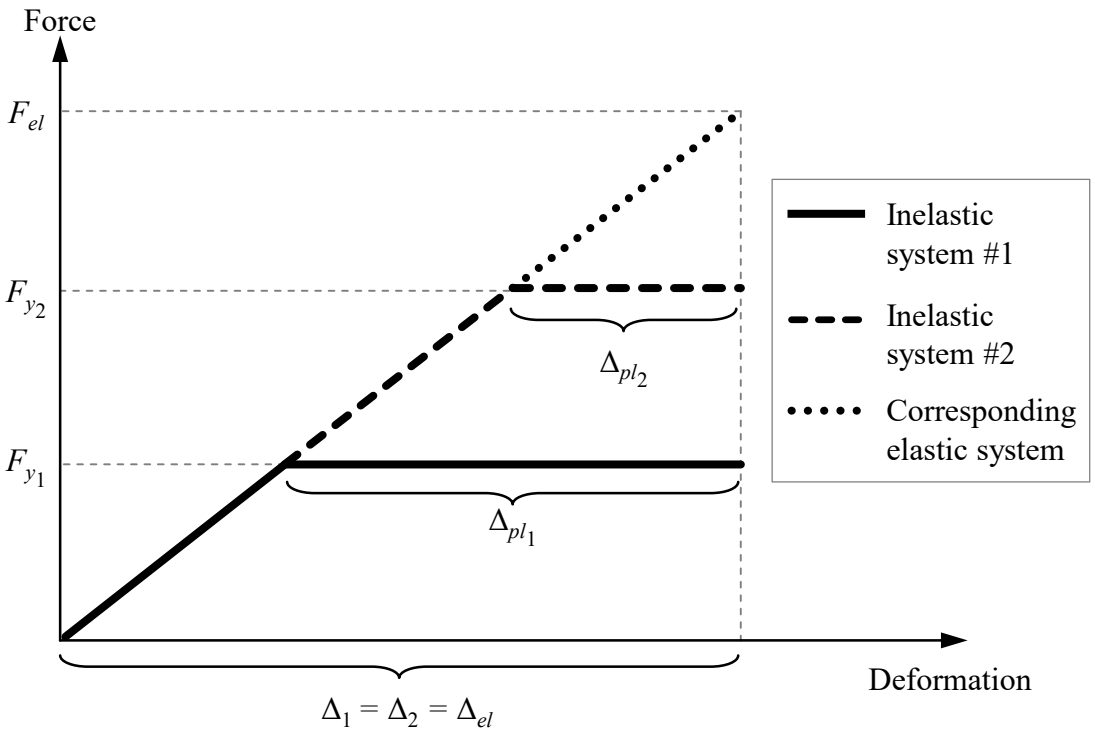

$F_{y_{1,2}}$	: Yield strength of system #1 and #2
F_{el}	: Force of the linear elastic system at maximum deformation
$\Delta_{1,2}$	: Maximum deformation of system #1 and #2
Δ_{el}	: Maximum deformation of the linear elastic system
$\Delta_{pl_{1,2}}$	: Plastic deformation of system #1 and #2

Figure 77. Illustration of equal displacement rule

The determination of the required yield strength to reach a target maximum plastic deformation needs a correlation between the force and deformation values. However, the force-deformation relationship is not linear for inelastic systems. At this point, the plastic strain energy developing in the system can be used to correlate the plastic deformation to the yield strength. It is a function of the exerted force and the resulting plastic deformation. Figure 78 shows the elastic and the plastic strain energy stored in an idealized elastoplastic system for a particular deformation beyond yield. The elastic energy is recoverable while the plastic strain energy is not.

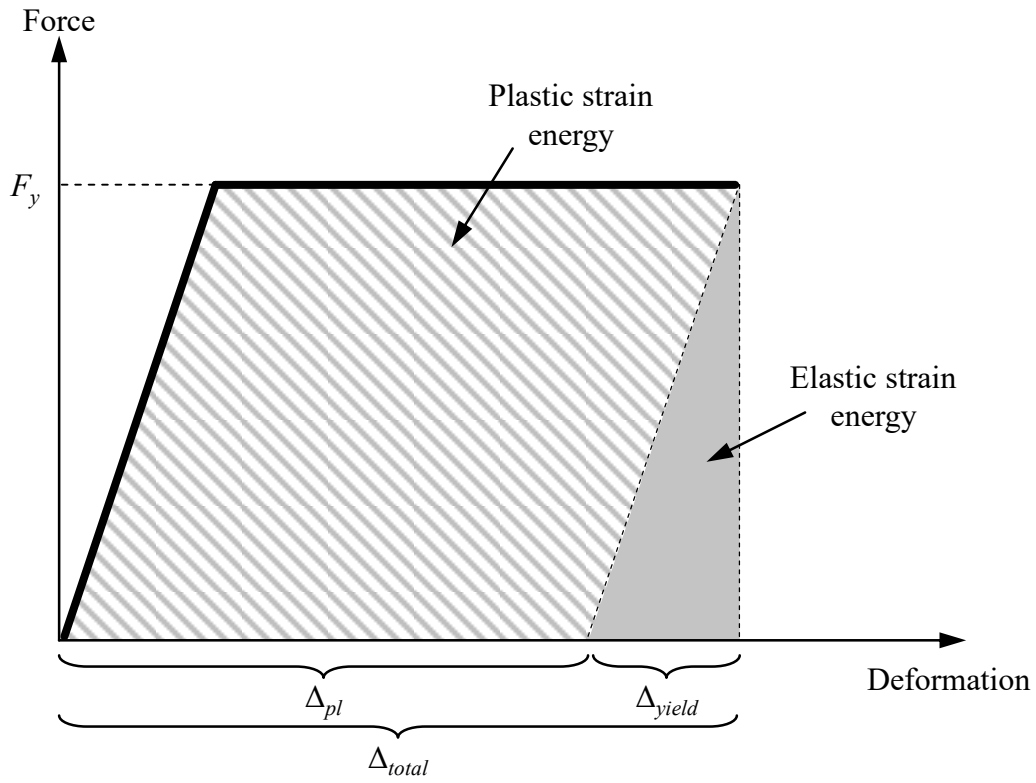

Figure 78. Elastic and plastic strain energy of an elastoplastic system

The plastic strain energy (E_{pl}), which is stored when the system is monotonically pushed to the maximum deformation experienced during the seismic action, can be used as a tool to determine the required yield strength for reaching a target plastic deformation. Figure 79 shows two systems with the same initial period but different yield strengths. The amount of plastic deformations (Δ_{pl}) along with the plastic strain energies are shown in the figure, as well.

As it can be observed from Figure 79, the amounts of the plastic strain energy for the two systems are

$$E_{pl_1} = F_{y_1} \Delta_{pl_1} \tag{5.1}$$

$$E_{pl_2} = F_{y_2} \Delta_{pl_2} \tag{5.2}$$

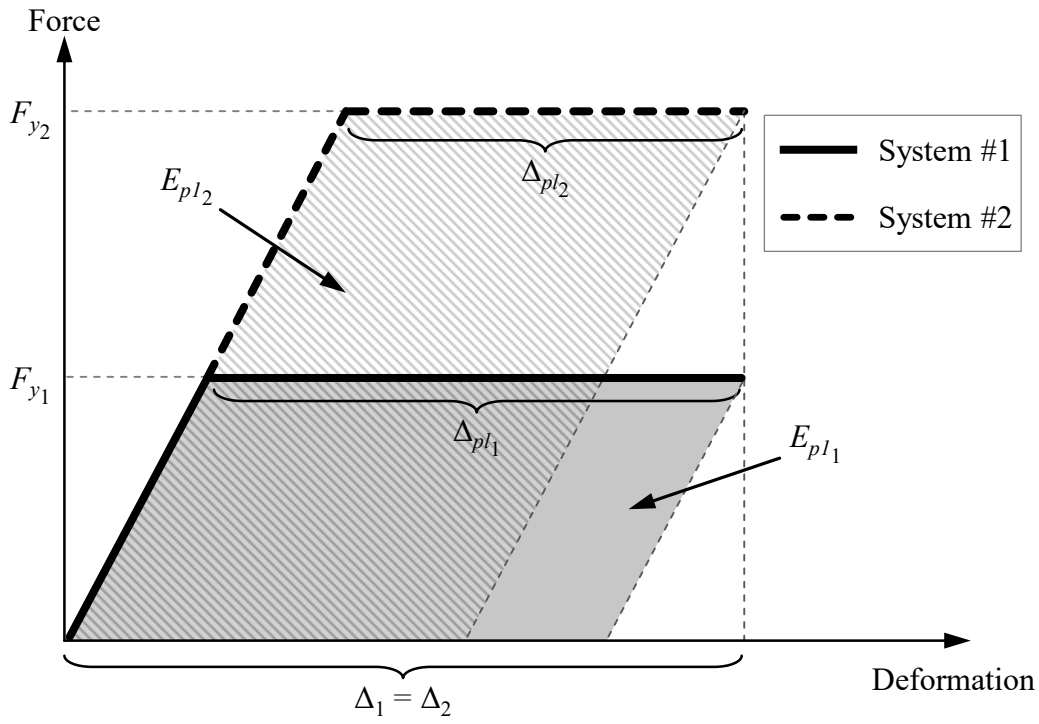

Figure 79. Plastic deformations and plastic strain energy of systems with different yield strengths

If the plastic deformation of the System #2 is desired to be equal to the target plastic deformation, $\Delta_{pl_2} = (\Delta_{pl})_{target}$, and the plastic strain energies of the two systems are assumed to be equal to each other ($E_{pl_1} = E_{pl_2}$);

$$F_{y_1}\Delta_{pl_1} = F_{y_2}(\Delta_{pl})_{target} \tag{5.3}$$

The required yield strength for the System #2 to undergo the target plastic deformation, $(F_{y_2})_{req}$, can then be determined by

$$(F_{y_2})_{req} = \frac{E_{pl_1}}{(\Delta_{pl})_{target}} = \frac{F_{y_1}\Delta_{pl_1}}{(\Delta_{pl})_{target}} \tag{5.4}$$

In the procedure above, the amounts of plastic strain energy for both systems are assumed equal. However, the plastic strain energy may change as the yield strength of the system (F_y) changes. In addition, the correlation between the cyclic and the monotonic responses of the same system is not exact, but approximate. Therefore, it is not possible to obtain the required yield strength directly. Instead, an iterative approach may be used by implementing the assumption mentioned above to obtain the required yield strength to attain a target plastic deformation during the cyclic response.

If the amount of plastic strain energy is assumed to remain constant between two subsequent steps, $(E_{pl})_{i+1} = (E_{pl})_i$, the steps of the iterative approach are as follows:

1. Select target maximum plastic deformation, $(\Delta_{pl})_{target}$.
2. Perform nonlinear time-history analysis (NLTHA) and determine the maximum total deformation, Δ_i, and maximum plastic deformation, $(\Delta_{pl})_i$, attained.
3. Check if the maximum plastic deformation is equal to the target plastic deformation. If it is, terminate the process.
4. If not, perform a pushover analysis of the system up to the total maximum deformation experienced in the NLTHA, Δ_i. Calculate the stored plastic strain energy, $(E_{pl})_i$.
5. Calculate the required yield strength $(F_y)_{i+1}$ to store the same amount of plastic strain energy up to the target plastic deformation using Equation (5.4). Revise the yield strength of the system and proceed to Step 2.

The flowchart and the schematic illustration of the iterative process are shown in Figure 80.

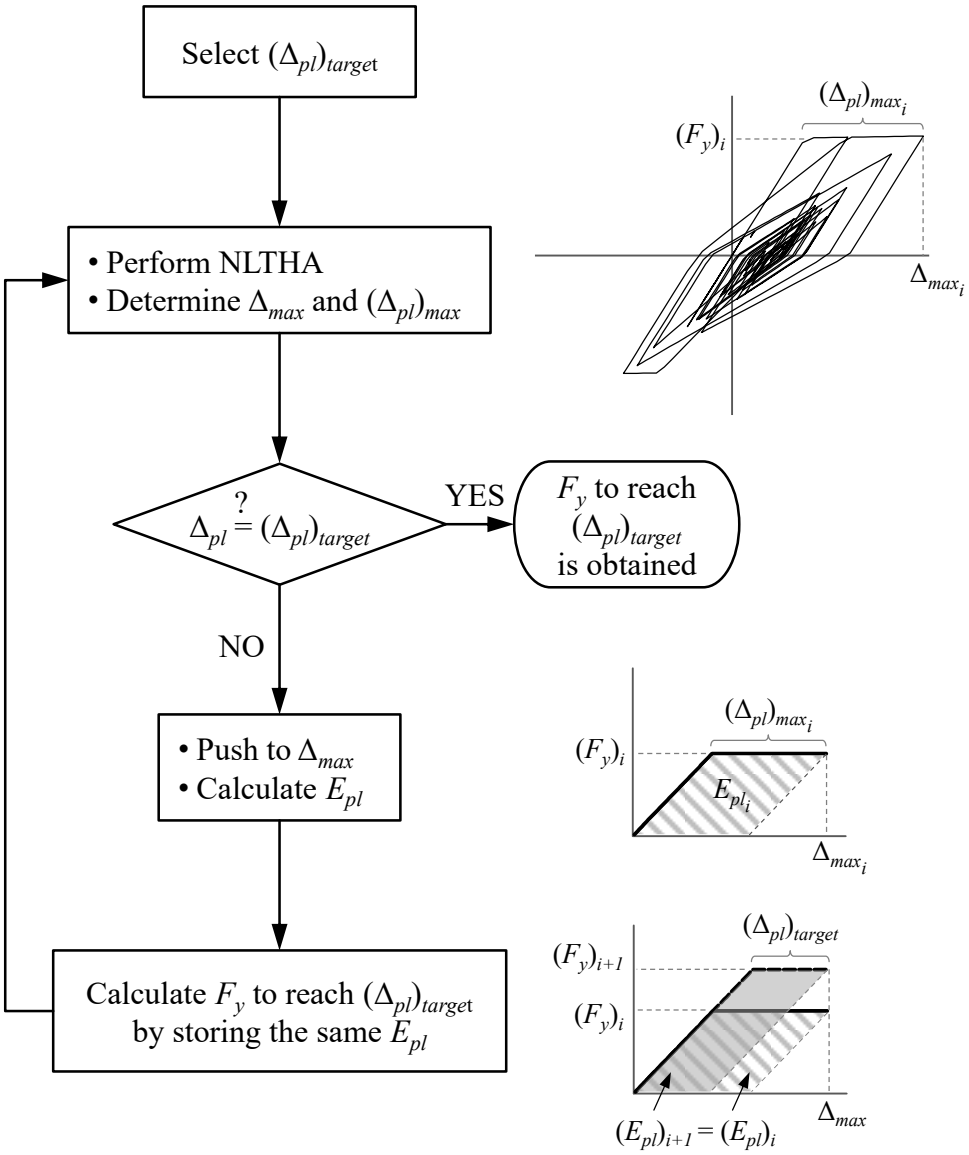

Figure 80. Flowchart and schematic illustration of the iterative process

5.3. Extending the Iterative Procedure to Reinforced Concrete Frames

As it is explained in the previous section, the drift distribution of the frames in the inelastic range can be controlled by manipulation of the plastic rotations at the member-ends. Since the maximum plastic rotation reached during the seismic excitation is of concern, the monotonic moment-rotation response of the member end-sections could be used to modify the yield moment by using the iterative procedure described above. As a result, the required yield moments for all elements that exhibit plastic behavior at their ends, can be determined to reach the target maximum plastic rotations during the seismic response. For seismic design purposes, time-history analyses are

generally performed using a suite of ground motion records. In the proposed procedure, the mean results of multiple time-history analyses are used when implementing the procedure.

In reinforced concrete sections, the dominant parameter for yield moment is the amount of the reinforcement for a given cross-section. Since the member cross-sections are proportioned in the first part of the proposed design procedure, the reinforcement ratio is to be modified to obtain the required yield moment calculated in the iterations. The member cross-section sizes are revised only if the modified reinforcement ratio goes beyond the code limitations.

The concentrated monotonic moment-rotation responses at the member ends were obtained by implementing the lumped plasticity. In this approach, the plastic action at the member ends is assumed to be restricted within a region of constant length (i.e. plastic hinge region). Thus, the moment-curvature backbones of the member end-sections can be used to calculate the monotonic moment-rotation relationship for the plastic hinge regions by multiplying the curvatures by the plastic hinge lengths.

The distribution of the ductility demand and the hysteretic energy among the members connected at a joint is governed by the yield moment ratios of the members with respect to each other. Therefore, at each step, the required yield moment is initially calculated for the beams. Then, the required yield moments of the columns are calculated at each joint to preserve the initial column-to-beam strength ratios (the ratio of the sum of moment capacities of all columns to the sum of moment capacities of beams at a joint). Thus, the strength relation between the connecting members remains unchanged throughout the iterations. However, a column may be connected to beams of different capacities at its upper and bottom ends. Therefore, different yield moments for the same column may be required at each end. In this case, the arithmetic mean of the required moments is used to determine the required column reinforcement. Furthermore, at an intermediate floor level, two columns are connected at each joint − one is of the top, the other one is of the bottom story. The moment capacities of these columns are different due to their axial load levels even if they have the same dimensions and reinforcements. The ratio of the moment capacities under the gravity loads is assumed constant when calculating the required column moment capacities to preserve the initial column-to-beam strength ratio.

The steps of the proposed inelastic design procedure, which includes the iterative yield-moment-modification procedure, are summarized below. Note that, the

preliminary sizing of the frame members should be performed prior to executing the procedure. In this study, member sizes are determined considering a target period. Refer to Chapter 3 and Chapter 7 for further details and application of the member sizing procedure.

1. Proportion the reinforcement of the beams and columns as per a selected seismic design code for the design-basis ground motion level. Select target maximum plastic rotation, $(\theta_{pl})_{target}$.
2. Perform multiple nonlinear time-history analyses (NLTHAs) and acquire the mean of the maximum plastic rotations at the plastic-hinges, $(\theta_{pl})_{max}$.
3. If the interstory drift ratio (IDR) distribution is sufficiently uniform and the mean maximum plastic rotations at all plastic hinges are sufficiently close to the target plastic rotation, finish the design of the frame.
4. If not, perform moment-curvature (M-φ) analysis for each end-section. Obtain the moment-rotation (M-θ) relationships for each plastic hinge by multiplying the curvatures by the plastic hinge lengths (L_p).
5. Calculate the plastic strain energy (E_{pl}) stored at each plastic hinge when deformed monotonically to the corresponding mean maximum plastic rotation obtained at the NLTHAs.
6. Calculate the required yield moment, $(M_y)_{req}$, at each beam plastic hinge to store the same amount of plastic strain energy up to the target maximum plastic rotation.
7. Modify the reinforcement ratio (ρ) at each beam end-section so as to have the required yield moment.
8. Calculate the required yield moment for columns to preserve the initial column-to-beam strength ratio and modify the reinforcement ratio accordingly.
9. Revise the numerical model and proceed to Step 2.

   Figure 81 shows the flowchart of the proposed iterative procedure.

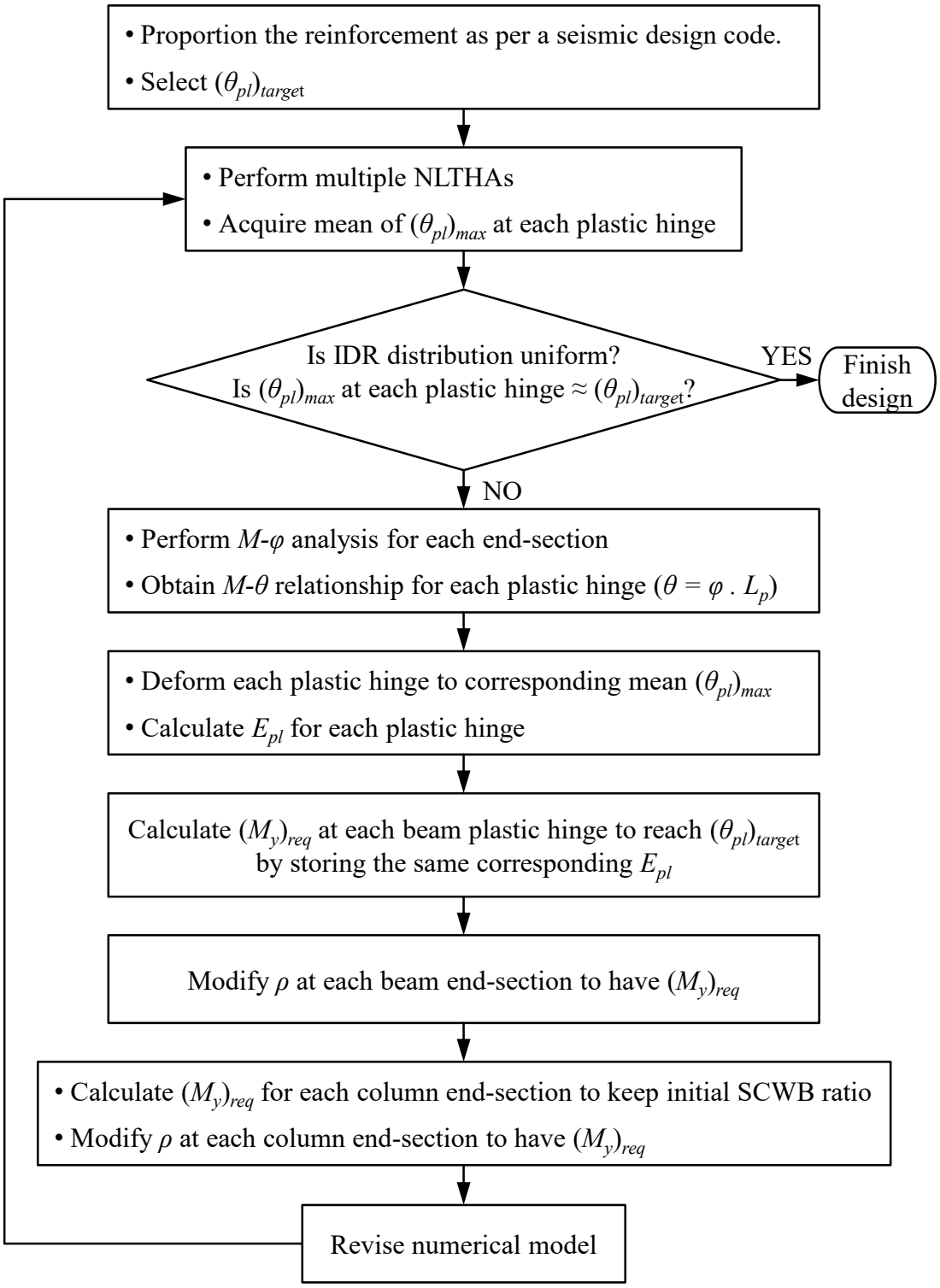

Figure 81. Flowchart of the iterative procedure

5.4. Illustrative Example

An illustrative example is presented in this section to facilitate the understanding and to demonstrate the application of the proposed iterative procedure. A single-bay, two-story, planar reinforced concrete frame is selected for this purpose.

5.4.1. Seismic Design

The initial seismic design of the model frame was performed as per the Turkish Earthquake Code (TEC2018) using the equivalent lateral load procedure and capacity design principles. The story height of the frame is 3.0 meters; the bay width is 5.0 meters. The characteristic strengths of the concrete and the reinforcing steel are 25 MPa and 420 MPa, respectively. An overview of the frame and the member tags are shown in Figure 82.

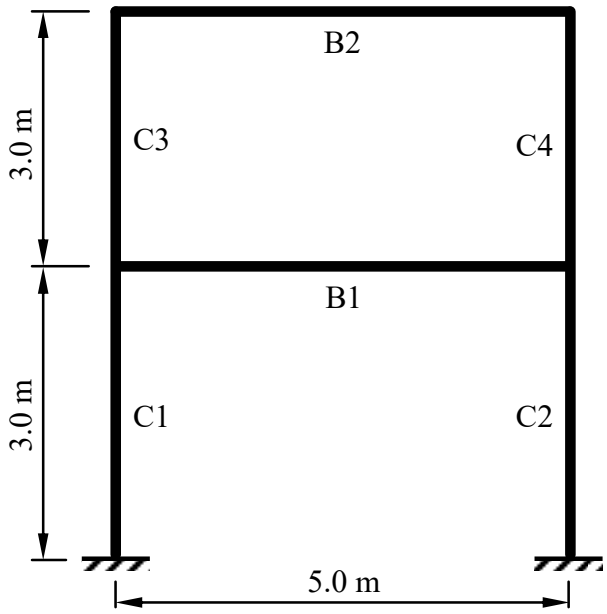

Figure 82. Overview of the model frame and member tags

The model frame was assumed to be located at a high-seismicity region on type ZD soil (stiff soil profile as per TEC2018). The distance of the site to the nearest active fault is assumed as 20 kilometers. The linear elastic acceleration design spectrum for the design earthquake level (10% probability of exceedance in 50 years) was obtained using the Turkish Earthquake Risk Map application as seen in Figure 83. The acceleration

values of the design spectrum were reduced by the response reduction factor, R, as described in TEC2018, while calculating the seismic design loads.

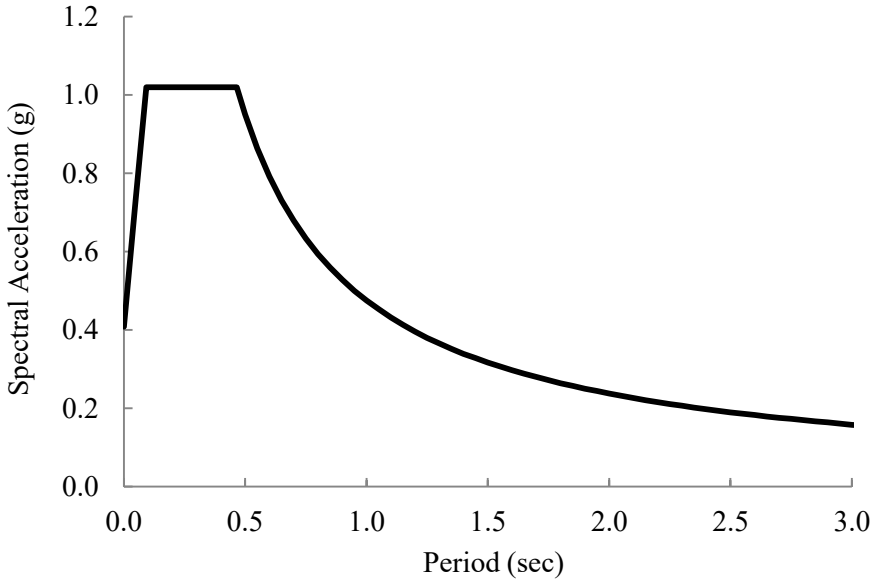

Figure 83. Linear elastic design spectrum for the selected location

The column cross-section dimensions were determined as 40×40 cm. The beam cross-sections were determined to be 25×50 cm. The slab thickness was assumed to be 12 cm and the slabs were assumed to extend 2.5 meters in both transverse directions. The mass of each floor was calculated to be 1.10 ton/m^2. The reinforcement ratios at the column and the beam-ends along with the cross-section dimensions are summarized in Table 9.

Table 9. Cross-section dimensions and longitudinal reinforcement ratios

Member	**Cross-section**		**Longitudinal Reinforcement Ratio, ρ (%)**	
	Width, b (cm)	**Depth, h (cm)**		
C1	40	40	1.15	
C2	40	40	1.15	
C3	40	40	1.15	
C4	40	40	1.15	
Member	**Cross-section**		**Longitudinal Reinforcement Ratio, ρ (%)**	
	Width, b (cm)	**Depth, h (cm)**	**Top**	**Bottom**
B1	25	50	0.87	0.52
B2	25	50	0.53	0.29

5.4.2. Numerical Model

The frame was modeled in the OpenSees platform. The frame members were modeled using the lumped plasticity element model (beamWithHinges). As explained in Chapter 4, beamWithHinges element type of OpenSees can implement either fiber-based sections or nonlinear rotational springs to model the plastic behavior at the member ends. In this study, the fiber-based sections are used for the columns, since they allow the axial load - moment interaction to be considered. For the beams, the moment-curvature response is simplified as a bilinear curve and assigned to the nonlinear rotational springs at the plastic hinge regions. These springs implement a uniaxial material model in OpenSees which is called as “hysteretic”. This model is a bilinear peak-oriented hysteretic model. Note that, using rigid diaphragm constraints to consider the contribution of the slabs may cause the development of artificial axial forces in the fiber sections due to the shifting of the neutral axis. Therefore, if rigid diaphragm constraints are used, the use of fiber sections for the beams should be avoided. Since the rigid diaphragm constraints were used in the numerical model, beam plastic hinges were modeled by rotational springs. For the “hysteretic” models, a 1% strain hardening ratio was used. Since none of these models account for the shear deformations, it is assumed that sufficient amount of shear reinforcement is present, and all members exhibit ductile flexural behavior. In addition, the shear force demands of the members are compared to the capacities and it is verified that the shear capacities are not exceeded in any case.

Effective flexural stiffness was defined at the elastic interior portions of the elements. There is not an agreement among the seismic design codes on the values of the effective stiffness factors to be used for beams and columns. Some codes suggest using constant factors for both, while some vary the factors depending on the axial load ratio. However, it is not easy and plausible to determine the exact factors that reduce the gross flexural stiffness to estimate the seismic response. Instead, it is more effective to modify the gross stiffness of the members with a plausible factor (Sözen, 2003). Therefore, half of the gross flexural stiffness was used for both the beams and the columns in the numerical model. The fundamental period of the frame was calculated as 0.52 seconds using the selected effective stiffnesses. A 2% damping ratio was used for the nonlinear time-history analyses. P-Δ effects are considered in the numerical model.

5.4.3. Strong Ground Motion Set

Nonlinear time-history analyses are performed after each step of the iterative procedure to evaluate the seismic response of the frames. For this purpose, eleven ground motion records were adopted from PEER NGA-West2 Strong Motion Database (Ancheta et al., 2013) in accordance with the site properties as per TEC2018. The selection criteria are as follows:

- Magnitude (M_w): 5.5 - 7.5
- Fault type: Strike-slip
- Distance to rupture surface (R_{rup}): > 15 km
- Shear wave velocity (V_{s30}): 180 - 360 m/s
- Duration: > 10 s

Initially, twenty ground motion records matching the criteria were selected. The selected ground motion records are scaled such that their mean acceleration spectrum does not fall below the elastic acceleration design spectrum in the period range from $0.2T$ to $1.5\ T$, where T is the fundamental period of the structure (TEC2018, 2018). Amplitude scaling technique was used for scaling the ground motion records. The records required a scale factor less than 0.5 and greater than 3.0 are omitted. Also, no more than two records from the same earthquake were used. The remaining records were scaled again to obtain the appropriate mean acceleration spectrum. Individual and mean (μ), mean-plus-one ($\mu+\sigma$) and mean-minus-one ($\mu-\sigma$) standard deviation spectra of the scaled records along with the elastic design spectrum are presented in Figure 84. Properties of the selected ground motion set and the scale factors are given in Table 10. Acceleration time histories of the ground motion records are given in Appendix A.

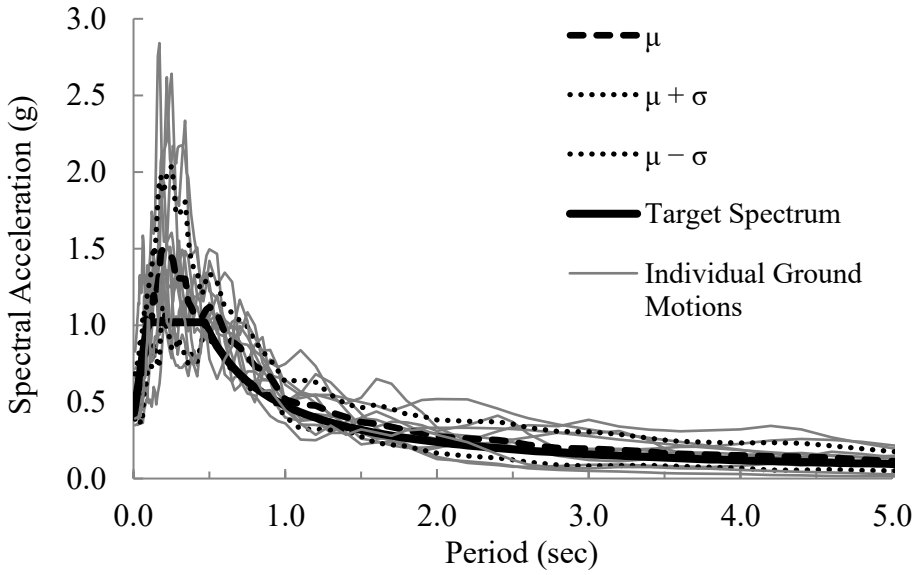

Figure 84. Linear acceleration response spectra of the scaled ground motion records

5.4.4. Implementation of the Iterative Procedure

The target plastic rotation for each beam plastic hinge was selected as 0.01 radians as per ASCE 41-13 (2013). This value corresponds to immediate occupation criteria for adequately detailed ductile beams. The selected target for the beam-end plastic rotations is within the reach, if the interstory drift concentrations are avoided. The nonlinear time-history analyses (NLTHA) of the designed frame were performed using the scaled ground motion records. The mean values of the maximum plastic rotations attained at each plastic hinge were obtained and presented in Table 11. The maximum of the two end rotations is used in the calculations for each member.

Table 10. Properties and scale factors of the ground motion records

Earthquake Name	Record Sequence Number	Station Name	Year	M_w	V_{s30} (m/s)	R_{rup} (km)	PGA (g)	PGV (cm/s)	PGD (cm)	Record Duration (s)	5-95% Duration (s)	Arias Intensity (m/s)	Scale Factor
Imperial Valley-06	169	Delta	1979	6.53	242	22	0.45	50.02	27.92	100	51.4	3.3	1.90
Imperial Valley-06	178	El Centro Array #3	1979	6.53	163	15	0.50	91.15	39.41	40	14.1	1.2	1.90
Victoria_Mexico	265	Cerro Prieto	1980	6.33	372	14	0.81	41.99	8.28	25	8.2	2.0	1.25
Westmorland	316	Parachute Test Site	1981	5.90	349	17	0.35	83.37	55.65	42	18.7	0.7	1.50
Chalfant Valley-02	549	Bishop - LADWP South St	1986	6.19	303	17	0.65	51.62	20.06	40	16.8	0.5	2.63
Superstition Hills-02	721	El Centro Imp. Co. Cent	1987	6.54	192	18	0.51	69.22	27.76	60	35.7	1.1	1.44
Landers	848	Coolwater	1992	7.28	353	20	0.56	55.24	36.41	28	10.6	2.2	2.00
Kobe_Japan	1115	Sakai	1995	6.90	256	28	0.42	43.55	30.19	100	60.1	0.6	2.75
Hector Mine	1762	Amboy	1999	7.13	383	43	0.48	72.62	35.93	60	26.7	0.9	2.63
El Mayor-Cucapah_Mexico	5990	El Centro Array #7	2010	7.20	211	28	0.71	60.34	43.50	80	42.5	1.6	2.80
Big Bear-01	6060	North Palm Springs Fire Sta #36	1992	6.46	368	42	0.39	36.93	10.24	28	12.9	0.4	2.75

Table 11. Maximum average plastic rotations at member ends after the first run of NLTHA

Member	Maximum Plastic Rotation (rad)	
	I-end	J-end
C1	0.011	–
C2	0.011	–
C3	–	–
C4	–	–
B1	0.011	0.012
B2	0.011	0.014

As can be seen from the table that the plastic hinges developed at both ends of the beams as well as at the bottom ends of the first story columns. In this example, only the plastic rotations are checked. The interstory drift distribution is not checked, since the model frame has two stories. It is observed that the maximum plastic rotations at the beams B1 and B2 are 0.012 and 0.014 radians, respectively. The plastic rotations observed in the columns are well below the life safety limits (~0.04 rad for the frame considered) suggested by ASCE 41-13 (2013). Since the maximum plastic rotations attained by the beams are beyond the target plastic rotation, the beam yield moments will be modified using the proposed procedure. The calculations are presented for each story, separately:

First Story:

The yield moment of beam B1 is $(M_y)_{B1}$ = 177 kN·m. Therefore, the monotonic plastic strain energy dissipated by the plastic hinge at the plastic rotation of 0.012 radians is

$$\left(E_{pl}\right)_{B1} = 177 \times \left(0.012\right) = 2.12 \text{ kN·m} \tag{5.5}$$

The yield moment required to store the same amount of plastic strain energy at the target plastic rotation, $(\theta_{pl})_{target}$ = 0.01 rad, is

$$\left(M_y\right)_{req}^{B1} = \frac{2.12}{0.01} = 212 \text{ kN·m} \tag{5.6}$$

The reinforcement ratio required to obtain the calculated yield moment is then calculated using a script written for this purpose as 1.07% at the top and 0.54% at the bottom of the end sections. The yield moment of beam B1 with the revised reinforcement ratios is $(M_y)'_{B1} = 218$ kN·m.

For columns C1 and C3, the required moment capacities are calculated such that the column-to-beam strength ratio, β, at the joint remains the same. Note that columns C2 and C4 are identical with C1 and C3, respectively. Therefore, the column calculations will be performed for only C1 and C3. The initial column-to-beam strength ratio at the first story joints is

$$\beta = \frac{(M_y)_{C1} + (M_y)_{C3}}{(M_y)_{B1}} = \frac{170 + 148}{177} = 1.8 \tag{5.7}$$

If the ratio between the moment capacities of the columns C1 and C3 are assumed to remain constant after the modifications, the required yield moments for the columns are calculated as follows.

$$\frac{(M_y)_{C3}}{(M_y)_{C1}} = \frac{148}{170} = 0.87 \tag{5.8}$$

$$(M_y)_{C3} = 0.87(M_y)_{C1} \tag{5.9}$$

Rearranging Equation (5.7) using Equation (5.9):

$$(M_y)'_{C1} + 0.87(M_y)'_{C1} = 1.8(M_y)'_{B1} \tag{5.10}$$

If $(M_y)'_{B1} = 218$ kN·m is substituted in Equation (5.10),

$$1.87(M_y)'_{C1} = 1.8 \times 218 \tag{5.11}$$

By solving Equation (5.11) and (5.9) successively, the required moment capacities for columns C1 and C3 are obtained as 210 kN·m and 183 kN·m, respectively. The reinforcement ratios required to obtain the calculated yield moments under gravity loads are 1.5% for both columns. The yield moments calculated with the modified reinforcements are 210 kN·m and 190 kN·m for C1 and C3, respectively.

Second Story:

The yield moment of beam B2 is $(M_y)_{B2}$ = 108 kN·m. Therefore, the monotonic plastic strain energy dissipated by the plastic hinge at the plastic rotation of 0.014 radians is

$$\left(E_{pl}\right)_{B2} = 108 \times \left(0.014\right) = 1.51 \text{ kN·m} \tag{5.12}$$

The yield moment required to store the same amount of plastic strain energy at the target plastic rotation, $(\theta_{pl})_{target}$ = 0.01 rad, is

$$\left(M_y\right)_{req}^{B2} \cong \frac{1.51}{0.01} = 151 \text{ kN·m} \tag{5.13}$$

The reinforcement ratio required to obtain the calculated yield moment is then calculated using a script written for this purpose as 0.77% at the top and 0.39% at the bottom of the end sections. The yield moment of beam B1 with the revised reinforcement ratios is $(M_y)'_{B1}$ = 158 kN·m.

For column C3, the required moment capacity is calculated such that the column-to-beam strength ratio, β, at the joint remains the same. Note that columns C4 is identical to C4. Therefore, the column calculations will be performed for only C3. The initial column-to-beam strength ratio at the second story joints is

$$\beta = \frac{(M_y)_{C3}}{(M_y)_{B2}} = \frac{148}{108} = 1.3 \tag{5.14}$$

The required yield moment for the column C3 is calculated by replacing the column and beam moments in Equation (5.14) with the new moment capacities as follows.

$$(M_y)'_{C3} = 1.3 \times 158 = 205 \text{ kN·m} \tag{5.15}$$

Since the required moment for C3 calculated at the first story (210 kN·m) is not very different from which calculated at the second story (190 kN·m), the same reinforcement ratios for the columns C3 and C4 will be used as those of C1 and C2.

The initial and the modified longitudinal reinforcement ratios for each member are shown in Table 12. Note that, the reinforcement ratios for all members are checked against the code limitations.

Table 12. Initial and revised reinforcement rations of the frame members

	Longitudinal Reinforcement Ratio, ρ (%)			
Column	**Initial Design**		**Modified Design**	
C1	1.15		1.50	
C2	1.15		1.50	
C3	1.15		1.50	
C4	1.15		1.50	
	Initial Design		**Modified Design**	
Beam	**Top**	**Bottom**	**Top**	**Bottom**
B1	0.87	0.52	1.07	0.54
B2	0.53	0.29	0.77	0.39

The numerical model of the frame was updated according to the modifications. Then, nonlinear time-history analyses were performed to assess the maximum plastic rotations attained at each plastic hinge. The mean values of the maximum plastic rotations are presented in Table 13.

As can be seen from the table, the target maximum plastic rotations are reached at both beams after the first iteration. Thus, no more iteration is required for this case.

Table 13. Maximum plastic rotations at member ends after the first run of NLTHA

Member	Maximum Plastic Rotation (rad)	
	I-end	J-end
C1	0.008	–
C2	0.008	–
C3	–	–
C4	–	–
B1	0.010	0.008
B2	0.009	0.010

5.4.4.1. Damage Index

The outcomes of the applied procedure were also evaluated in terms of the damage index. A modified form of the Park and Ang damage index (Park & Ang, 1985), which is one of the most referenced damage indices in the literature, was employed for this purpose. This damage index accounts for the damage in a member due to maximum plastic excursions, as well as the damage due to cumulative deformations. Therefore, it is possible to observe the damage not only due to the maximum deformations attained, but also due to the hysteretic energy dissipated during cyclic response. The damage index combines both sources of the damage linearly to obtain the damage state using Equation (5.16).

$$DI = \frac{\delta_m}{\delta_u} + \frac{\beta}{\delta_u P_y} \int dE_h \tag{5.16}$$

where δ_m is the maximum experienced deformation, δ_u is the ultimate deformation of the element, P_y is the yield strength of the element, $\int dE_h$ is the cumulative hysteretic energy absorbed by the element during the response history, and β is a model constant parameter that correlates the dissipated energy to the monotonic energy storage capacity of the member. A value of 0.1 for this parameter has been suggested by Park and Ang (1985) based on a large amount of experimental data.

Kunnath et al. (1992) modified the Park and Ang damage index formulation to be used in the evaluation of the damage state at plastic hinges as follows.

$$DI = \frac{\theta_m - \theta_r}{\theta_u - \theta_r} + \frac{\beta}{M_y \theta_u} E_h \tag{5.17}$$

where θ_m is the maximum rotation attained during the loading history, θ_u is the ultimate rotation capacity of the section, θ_r is the recoverable rotation when unloading (for elastoplastic systems, it corresponds to the yield rotation), M_y is the yield moment of the plastic hinge, and E_h is the cumulative dissipated energy at the plastic hinge. The overall damage for a member is defined as the biggest damage index of the two end-sections. For the cases where a section has unsymmetrical reinforcement (e.g. beams), the maximum rotation attained during the loading, the ultimate rotation capacity, and the yield moment is different for positive and negative bending directions. However, no explanation is available regarding this case in Kunnath et al. (1992). Therefore, the average of the two bending directions was used in this study for the beams.

Furthermore, Kunnath et al. (1992) proposed two additional damage indices for assessing the damage at the story level and the global level. These indices are computed using weighting factors based on the hysteretic energy dissipation amount of the members and stories for the story and the global levels, respectively. The interpretation of the Park and Ang damage index ranges is presented in Table 14.

Table 14. Interpretation of overall damage index (Park et al., 1987)

Limit State Damage Index	Degree of Damage	Damage (Service) State	Usability	Appearance
0.00	None	Undamaged	Usable	Undeformed / uncracked
0.20 - 0.30	Slight	Serviceable		Moderate to severe cracking
	Minor	Repairable		Spalling of the concrete cover
0.50 - 0.60	Moderate		Temporarily unusable	
	Severe	Unrepairable		Buckled bars, exposed core
> 1.00	Collapse	Collapse	Unusable	Loss of shear/axial capacity

The story damage index is calculated as a sum of the weighted member damage indices at a story. A weighting factor, $\lambda_{component}$, is used. It is the ratio of the dissipated hysteretic energy (E) by an element at the i^{th} story by the total hysteretic energy dissipated at the same story.

$$DI_{story} = \sum (\lambda_i)_{component} (DI_i)_{component} \tag{5.18}$$

where

$$(\lambda_i)_{component} = \left(\frac{E_i}{\sum E_i} \right)_{component} \tag{5.19}$$

The overall damage index for the global damage of the frame is calculated as a sum of the weighted story damage indices. A weighing factor, λ_{story}, is used which is the ratio of the dissipated hysteretic energy at the i^{th} story by the total hysteretic energy dissipated in the structure.

$$DI_{overall} = \sum (\lambda_i)_{story} (DI_i)_{story} \tag{5.20}$$

where

$$(\lambda_i)_{story} = \left(\frac{E_i}{\sum E_i} \right)_{story} \tag{5.21}$$

A script for assessing all damage indices was written for this study in MATLAB (2015). Table 15 compares the member, story, and global damage indices for the initial and the modified design of the model frame.

Table 15. Member, story, and global damage indices for the initial and modified designs

	Damage Index	
	Initial Design	**Modified Design**
C1	0.15	0.12
C2	0.15	0.12
C3	0.00	0.00
C4	0.00	0.00
B1	0.24	0.27
B2	0.33	0.27
1st Story	0.21	0.24
2nd Story	0.33	0.25
Global	0.25	0.22

As it can be observed from the table, the damage index of beam B2 decreased to 0.27 from 0.33, while that of beam B1 increased from 0.24 to 0.27. As a result, the damage was distributed almost equally among the stories of the frame. In addition, the damage indices of the first story columns were decreased by 20% in the modified design. Consequently, the global damage index of the frame decreased from 0.25 to 0.22. Even the main aim of the proposed procedure is to distribute the plastic deformations equally among the beams; it also contributed the overall damage to decrease by 12%.

5.5. Summary and Concluding Remarks

An iterative inelastic design procedure was proposed to mitigate the interstory drift concentrations during the inelastic response of the frames under seismic excitations. The proposed procedure is based on controlling the distribution of the interstory drifts by means of controlling the maximum plastic rotations at member end-sections. Since the interstory drift distribution in the elastic range is controlled by the procedure described in Chapter 3, the drift distribution in the inelastic range greatly depends on the distribution of the plastic rotations at member-ends.

The proposed procedure makes use of the equal displacement rule and the monotonic plastic strain energy to calculate the required member strengths to obtain similar target maximum plastic rotations at the plastic hinges of the beams. The application of the procedure is limited to the frame structures with proper column-to-

beam strength ratios (i.e. strong column - weak beam condition is satisfied). The yield strengths of the members are revised using the proposed procedure until the target maximum plastic rotation and the target interstory drift distribution (i.e. uniform interstory drift distribution) are reached. Since the yield strength of a reinforced concrete member is significantly affected by the reinforcement ratio, the member sizes remain unchanged and only the reinforcement ratio is modified.

The application and the success of the iterative procedure were demonstrated using an illustrative example. A two-story, single-bay reinforced concrete frame was used for this purpose. The proposed inelastic design method was shown to be effective for modifying the initial design to obtain the targeted maximum plastic rotations at the beam-ends. The damage state of the frame was also enhanced depending on the performed modifications.

This procedure complements the proposed elastic design procedure presented in Chapter 3. Therefore, the interstory drift concentrations in frame structures under earthquake demands can be mitigated by applying the elastic and the inelastic design procedures, which are proposed in this thesis, subsequently. The following chapters consist of various case studies where the effectiveness of the proposed elastic and inelastic seismic design procedures are evaluated.

CHAPTER 6

CASE STUDIES

6.1. Introduction

In order to evaluate the performance of the proposed seismic design procedure three case studies are performed and presented in this chapter. Five-story single-bay, five-story three-bay, and ten-story three-bay planar frames are studied for this purpose. Each type consists of two frames − a frame designed with conventional seismic approach (labeled as *conventional frame*), and a frame designed with the proposed approach (labeled as *proposed frame*). Nonlinear time-history analyses are performed to compare the drift behavior and the damage levels of the frames for design-level earthquakes. The results of each intermediate iteration (labeled as *run*) for the designed frames using the proposed approach are also included to demonstrate the mid-steps of the design process.

6.2. Case Study I: Five-Story Single-Bay Frames

Initially, two five-story single-bay frames were designed. The conventional frame was entirely designed per Turkish Earthquake Code (2018). The preliminary proportions of the proposed frame were determined using the method proposed in Chapter 3. Then, the reinforcement detailing was performed as per TEC2018. Subsequent to the first run of nonlinear time-history analyses, the reinforcement ratios of the proposed frame were revised using the procedure described in Chapter 5. This process was repeated until the interstory drift distribution of the frame becomes about uniform.

6.2.1. Properties of the Frames

The frames were assumed to be located at the interior axis of a 3-D moment frame. The story height is 3.0 meters at all floors and the bay width is 5.0 meters. The

overview of the frames is shown in Figure 85. The slab thickness was assumed as 12 cm and the slabs were assumed to extend 2.5 meters in both transverse directions for gravity load calculations. The mass of each floor was calculated to be 1.10 ton/m^2. The characteristic strengths of the concrete and the reinforcing steel were selected as 25.0 MPa and 420 MPa, respectively.

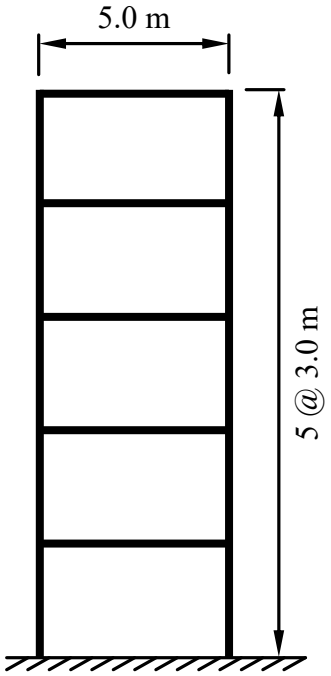

Figure 85. Overview of the five-story single-bay frames

The target fundamental period was selected as 0.7 seconds for both frames based on the gross flexural stiffnesses. This value is greater than the expected period for a well-designed five-story frame and selected on purpose. The aim is to have a high drift demand and observe the performance of the proposed seismic design method at relatively higher displacement demands. The member cross-sections were determined to satisfy the target fundamental period. In the conventional frame, the same column and beam sizes were used at all stories. In the proposed frame, the member sizes were determined using the proposed design procedure in Chapter 3. The limitations of TEC2018 were checked for minimum member dimensions, as well as for the allowed axial load levels for the columns. The member cross-section dimensions for the conventional and the proposed frame are summarized in Table 16. Based on the selected member sizes, the fundamental periods were calculated as 0.7 seconds for both frames. The fundamental periods of both frames were calculated as 1.1 seconds based on the

effective flexural stiffnesses. The effective flexural stiffnesses were taken as the half of the gross flexural stiffnesses.

Table 16. Member cross-section dimensions for the frames (width×height in cm)

	Conventional Frame		Proposed Frame	
Story	**Columns**	**Beams**	**Columns**	**Beams**
5	50×50	25×55	50×50	20×45
4	50×50	25×55	50×50	20×50
3	50×50	25×55	50×50	25×55
2	50×50	25×55	50×50	30×55
1	50×50	25×55	50×50	30×55

6.2.2. Seismic Design

The initial seismic design of both frames was performed as per TEC2018 using the equivalent lateral load procedure and the capacity design principles following the sizing of the members. The frames were assumed to be at a high-seismicity region on type ZD soil (stiff soil profile as per TEC2018). The distance of the nearest active fault was assumed as 20 kilometers to the selected site. Linear elastic acceleration design spectrum for the design-basis earthquake (10% probability of exceedance in 50 years) was obtained from the Turkish Earthquake Risk Map. The linear elastic design spectrum for the selected site and earthquake level is given in Figure 86.

Table 17 shows the design moments (M_d), tension reinforcement ratios (ρ), provided moment capacities (M_r) for the beam end-sections of the conventional and the proposed frame along with the cross-section dimensions. Since the fundamental periods and the masses of both frames are equal, the design lateral loads and the resulting design moments are quite similar to each other. Note that, half the amount of the tension reinforcement was provided as the compression reinforcement at all beam end-sections. All reinforcement ratios were checked against TEC2018 limitations.

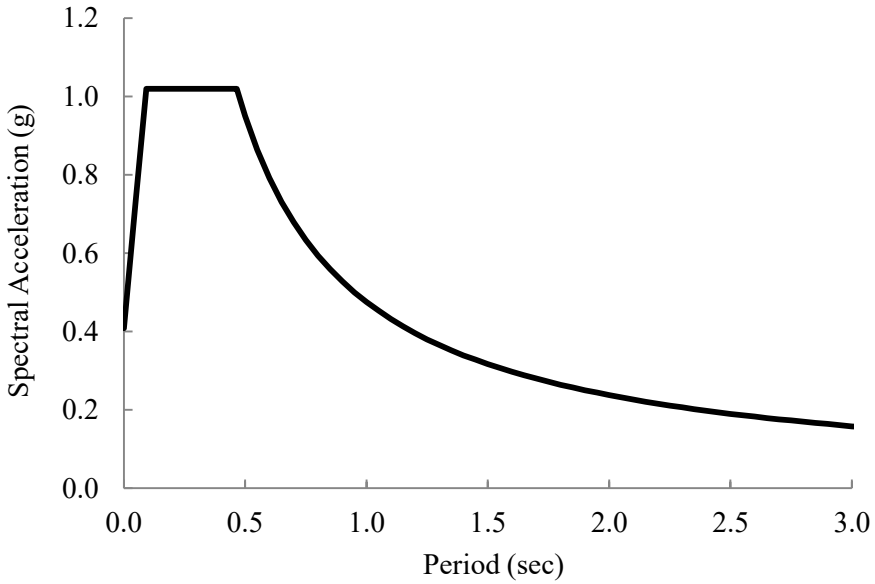

Figure 86. Linear elastic design spectrum for the selected location and design-basis earthquake

Table 17. Cross-section dimensions, design moments, tension reinforcement ratios, and provided moment capacities for beams

Story	Conventional Frame				Proposed Frame			
	$b \times h$ (cm)	M_d (kN·m)	ρ (%)	M_r (kN·m)	$b \times h$ (cm)	M_d (kN·m)	ρ (%)	M_r (kN·m)
5	25×55	82	0.4	103	20×45	81	0.7	83
4	25×55	131	0.6	145	20×50	124	1.0	163
3	25×55	154	0.8	182	25×55	157	0.9	182
2	25×55	167	0.9	215	30×55	172	0.8	216
1	25×55	154	0.8	182	30×55	157	0.7	183

For the columns of both frames, the minimum reinforcement ratio, 1%, governed the design. Therefore, sixteen 16 mm-diameter bars were used at all columns, which resulted in a reinforcement ratio of 1.29%. Based on the proportioning of the frame members, column-to-beam strength ratios (the ratio of the sum of moment capacities of all columns to the sum of moment capacities of beams at a joint), β, at all joints were calculated. Table 18 shows the β values at each floor joint for both frames. It can be seen that the β values are also very similar in both frames.

Table 18. Column-to-beam strength ratios at the joints, β, for both frames

Story	Conventional Frame	Proposed Frame
5	3.7	3.1
4	4.0	3.5
3	3.4	3.4
2	3.0	3.0
1	3.8	3.8

6.2.3. Numerical Model and Strong Ground Motion Set

The frames were modeled in the OpenSees platform as described in Section 5.4.2. For these frames, a 2% damping ratio was assigned to the first mode, and the mode at which the cumulative mass participation exceeds 95%.

The scaled ground motion set, which is described in Section 5.4.3, was used for the nonlinear time-history analyses of the frames.

6.2.4. Linear Time-History Analyses

Initially, two frames were subjected to the scaled ground motion records using elastic sections to observe the linear drift behavior. Figure 87 and Figure 88 shows the envelope interstory drift ratios for each ground motion (GM) record, as well as the means of the distributions for the conventional and the proposed frames, respectively. Figure 89 compares the mean envelope interstory drift ratios of the frames.

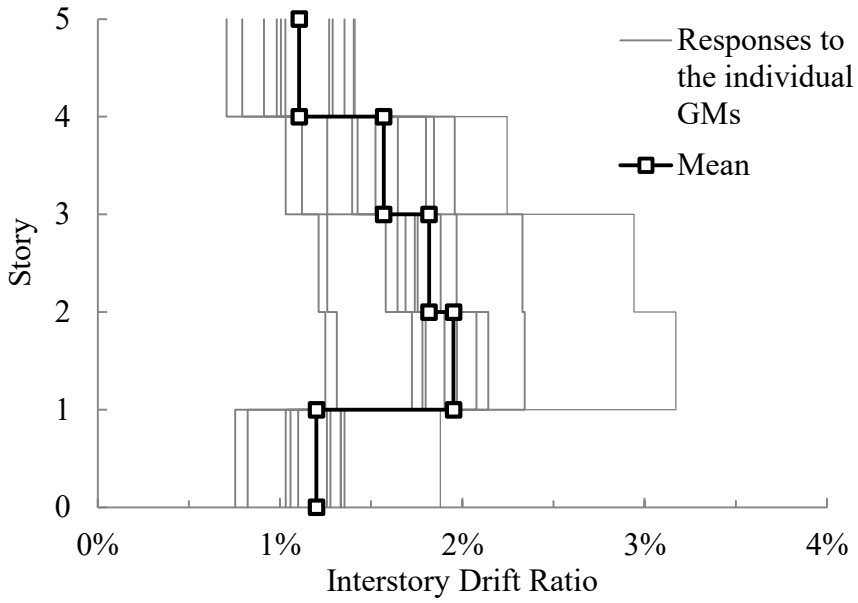

Figure 87. Envelope interstory drift ratios of conventional frame for linear case

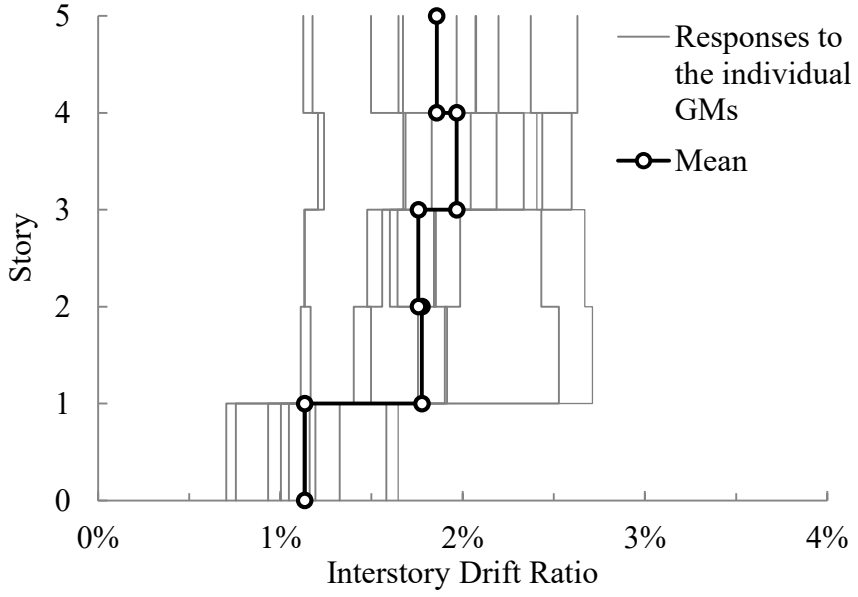

Figure 88. Envelope interstory drift ratios of proposed frame for linear case

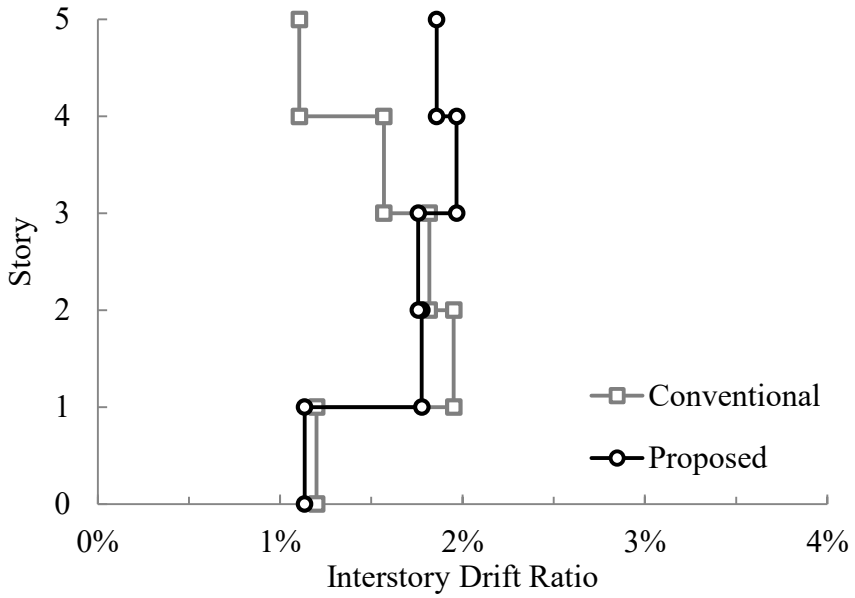

Figure 89. Comparison of mean envelope interstory drift distributions for linear case

As can be observed from the figures above, the proposed frame had well-distributed interstory drift ratios. The coefficients of variation (COV) of the interstory drifts ratios were calculated for both frames as an indicator of the deviation from a uniform pattern. The interstory drift ratio of the first story was neglected in the calculations of COV, since it is limited by the effect of base-fixity. The COV for the conventional frame is 0.23, while it is 0.05 for the proposed frame.

The maximum mean envelope interstory drift ratio is 2% for both frames while the average maximum roof drift ratio (i.e. the ratio of the maximum deflection attained at the top story to the building height) is 1.42% and 1.53% for the conventional and the proposed frames, respectively. Figure 90 shows the maximum roof drift ratios for individual ground motions. The ground motion records are referred to by the record sequence number (RSN) in the figure. The mean maximum roof drift of the proposed frame is 8% larger than that of the conventional frame.

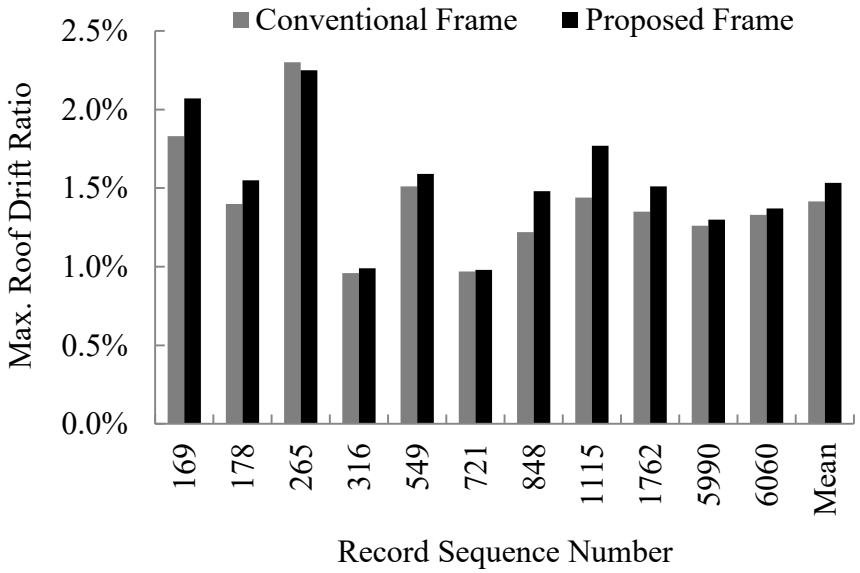

Figure 90. Maximum roof drift ratios for individual ground motion records in linear case

6.2.5. Nonlinear Time-History Analyses (Run #1)

The results of the first run of nonlinear time-history analyses are presented in terms of the envelope interstory drift distributions in Figure 91 and Figure 92 for the conventional and the proposed frame, respectively. The figures include the results for individual ground motions, as well as the means of them. Figure 93 compares the mean envelope interstory drift distribution of both frames on the same plot.

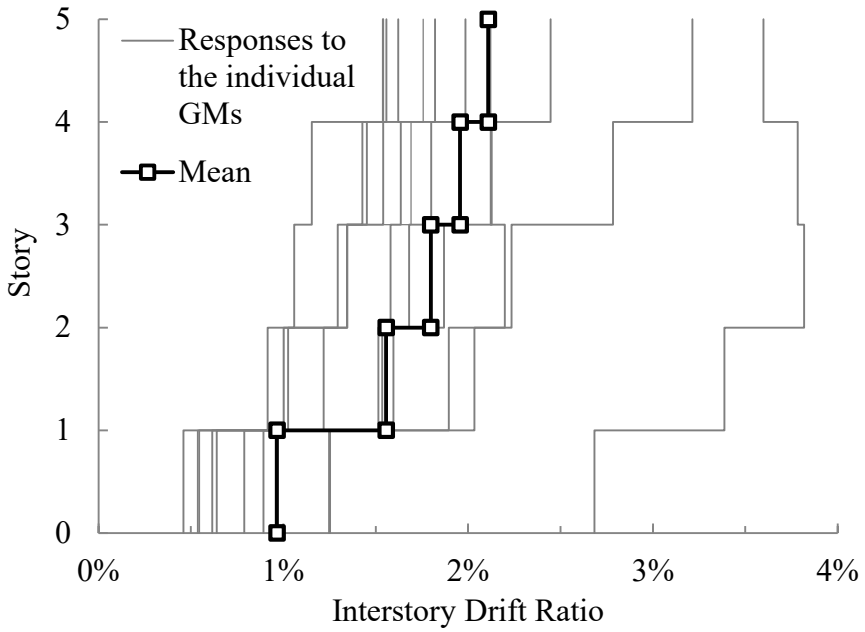

Figure 91. Envelope interstory drift ratios of conventional frame

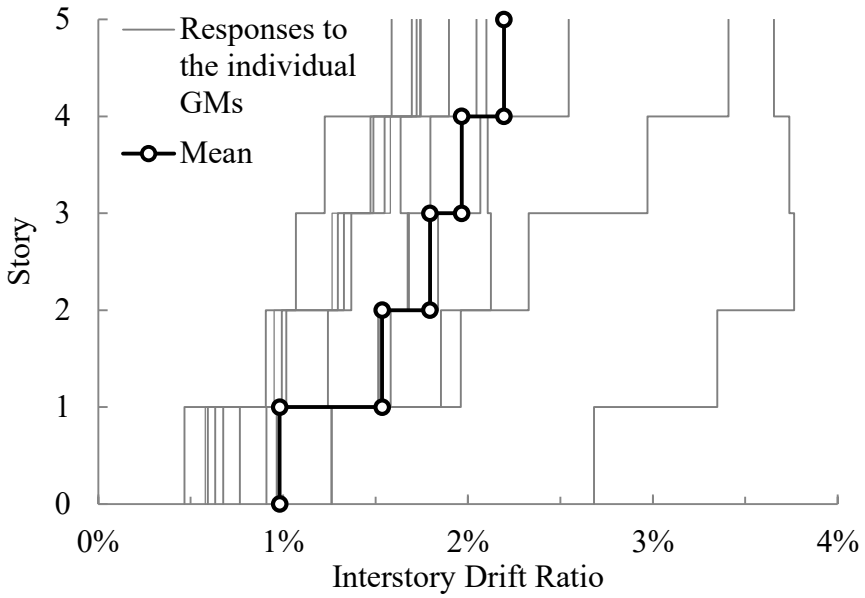

Figure 92. Envelope interstory drift ratios of proposed frame (Run #1)

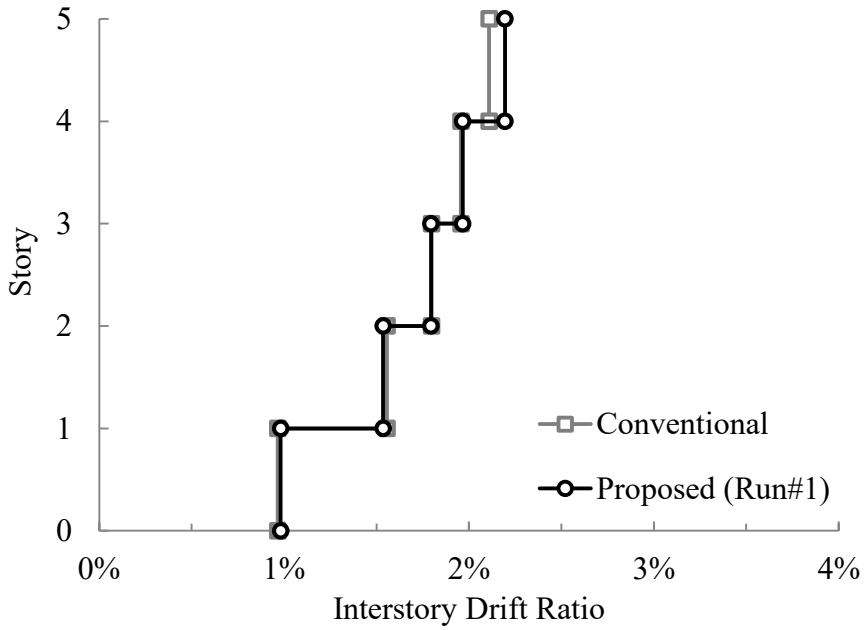

Figure 93. Comparison of mean envelope interstory drift distributions after Run #1

As seen in the figures, both frames had similar envelope interstory drift distributions after the first run of nonlinear time-history analyses. The maximum mean interstory drift ratio was observed at the top story as 2.1% and 2.2% for the conventional and the proposed frames, respectively. The drift distributions are considerably different from those of the linear case. The interstory drifts concentrated towards the upper parts of the frames in the nonlinear case. The COVs of envelope interstory drifts are 0.13 and 0.15 for the conventional and the proposed frame, respectively. Note that, the interstory drifts of the first stories are neglected in the calculations due to the effect of the base-fixity.

The maximum roof drift ratios attained during the ground motions are quite similar in both frames, as well. Figure 94 shows the maximum roof drift ratios for each ground motion and means of the maximum roof drift ratios. The greatest maximum roof drift ratio among all ground motions was attained during the RSN178 record as 3.5% for both frames. The average maximum roof drift ratio of all ground motions is calculated as 1.5%.

Apart from the maximum deflections, the total dissipated hysteretic energy is a means for assessing the cumulative damage experienced during cyclic motions. Therefore, the total dissipated hysteretic energy at each ground motion for both frames was calculated and shown in Figure 95. It can be observed from the figure that the hysteretic energy demand varies greatly depending on the intensity and the duration of

the earthquake. The minimum amount of hysteretic energy was dissipated during the RSN316 record as 75 kN·m. The maximum was dissipated during the RSN1762 record as 350 kN·m being 4.7 times greater than that of the RSN316. The mean dissipated hysteretic energy is approximately 160 kN·m for both frames.

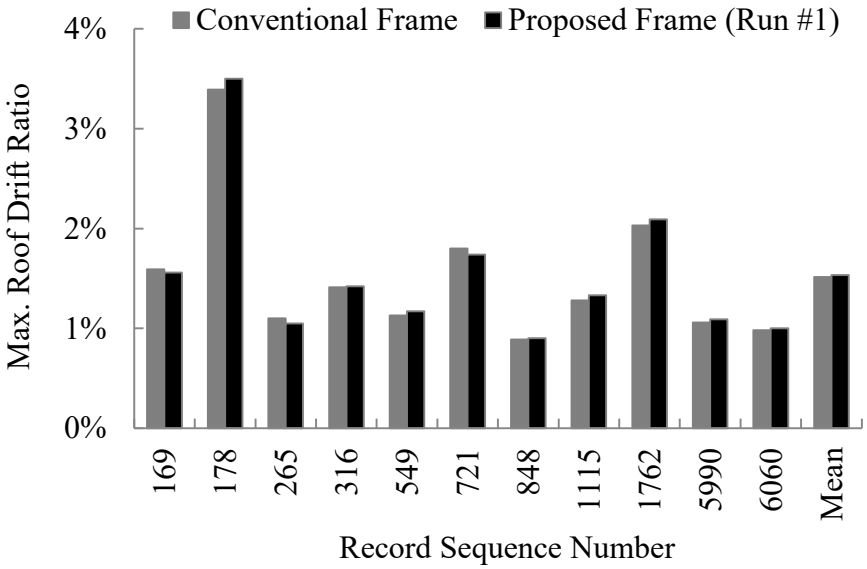

Figure 94. Maximum roof drift ratios for individual ground motion records after Run #1

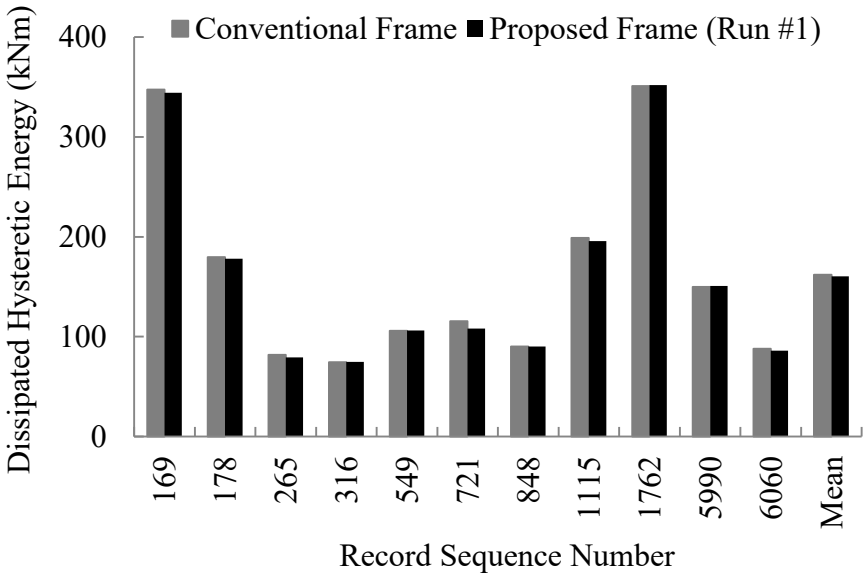

Figure 95. Total dissipated hysteretic energy for both frames after Run #1

Furthermore, the damage indices were calculated to observe the combined effect of the maximum deflections and the total dissipated hysteretic energies on the damage

levels of the frames. The damage levels of the frames were calculated both at the story levels and at the global level based on the Park-Ang Damage Index as described in Section 5.4.4.1. Figure 96 and Figure 97 show the story damage indices for individual ground motion records, as well as the mean story damage indices for both frames. Figure 98 compares the mean story damage indices for both frames. Table 14 may be referred to for the interpretation of the Park-Ang damage indices.

As it can be observed from the figures, the distributions of story damage indices are analogous to the distribution of the envelope interstory drift ratios for both frames. The story damage indices increase gradually towards the top of the frames from 0.25 to 0.60. The overall damage indices after the first run are 0.46 and 0.43 for the conventional and the proposed frames, respectively.

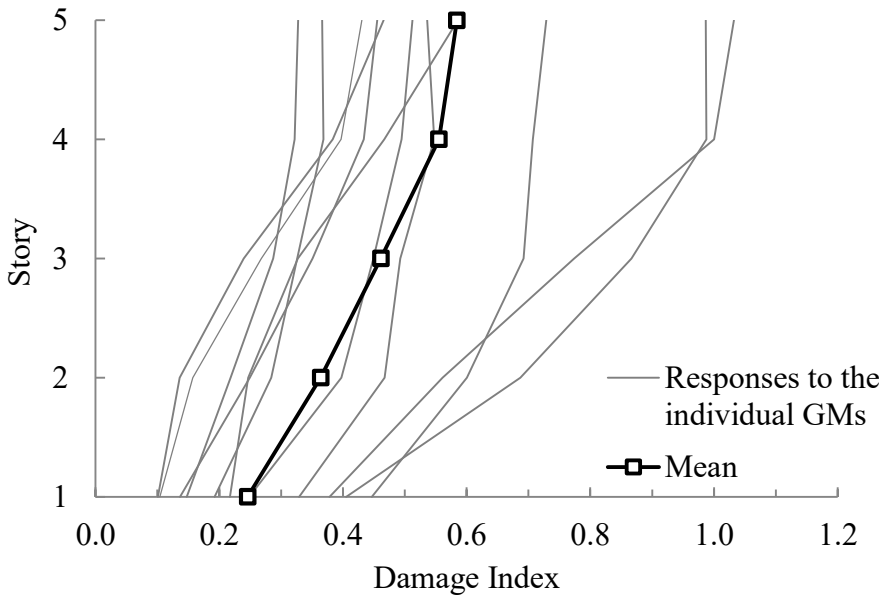

Figure 96. Story damage indices of the conventional frame

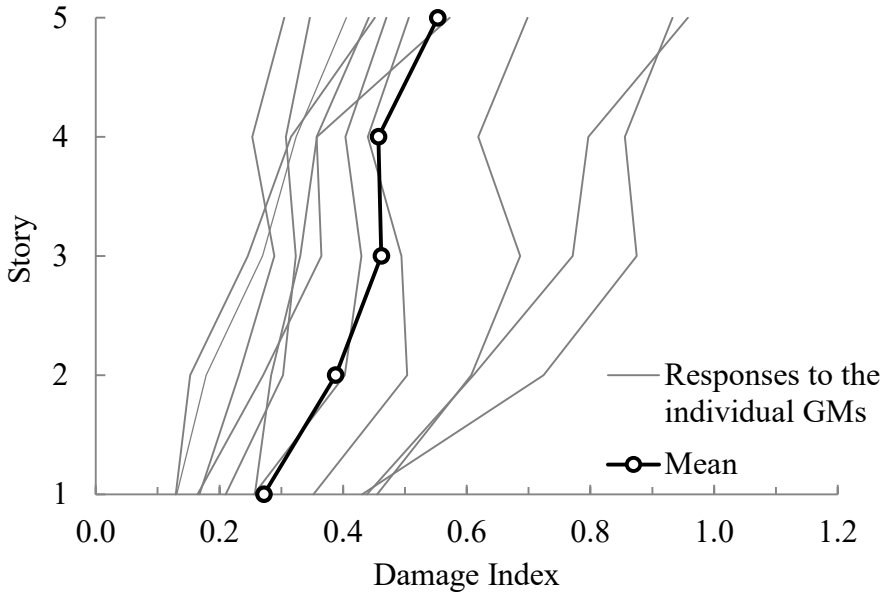

Figure 97. Story damage indices of the proposed frame after Run #1

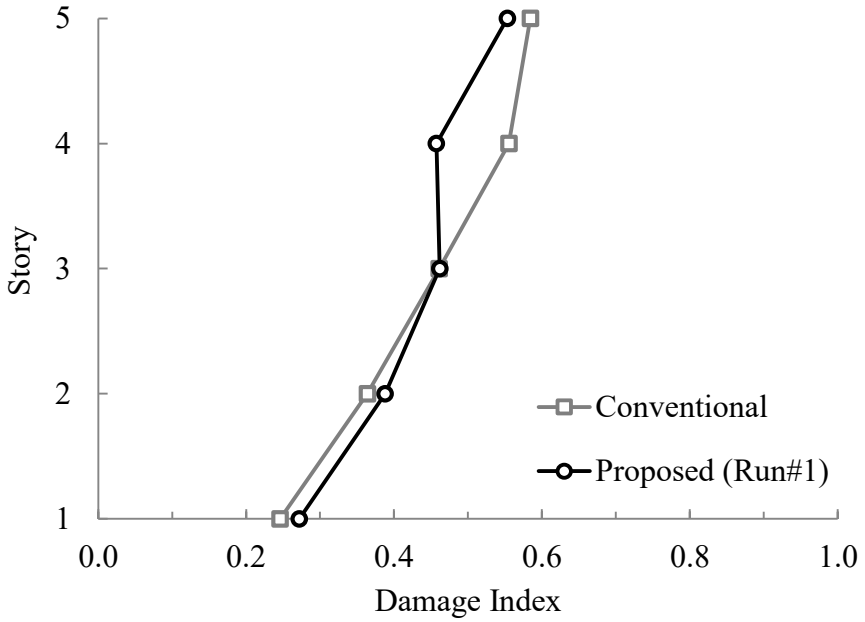

Figure 98. Comparison of mean story damage indices of the frames after Run #1

Since the proposed iterative procedure is based on controlling the maximum plastic rotation in plastic hinges, the means of the maximum plastic rotations attained at the end-sections of the members are given in Figure 99 for both frames. The maximum of the two ends was taken as the maximum plastic rotation at a member. The target maximum plastic rotation for the beams was selected as 0.01 radians as per ASCE 41-

13 (2013) and shown on the plot, as well. This value corresponds to the life safety criteria for adequately detailed ductile beams.

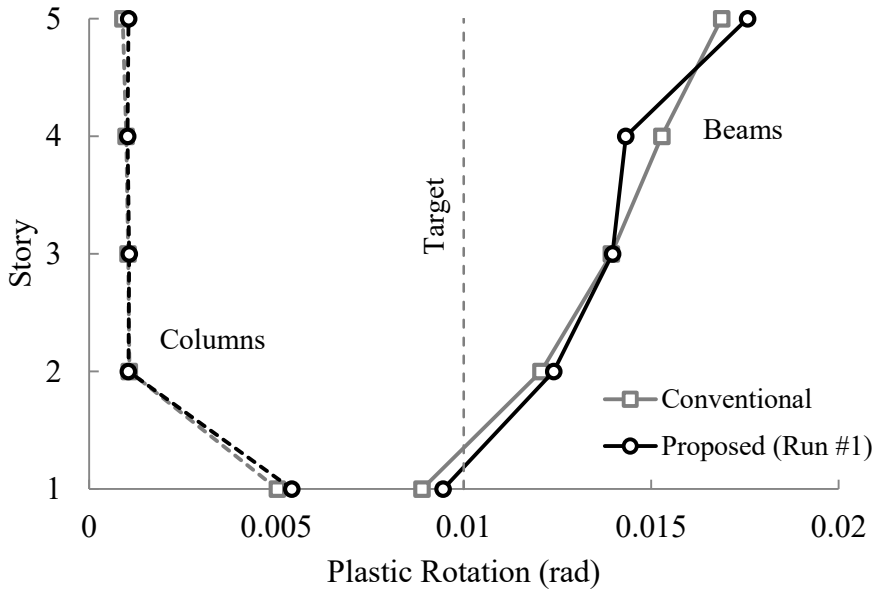

Figure 99. Mean maximum plastic rotations at columns and beams after Run #1

As it can be inferred from Figure 99, plastic hinges developed at the beam-ends and the base of the first story columns, as intended. The maximum plastic rotation distribution at the beam-ends is quite similar to the interstory drift distribution. The maximum plastic rotations at the beam-ends increase gradually towards the top. The target plastic rotation was exceeded at all beams except those of the first story. The greatest maximum plastic rotation was observed at the top story beams as approximately 0.017 radians. The mean maximum plastic rotations at the first story columns are approximately at the immediate occupancy limit of ASCE41-13.

6.2.6. Design Revision for Run #2

Since the interstory drift distribution of the proposed frame is not uniform, the reinforcements of the frame need to be revised using the proposed procedure in Chapter 5. Based on the results of Run #1, the reinforcement ratios of the beams were revised initially. Then, the reinforcement ratios of the columns were revised so that the initial column-to-beam strength ratios are preserved as much as possible. The required moment capacities (M_{req}), the provided reinforcement ratios (ρ), and the provided

moment capacities (M_r) of the proposed frame for the second run are given and compared to those of the first run in Table 19. The reinforcement ratios and the moment capacities of all beams except those at the first story were increased for the second run. The reinforcements of the columns were also increased accordingly. The reinforcement ratios of the columns for Run #1 and Run #2 are given in Table 20.

Table 19. Required moment capacities, provided reinforcement ratios, and moment capacities of the beams for Run #1 and Run #2

Story	Proposed Frame (Run #1)			Proposed Frame (Run #2)		
	M_d (kN·m)	ρ (%)	M_r (kN·m)	M_{req} (kN·m)	ρ (%)	M_r (kN·m)
5	81	0.7	83	160	1.3	160
4	124	1.0	163	228	1.4	220
3	157	0.9	182	255	1.0	246
2	172	0.8	216	260	0.8	249
1	157	0.7	183	183	0.7	183

Table 20. Reinforcement ratios of the columns for Run #1 and Run #2

Story	Reinforcement Ratio (%)	
	Proposed Frame (Run #1)	Proposed Frame (Run #2)
5	1.29	2.01
4	1.29	2.01
3	1.29	2.01
2	1.29	1.62
1	1.29	1.62

The column-to-beam strength ratios, β, at the joints for the revised design are shown together with those of the initial design in Table 21. It was not possible to maintain the same β for all joints, since the amount of change in the moment capacities required at the beams of different stories are not equal. However, the difference between the initial and the revised design is not substantial.

Table 21. Column-to-beam strength ratios for Run #1 and Run #2

Story	Proposed Frame (Run #1)	Proposed Frame (Run #2)
5	3.1	2.5
4	3.5	3.7
3	3.4	3.5
2	3.0	3.4
1	3.8	4.4

After revising the reinforcement ratios of the members, the numerical models of the frames were updated, and the nonlinear time-history analyses were performed again.

6.2.7. Nonlinear Time-History Analyses (Run #2)

The results of the second run of nonlinear time-history analyses are presented in terms of envelope interstory drift distributions in Figure 100 for the revised design. Figure 101 compares the mean envelope interstory drift distribution of the second run with those of the first run.

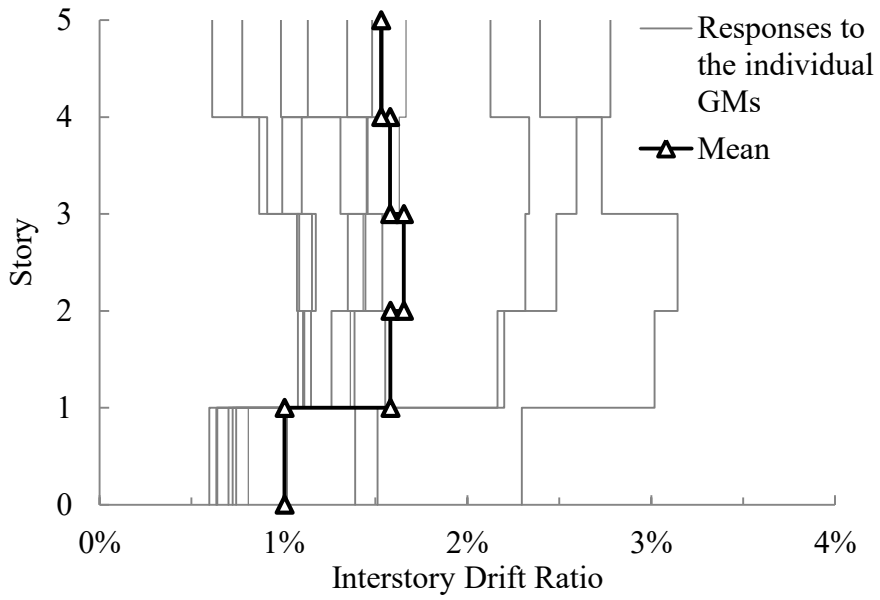

Figure 100. Envelope interstory drifts for the proposed frame (Run #2)

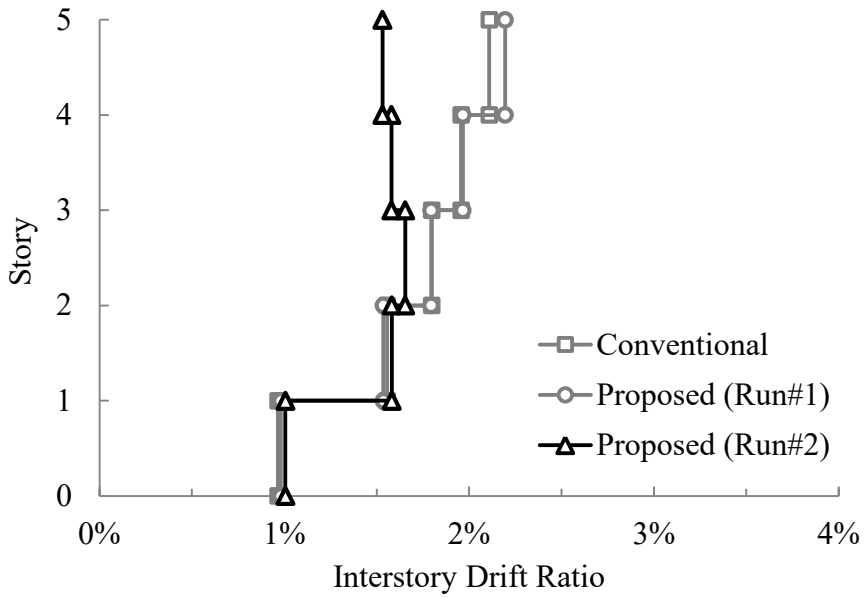

Figure 101. Comparison of mean envelope interstory drift distributions after Run #2

From the figures, it can be observed that the revised design resulted in a significantly balanced interstory drift distribution. The interstory drift concentrations observed at the upper floors were mitigated. The interstory drift of the top story decreased by 32% compared to the initial proposed design. The COV of the interstory drifts is 0.03 while it was 0.13 and 0.15 for the conventional and the initial proposed frame, respectively. The maximum mean envelope drift for the revised design is 1.7%, which is 25% lower than that of the initial proposed design.

The maximum roof drift ratios attained at each ground motion and the mean maximum roof drift ratios are presented in Figure 102 for all designs.

It can be seen from the figure that the maximum roof drift ratios did not change significantly after the design revision. The mean maximum roof drift ratio decreased by approximately 14%. It should also be noted that the maximum roof drift did not decrease at all ground motions; it increased for three of the records. However, the change is negligible for most earthquakes.

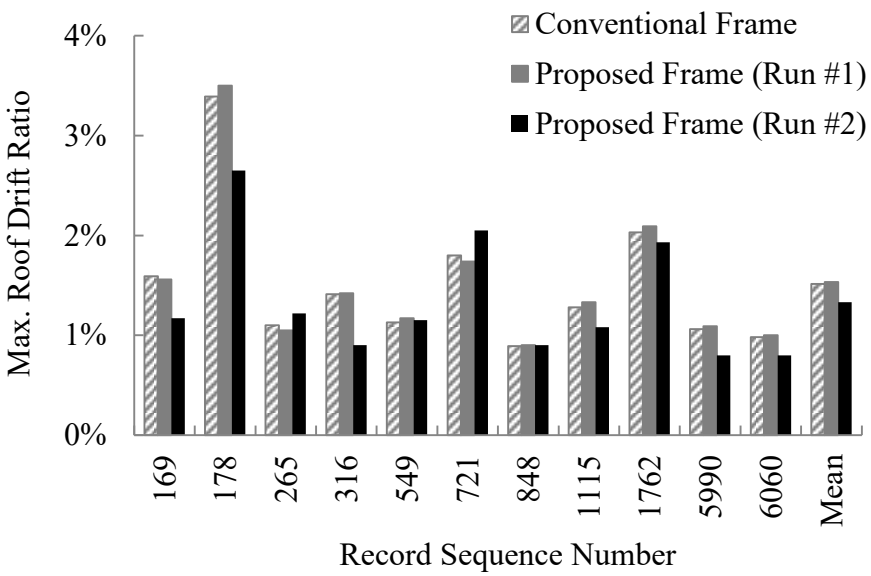

Figure 102. Maximum roof drift ratios for individual ground motion records after Run #2

The total dissipated hysteretic energy at each ground motion for all frames is shown in Figure 103.

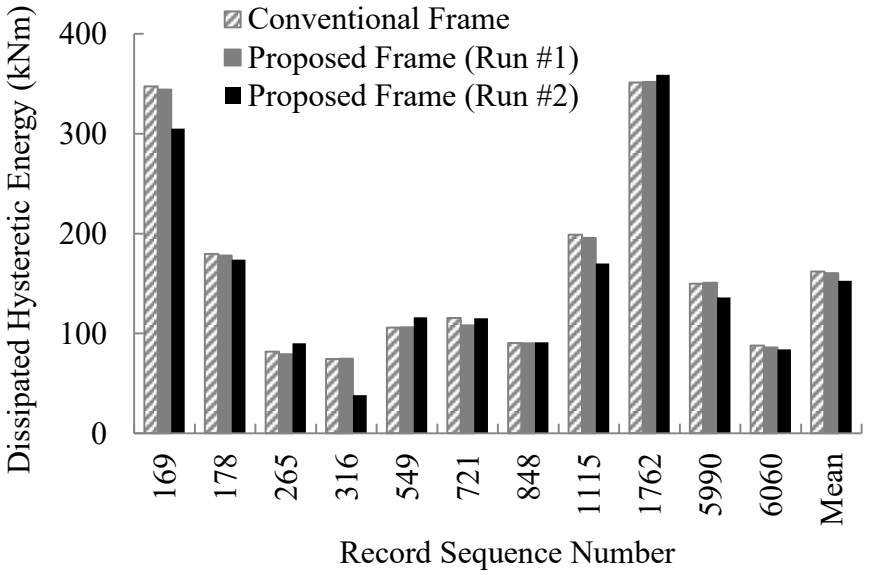

Figure 103. Total dissipated hysteretic energy for all frames after Run #2

It can be observed from the figure that the hysteretic energy demand is almost constant for all designs. The mean hysteretic energy dissipation decreased by 5% in the revised design. Therefore, it can be implied that the hysteretic energy demand is almost

constant for all designs. However, the distribution of the energy dissipation throughout the frame is not the same as that of the initial design. Furthermore, it was seen that the distribution of the interstory drifts is also more balanced. The story damage indices demonstrate the combined effect of these two changes. Figure 104 shows the story damage indices for individual ground motion records, as well as the mean damage indices for the revised frame. Figure 105 shows the mean story damage indices for all frames.

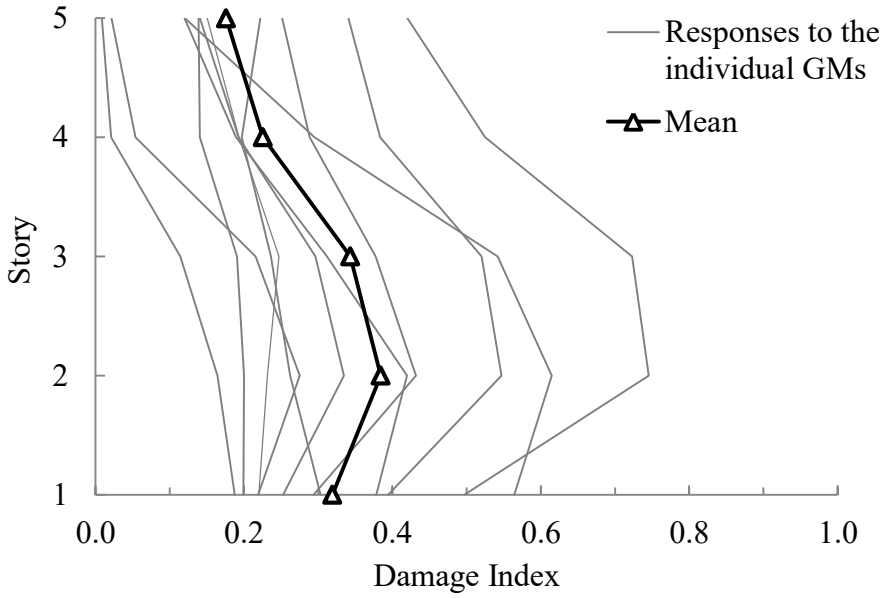

Figure 104. Story damage indices of the proposed frame after Run #2

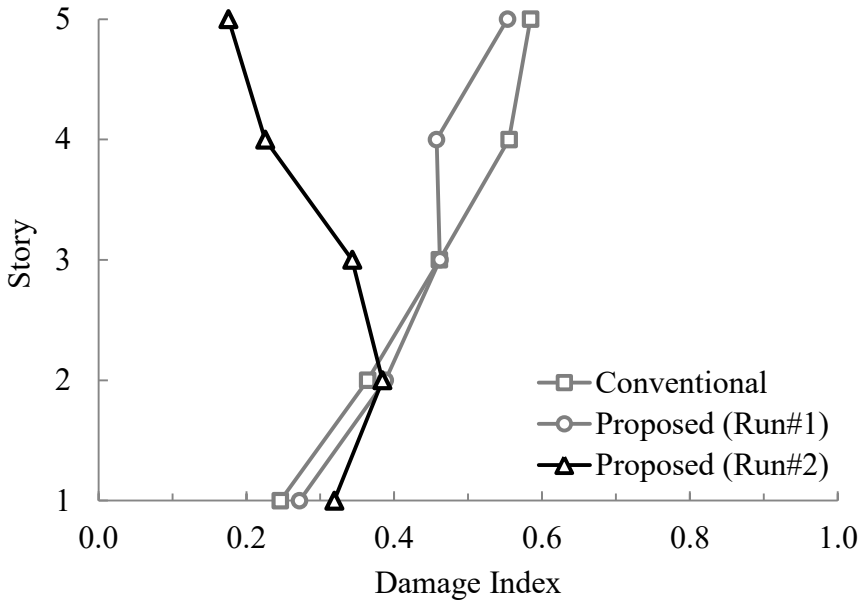

Figure 105. Comparison of mean story damage indices of the frames after Run #2

As can be seen from the figures, the excessive story damage indices of the upper floors were decreased at the revised design. The maximum mean story damage index was observed at the second floor as 0.38, while the minimum damage was experienced at the top floor as 0.18. Furthermore, the revised design resulted in a relatively balanced damage distribution. Note that, although the maximum roof drift and the total dissipated hysteretic energy did not change significantly after the revision, the mean overall damage was reduced by 25% in the revised design by both modifying the strength of the members and shifting the demands to the stories with more energy dissipation capacity. Figure 106 shows the mean overall damage indices for all designs.

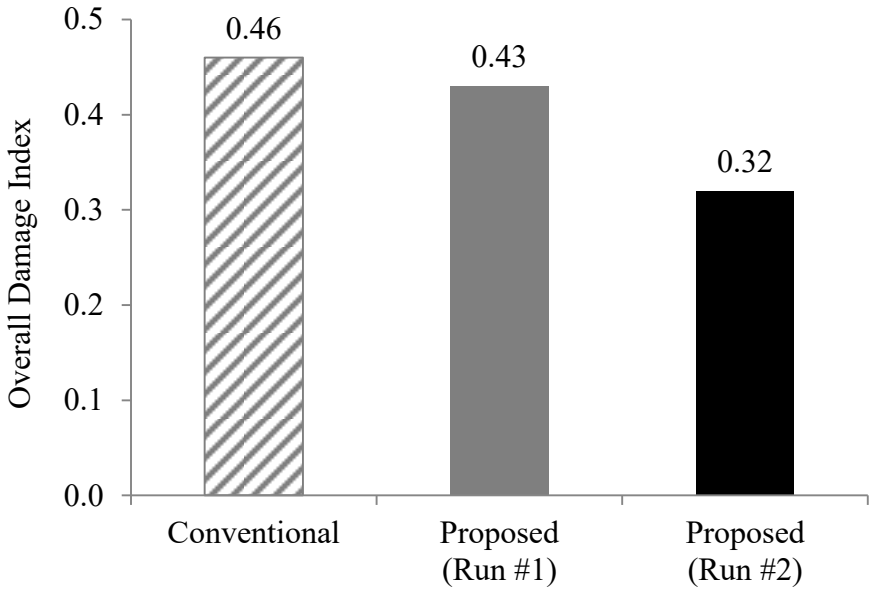

Figure 106. Mean overall damage indices for all frames after Run #2

The means of the maximum plastic rotations attained at the end-sections of the beams and columns are given in Figure 107 for all frames.

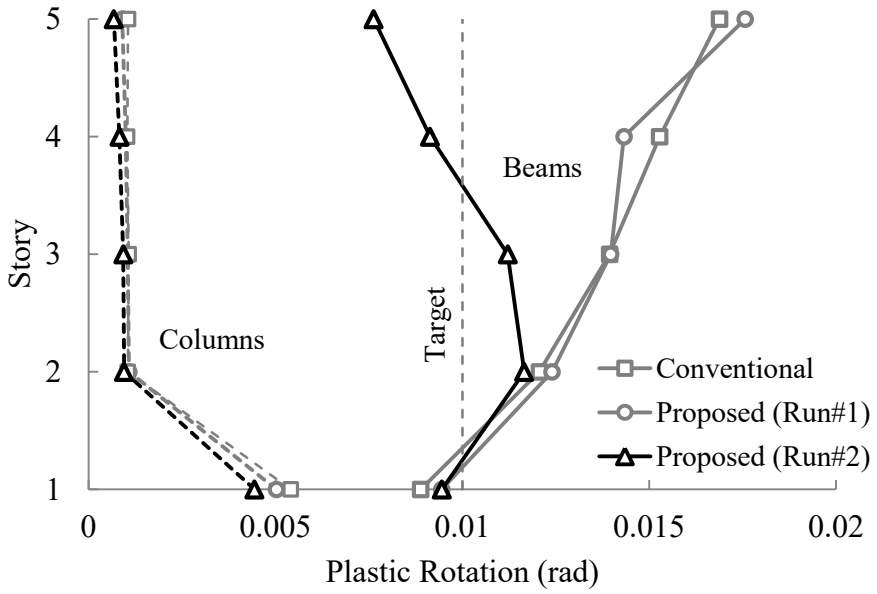

Figure 107. Mean maximum plastic rotations at columns and beams after Run #2

As it can be observed from the figure, the mean maximum plastic rotations at the beam-ends are close to the target maximum plastic rotation (0.01 rad) for the revised design. The excessive plastic rotations at the upper story beams were effectively reduced in the revised design.

All results are summarized from Figure 108 to Figure 110 for each design, respectively.

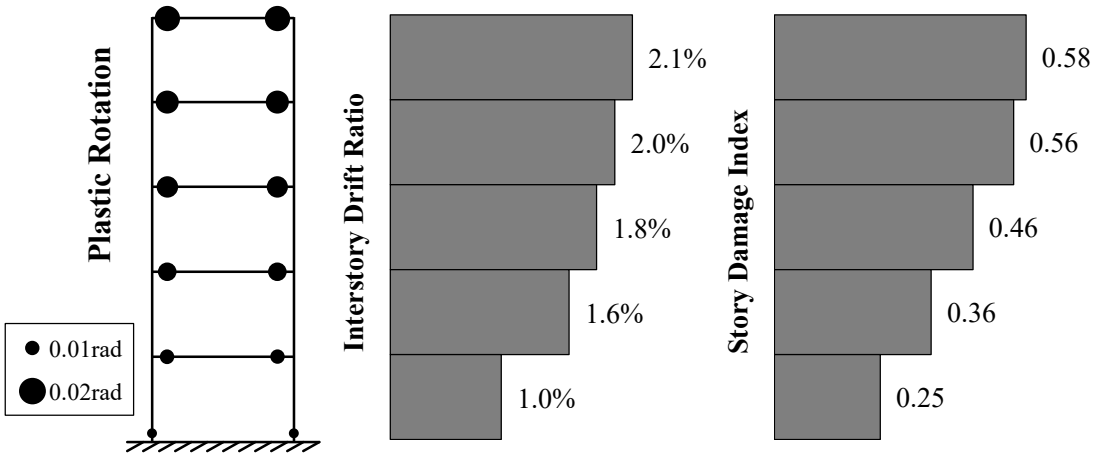

Figure 108. Summary of results for conventional frame

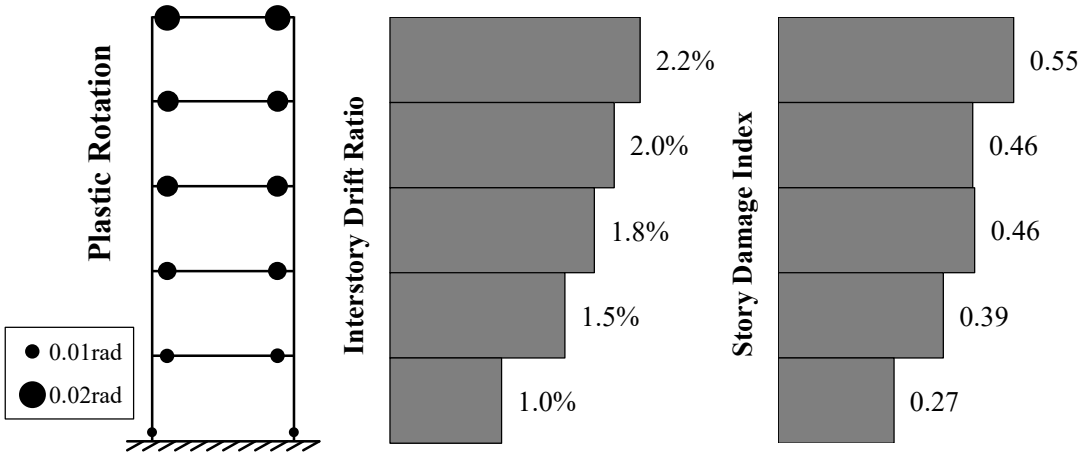

Figure 109. Summary of results for proposed frame (Run #1)

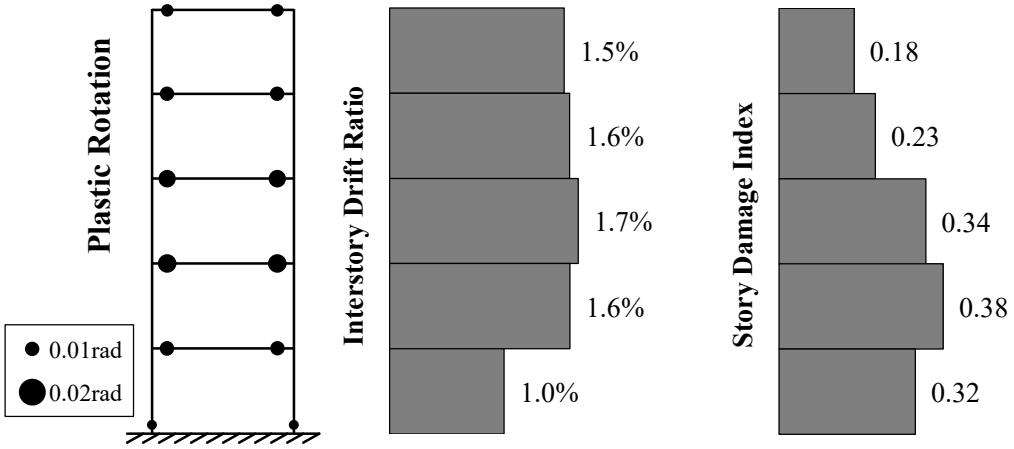

Figure 110. Summary of results for proposed frame (Run #2)

Figure 111 shows the beam moment capacities for all designs. It can be seen that the moment capacities, which satisfy the code demands, are not sufficient to control the interstory drift and the damage distribution.

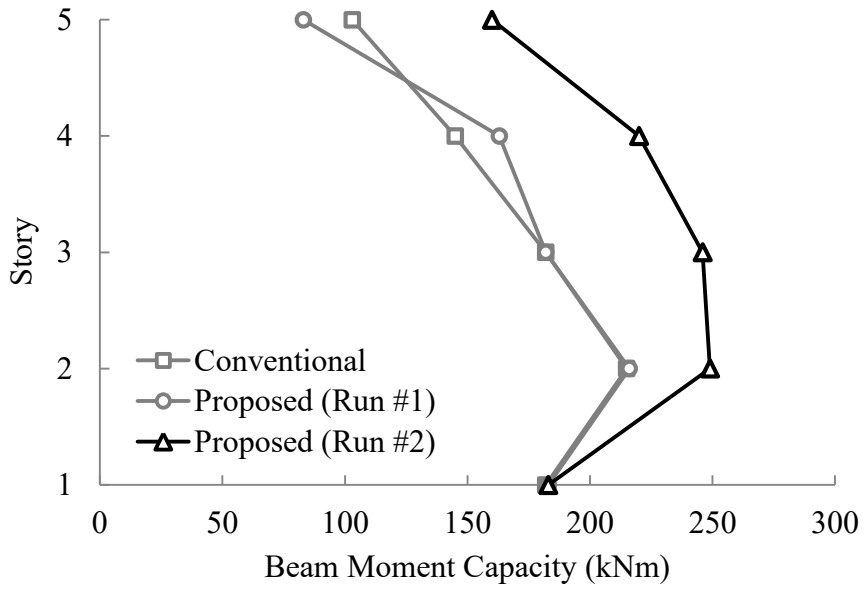

Figure 111. Beam moment capacities for all designs after Run #2

Since the interstory drift distribution is satisfactorily uniform after Run #2, no further design revision is required for the frame considered in this case study. The proposed seismic design method succeeded at preventing the interstory drift concentrations with only one revision step.

6.2.8. Pushover Analyses

All designs were subjected to nonlinear pushover analyses to observe the change in the base shear coefficient (the ratio of the base shear to the total weight of the frame) and the effective stiffness. Here, the effective stiffness refers to the secant stiffness at the maximum roof displacement (Sozen, 2003). The frames were "pushed" to the mean maximum roof drift ratios obtained from the nonlinear time-history analyses (i.e. 1.51%, 1.53%, and 1.33% for the conventional frame, the proposed frame after Run #1, and the proposed after Run #2, respectively). Figure 112 shows the pushover curves and the effective stiffnesses of all frames.

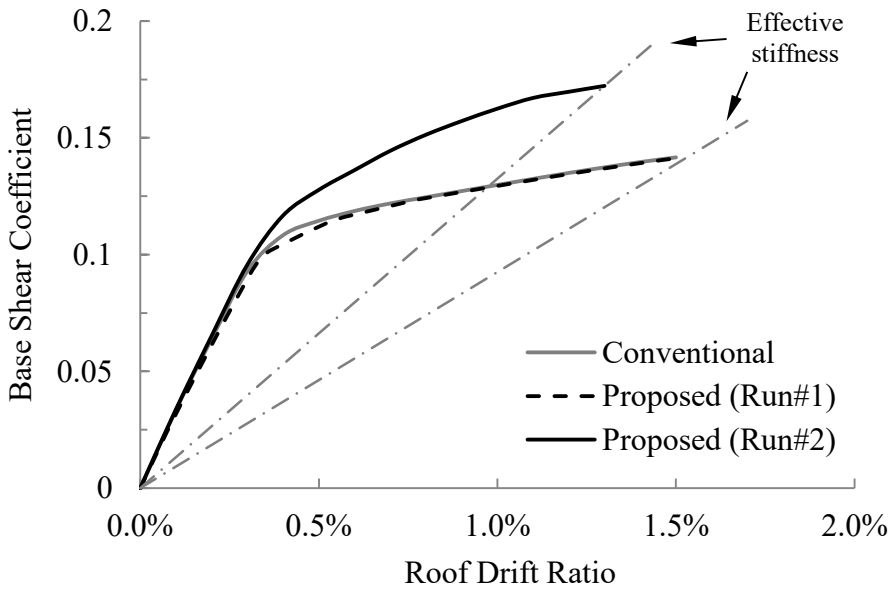

Figure 112. Pushover curves and effective stiffnesses for all frames

It can be observed from the figure that the pushover curves of the initial designs are almost identical. The base shear coefficient at the maximum roof drift is 0.14 for the initial designs. After the revised design, the base shear coefficient increased by 20%, and the effective stiffness increased by 40%. Therefore, the global ductility demand decreased after the revision, which also leads to reduced overall damage throughout the frame.

Furthermore, it is observed that the square root of the ratio of the final effective stiffness ($K_{eff,2}$) to the initial effective stiffness ($K_{eff,1}$) approximates the ratio of the maximum roof drifts of the initial and the final designs, MRD_1 and MRD_2. Figure 113 compares the two parameters for individual ground motions, as well as for the mean results.

It can be seen that the mean maximum roof drift of Run #2 decreased to 87% of the mean maximum roof drift of Run #1. Similarly, the square root of the ratio of the initial effective stiffness to the final effective stiffness is 0.84. Therefore, this parameter can be used to estimate the average change in the peak roof displacement during ground motions between design revisions.

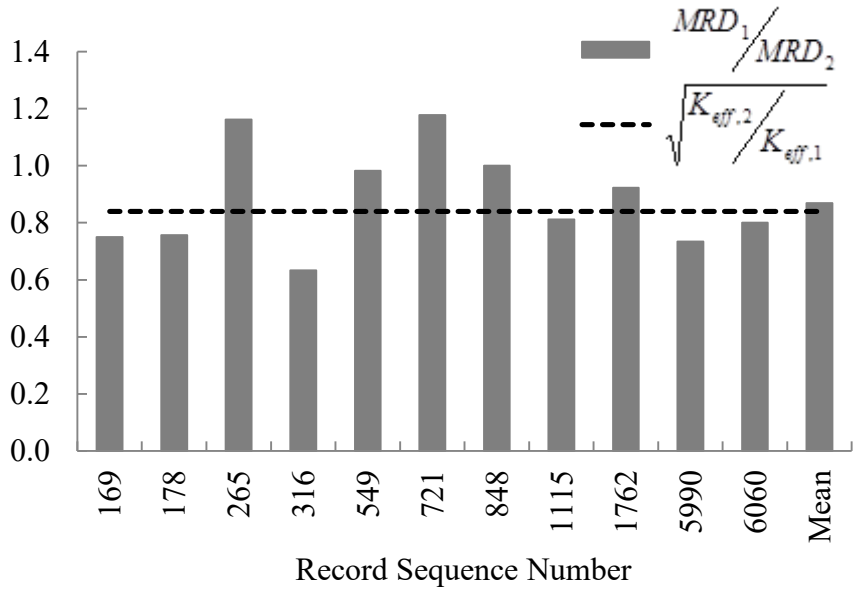

Figure 113. Relationship between the change in the maximum roof drift and the change in the effective stiffness

6.3. Case Study II: Five-Story Three-Bay Frames

Similar to the previous case study, two five-story frames, labeled as *conventional* and *proposed*, were designed initially. To verify the procedure's efficiency on a multiple bay frames, three-bay five-story frames are studied.

6.3.1. Properties of the Frames

All the geometric and material properties of the frames kept the same as those of the previous study. All bays have equal span lengths of 5.0 meters. The overview of the frames is shown in Figure 114. The target fundamental period was also kept the same (0.7 seconds)

The member sizes that satisfy the selected fundamental period are given in Table 22 for both frames. Only the column cross-section dimensions are different from those of the single-bay frames by a small amount. The fundamental periods were calculated as 0.7 and 1.1 seconds for both frames based on the gross and the effective flexural stiffness properties, respectively.

.

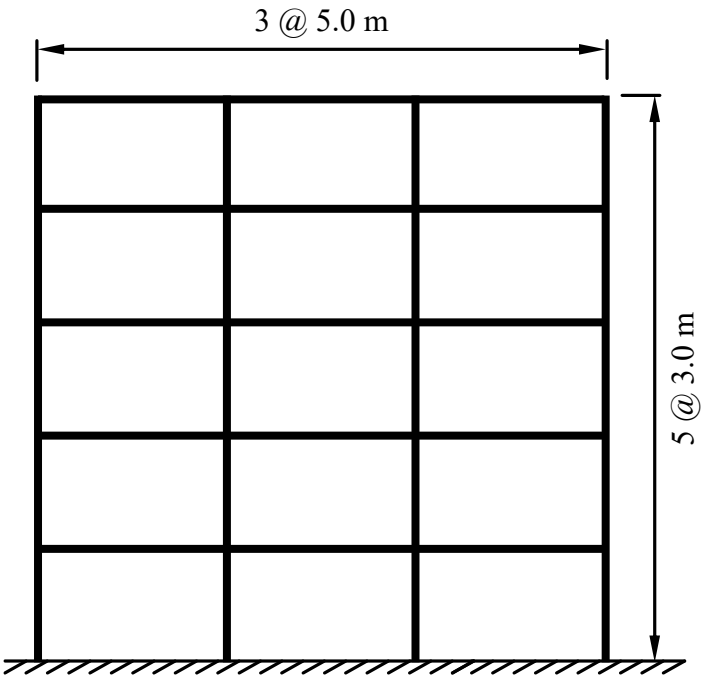

Figure 114. Overview of the five-story three-bay frames

Table 22. Member cross-section dimensions for the frames (width×height in cm)

	Conventional Frame		Proposed Frame	
Story	**Columns**	**Beams**	**Columns**	**Beams**
5	55×55	25×55	55×55	20×45
4	55×55	25×55	55×55	20×50
3	55×55	25×55	55×55	25×55
2	55×55	25×55	55×55	30×55
1	55×55	25×55	55×55	30×55

6.3.2. Seismic Design

The initial seismic design of the frames was performed as described in Section 6.2.2. Table 23 shows the design moments (M_d), tension reinforcement ratios (ρ), provided moment capacities (M_r) for the beam end-sections of the conventional and the proposed frame along with the cross-section dimensions. Since the fundamental periods and the masses of both frames are equal, the design lateral loads and the resulting design moments are quite similar to each other. Note that, half the tension reinforcement was provided as the compression reinforcement at all beam end-sections. In addition,

beams of the same story are set to have the same reinforcements. All reinforcement ratios were checked against TEC2018 limitations.

Table 23. Cross-section dimensions, design moments, tension reinforcement ratios, and moment capacities for beams

Story	Conventional Frame				Proposed Frame			
	$b \times h$ (cm)	M_d (kN·m)	ρ (%)	M_r (kN·m)	$b \times h$ (cm)	M_d (kN·m)	ρ (%)	M_r (kN·m)
5	25×55	76	0.3	82	20×45	73	0.7	89
4	25×55	120	0.6	145	20×50	113	0.9	129
3	25×55	143	0.8	182	25×55	146	0.7	166
2	25×55	155	0.8	182	30×55	162	0.7	183
1	25×55	143	0.8	182	30×55	148	0.7	183

The minimum reinforcement ratio, 1%, governed the design at the columns for both frames. Therefore, sixteen bars of 16 mm were used at all columns, which resulted in a reinforcement ratio of 1.06%. Based on the proportioning of the frame members, column-to-beam strength ratios, β, at all joints were calculated. Table 24 shows the β values at the internal and external joints for both frames. It can be seen that the β values are also similar in both frames.

Table 24. Column-to-beam strength ratios at the joints, β, for both frames

Story	Conventional Frame		Proposed Frame	
	External Joint	Internal Joint	External Joint	Internal Joint
5	3.6	2.5	3.4	2.3
4	4.3	3.1	4.9	3.5
3	3.8	2.8	4.1	3.0
2	4.0	3.0	4.0	3.0
1	4.3	3.2	4.3	3.2

6.3.3. Numerical Model and Strong Ground Motion Set

The frames were modeled in OpenSees platform as described in Section 5.4.2 For these frames, a 2% damping ratio was assigned to the first mode, and the mode at which the cumulative mass participation exceeds 95%.

The ground motion set, which is described in Section 5.4.3, was used for the nonlinear time-history analyses of the frames.

6.3.4. Linear Time-History Analyses

Initially, two frames were subjected to the scaled ground motion records using elastic sections to observe the linear drift behavior. Figure 115 and Figure 116 shows the envelope interstory drift ratios for each ground motion (GM) record, as well as the mean distributions for the conventional and the proposed frames, respectively. Figure 117 compares the mean envelope interstory drift ratios of the frames.

As it can be observed from the figures, the proposed frame had a balanced interstory drift distribution in the linear case. The coefficients of variation (COV) of the interstory drifts were calculated for both frames as an indicator of the deviation from a uniform pattern. The interstory drift ratio of the first story was neglected in the calculations of COV, since it is limited by the effect of base-fixity. The COV for the conventional frame is 0.24, while it is 0.04 for the proposed frame.

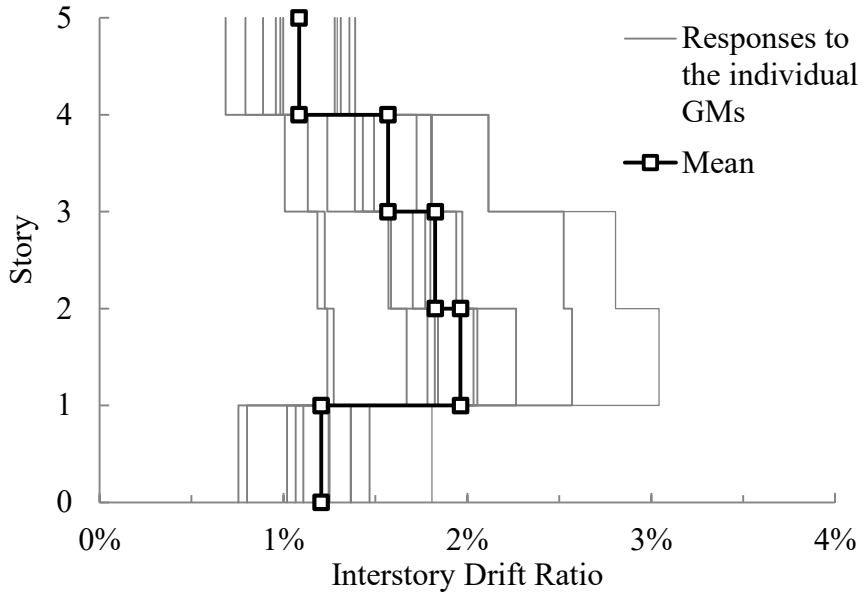

Figure 115. Envelope interstory drift ratios of conventional frame for linear case

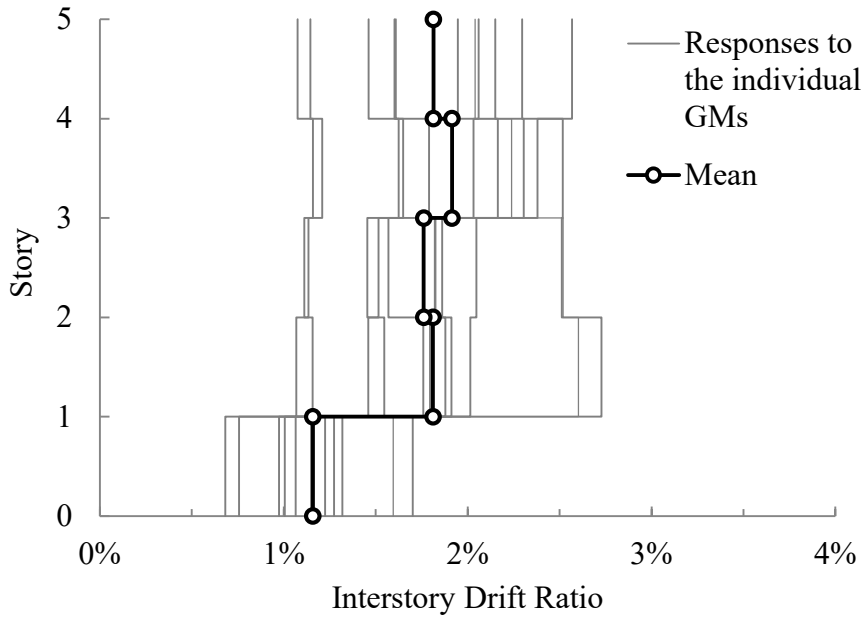

Figure 116. Envelope interstory drift ratios of proposed frame for linear case

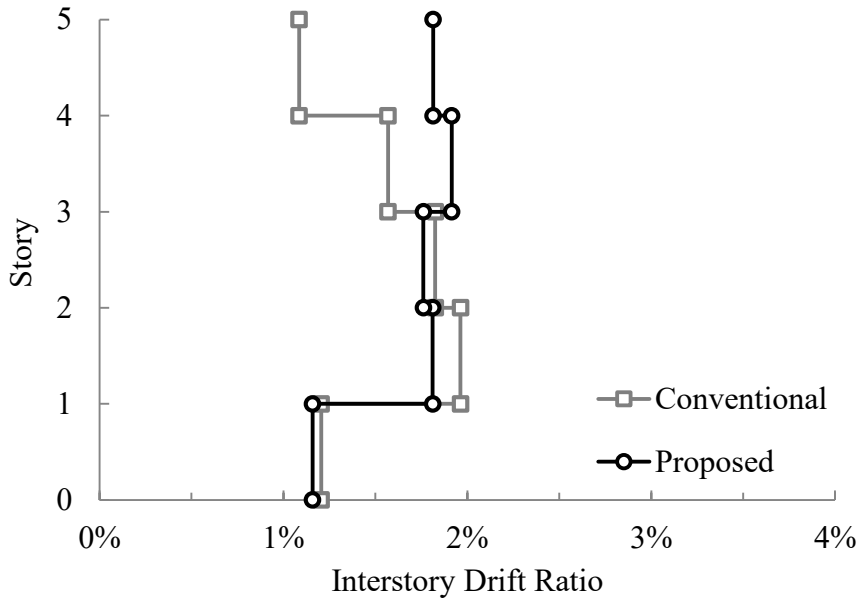

Figure 117. Comparison of mean envelope interstory drift distributions for linear case

The maximum envelope interstory drift ratio is 2% for both frames while the average maximum roof drift ratio is 1.42% and 1.52% for the conventional and the proposed frames, respectively. Figure 118 shows the maximum roof drift ratios for individual ground motions and the mean maximum roof drift ratios. The mean maximum roof drift of the proposed frame is 7% larger than that of the conventional frame.

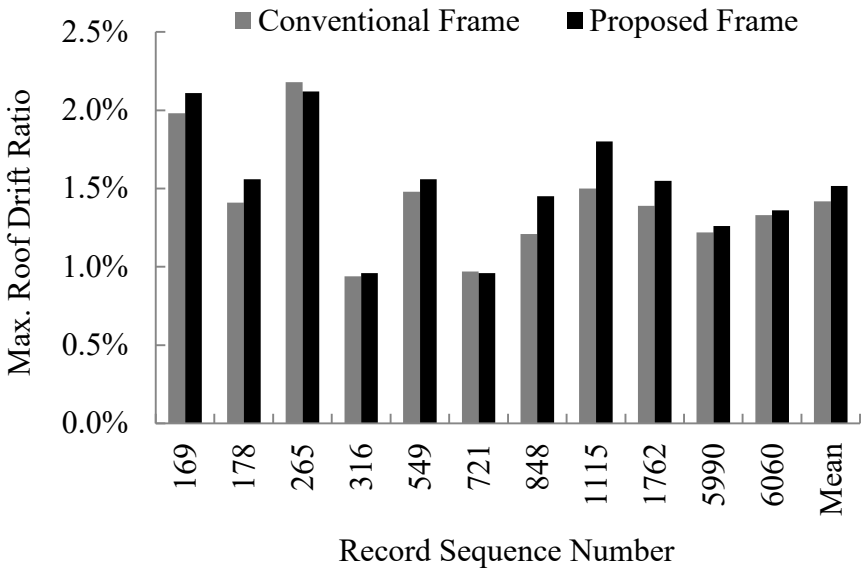

Figure 118. Maximum roof drift ratios for individual ground motion records in linear case

6.3.5. Nonlinear Time-History Analyses (Run #1)

The results of the first run of nonlinear time-history analyses are presented in terms of the envelope interstory drift distributions in Figure 119 and Figure 120 for the conventional and the proposed frame, respectively. Figure 121 compares the mean envelope interstory drift distribution of both frames on the same plot.

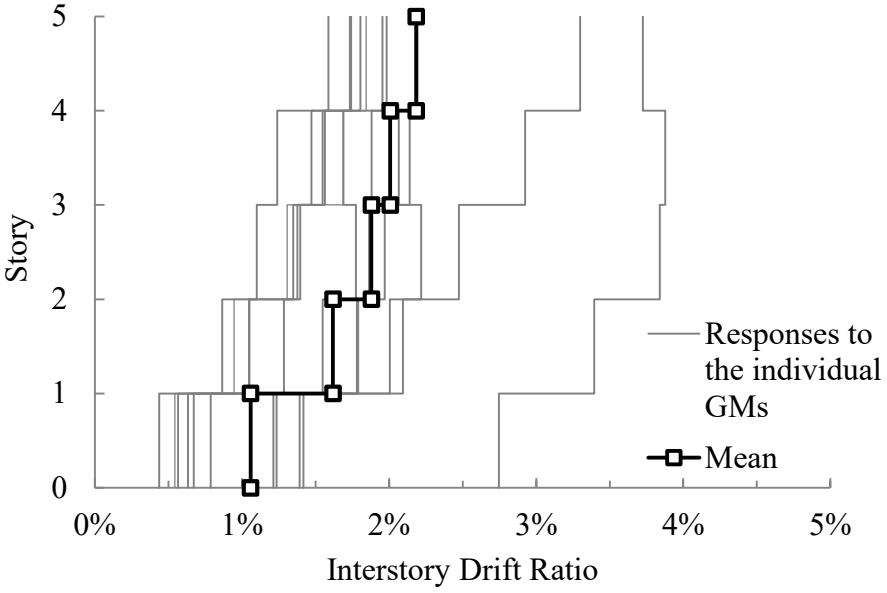

Figure 119. Envelope interstory drift ratios of conventional frame

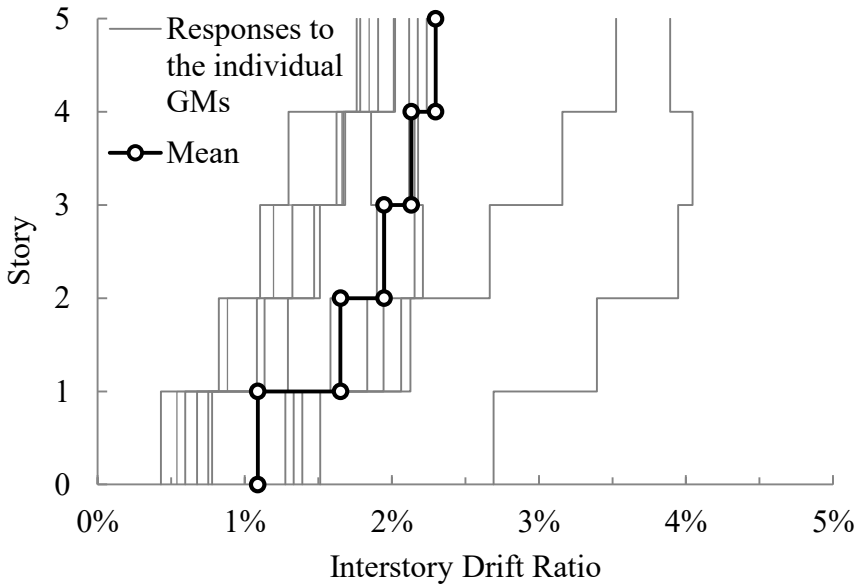

Figure 120. Envelope interstory drift ratios of proposed frame (Run #1)

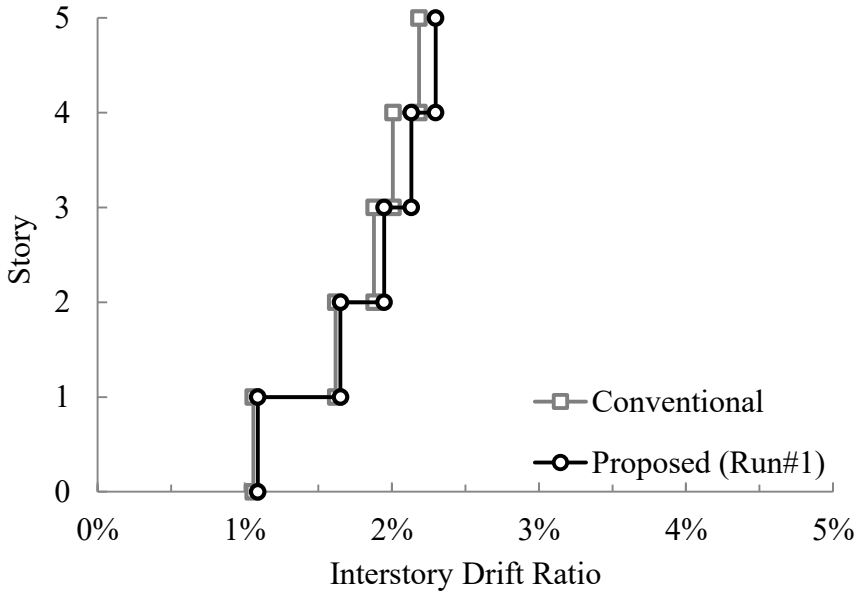

Figure 121. Comparison of mean envelope interstory drift distributions after Run #1

As it can be observed from the figures, both frames had similar envelope interstory drift ratio distributions after the first run of nonlinear time-history analyses. The maximum mean interstory drift ratio was observed at the top story as 2.2% and 2.3% for the conventional and the proposed frames, respectively. The drift distributions are significantly different from those of the linear case. The interstory drifts concentrated towards the upper parts of the frames in the nonlinear case. The COVs of

envelope interstory drifts are 0.12 and 0.14 for the conventional and the proposed frame, respectively. Note that, the interstory drifts of the first stories are neglected in the calculations due to the effect of the base-fixity.

The maximum roof drift ratios are quite similar in both frames, as well. Figure 122 shows the maximum roof drift ratios for each ground motion and means of the maximum roof drift ratios. The greatest maximum roof drift ratio was attained during the RSN178 record as 3.5% for both frames. The average maximum roof drift ratio of all ground motions is 1.61% and 1.68% for the conventional and the proposed frame, respectively.

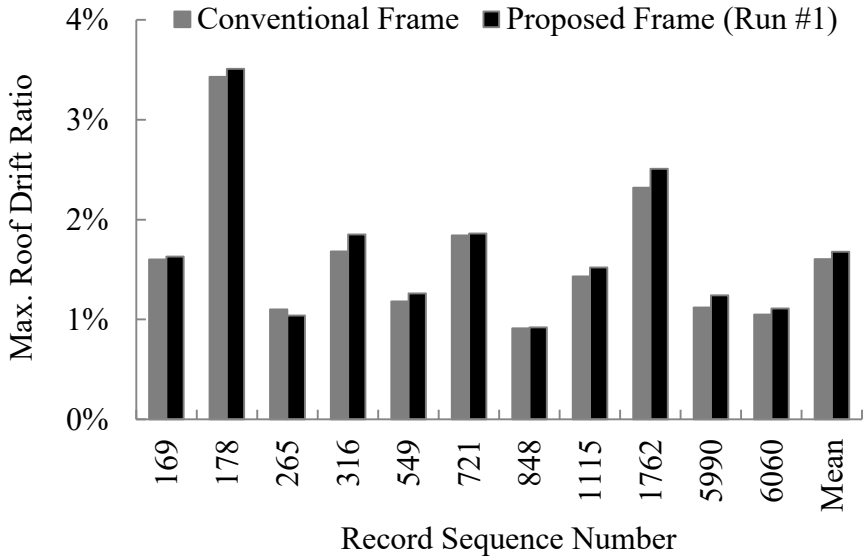

Figure 122. Maximum roof drift ratios for individual ground motion records after Run #1

The total dissipated hysteretic energy of the frames at each ground motion is shown in Figure 123. The minimum amount of hysteretic energy was dissipated during the RSN316 record as 247 kN·m and 263 kN·m for the conventional and the proposed frame, respectively. The maximum was dissipated during the RSN1762 record as 1046 kN·m and 1034 kN·m for the conventional and the proposed frame, respectively. These amounts are approximately four times greater than those of the RSN316. The mean dissipated hysteretic energy is approximately 480 kN·m for both frames. This is about three times greater than that of the single-bay frames.

The story damage indices for individual ground motion records, as well as the mean story damage indices for both frames are given in Figure 124 and Figure 125. A comparison of the mean story damage indices for both frames is shown in Figure 126.

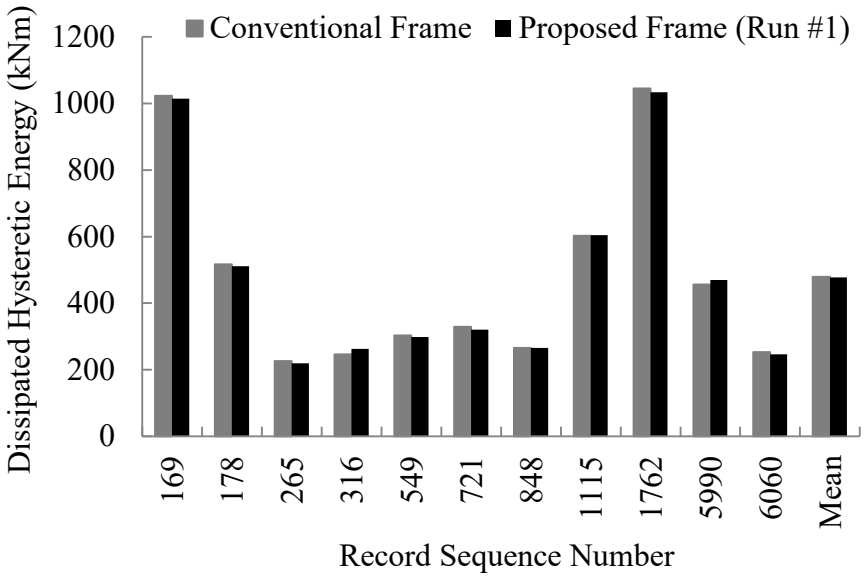

Figure 123. Total dissipated hysteretic energy for both frames after Run #1

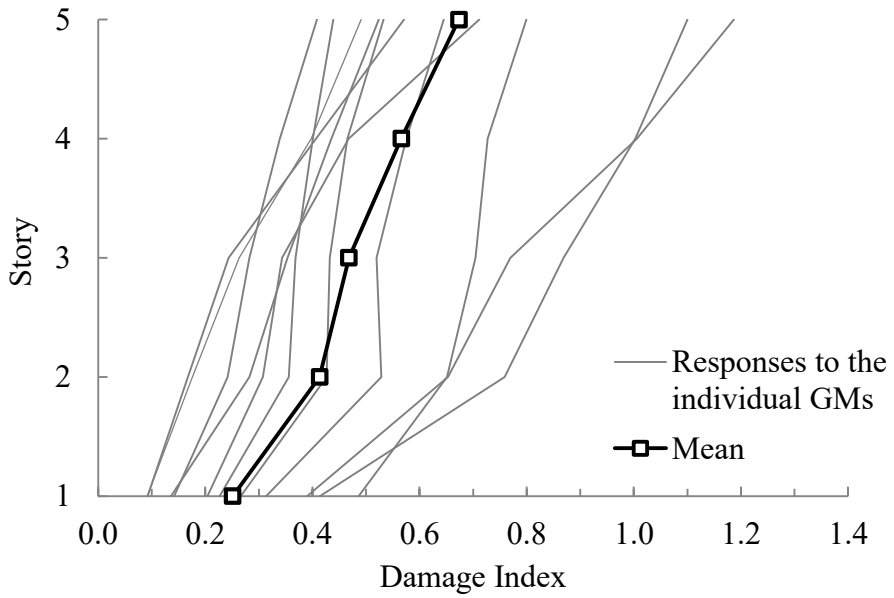

Figure 124. Story damage indices of the conventional frame

As it can be observed from the figures, the story damage index gradually increases towards the top at the conventional frame from 0.27 to 0.67. For the proposed frame, only the damage indices at the fourth and the fifth stories are lower than those of

the conventional frame. The damage indices at these stories are approximately 0.50 at the proposed frame. The overall damage indices after the first run are 0.48 and 0.45 for the conventional and the proposed frames, respectively.

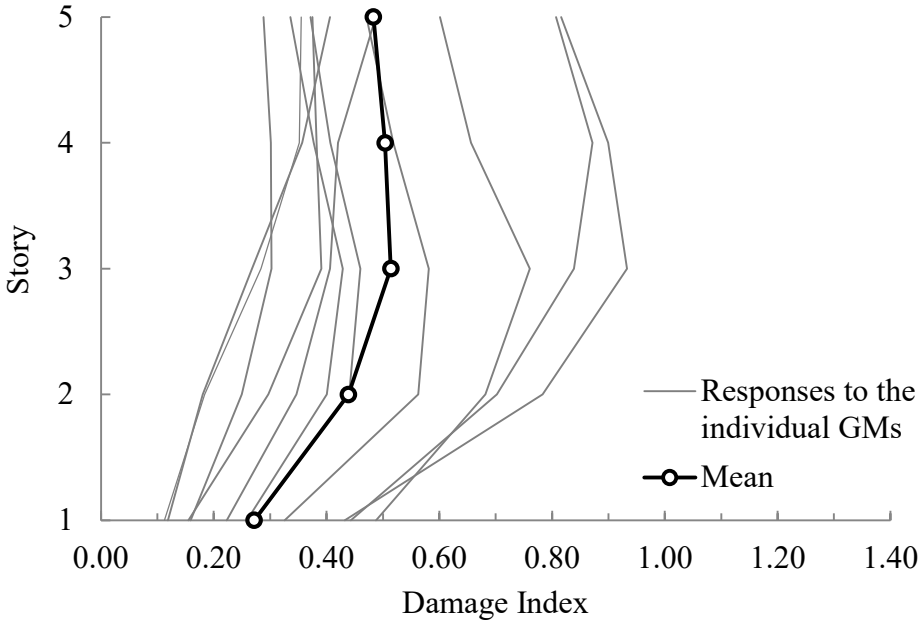

Figure 125. Story damage indices of the proposed frame after Run #1

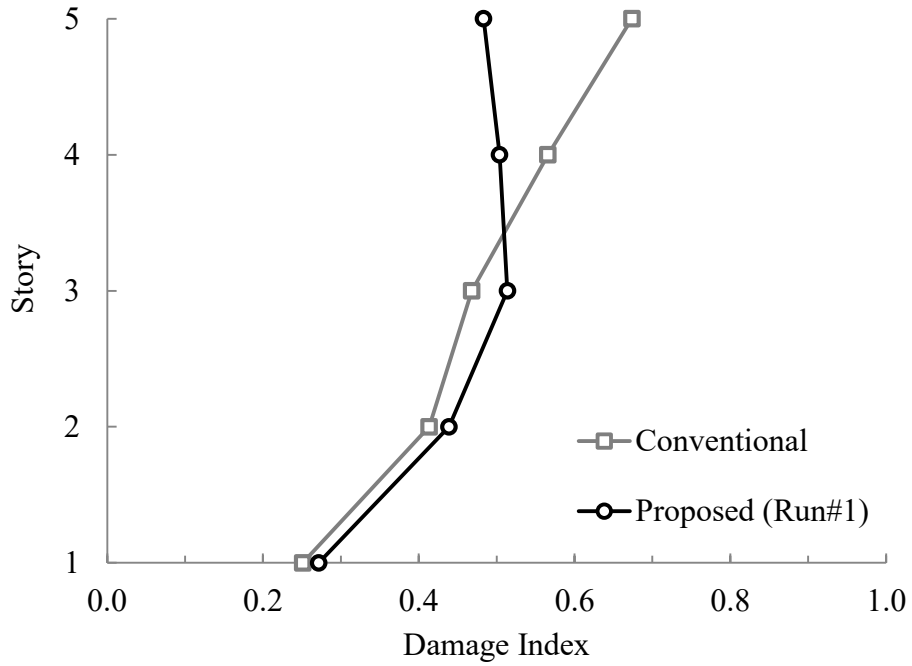

Figure 126. Comparison of mean story damage indices of the frames after Run #1

The means of the maximum plastic rotations attained at the end-sections of the beams and columns are given in Figure 127 for both frames. The maximum of the two ends was taken as the maximum plastic rotation at a member. The maximum plastic rotations are presented separately for the interior and the exterior members.

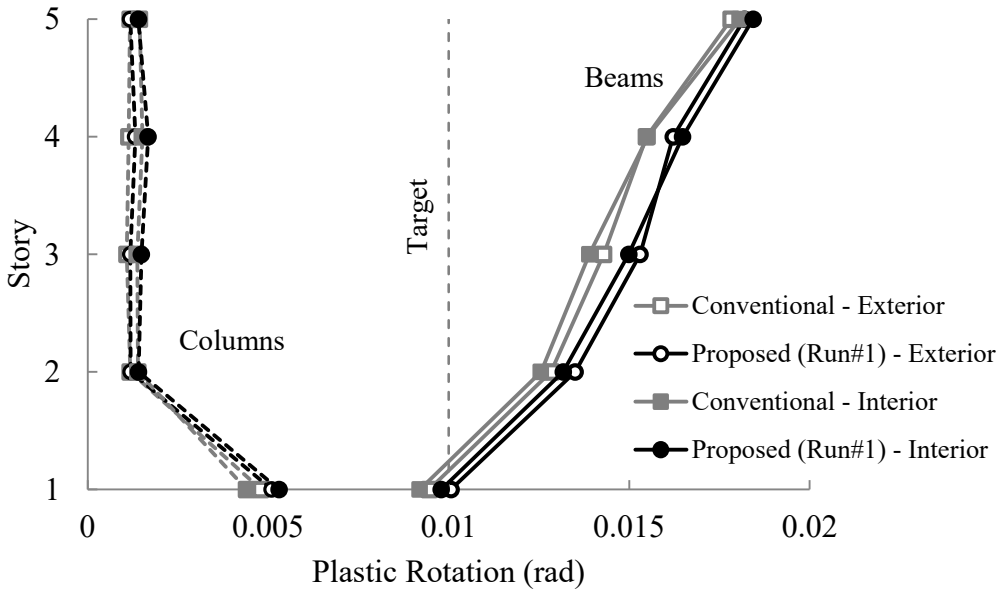

Figure 127. Mean maximum plastic rotations at columns and beams after Run #1

As it can be inferred from the figure, plastic hinges developed at the beam-ends and the base of the first story columns, as intended. The maximum plastic rotation distribution is quite similar to the interstory drift distribution. The maximum plastic rotations increase gradually towards the top. The target plastic rotation at the beam-ends was exceeded at all beams except those of the first story. The maximum plastic rotation was observed at the top story beams as approximately 0.018 radians. The mean maximum plastic rotations at the first story columns are approximately at the immediate occupancy limit of ASCE 41-13.

6.3.6. Design Revision for Run #2

Since the interstory drift distribution of the proposed frame is not uniform, the reinforcements of the frame were modified using the proposed procedure. Initially, the reinforcement ratios of the beams were revised using the proposed procedure. Then, the reinforcement ratios of the columns were revised so that the initial column-to-beam

strength ratios are preserved as much as possible. The required moment capacities (M_{req}), the provided reinforcement ratios (ρ), and the provided moment capacities (M_r) of the proposed frame for the second run are given and compared to those of the first run in Table 25. The reinforcement ratios of the columns for Run #1 and Run #2 are given in Table 26.

Table 25. Required moment capacities, provided reinforcement ratios, and moment capacities of the beams for Run #1 and Run #2

Story	Proposed Frame (Run #1)			Proposed Frame (Run #2)		
	M_d (kN·m)	ρ (%)	M_r (kN·m)	M_{req} (kN·m)	ρ (%)	M_r (kN·m)
5	73	0.7	89	160	1.4	160
4	113	0.9	129	206	1.5	219
3	146	0.7	166	249	1.1	246
2	162	0.7	183	238	0.9	248
1	148	0.7	183	183	0.7	183

Table 26. Reinforcement ratios of the columns for Run #1 and Run #2

Story	Reinforcement Ratio (%)	
	Proposed Frame (Run #1)	Proposed Frame (Run #2)
5	1.06	1.83
4	1.06	1.83
3	1.06	1.66
2	1.06	1.35
1	1.06	1.35

The column-to-beam strength ratios, β, at the joints for the revised design are shown together with those of the initial design in Table 27. It was not possible to maintain the same β for all joints, since the amount of change in the moment capacities required at the beams of different stories are not equal. However, the difference between the initial and the revised design is not substantial.

Table 27. Column-to-beam strength ratios for Run #1 and Run #2

	Proposed Frame (Run #1)		Proposed Frame (Run #2)	
Story	**External Joint**	**Internal Joint**	**External Joint**	**Internal Joint**
5	3.4	2.3	3.1	2.1
4	4.9	3.5	4.7	3.2
3	4.1	3.0	4.2	2.9
2	4.0	3.0	3.9	2.8
1	4.3	3.2	5.1	3.7

6.3.7. Nonlinear Time-History Analyses (Run #2)

The results of the second run of nonlinear time-history analyses are presented in terms of the envelope interstory drift ratio distributions in Figure 128 for the revised design. Figure 129 compares the mean envelope interstory drift distribution ratio of the second run with those of the first run.

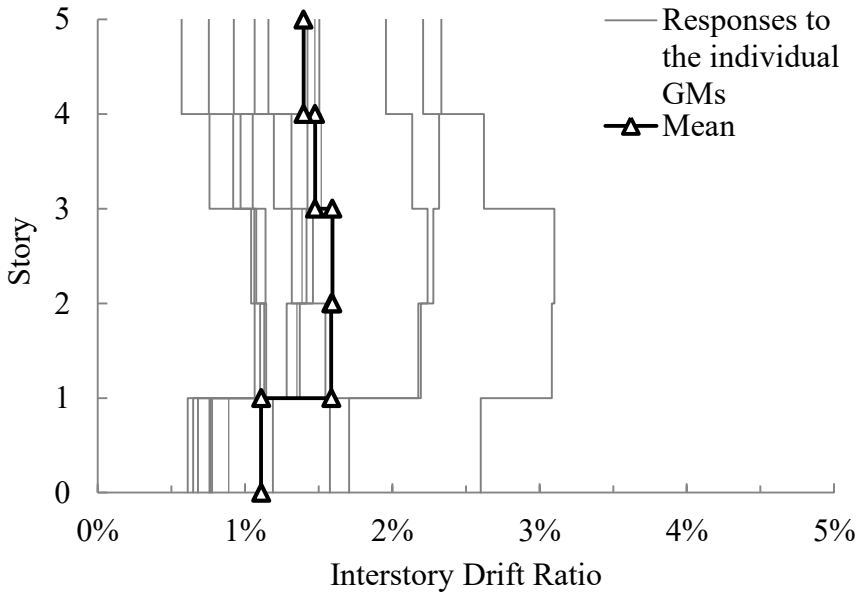

Figure 128. Envelope interstory drifts for the proposed frame (Run #2)

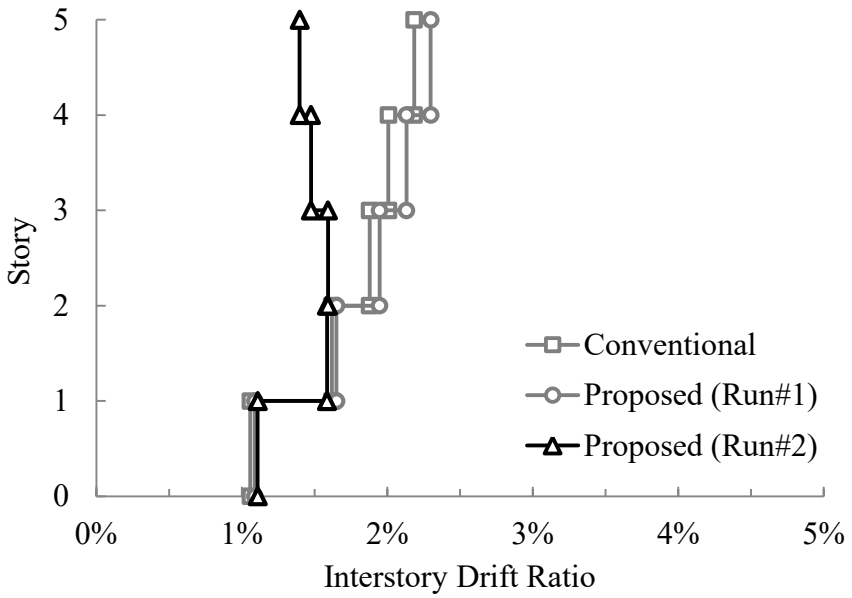

Figure 129. Comparison of mean envelope interstory drift distributions after Run #2

From the figures, it can be observed that the revised design resulted in a considerably balanced interstory drift distribution compared to the initial and the conventional design. The interstory drift concentrations observed at the upper floors were reduced significantly. The interstory drift ratio of the top story decreased by 40% compared to the initial proposed design. The COV of the interstory drifts is 0.06 while it was 0.12 and 0.14 for the conventional and the initial proposed frame. The maximum mean envelope drift for the revised design is 1.6%, which is 30% lower than that of the initial proposed design.

The maximum roof drift ratios attained at each ground motion record and mean maximum roof drift ratios are presented in Figure 130 for all designs.

It can be seen from the figure that the mean maximum roof drift ratio decreased by 20% compared to the first run after the design revision. It is 1.3% for the revised frame. The maximum roof drift did not decrease at all ground motions; it increased for two of the records.

The total dissipated hysteretic energy at each ground motion for all frames is shown in Figure 131. It can be observed from the figure that the hysteretic energy demand does not change significantly in most ground motions. The mean hysteretic energy dissipation decreased by 6% in the revised design.

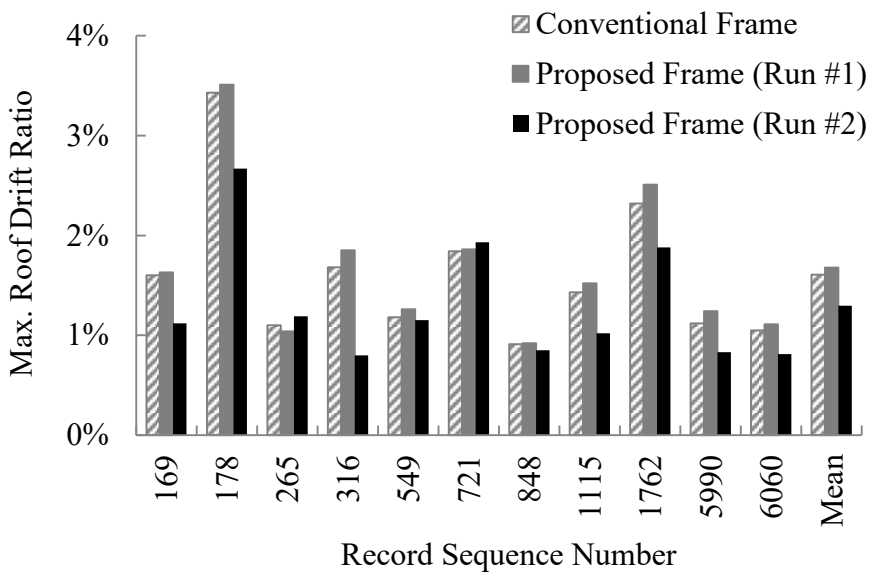

Figure 130. Maximum roof drift ratios for individual ground motion records after Run #2

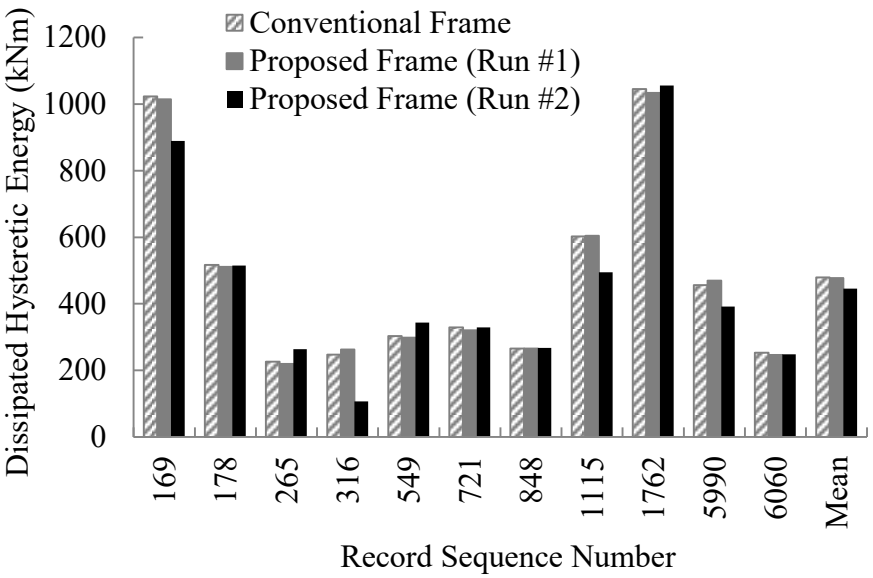

Figure 131. Total dissipated hysteretic energy for all frames after Run #2

Figure 132 shows the story damage indices for individual ground motion records, as well as the mean damage indices for the revised frame. Figure 133 shows the mean story damage indices for all frames.

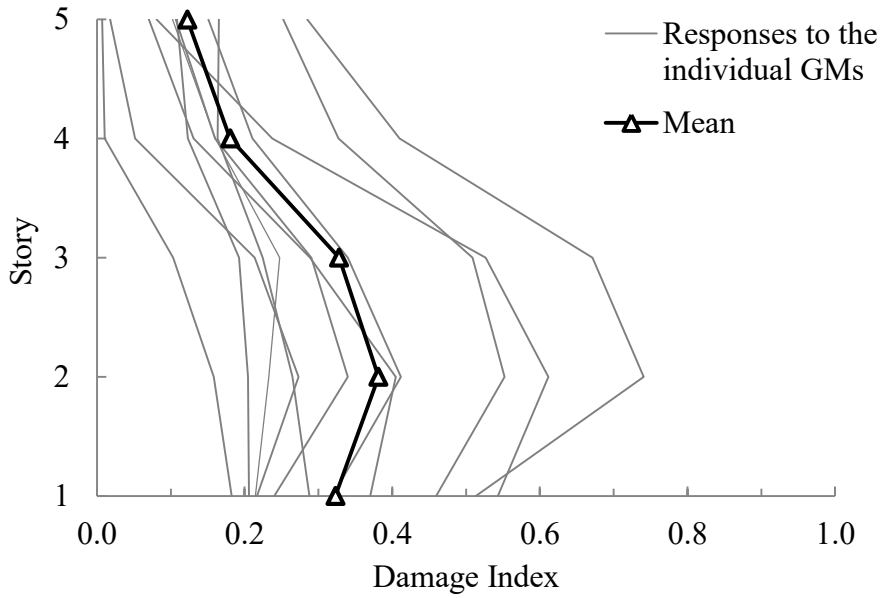

Figure 132. Story damage indices of the proposed frame after Run #2

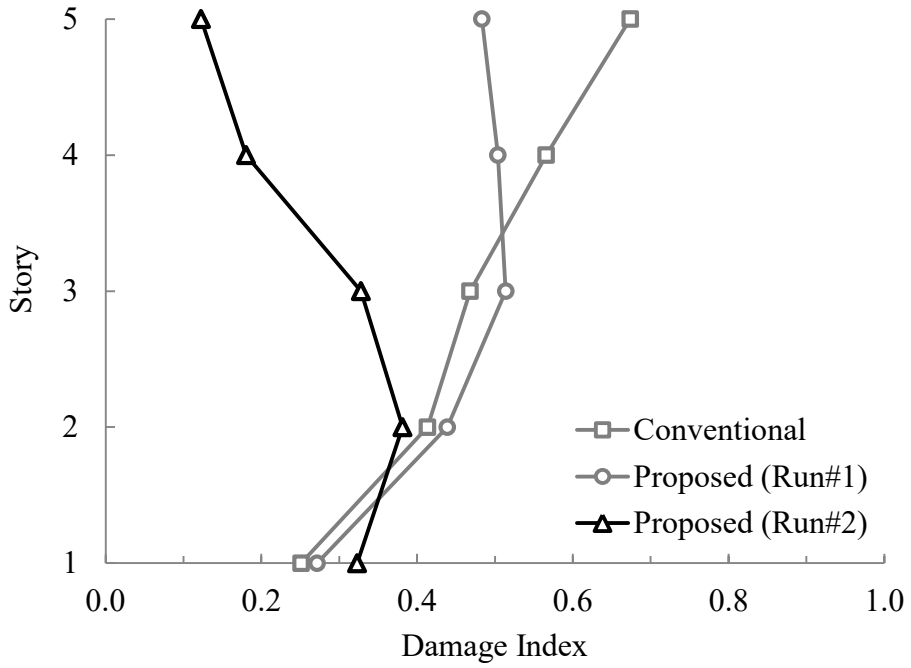

Figure 133. Comparison of story damage indices of the frames after Run #2

As can be seen from the figures, the excessive story damage indices of the upper floors were decreased at the revised design. The maximum mean story damage index was observed at the second floor as 0.38, while the minimum damage was experienced at the top floor as 0.12. Furthermore, the revised design resulted in a relatively balanced and better damage distribution. Note that, although the maximum roof drift and the total

dissipated hysteretic energy decreased by 20% and 6%, respectively; the mean overall damage was reduced by 30% in the revised design by increasing the strength and the energy dissipation capacity of the members. The overall damage level of the proposed frame was reduced from moderate to slight damage at the end of the iterative design procedure. Figure 134 shows the mean overall damage indices for all designs.

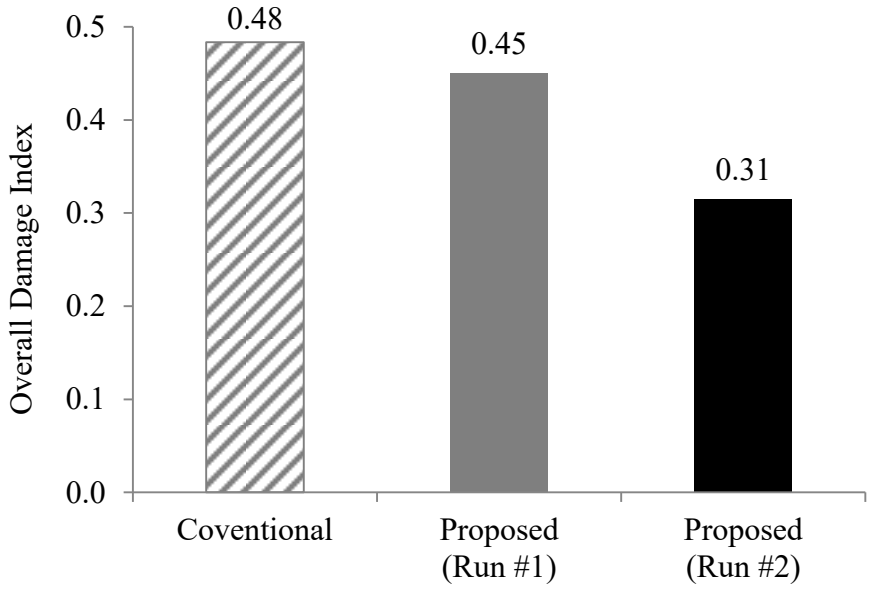

Figure 134. Mean overall damage indices for all frames after Run #2

The means of the maximum plastic rotations attained at the end-sections of the beams and columns are given in Figure 135 for all frames.

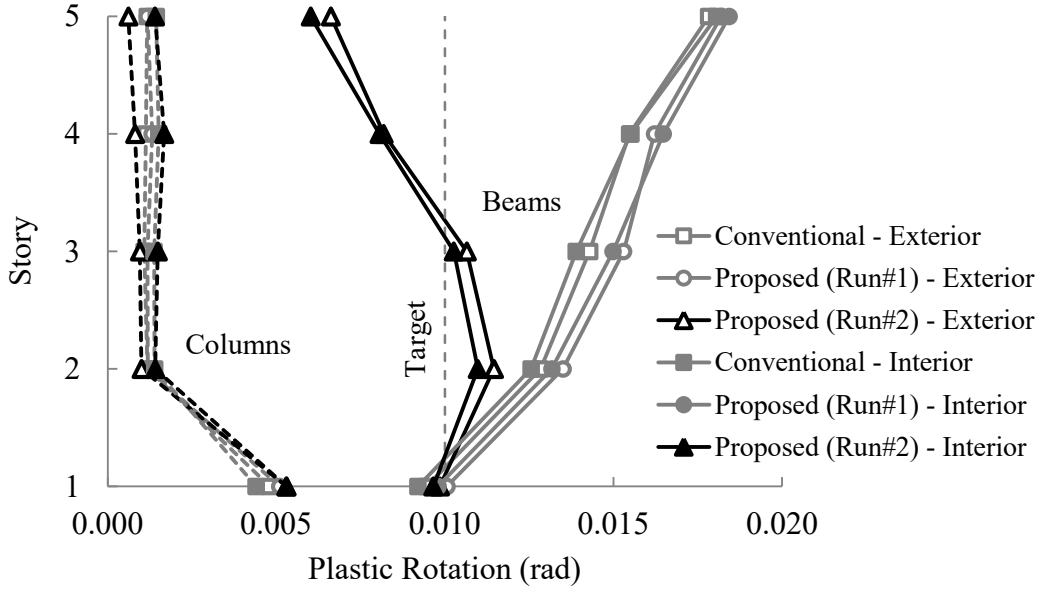

Figure 135. Mean maximum plastic rotations at columns and beams after Run #2

As it can be observed from the figure, the mean maximum plastic rotations at the beam-ends are close to the target maximum plastic rotation (0.01 rad) for the revised design. The excessive plastic rotations at the upper story beams were successfully reduced in the revised design.

All results are summarized from Figure 136 to Figure 138 for each design, respectively.

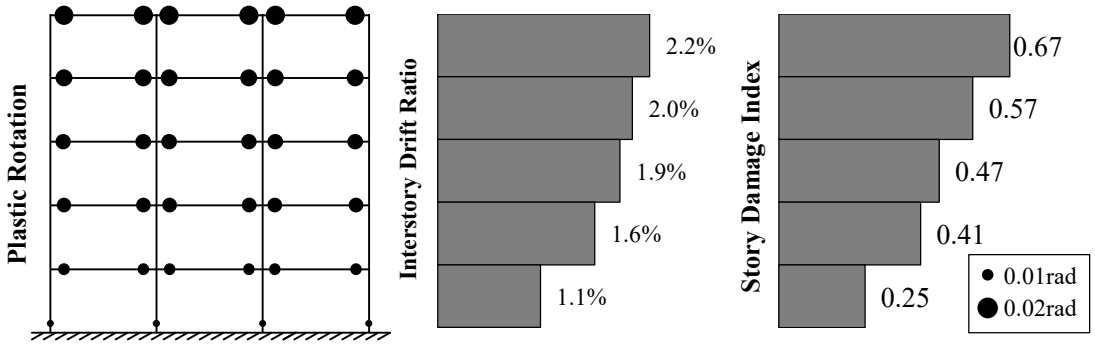

Figure 136. Summary of results for conventional frame

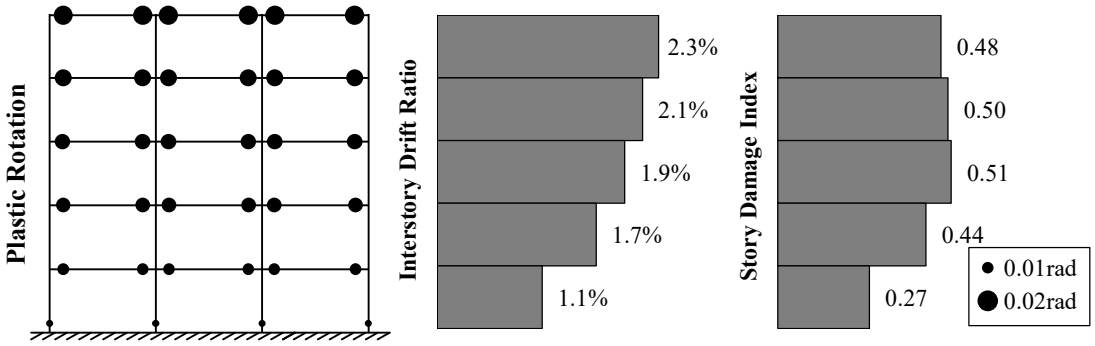

Figure 137. Summary of results for proposed frame (Run #1)

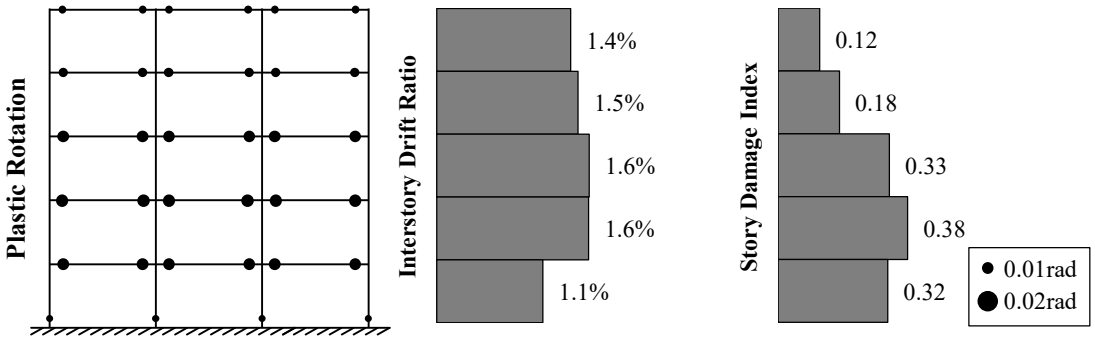

Figure 138. Summary of results for proposed frame (Run #2)

Figure 139 shows the beam moment capacities for all designs. It can be seen that the moment capacities, which satisfy the code demands, are not sufficient to have a well-distributed interstory drift and the damage index.

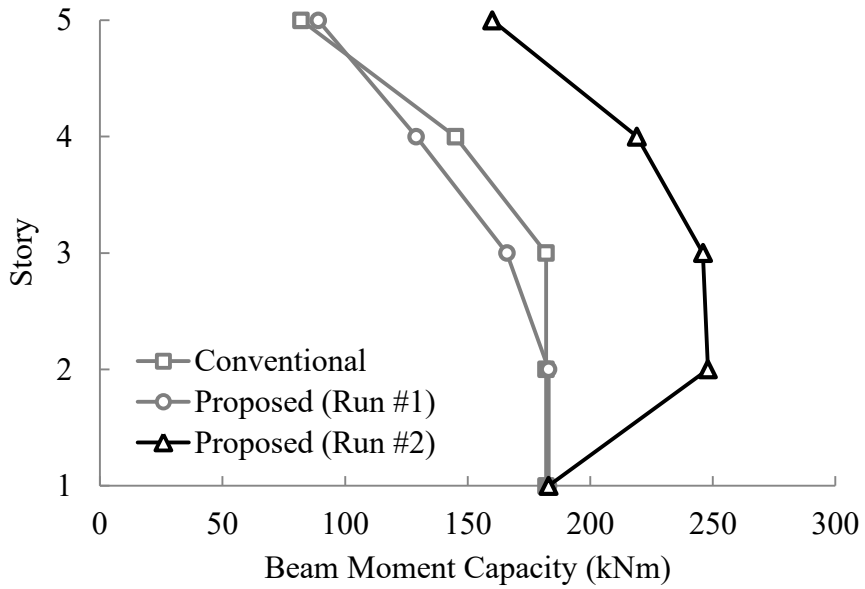

Figure 139. Beam moment capacities for all designs after Run #2

Although the interstory drift distribution after Run #2 was satisfactory, another run was performed to observe the stability of the proposed iterative procedure. Run #3 required modifications to the columns of the top two stories and the beams at the top story only. The reinforcement ratio of those columns was decreased from 1.83% to 1.66%, while that of the beams was decreased from 1.4% to 1.2%. Figure 140 shows the envelope interstory drift distribution of the proposed frame after Run #3. Figure 141 compares the mean envelope interstory drift distributions of all designs.

From the figures, it can be implied that the proposed iterative procedure is stable and did not make considerable differences compared to Run #2. The envelope interstory drift distribution is slightly more balanced after Run #3. The COV of interstory drifts decreased from 0.06 to 0.04.

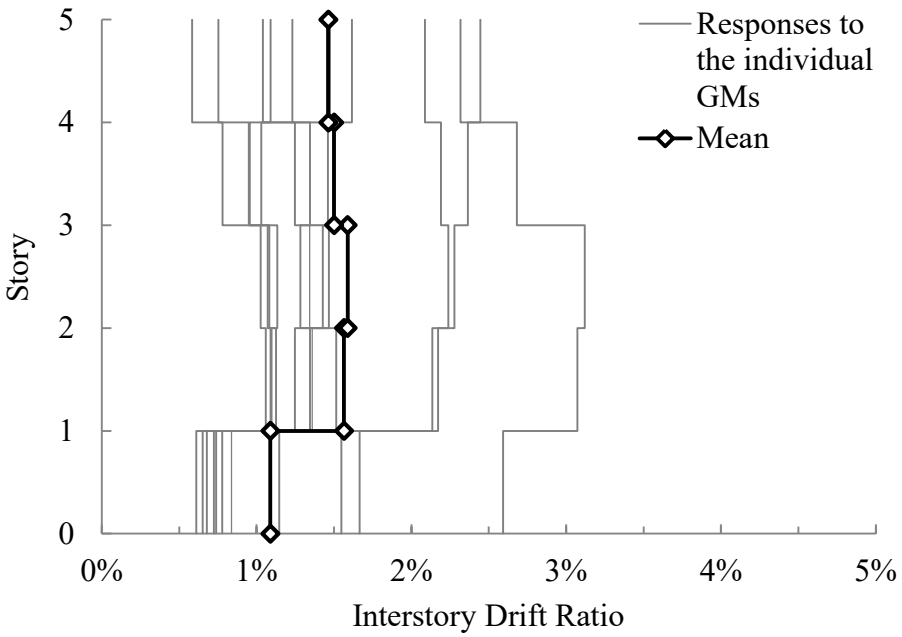

Figure 140. Envelope interstory drifts for the proposed frame (Run #3)

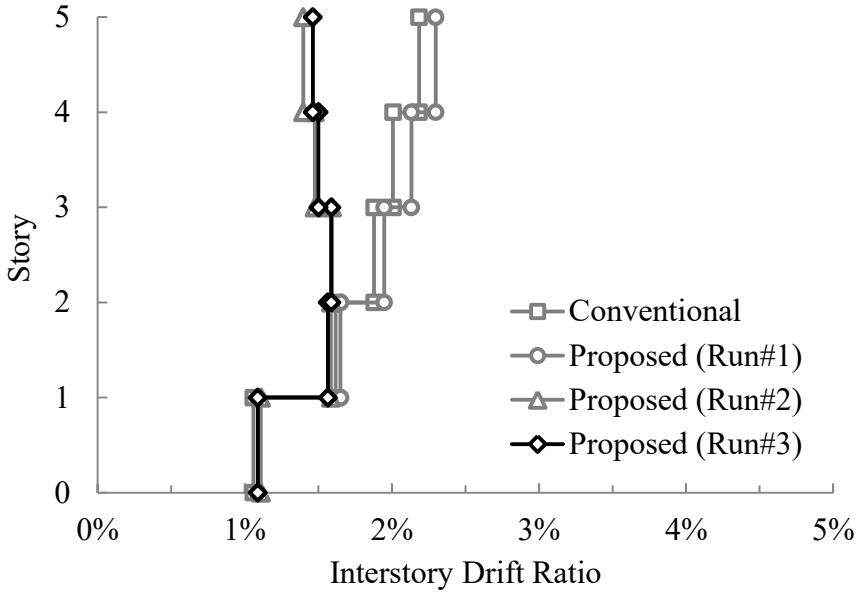

Figure 141. Comparison of mean envelope interstory drift distributions after Run #3

6.3.8. Pushover Analyses

All designs were subjected to nonlinear pushover analyses to observe the change in the base shear coefficient and the effective stiffness. The frames were "pushed" to the mean maximum roof drift ratios obtained from the nonlinear time-history analyses (i.e. 1.61%, 1.68%, and 1.30% for the conventional frame, the proposed frame after Run #1,

and the proposed after Run #2, respectively). Figure 142 shows the pushover curves and the effective stiffnesses of all frames.

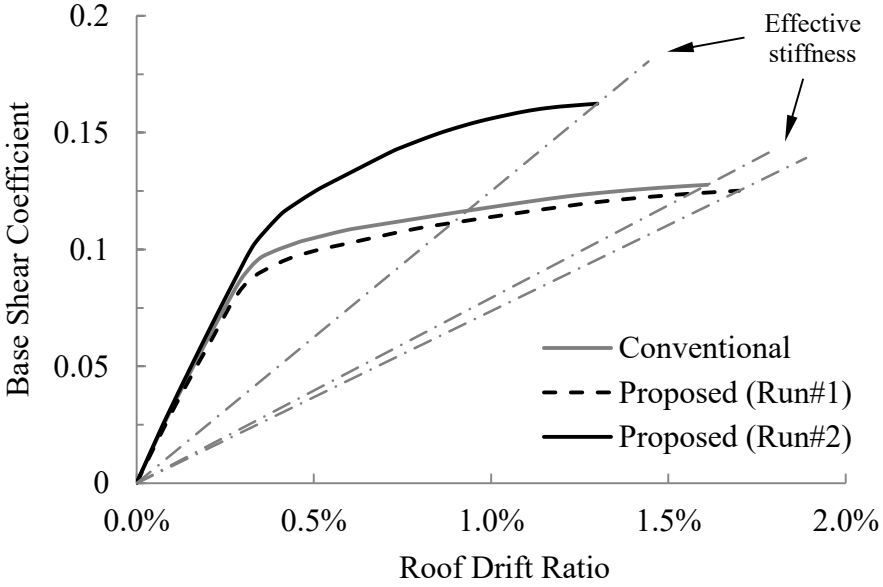

Figure 142. Pushover curves and effective stiffnesses for all designs

It can be observed from the figure that the pushover curves of the initial designs are almost identical. The base shear coefficient at the maximum roof drift is 0.13 for the initial designs. After the revised design, the base shear coefficient increased by 30%, and the effective stiffness increased by 70%. Therefore, the global ductility demand decreased after the revision, which also leads to reduced overall damage throughout the frame.

Furthermore, it is observed that the square root of the ratio of the final effective stiffness ($K_{eff,2}$) to the initial effective stiffness ($K_{eff,1}$) approximates the ratio of the maximum roof drifts of the initial and the final designs, MRD_1 and MRD_2. Figure 143 compares the two parameters for individual ground motions, as well as for the mean results.

It can be seen that the mean maximum roof drift of Run #2 decreased to 77% of the mean maximum roof drift of Run #1. Similarly, the square root of the ratio of the initial effective stiffness to the final effective stiffness is 0.77. Therefore, this parameter can be used to estimate the average change in the peak roof displacement during ground motions between design revisions.

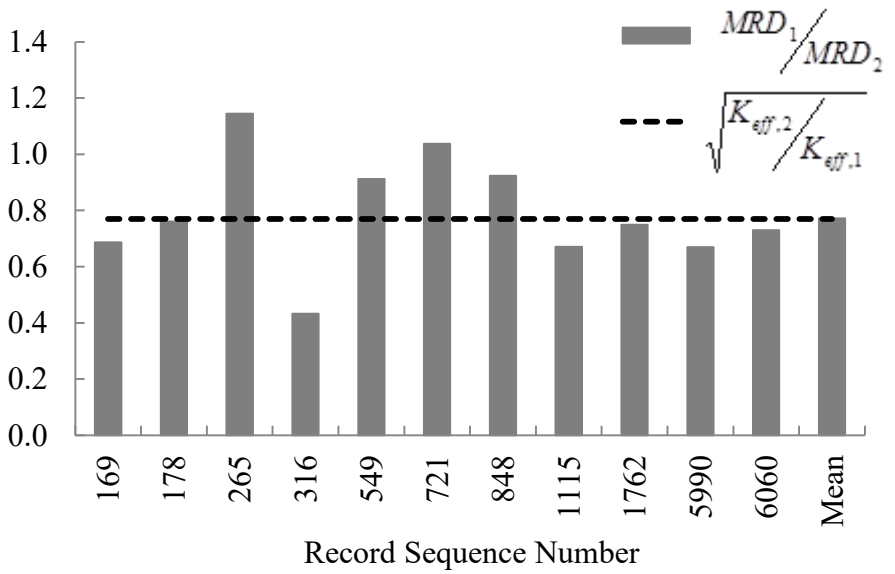

Figure 143. Relationship between the change in the maximum roof drift and the change in the effective stiffness

6.4. Case Study III: Ten-Story Three-Bay Frames

Following the case studies of five-story frames, ten-story three-bay frames were designed to evaluate the effectiveness of the proposed method on relatively higher buildings. A conventional frame and a proposed frame are studied as in the previous case studies.

6.4.1. Properties of the Frames

All geometric and material properties of the ten-story frames are the same as those of the five-story frames, except the number of stories. An overview of the frames is shown in Figure 144.

The target fundamental period was selected as 1.4 seconds for both frames based on the gross flexural stiffnesses. Similar to the previous frames, this value is greater than the expected period for a usual ten-story frame and selected on purpose. The aim here is to increase the drift demand and observe the performance of the proposed seismic design method for relatively higher displacement demands. The member cross-section dimensions for the conventional and the proposed frame are given in Table 28. Based on the selected member sizes, the fundamental periods were calculated as 1.4

seconds for both frames. The fundamental periods were calculated as 2.0 seconds based on the effective flexural stiffnesses.

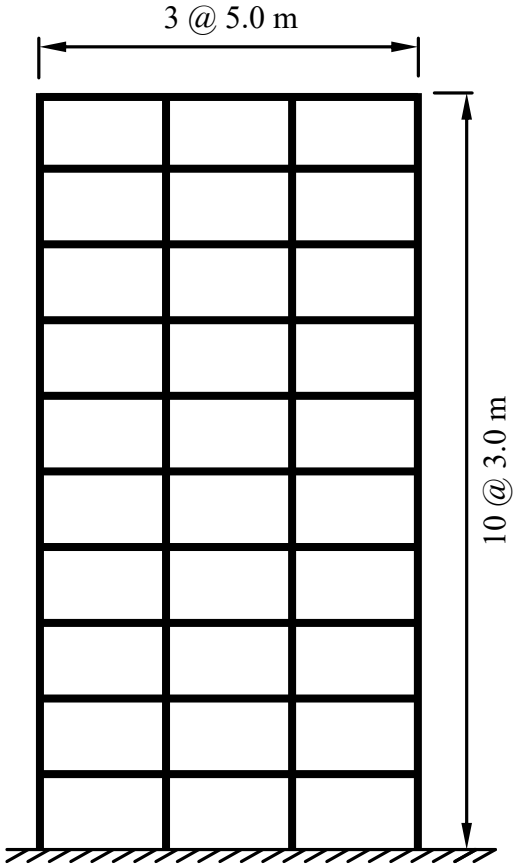

Figure 144. Overview of the ten-story three-bay frames

Table 28. Member cross-section dimensions for the frames (width×height in cm)

	Conventional Frame		**Proposed Frame**	
Story	**Columns**	**Beams**	**Columns**	**Beams**
10	55×55	30×50	55×55	20×40
9	55×55	30×50	55×55	20×45
8	55×55	30×50	55×55	20×45
7	55×55	30×50	55×55	25×50
6	60×60	30×50	60×60	25×50
5	60×60	30×50	60×60	25×55
4	60×60	30×50	60×60	25×55
3	70×70	30×50	70×70	25×60
2	70×70	30×50	70×70	25×55
1	70×70	30×50	70×70	25×55

6.4.2. Seismic Design

The initial seismic design of the frames was performed as described in Section 6.2.2. Table 29 shows the design moments (M_d), tension reinforcement ratios (ρ), provided moment capacities (M_r) for the beam end-sections of the conventional and the proposed frame along with the cross-section dimensions. Since the fundamental periods and the masses of both frames are equal, the design lateral loads and the resulting design moments are quite similar to each other. Note that, half the amount of the tension reinforcement was provided as the compression reinforcement at all sections. In addition, beams of the same story have the same reinforcements. All reinforcement ratios were checked against TEC2018 limitations.

For the columns of both frames, the minimum reinforcement ratio, 1%, governed the design. Therefore, steel reinforcement that provides a 1% ratio was provided at all columns. Based on the proportioning of the frame members, column-to-beam strength ratios (the ratio of the sum of moment capacities of all columns to the sum of moment capacities of beams at a joint), β, at all joints were calculated. Table 30 shows the β values at the internal and external joints for both frames.

Table 29. Cross-section dimensions, design moments, tension reinforcement ratios, and moment capacities for beams

Story	Conventional Frame				Proposed Frame			
	$b \times h$ (cm)	M_d (kN·m)	ρ (%)	M_r (kN·m)	$b \times h$ (cm)	M_d (kN·m)	ρ (%)	M_r (kN·m)
10	30×50	82	0.4	101	20×40	78	1.0	88
9	30×50	126	0.6	147	20×45	121	1.2	144
8	30×50	148	0.7	165	20×45	131	1.2	144
7	30×50	169	0.9	202	25×50	174	1.0	201
6	30×50	187	1.0	222	25×50	178	1.0	201
5	30×50	200	1.0	222	25×55	208	1.1	246
4	30×50	207	1.1	244	25×55	206	1.1	246
3	30×50	207	1.1	244	25×60	232	1.0	272
2	30×50	196	1.0	222	25×55	192	0.9	203
1	30×50	151	0.8	183	25×55	158	0.8	182

Table 30. Column-to-beam strength ratios at the joints, β, for both frames

	Conventional Frame		Proposed Frame	
Story	**External Joint**	**Internal Joint**	**External Joint**	**Internal Joint**
10	3.5	2.4	4.0	1.7
9	4.9	3.5	5.0	3.5
8	4.7	3.4	5.4	3.9
7	4.1	3.0	4.1	3.0
6	4.2	3.1	4.6	3.4
5	4.7	3.5	4.2	3.1
4	4.5	3.3	4.4	3.3
3	5.8	4.3	5.2	3.8
2	7.8	5.7	8.6	6.3
1	9.8	7.2	9.8	7.2

6.4.3. Numerical Model and Strong Ground Motion Set

The frames were modeled in the OpenSees platform as described in Section 5.4.2. For these frames, a 2% damping ratio was assigned to the first mode, and the mode at which the cumulative mass participation exceeds 95%.

The ground motion set, which is described in Section 5.4.3, was used for the nonlinear time-history analyses of the frames.

6.4.4. Linear Time-History Analyses

Initially, both frames were subjected to the scaled ground motion records using elastic section properties to observe the linear drift behavior. Figure 145 and Figure 146 shows the envelope interstory drift ratios for each ground motion (GM) record, as well as the means of the distributions for the conventional and the proposed frames, respectively. Figure 147 compares the mean envelope interstory drift ratios of the frames.

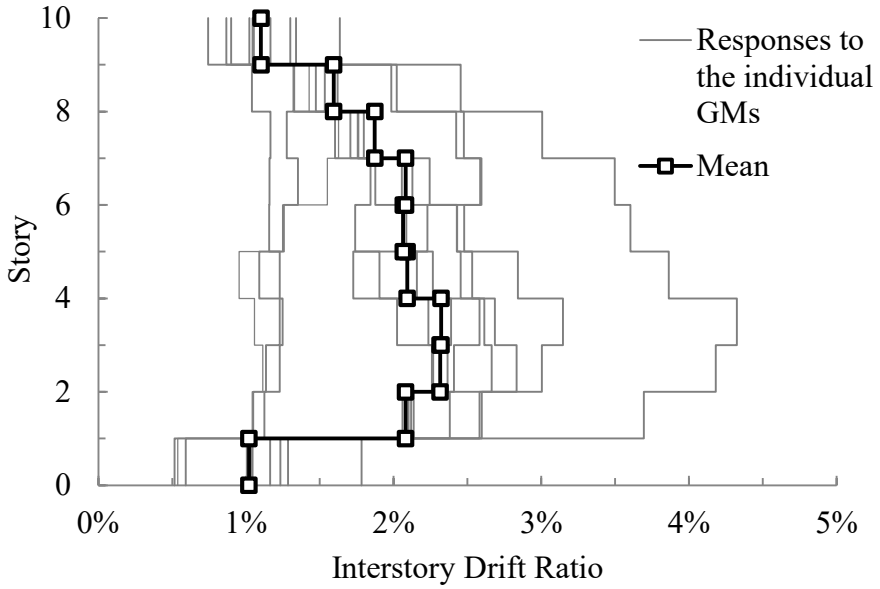

Figure 145. Envelope interstory drift ratios of conventional frame for linear case

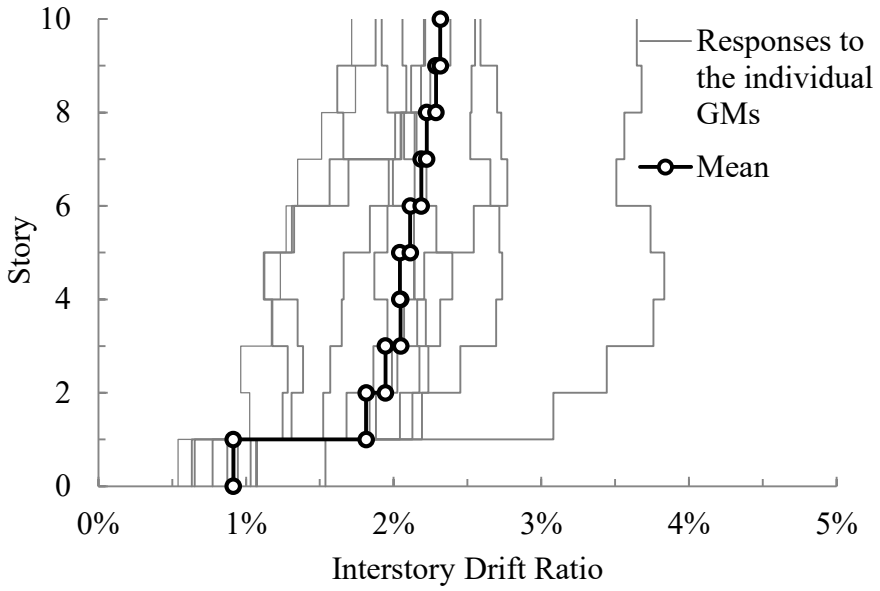

Figure 146. Envelope interstory drift ratios of proposed frame for linear case

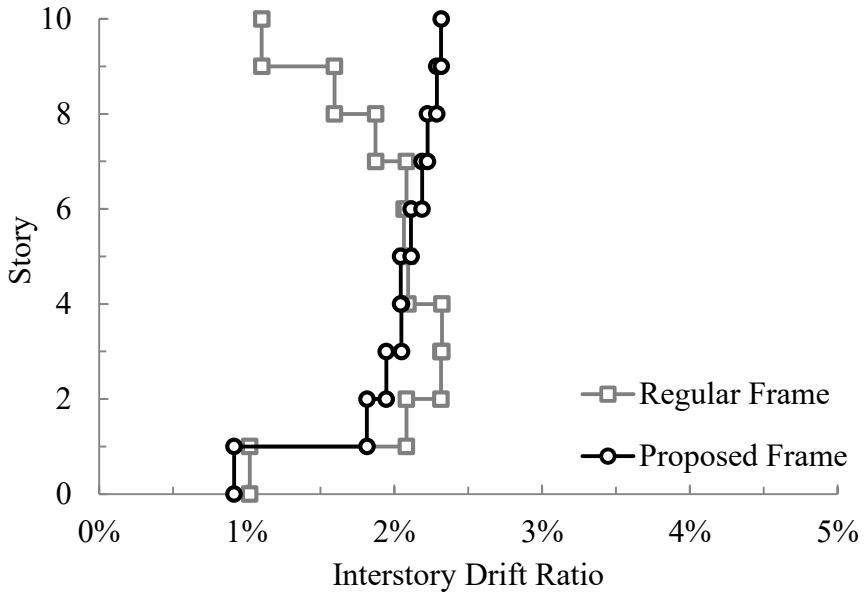

Figure 147. Comparison of mean envelope interstory drift distributions for linear case

As it can be observed from the figures above, the proposed frame had a more balanced interstory drift distribution in the linear case. The COV for the conventional frame is 0.20, while it is 0.08 for the proposed frame.

The maximum envelope interstory drift ratio is 2.3% for both frames while the average maximum roof drift ratio is 1.51% and 1.66% for the conventional and the proposed frames, respectively. Figure 148 shows the maximum roof drift ratios for individual ground motions. The mean maximum roof drift of the proposed frame is 10% larger than that of the conventional frame.

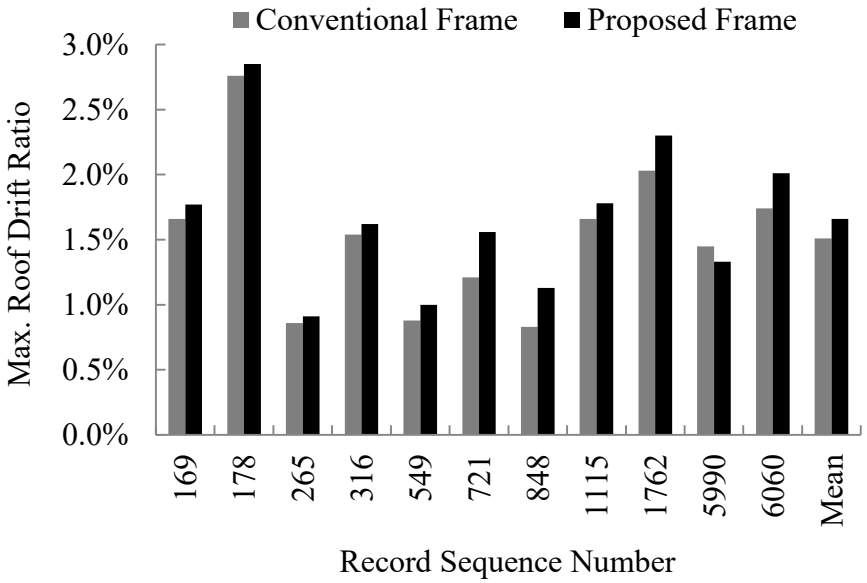

Figure 148. Maximum roof drift ratios for individual ground motion records in linear case

6.4.5. Nonlinear Time-History Analyses

The proposed frame considered in this case study required three design revisions to reach a uniform interstory drift distribution. Therefore, four nonlinear time-history runs were carried out for the proposed frame. Instead of presenting the properties and the results of each run separately, the results are presented together to permit easy follow up of the design. As in previous case studies, the target maximum plastic rotation for the beam-ends was taken as 0.01 radians.

The provided reinforcement ratios and the moment capacities of the beam-ends for each design are given in Table 31. Note that, half the amount of the tension reinforcement was provided as the compression reinforcement at all beam end-sections. In addition, all beams at the same story have the same reinforcements. The reinforcement ratios of the columns for each design are presented in Table 32.

. All reinforcement ratios were checked against TEC2018 limitations. The underlined numbers in the tables indicate that the maximum allowed reinforcement ratio was reached at the corresponding members. Table 33 presents the column-to-beam strength ratios, β, at all external and internal joints for all designs. It can be seen that the reinforcement ratios and the moment capacities had to be increased significantly to limit

the plastic rotations. Some members reached the maximum allowable reinforcement ratios.

The results of the nonlinear time-history analyses are presented in terms of the individual and the mean envelope interstory drift distributions in Figure 149 for all designs. Figure 150 compares the mean envelope interstory drift distribution of the final design with the initial designs. Figure 151 shows the change in the COV of the envelope interstory drift distributions.

Table 31. Provided reinforcement ratios and moment capacities of the beams for all designs

	Conventional		**Proposed (Run #1)**		**Proposed (Run #2)**		**Proposed (Run #3)**		**Proposed (Run #4)**	
Story	**ρ (%)**	**M_r (kN·m)**	**ρ (%)**	**M_r (kN·m)**	**ρ (%)**	**M_r (kN·m)**	**ρ (%)**	**M_r (kN·m)**	**ρ (%)**	**M_r (kN·m)**
10	0.4	101	1.0	88	1.5	140	1.0	88	2.0	154
9	0.6	147	1.2	144	1.5	194	1.2	144	2.0	211
8	0.7	165	1.2	144	1.5	194	1.4	160	2.0	211
7	0.9	202	1.0	201	1.6	310	1.7	308	2.0	356
6	1.0	222	1.0	201	1.6	310	1.8	332	1.8	332
5	1.0	222	1.1	246	1.5	344	1.9	426	1.9	426
4	1.1	244	1.1	246	1.4	318	1.9	426	1.9	426
3	1.1	244	1.0	272	1.2	324	1.7	471	1.7	471
2	1.0	222	0.9	203	0.9	203	1.3	294	1.3	294
1	0.8	183	0.8	182	0.4	96	0.5	128	0.5	128

Table 32. Provided reinforcement of the columns for all designs

Story	Reinforcement Ratio (%)				
	Conventional	Proposed (Run #1)	Proposed (Run #2)	Proposed (Run #3)	Proposed (Run #4)
10	1.0	1.0	2.6	1.1	3.7
9	1.0	1.0	2.6	1.1	3.7
8	1.0	1.0	3.0	2.6	4.0
7	1.0	1.0	3.7	3.7	4.0
6	1.0	1.0	2.7	3.1	3.1
5	1.0	1.0	2.7	3.6	3.6
4	1.0	1.0	2.4	3.6	3.6
3	1.0	1.0	1.7	3.0	3.0
2	1.0	1.0	1.0	2.6	2.6
1	1.0	1.0	1.0	1.0	1.0

Table 33. Column-to-beam strength ratios at the joints, β, for all designs

Story	Conventional		Proposed (Run #1)		Proposed (Run #2)		Proposed (Run #3)		Proposed (Run #4)	
	β_{ext}	β_{int}	β_{ext}	β_{int}	β_{ext}	β_{int}	β_{ext}	β_{int}	β_{ext}	β_{int}
10	3.5	2.4	4.0	1.7	3.3	2.2	3.6	2.5	3.5	2.4
9	4.9	3.5	5.0	3.5	4.9	3.3	4.6	3.2	4.5	3.0
8	4.7	3.4	5.4	3.9	5.3	3.7	5.3	3.8	5.1	3.6
7	4.1	3.0	4.1	3.0	3.7	2.6	3.6	2.5	3.4	2.4
6	4.2	3.1	4.6	3.4	4.1	2.9	3.9	2.8	3.9	2.8
5	4.7	3.5	4.2	3.1	4.0	2.8	3.4	2.4	3.4	2.4
4	4.5	3.3	4.4	3.3	4.3	3.1	3.6	2.5	3.6	2.5
3	5.8	4.3	5.2	3.8	4.8	3.5	3.8	2.7	3.8	2.7
2	7.8	5.7	8.6	6.3	8.2	6.1	7.0	5.0	7.0	5.0
1	9.8	7.2	9.8	7.2	16.7	12.5	14.3	10.5	14.3	10.5

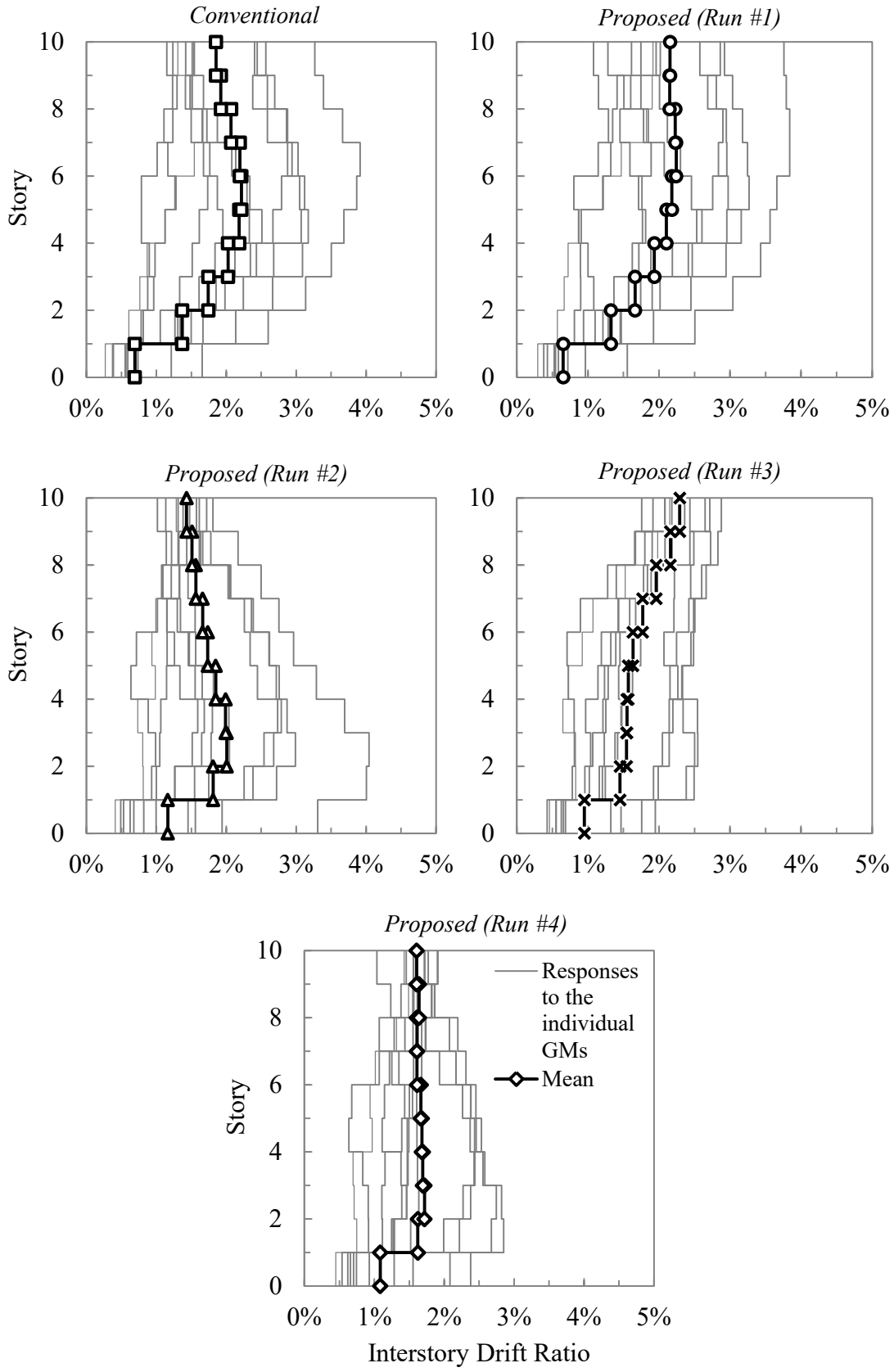

Figure 149. Envelope interstory drift distributions of all designs

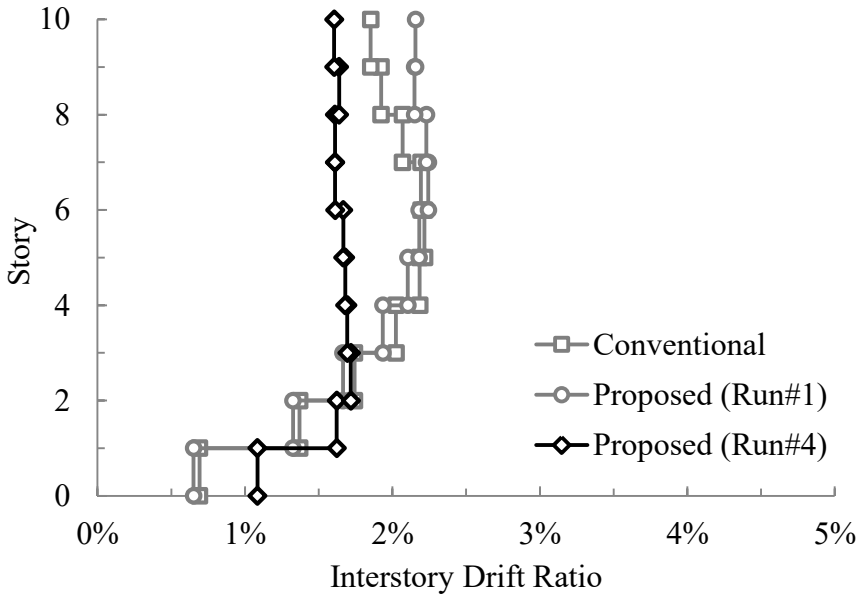

Figure 150. Comparison of mean envelope interstory drifts for initial designs and final design

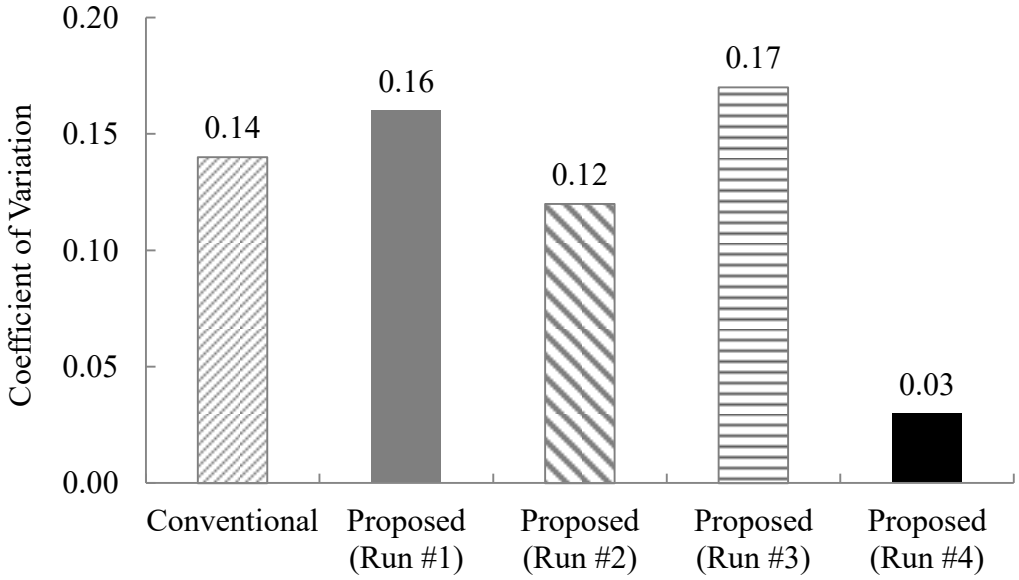

Figure 151. Coefficient of variations of envelope interstory drift distributions for all designs

From the figures, it can be observed that at the end of the iterative procedure the proposed frame had a nearly uniform interstory drift distribution. The COV of the envelope interstory drift distributions decreased by 80% compared to the initial proposed design. In addition, the maximum envelope drift was reduced from 2.2% to

1.7% (i.e. by 25%) in the final design. Figure 152 shows the maximum roof drift ratios at all ground motions, as well as the means, for all designs.

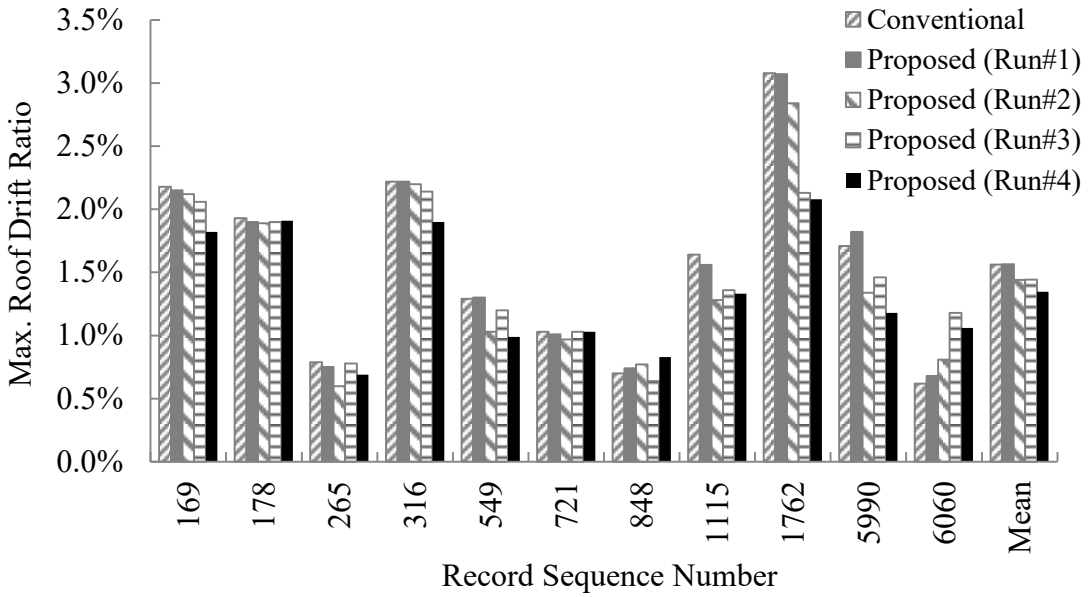

Figure 152. Maximum roof drift ratios at individual ground motions for all designs

It can be seen from the figure that the mean maximum roof drift ratio decreased by 14% compared to the first run after the design revisions. It is 1.35% for the final design.

The total dissipated hysteretic energy at each ground motion for all designs are shown in Figure 153. It can be observed from the figure that the hysteretic energy demand does not change significantly in most ground motions. The mean hysteretic energy dissipation increased by 4% in the revised design.

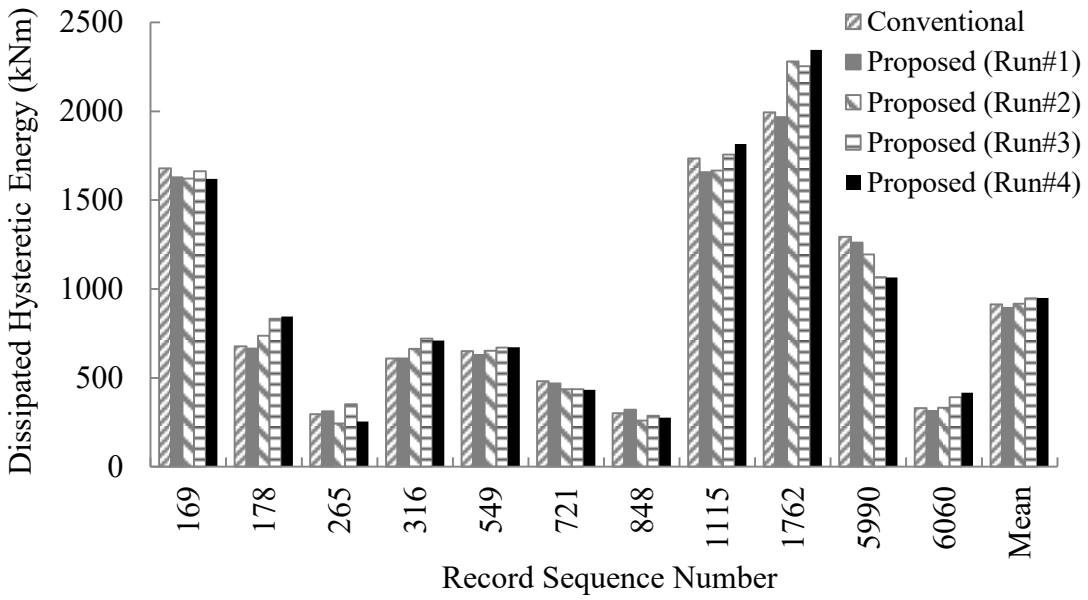

Figure 153. Total dissipated hysteretic energy at individual ground motions for all designs

The story damage indices for individual ground motion records, as well as the mean story damage indices for all designs, are given in Figure 154. The mean story damage indices of all designs are compared in Figure 155.

As can be seen from the figures, the final design resulted in effectively reduced story damage indices. The maximum mean story damage indices for the initial designs were observed at the top stories as 0.45. In the final design, it was 0.33 at the second story. The minimum damage, on the other hand, was experienced by the top story as the mean story damage index of 0.15. It can be implied that the final design had a reduced and evenly distributed damage throughout the elevation compared to the initial design. Note that, although the maximum roof drift and the total dissipated hysteretic energy did not change notably, the mean overall damage was reduced by 33% in the revised design by both increasing the strength of the members and shifting the demands to the stories with more energy dissipation capacity. The overall damage level of the proposed frame was reduced from moderate to slight damage at the end of the iterative design procedure. Figure 156 shows the mean overall damage indices for all designs.

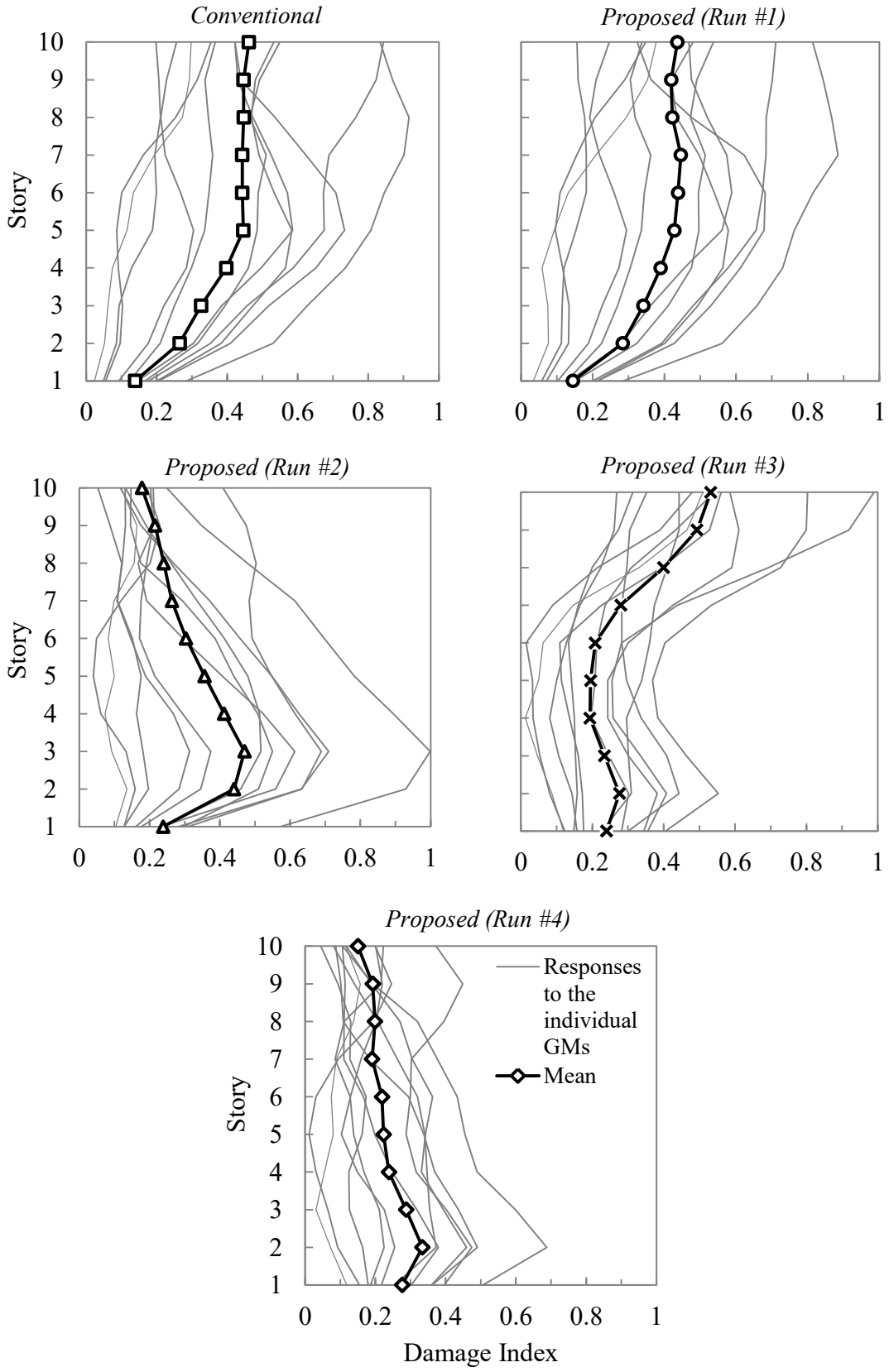

Figure 154. Story damage indices of all designs

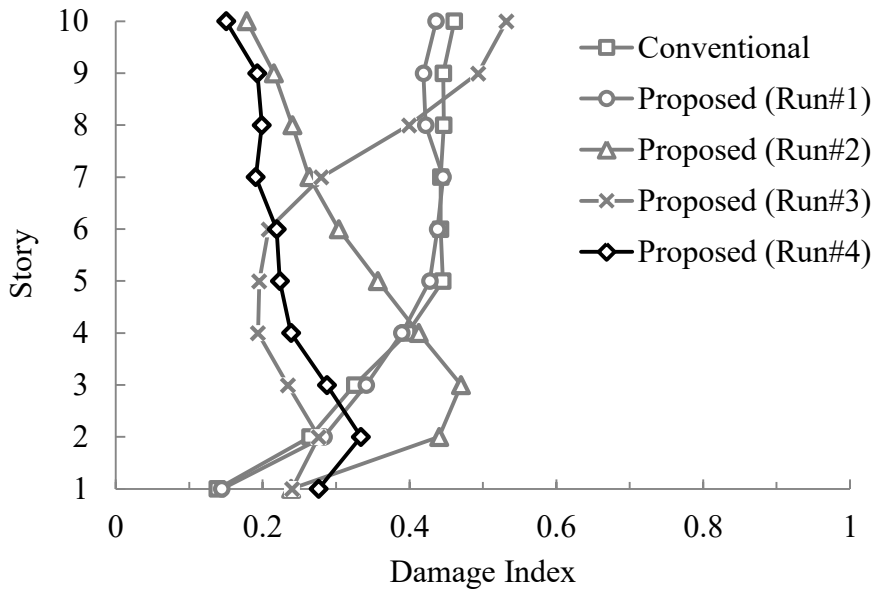

Figure 155. Comparison of story damage indices for all designs

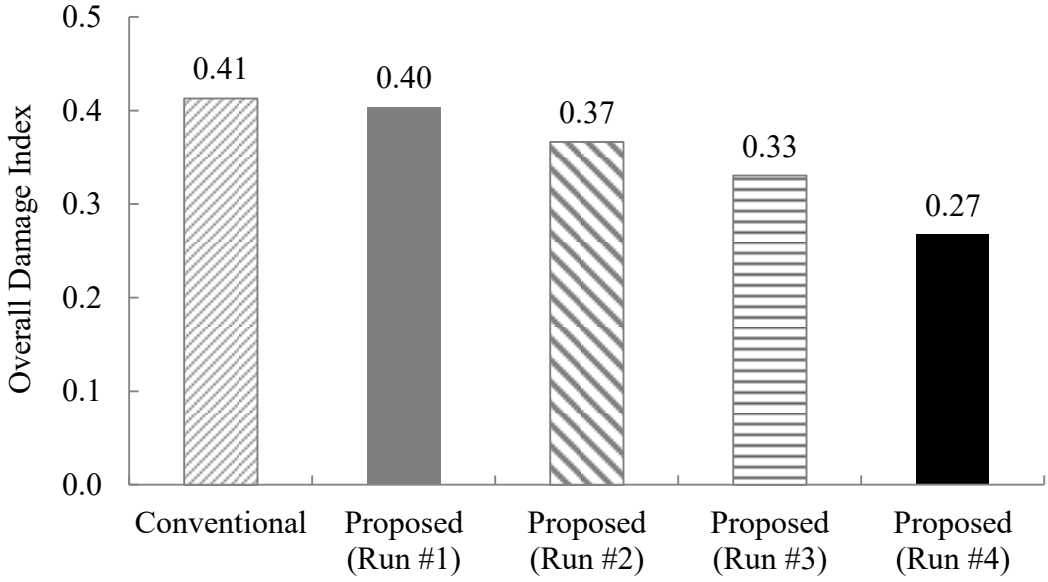

Figure 156. Mean overall damage indices for all designs

The means of the maximum plastic rotations attained at the end-sections of the beams and columns are given in Figure 157 for all designs.

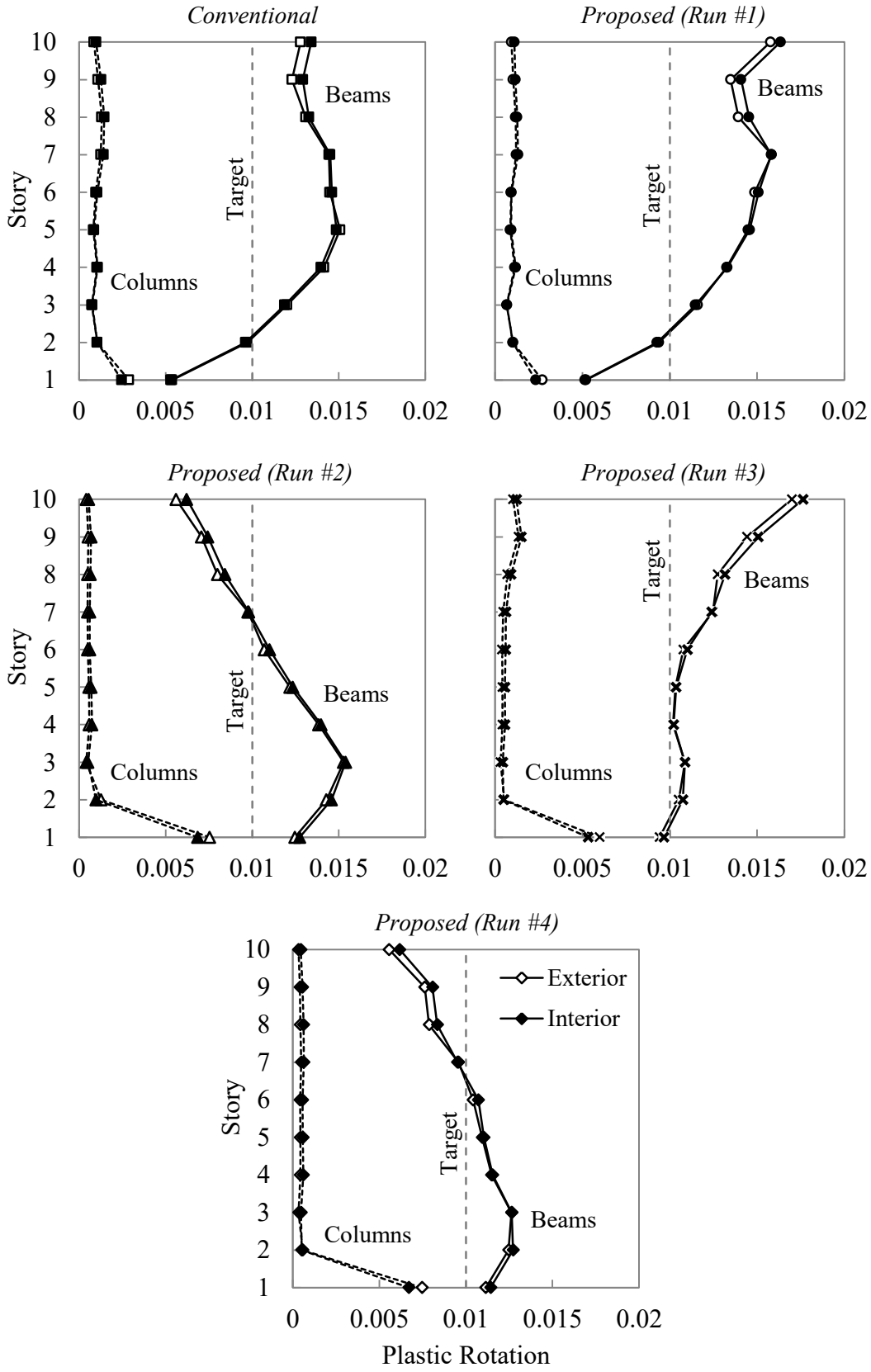

Figure 157. Mean maximum plastic rotations at columns and beams for all designs

As it can be observed from the figure, the mean maximum plastic rotations at the beam-ends are close to the target maximum plastic rotation (0.01 rad) for the final design. The excessive plastic rotations at the upper story beams were successfully reduced in the revised design.

All results are summarized from Figure 158 to Figure 160 for each design, respectively. These figures help show the relationship between the distribution of the plastic rotations, interstory drifts, and the story damage throughout the building height.

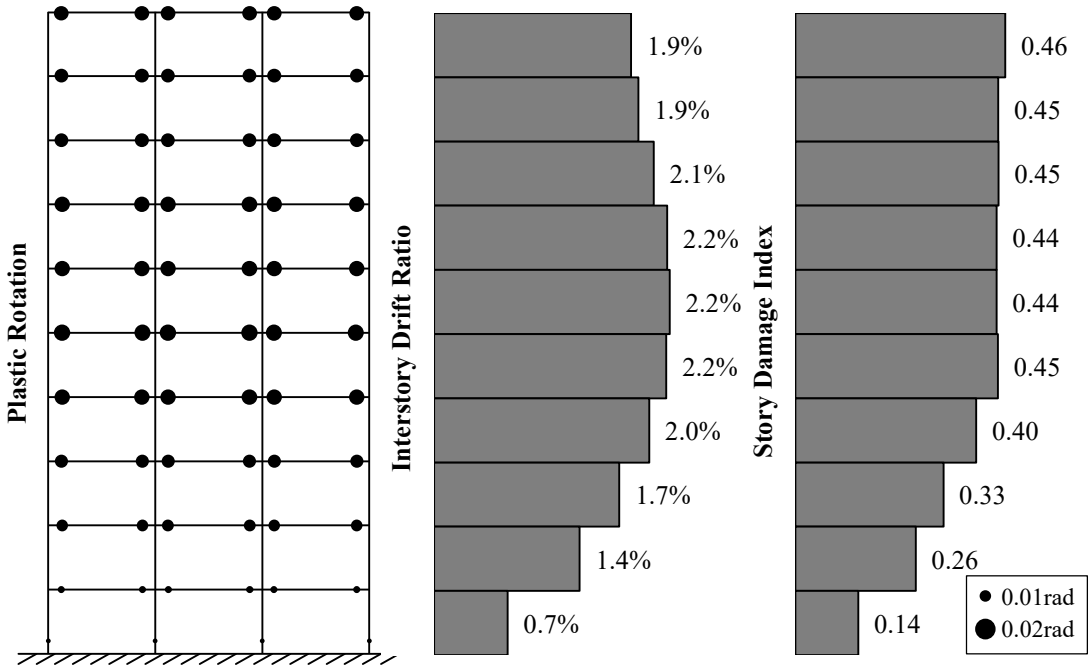

Figure 158. Summary of results for conventional frame

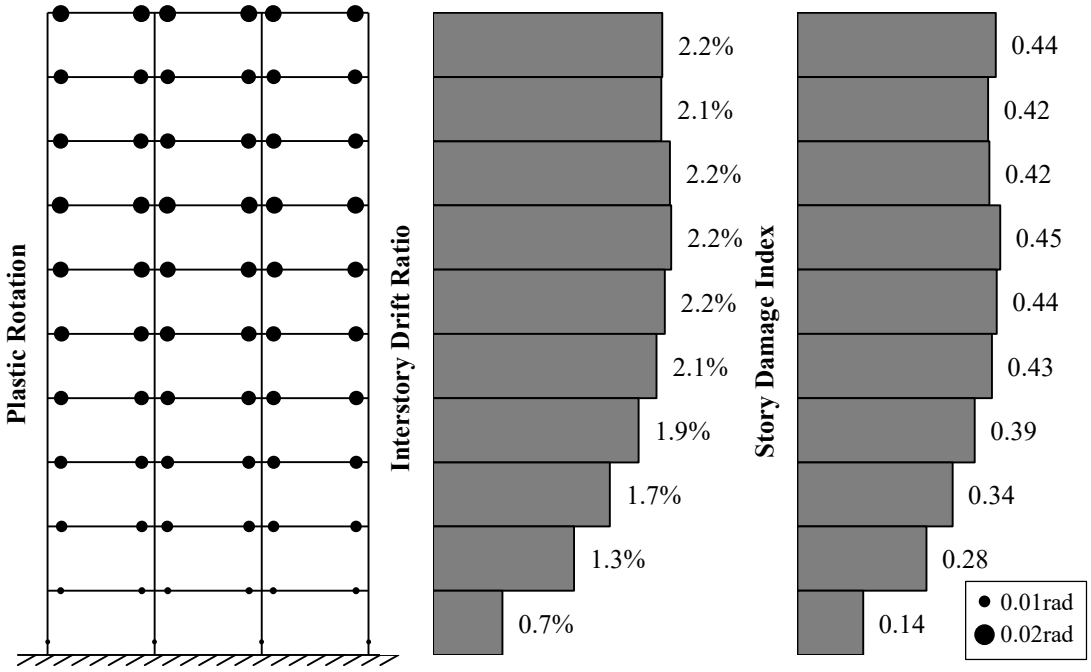

Figure 159. Summary of results for proposed frame (Run #1)

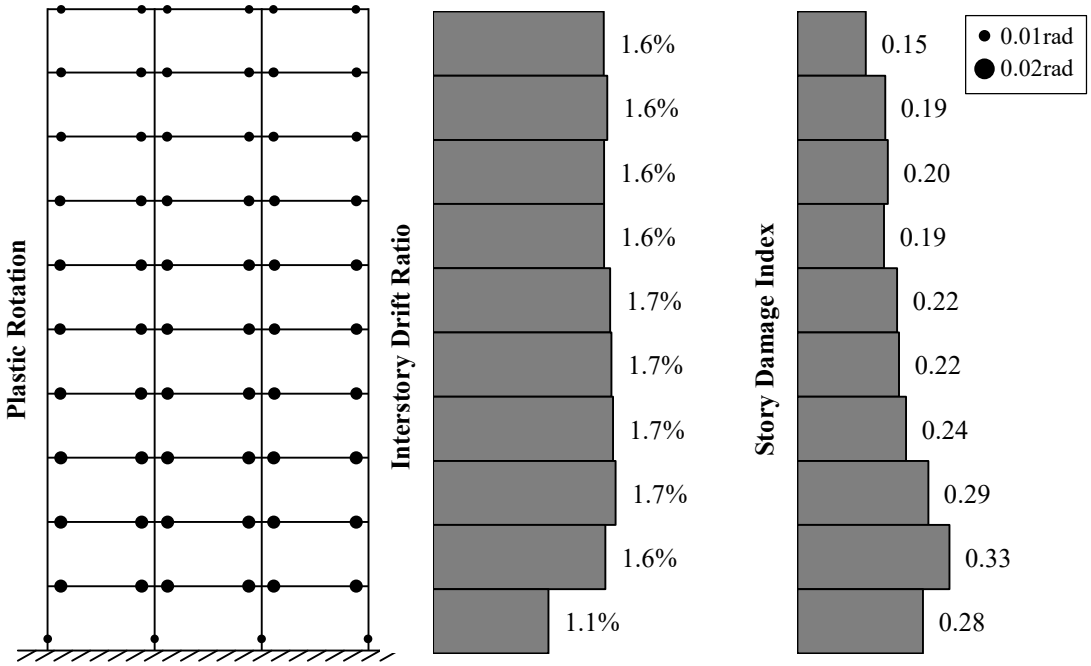

Figure 160. Summary of results for proposed frame (Run #4)

Figure 161 shows the beam moment capacities for all designs. It can be seen that the moment capacities, which satisfy the code demands, are not sufficient to control the interstory drift and the damage distribution.

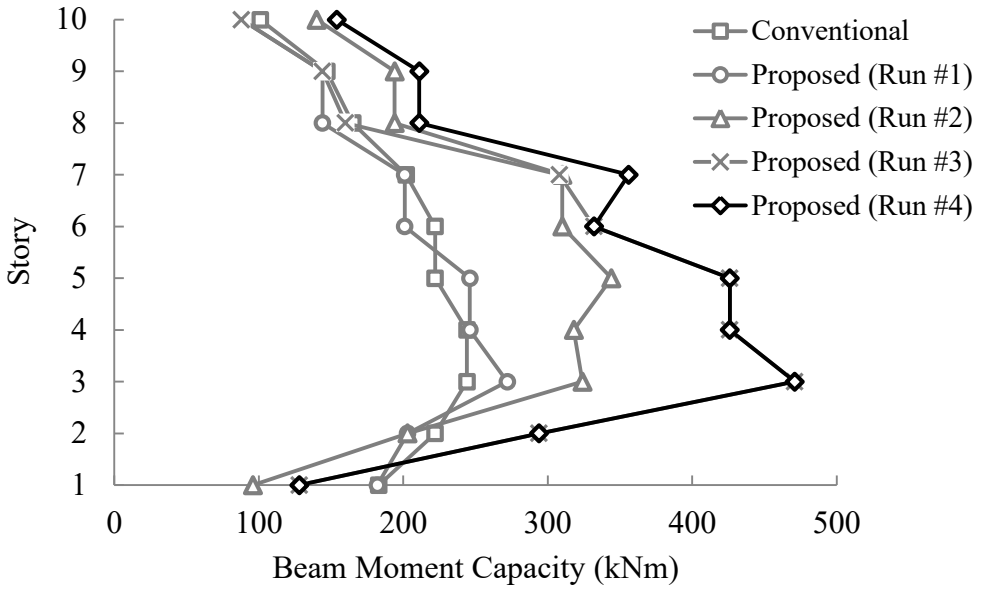

Figure 161. Beam moment capacities for all designs

6.4.5.1. Response at Service-level Earthquake

In most seismic design codes, no structural and minor non-structural damage is expected under service-level earthquakes. The structure must remain fully functional after such an earthquake. The service-level earthquake is defined with a 43-year return period (68% probability of exceedance in 50 years) and named as *DD4-level* in TEC2018. The conventional frame and the final design of the proposed frame (Run #4) were subjected to service-level ground motions to assess the responses of the frames under such an event.

The same ground motion set used in the previous case studies was scaled so as to satisfy the requirements of service-level earthquake as per TEC2018 for the selected location. The scale factors used to obtain the ground motion set for the service-level earthquake are given in Table 34. The linear acceleration response spectra of the scaled earthquakes, as well as the target and the mean spectra, are given in Figure 162.

Table 34. Scale factors used to obtain service-level earthquake set

RSN	Earthquake Name	Station Name	Scale Factor
169	Imperial Valley-06	Delta	0.75
178	Imperial Valley-06	El Centro Array #3	0.75
265	Victoria_ Mexico	Cerro Prieto	0.50
316	Westmorland	Parachute Test Site	0.60
549	Chalfant Valley-02	Bishop - LADWP South St	1.05
721	Superstition Hills-02	El Centro Imp. Co. Cent	0.58
848	Landers	Coolwater	0.80
1115	Kobe_ Japan	Sakai	1.10
1762	Hector Mine	Amboy	1.05
5990	El Mayor-Cucapah_ Mexico	El Centro Array #7	1.12
6060	Big Bear-01	North Palm Springs Fire Sta #36	1.10

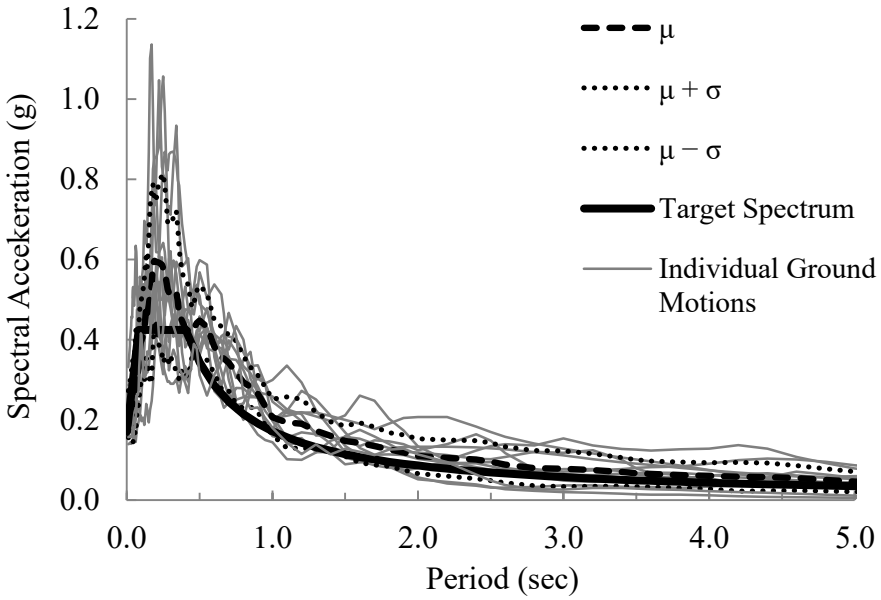

Figure 162. Linear acceleration response spectra for service-level earthquake

The mean envelope interstory drift ratios of the conventional and the final proposed designs are shown in Figure 163.

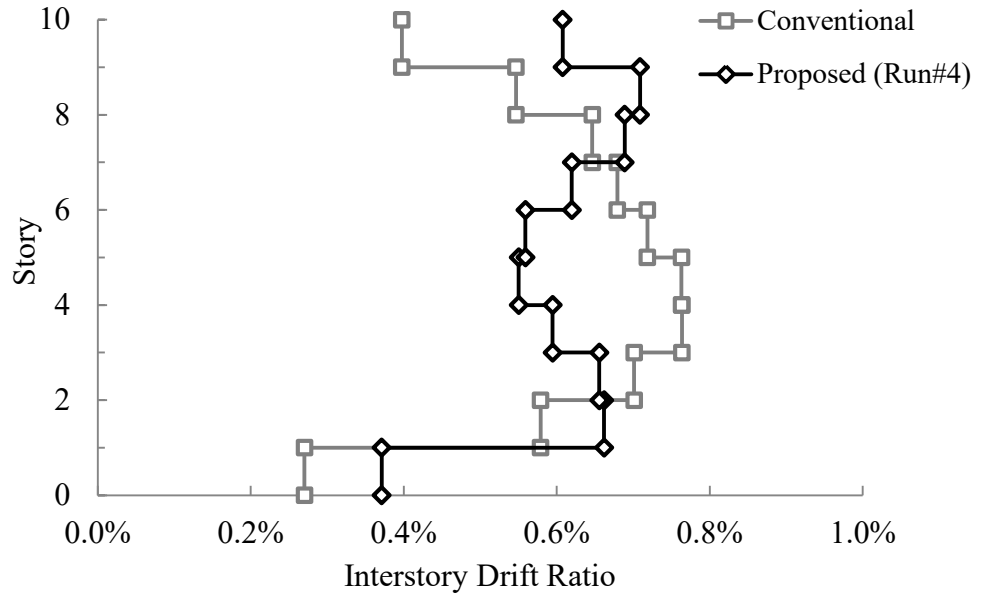

Figure 163. Mean envelope interstory drift ratios of conventional and final proposed designs under service-level earthquake

From the figure, it can be seen that the envelope interstory drift ratios are below 0.8% for both frames. Structural damage is not expected for this drift levels in reinforced concrete frames. Figure 164 shows the story damage indices for both frames. It can be seen that the structural damage at both frames is at negligible levels.

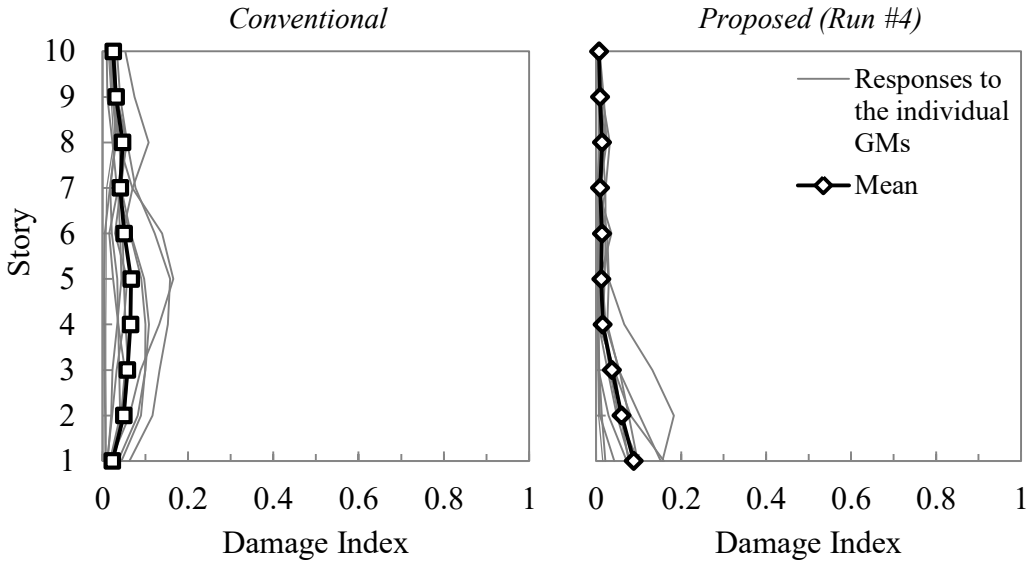

Figure 164. Story damage indices for conventional frame and proposed frame (Run #4) under service-level earthquake

However, it is known that in most of the earthquake-prone regions, hollow clay tile infill walls are quite common for the residential buildings such as the ones considered in this study (Fardis, 2006; Yakut, 2004). These walls are stiff elements but they are very brittle in nature. Therefore, they are likely to be damaged at relatively low drift levels (less than 1%), unless they are isolated from the surrounding frame members. Therefore, it can be implied that if these frames had non-isolated infill walls within some bays, these walls would have been damaged up to some extent under service-level earthquake

6.4.6. Pushover Analyses

All designs were subjected to nonlinear pushover analyses to observe the change in the base shear coefficient and the effective stiffness. The frames were "pushed" to the mean maximum roof drift ratios obtained from the nonlinear time-history analyses (i.e. 1.56%, 1.56%, 1.44%, 1.44%, and 1.30% for the conventional frame, the proposed frame after Run #1, Run #2, Run #3 and Run #4, respectively). Figure 165 shows the pushover curves and the effective stiffnesses of all frames.

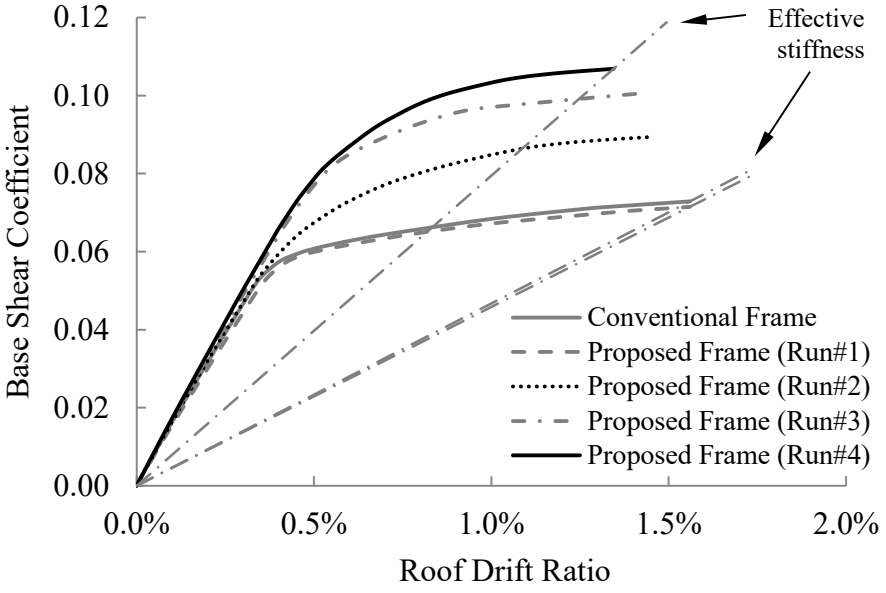

Figure 165. Pushover curves of all designs and effective stiffnesses for initial and final designs

It can be observed from the figure that the pushover curves of the initial designs are almost identical. The base shear coefficient at the maximum roof drift is 0.07 for the initial designs. For the final design, the base shear coefficient increased by 50%, and the effective stiffness increased by 75%. Therefore, the global ductility demand decreased after the revision, which also leads to reduced overall damage throughout the frame.

Furthermore, it is observed that the square root of the ratio of the final effective stiffness ($K_{eff,2}$) to the initial effective stiffness ($K_{eff,1}$) approximates the ratio of the maximum roof drifts of the initial and the final designs, MRD_1 and MRD_2. Figure 143 compares the two parameters for individual ground motions, as well as for the mean results.

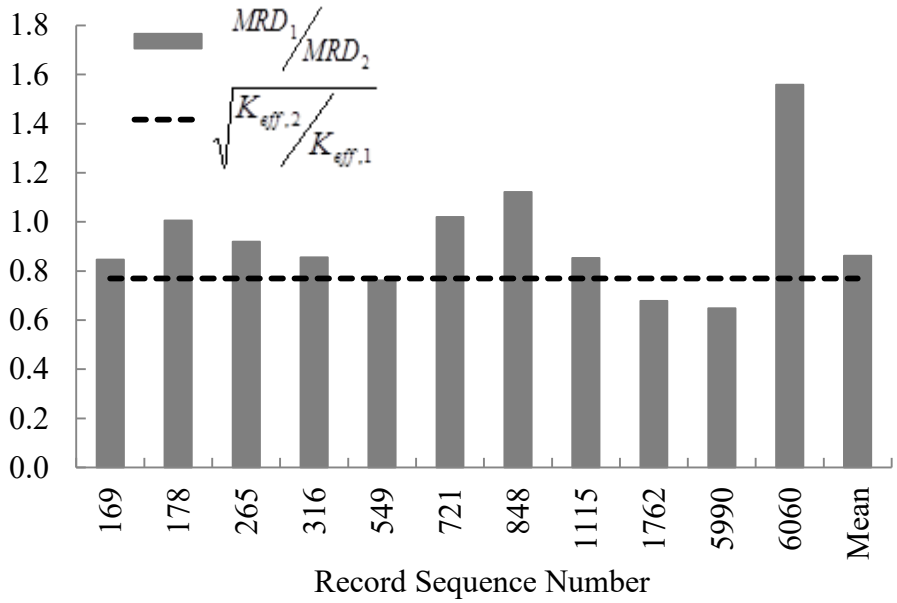

Figure 166. Relationship between the change in the maximum roof drift and the change in the effective stiffness

It can be seen that the mean maximum roof drift of Run #4 decreased to 86% of the mean maximum roof drift of Run #1. Similarly, the square root of the ratio of the initial effective stiffness to the final effective stiffness is 0.77. Therefore, this parameter can be used to estimate the average change in the peak roof displacement during ground motions between design revisions.

6.5. Discussion of the Results

The results of the case studies point out that the proposed seismic design procedure is effective at mitigating the interstory drift concentrations in low- and mid-rise reinforced concrete moment frames. In the linear range, the proposed primary design procedure resulted in more balanced interstory drift ratios compared to the conventional designs. This result is important particularly for the frames with infill walls since infills are likely to fail at relatively low drifts (i.e. when the frames are still in the elastic range). Therefore, it can be inferred that the proposed design procedure inhibits non-structural damage concentrations in low- and mid-rise frames.

For the inelastic range, it was observed that the interstory drift distributions are entirely different from those of the elastic range. While the elastic drift response is controlled by the elastic modal properties − particularly by the stiffness distribution, the inelastic drift response is observed to be governed by the yield strength of the members. In all case studies, the initial designs of both the conventional and the proposed frames were performed using the equivalent lateral load procedure and the capacity design principles. Story masses and the fundamental periods are used to determine the amount and the distribution of the design lateral loads in this procedure. Since these properties are identical in both frames, the design moments are almost identical, as well. As a result, the interstory drift distributions of the conventional and the initial proposed designs are almost the same in all case studies.

The proposed iterative procedure was shown to be effective at limiting the maximum plastic deformations and balancing the interstory drift distributions. The maximum story drifts were also reduced to some extent due to the increase in the effective stiffness of the system at maximum deformation levels. As a result, the damage throughout the frame was reduced notably. It should be noted that the total dissipated hysteretic energy remained almost constant in the conventional and proposed frames. This result indicates that the distributing the hysteretic energy demand uniformly along the height of the frames by adjusting the yield strengths of the members could mitigate the damage concentrations. In addition, the energy dissipation capacities of the members were enhanced with the increase in the yield strength, even the deformation capacities do not change notably. If these two points are considered together, the damage levels are expected to decrease as observed in the case studies.

These observations point out that even the hysteretic energy demand remains constant, it is possible to limit the plastic deformations and damage of the individual members by adjusting the yield strength throughout the structure. In addition, the amounts of the yield strengths and their distributions over the final designs of the frames were observed to be quite different from those obtained from the conventional design methods. This observation indicates that the conventional design procedures do not account for the change in the behavior after the structure passes beyond the elastic range.

The target fundamental periods for all frames were intentionally selected relatively longer to increase the displacement demands. This choice led to smaller member cross-sections. However, the target maximum plastic rotation for the beams was selected relatively lower (immediate occupancy limit in ASCE 41-13) to test the effectiveness of the proposed procedure. As a result of these choices, relatively higher amounts of reinforcement were required at some members to achieve the target maximum plastic rotation. However, slight changes in column sizes and beam widths may reduce the reinforcement ratios, if needed, without influencing the linear drift behavior notably.

The proposed iterative procedure was shown to be very effective at optimizing the drift behavior of the considered frames. For the five-story frames, only one revision was sufficient to reach the uniform interstory drift distribution, while it took three iteration steps for the ten-story frame.

6.6. Summary and Concluding Remarks

Three case studies were performed to evaluate the performance of the proposed seismic design procedure. Pairs of five-story single-bay, five-story three-bay, and ten-story three-bay planar frames are used for this purpose. Each pair consists of a frame designed using a conventional seismic design approach, and a frame designed using the proposed approach. The yield strengths of the latter were modified after the nonlinear time-history analyses until a uniform interstory drift distribution is obtained. The results showed that the proposed procedure results in the target interstory drift distribution with a low number of iteration steps.

The main outcome of the case studies is that the yield strength of the members and their distribution over the height play a crucial role in controlling the distribution of

the story drifts and the damage throughout the frame during strong ground motions. It was observed that the total amount of the dissipated hysteretic energy is almost constant between the design iterations. However, the plastic energy demand imparted to the structure is distributed efficiently between the members according to their energy dissipation capacity by adjusting the yield strengths. Consequently, the interstory drift and the damage distribution became more balanced while the overall damage decreased by approximately 30%.

CHAPTER 7

SEISMIC DESIGN FOR A TARGET DRIFT

7.1. Introduction

In the previous chapter, the proportioning of the frame members was performed to satisfy the predefined periods. These periods were selected to be longer than the expected periods. The purpose was to increase the displacement demand and observe the effectiveness of the proposed design procedure at high demand levels. In this chapter, the design will start with a predefined drift target rather than a period. For this purpose, the relationship between the period of the building and its maximum drift response is used. Ten-story frames were used to illustrate the procedure and results investigated. Frames consist of a *conventional* and a *proposed* frame, as similar to the description in Chapter 6. The proposed seismic design procedure was applied to the proposed frame. The results of the analyses are compared with those of the 10-story frame designed in Section 6.3. In order to investigate whether the success of the proposed iterative procedure is dependent on the performed manipulation of the modal vectors of the elastic structure (as defined in Chapter 3) or not, the iterative procedure is also applied to a conventional frame.

7.2. Design of a Ten-Story Three-Bay Frame under Seismic Demands for a Target Drift

The seismic designs of two 10-story 3-bay frames were performed for a predefined target drift. One of the frames (conventional frame) was designed using conventional methods as per TEC2018. The other frame (proposed frame) was designed using the proposed seismic design procedure. Figure 167 shows the flowchart used for this design. All geometric and material properties of the frames kept the same as those of the 10-story frames used in Section 6.3. The story height is 3.0 meters, and the bay widths are 5.0 meters for both frames.

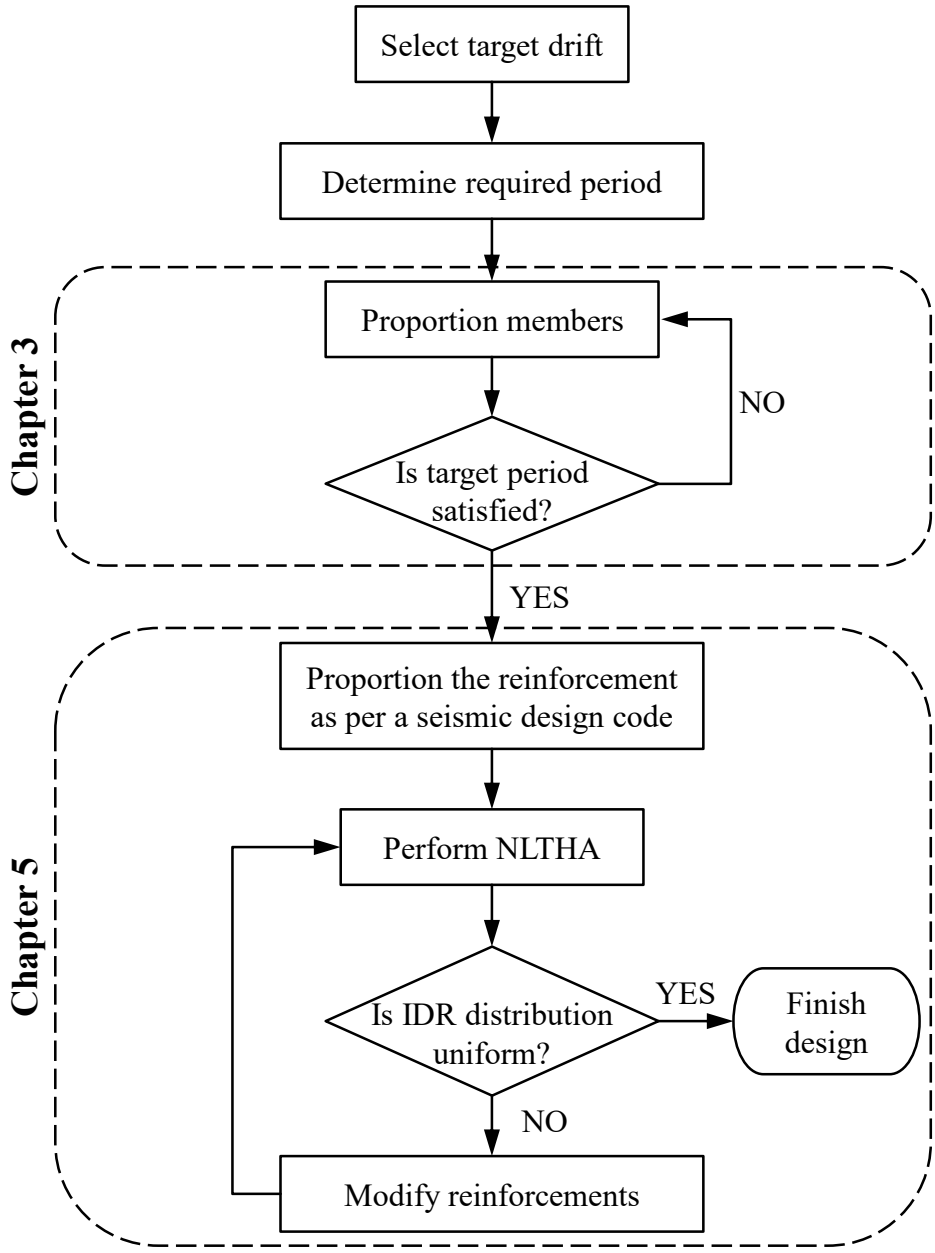

Figure 167. Flowchart of the proposed seismic design procedure for a target drift

7.2.1. Selecting the Target Period for a Target Drift

Newmark et al. (1973) observed that the effective ground motion parameter, whether it is acceleration, velocity, or displacement, of a single-degree-of-freedom system for a given earthquake is dependent on its period. Based on this observation, the response for a given damping factor is represented by idealizing the response spectra in three regions: nearly constant displacement, velocity, and acceleration. It appears that by using this idealization, the maximum displacement of a system with a given period and damping can be estimated for a particular site. Shimazaki and Sozen (1984)

proposed that the maximum nonlinear drift response of reinforced concrete structures with periods (T) exceeding the nearly constant acceleration region may be estimated using the effective period, $\sqrt{2}T$, and an idealized linear displacement response spectrum for 2% damping factor. Lepage (1997) extended the method so as to be used for the entire period range. The maximum drift response, *MDR*, of reinforced concrete structures can be estimated using Equation (7.1) which is based on the idealized displacement response spectrum defined by Lepage (1997). See Section 3.4.2 for further details about the idealized displacement response spectrum.

$$MDR = \gamma \cdot c \cdot \sqrt{2} \cdot T \tag{7.1}$$

In Equation (7.1), γ is the participation factor of the considered mode, c is the slope of the idealized displacement response spectrum, and T is the building period calculated based on the gross flexural stiffnesses of the members. Here, the parameter c is calculated using Equation (3.18). A reasonable value for the parameter γ was proposed as 1.25 by Lepage (1997).

Equation (7.1) can be rearranged to estimate the fundamental period of a structure for a prescribed drift limit as in Equation (7.2).

$$T \leq \frac{MDR}{\gamma \cdot c \cdot \sqrt{2}} \tag{7.2}$$

For the frame considered in this case study, the maximum drift target was selected as 1.5% of the building height. For the selected ground motion set (Section 5.4.3), the parameter c was calculated for each record, initially. Then, the one, which gives the closest idealized displacement response spectrum to the mean displacement response spectrum of the scaled records, was selected. According to this, the idealized displacement response spectrum obtained using the RSN316 record was used to calculate the parameter c where T_g and α for this record is 0.66 seconds and 0.35g, respectively.

$$c = \frac{(3.75) \cdot (0.35) \cdot 9810 \cdot (0.66)}{(2\pi)^2} = 215 \text{ (mm)} \tag{7.3}$$

Figure 168 shows the displacement response spectra of the scaled ground motions set for a 2% damping ratio and the idealized displacement response spectrum calculated based on RSN316.

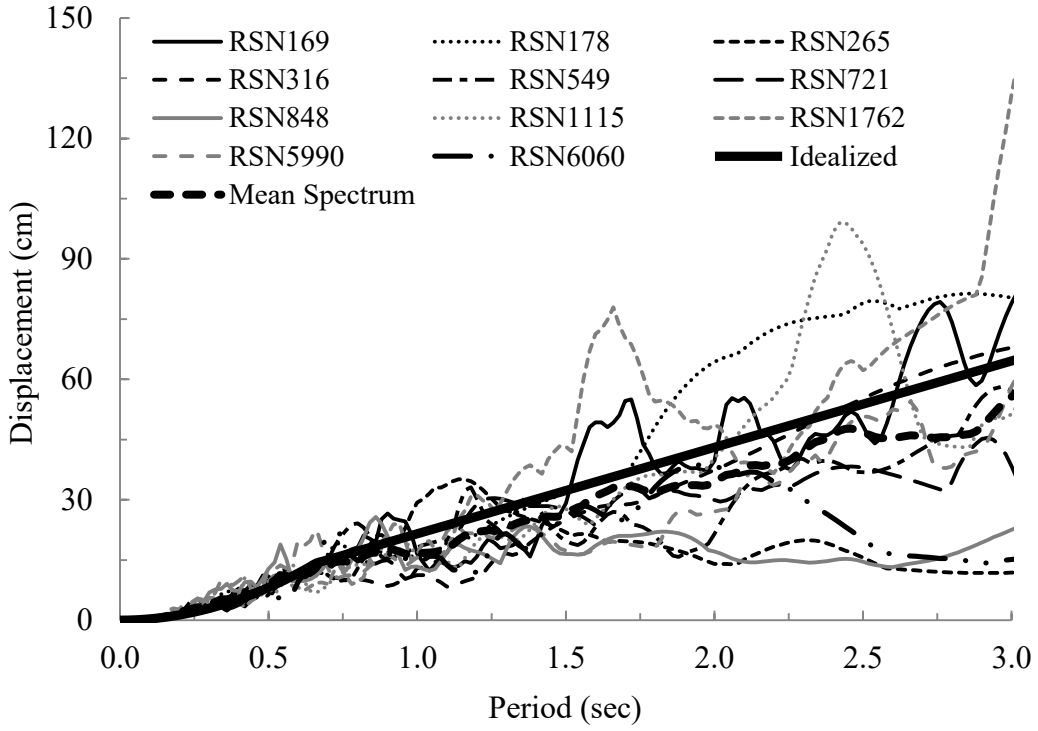

Figure 168. Displacement response spectra for scaled ground motions and idealized displacement response spectrum based on RSN316

For the selected drift target, the target period can be calculated from Equation (7.2) as

$$T = \frac{(0.015)\cdot(30{,}000\text{ mm})}{(1.25)\cdot 215\cdot\sqrt{2}} = 1.18\text{ s} \tag{7.4}$$

Since the fundamental period for the frames in this chapter are shorter than that of the 10-story frames in the previous chapter (T=1.4 s), the former will be labeled as *short-period frames*, while the latter will be labeled as *long-period frames* for the comparisons.

It should be noted that this method is not the only way to estimate the expected spectral displacement. It could be estimated using other approaches in the literature.

7.2.2. Proportioning the Member Cross-sections

The member cross-sections were determined to satisfy the target fundamental period. In the conventional frame, the same beam sizes were used at all stories. In the proposed frame, the member sizes were determined using the proposed primary design procedure in Chapter 3. The limitations of TEC2018 were checked for minimum member dimensions, as well as for the allowed axial load levels for the columns. The member cross-section dimensions for the conventional and the proposed frame are summarized in Table 35. Based on the selected member sizes, the fundamental periods were calculated as 1.1 seconds for both frames. The fundamental periods of both frames based on the effective flexural stiffnesses were calculated as 1.5 seconds.

Table 35. Member cross-section dimensions for the frames (width×height in cm)

	Conventional Frame		**Proposed Frame**	
Story	**Columns**	**Beams**	**Columns**	**Beams**
10	60×60	30×55	60×60	20×45
9	60×60	30×55	60×60	25×45
8	70×70	30×55	70×70	25×50
7	70×70	30×55	70×70	30×50
6	80×80	30×55	80×80	30×55
5	80×80	30×55	80×80	30×55
4	80×80	30×55	80×80	30×60
3	90×90	30×55	90×90	30×60
2	90×90	30×55	90×90	30×60
1	90×90	30×55	90×90	30×60

7.2.3. Seismic Design

The initial seismic design of the frames was performed as described in Section 6.2.2. Table 36 shows the design moments (M_d), tension reinforcement ratios (ρ), provided moment capacities (M_r) for the beam end-sections of the conventional and the proposed frame along with the cross-section dimensions. Since the fundamental periods and the masses of both frames are equal, the design lateral loads and the resulting design moments are quite similar to each other. Note that, half the amount of the tension

reinforcement was provided as the compression reinforcement at all sections. In addition, beams of the same story have the same reinforcements. All reinforcement ratios were checked against TEC2018 limitations.

Table 36. Cross-section dimensions, design moments, tension reinforcement ratios, and provided moment capacities for beams

Story	Conventional Frame				Proposed Frame			
	$b \times h$ (cm)	M_d (kN·m)	ρ (%)	M_r (kN·m)	$b \times h$ (cm)	M_d (kN·m)	ρ (%)	M_r (kN·m)
10	30×55	82	0.3	97	20×45	78	0.9	89
9	30×55	125	0.5	145	25×45	115	0.9	130
8	30×55	131	0.5	145	25×50	142	0.8	164
7	30×55	168	0.7	204	30×50	160	0.8	183
6	30×55	185	0.7	204	30×55	189	0.8	225
5	30×55	193	0.8	225	30×55	188	0.7	225
4	30×55	196	0.8	225	30×60	214	0.7	248
3	30×55	190	0.8	225	30×60	202	0.7	224
2	30×55	174	0.7	204	30×60	185	0.7	224
1	30×55	136	0.6	164	30×60	144	0.5	160

It has to be noted that, in TEC2018, the total equivalent lateral load, V_{tE}, for the seismic design is calculated as the maximum of the two expressions below.

$$V_{tE} = \max \begin{cases} m_t \, S_{aR} \, T_P \\ 0.04 m_t \, I \, S_{DS} \, g \end{cases} \tag{7.5}$$

where m_t is the total mass of the building, S_{aR} is the reduced design spectral acceleration, T_P is the fundamental period of the building, I is the building importance factor, S_{DS} is the spectral acceleration for the short period region, g is the acceleration of gravity.

In the previous chapter, for the long-period 10-story frames, the total base shear was calculated from the second expression, since its result was greater than the first expression for both frames. Similarly, for the frames considered here, the second expression results in greater than the first expression, as well. In addition, since the

second expression is independent of the building period, the total equivalent lateral load is equal for both the long-period and the short-period frames. Therefore, the design moments and the provided moment capacities for the considered frames are not very different from those of the long-period frames for the initial designs.

For the columns of both frames, the minimum reinforcement ratio, 1%, governed the design. Therefore, steel reinforcement that provides a 1% ratio was provided at all columns. Based on the proportioning of the frame members, column-to-beam strength ratios (the ratio of the sum of moment capacities of all columns to the sum of moment capacities of beams at a joint), β, at all joints were calculated. Table 37 shows the β values at the internal and external joints for both frames.

Table 37. Column-to-beam strength ratios at the joints, β, for both frames

	Conventional Frame		**Proposed Frame**	
Story	**External Joint**	**Internal Joint**	**External Joint**	**Internal Joint**
10	4.1	2.9	3.8	2.6
9	5.9	4.2	5.3	3.7
8	6.1	4.4	6.9	5.0
7	6.7	4.9	6.0	4.4
6	6.6	5.0	7.3	5.5
5	7.8	6.0	8.7	6.0
4	7.4	5.7	8.2	6.3
3	9.7	7.5	9.7	7.5
2	11.2	8.7	12.3	9.6
1	16.2	12.7	15.8	12.4

It can be seen that the β values of these frames are significantly larger than those of the long-period frames. This situation is a consequence of two different factors: The first factor is the column moment capacities. The minimum allowable reinforcement ratio governs the design of the columns in both cases. Since the columns of the short-period frames are larger than those of the long-period frames, 1% of longitudinal reinforcement provides significantly higher moment capacities. The second factor is the beam moment capacities. As mentioned above, beam design moments are quite similar to each other in both cases. Therefore, TEC2018 design procedure resulted in short-period frames with “stronger” columns compared to the long-period frames, while the

beam strengths are similar for both cases. Consequently, the β values are considerably larger in this case study.

7.2.4. Numerical Model and Strong Ground Motion Set

The frames were modeled in the OpenSees platform as described in Section 5.4.2. For these frames, a 2% damping ratio was assigned to the first mode, and the mode at which the cumulative mass participation exceeds 95%.

The same ground motion set that is described in Section 5.4.3, was used for the nonlinear time-history analyses of the frames.

7.2.5. Linear Time-History Analyses

Initially, two designs were subjected to the scaled ground motion records using elastic section properties to observe the linear drift behavior. Figure 169 and Figure 170 shows the envelope interstory drift ratios for each ground motion (GM) record, as well as the means of the distributions for the conventional and the proposed frames, respectively. In addition, the mean results for the long-period frames are shown with a thick grey line for comparison purposes. Figure 171 compares the mean envelope interstory drift ratios of the frames.

As it can be observed from the figures, both frames had lower envelope interstory drifts ratios compared to the long-period frame. The interstory drift ratios are concentrated at the lower parts of the conventional frame, while they increased towards the top at the proposed frame. The COVs of the envelope interstory drifts for both frames are 0.18. The maximum envelope interstory drift ratio of the conventional frame was observed at the fourth story as 2.0%. For the proposed frame, it is observed as 2.4% at the ninth story.

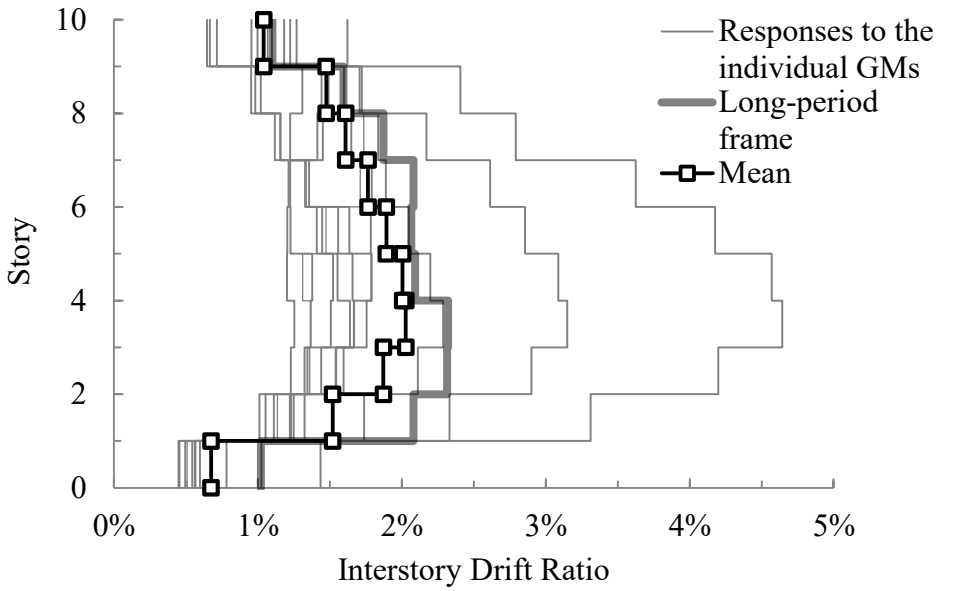

Figure 169. Envelope interstory drift ratios of conventional frame for linear case

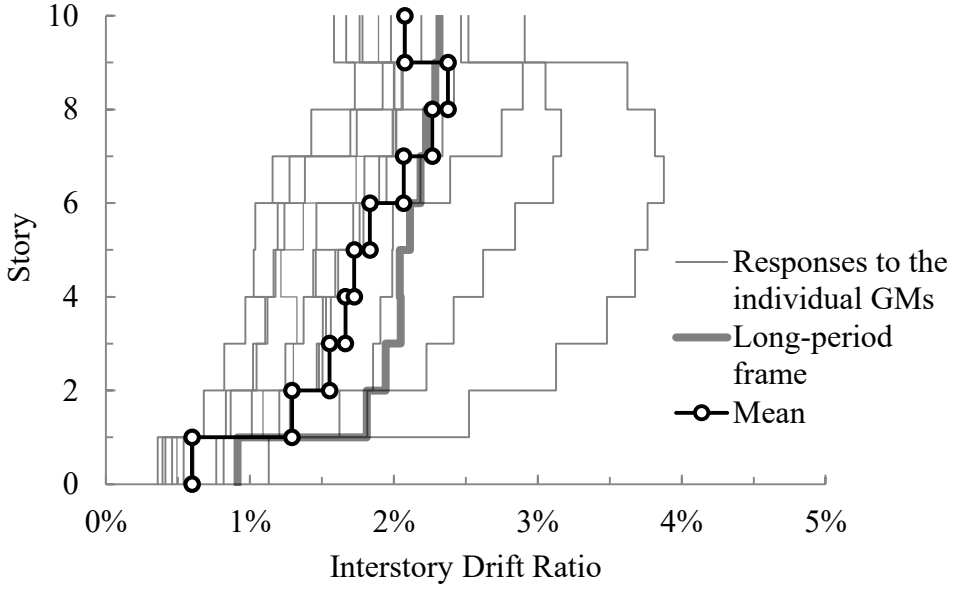

Figure 170. Envelope interstory drift ratios of proposed frame for linear case

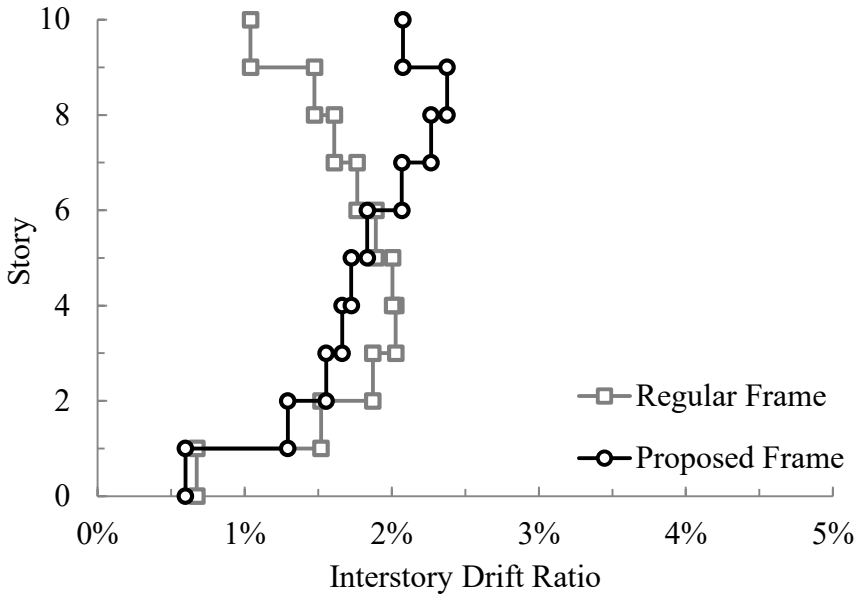

Figure 171. Comparison of mean envelope interstory drift distributions for linear case

Figure 172 shows the maximum roof drift ratios for individual ground motions. The average maximum roof drift ratio is 1.41% and 1.50% for the conventional and the proposed frame, respectively. Those were 1.51% and 1.66% for the long-period conventional and proposed frames, respectively.

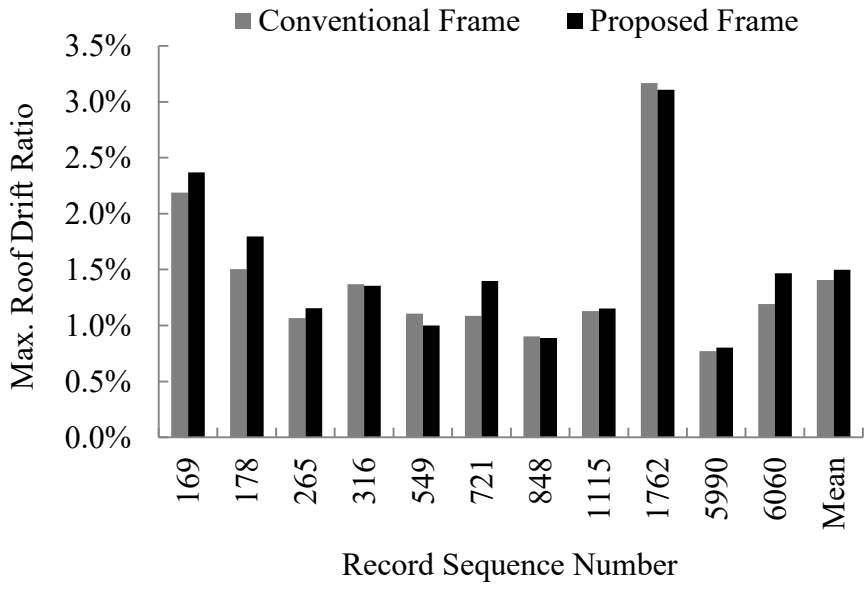

Figure 172. Maximum roof drift ratios for individual ground motion records in linear case

7.2.6. Nonlinear Time-History Analyses

The proposed frame considered in this chapter required one design revision to obtain a uniform interstory drift distribution. Therefore, discussion will contain the results of two nonlinear time-history runs carried out for the proposed frame. The results of each run are given together in this section. As in previous case studies, the target maximum plastic rotation for the beam-ends was taken as 0.01 radians.

The provided reinforcement ratios and the moment capacities of the beam-ends for each design are given in Table 38. Note that, half the amount of the tension reinforcement was provided as the compression reinforcement at all beam end-sections. In addition, all beams at the same story have the same reinforcements. The reinforcement ratios of the columns for each design are presented in Table 39. The underlined numbers in this table indicate that the reinforcements of the corresponding columns should have been decreased, but this could not be done due to the minimum allowable reinforcement ratio limit. All reinforcement ratios were checked against TEC2018 limitations. Table 40 presents the column-to-beam strength ratios, β, at all external and internal joints for all designs.

Table 38. Provided reinforcement ratios and moment capacities of the beams for all designs

Story	Conventional		Proposed (Run #1)		Proposed (Run #2)	
	ρ (%)	M_r (kN·m)	ρ (%)	M_r (kN·m)	ρ (%)	M_r (kN·m)
10	0.3	97	0.9	89	1.5	176
9	0.5	145	0.9	130	1.9	272
8	0.5	145	0.8	164	1.5	285
7	0.7	204	0.8	183	1.4	311
6	0.7	204	0.8	225	1.2	321
5	0.8	225	0.7	225	1.1	296
4	0.8	225	0.7	248	0.9	285
3	0.8	225	0.7	224	0.6	196
2	0.7	204	0.7	224	0.5	157
1	0.6	164	0.5	160	0.3	93

Table 39. Provided reinforcement of the columns for all designs

Story	Reinforcement Ratio (%)		
	Conventional	Proposed (Run #1)	Proposed (Run #2)
10	1.0	1.0	3.6
9	1.0	1.0	3.6
8	1.0	1.0	3.3
7	1.0	1.0	3.0
6	1.0	1.0	2.3
5	1.0	1.0	2.0
4	1.0	1.0	1.1
3	1.0	1.0	1.0
2	1.0	1.0	1.0
1	1.0	1.0	1.0

Table 40. Column-to-beam strength ratios at the joints, β, for all designs

Story	Conventional		Proposed (Run #1)		Proposed (Run #2)	
	β_{ext}	β_{int}	β_{ext}	β_{int}	β_{ext}	β_{int}
10	4.1	2.9	3.8	2.6	3.6	2.4
9	5.9	4.2	5.3	3.7	4.7	3.2
8	6.1	4.4	6.9	5.0	5.5	3.8
7	6.7	4.9	6.0	4.4	5.9	4.1
6	6.6	5.0	7.3	5.5	6.3	4.6
5	7.8	6.0	8.7	6.0	7.5	5.5
4	7.4	5.7	8.2	6.3	7.3	5.4
3	9.7	7.5	9.7	7.5	11.2	8.5
2	11.2	8.7	12.3	9.6	15.9	12.2
1	16.2	12.7	15.8	12.4	27.9	21.1

The results of the nonlinear time-history analyses are presented in terms of the individual and the mean envelope interstory drift distributions in Figure 173 for all designs. In addition, the mean results for the long-period frames are shown with a thick

grey line for comparison purposes. Figure 174 compares the mean envelope interstory drift distribution of the final design with the initial designs. Figure 175 shows the change in the COV of the envelope interstory drift distributions.

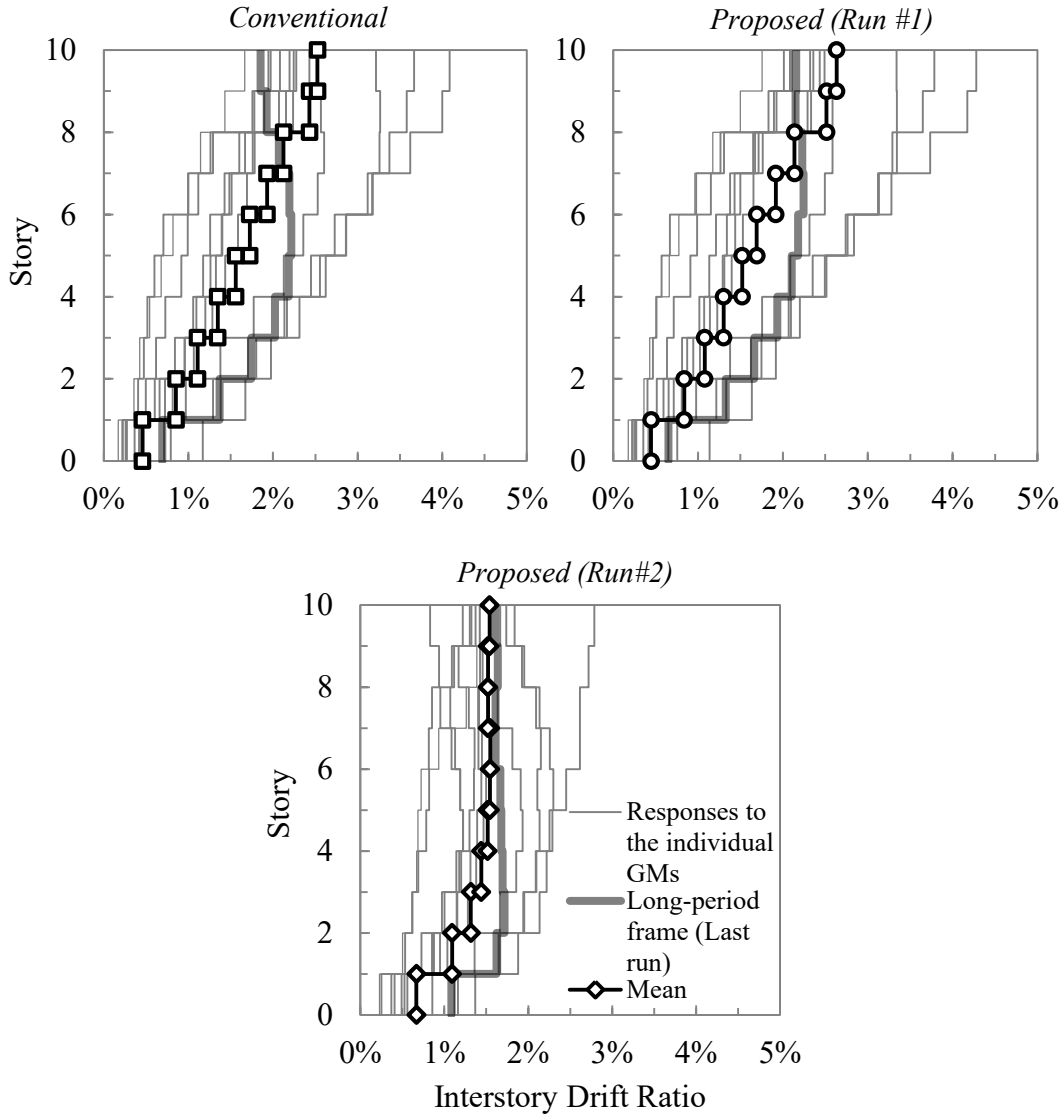

Figure 173. Envelope interstory drift distributions of all designs

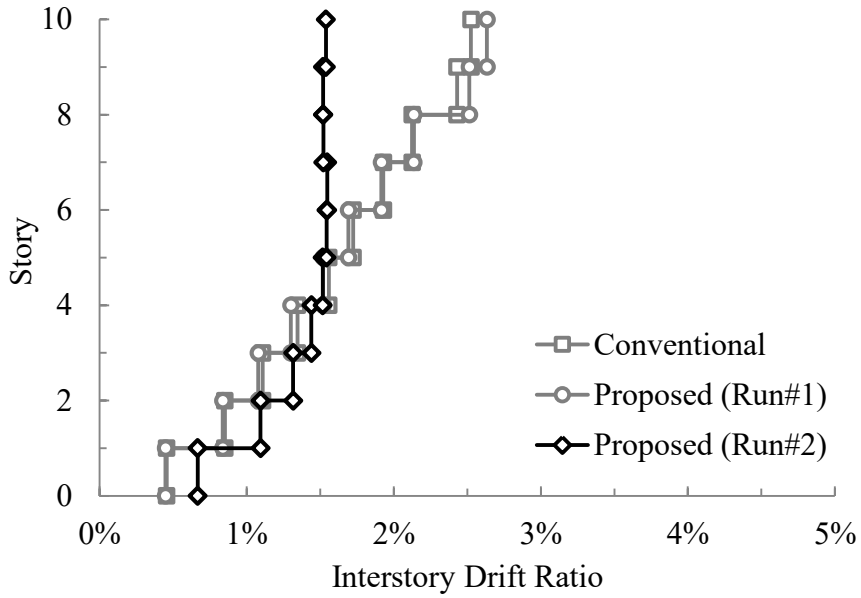

Figure 174. Comparison of mean envelope interstory drifts for initial designs and final design

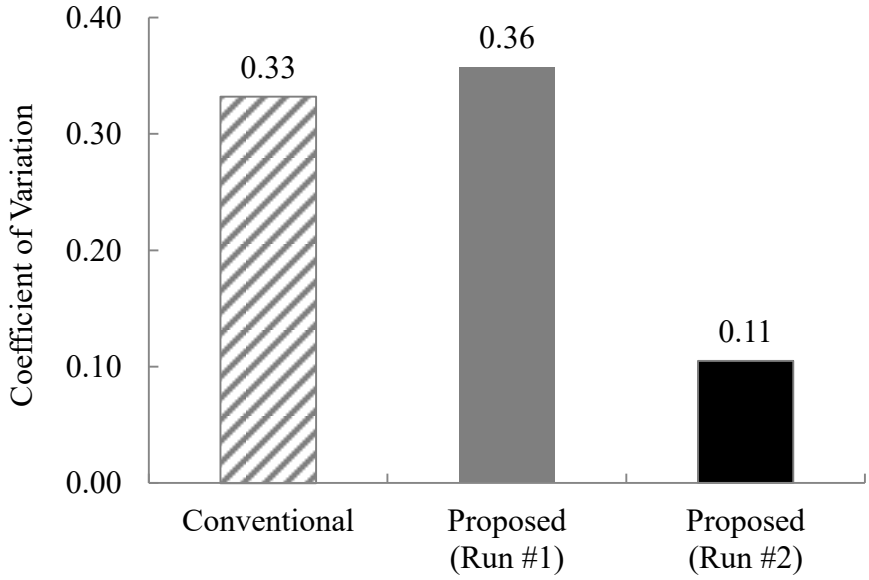

Figure 175. Coefficient of variations of envelope interstory drift distributions for all designs

It can be observed that the short-period frames had significantly lower interstory drifts at the lower two-thirds of their heights compared to the corresponding long-period frames. It can also be seen that the proposed frame had a nearly uniform interstory drift distribution after a single design iteration. The COV of the envelope interstory drift distributions decreased by 70% compared to the initial proposed design. In the final

design, the interstory drifts of the lower four stories are increasingly lower than the upper portion of the frame since the column reinforcements could not be decreased due to the code limitations although they had to be for keeping the ratio in the original proposal. However, this condition is beneficial for the frame since it limits the damage in the lower stories, as well as the roof drift. The maximum envelope drift was reduced from 2.6% to 1.5% (i.e. by 40%) in the final design.

Figure 176 shows the maximum roof drift ratios at all ground motions, as well as the means, for all designs.

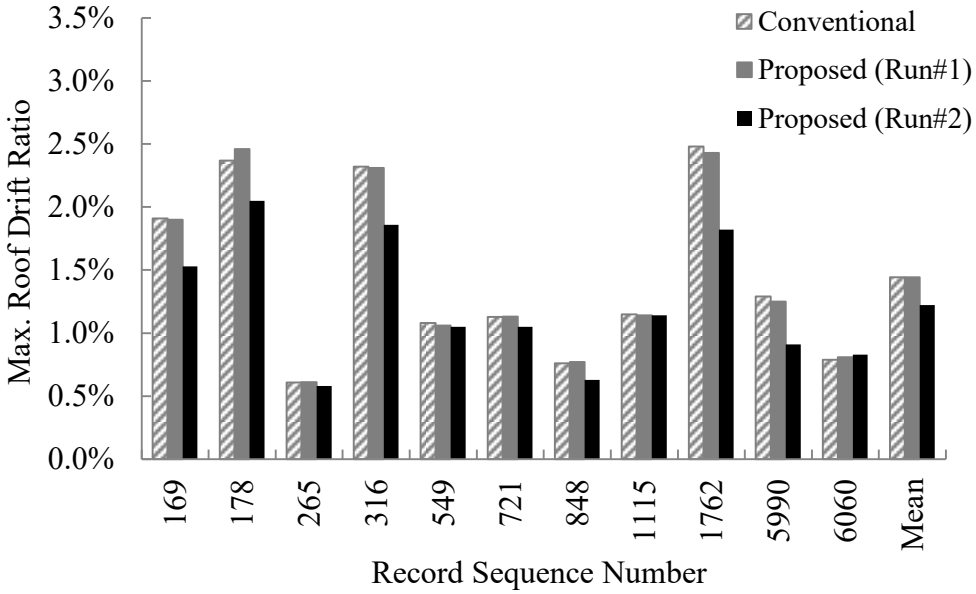

Figure 176. Maximum roof drift ratios at individual ground motions for all designs

It can be seen that the mean maximum roof drift ratio is below the target drift ratio, 1.5%, for all designs. In the final design, it decreased by 15% compared to the first run and became 1.22%. It is 10% lower than that of the long-period frame.

The total dissipated hysteretic energy at each ground motion for all designs are shown in Figure 177. As in the previous case studies, the hysteretic energy demand does not change significantly between the design iterations. In addition, the demand is almost the same as the long-period frames.

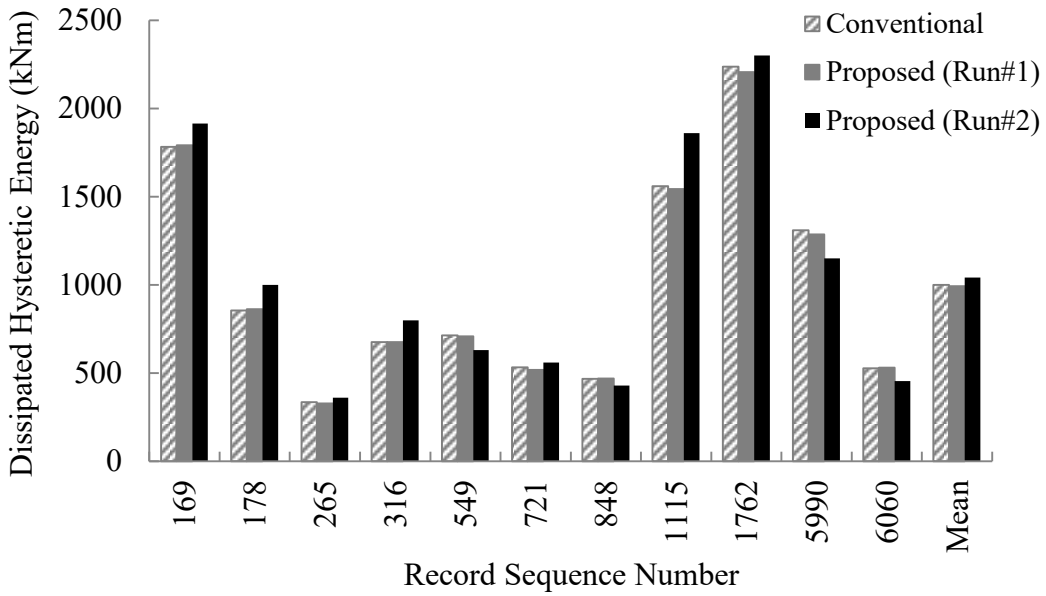

Figure 177. Total dissipated hysteretic energy at individual ground motions for all designs

The story damage indices for individual ground motion records, as well as the mean story damage indices for all designs, are given in Figure 178. In addition, the mean results for the corresponding designs of the long-period frames are shown with a thick grey line for comparison purposes. Note that, the final design for the long-period frame corresponds to Run #4. Figure 179 compares the mean story damage indices of all designs.

As it can be observed from Figure 178, the initial designs experienced more damage at their upper halves, compared to the long-period frames. The damage levels at those stories indicate that those stories suffered severe damage during the design-level earthquake. The final design experienced more damage at all stories except the first two, when compared to the final design of the long-period frame, as well. However, all stories sustained slight damage.

From Figure 179, it can be observed that, in the final design, the extensive damage of the upper stories was reduced effectively. At the same time, the damage distribution became quite balanced throughout the height. The maximum mean story damage index for the final design is 0.36, while the minimum is 0.17.

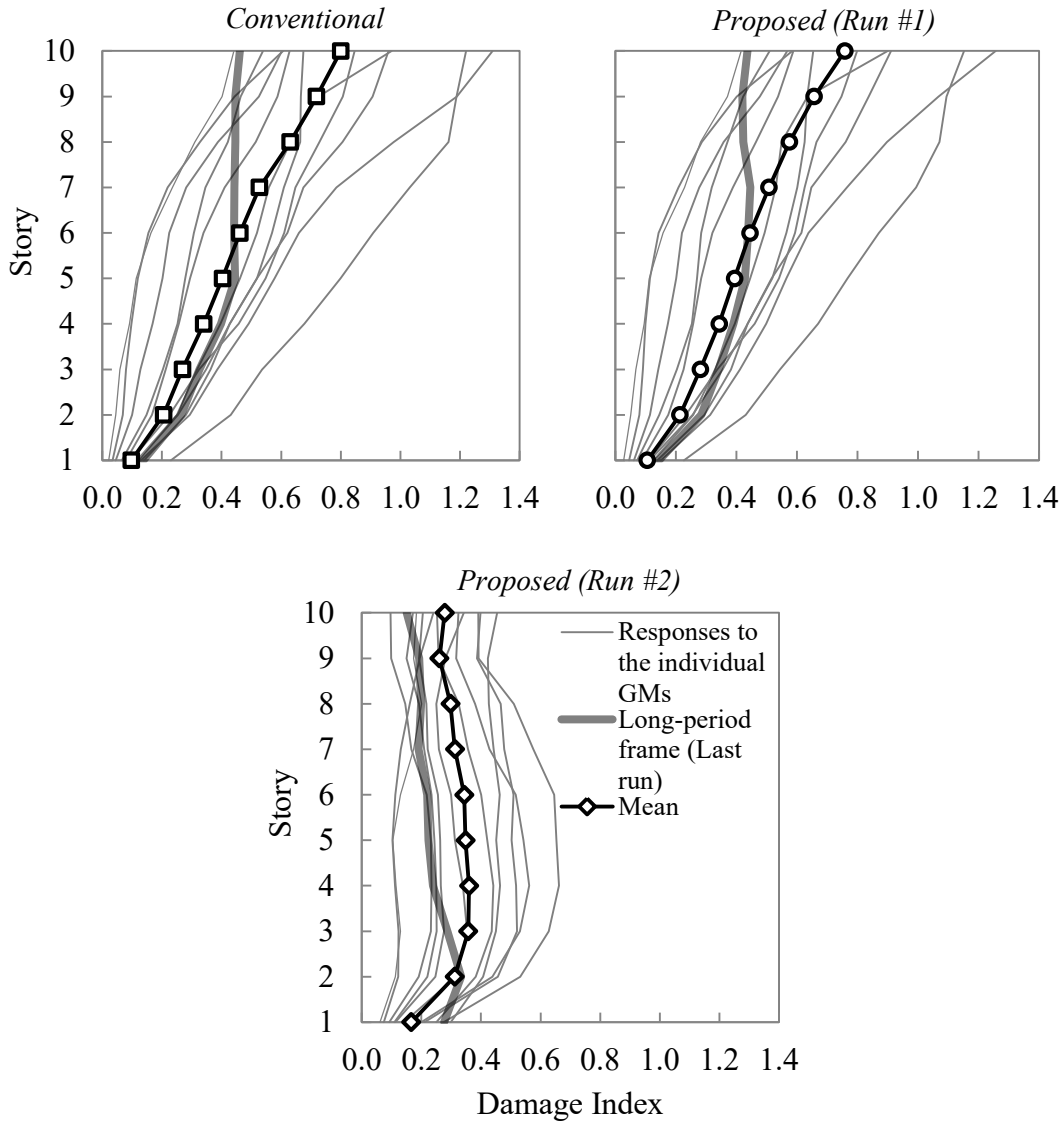

Figure 178. Story damage indices of all designs

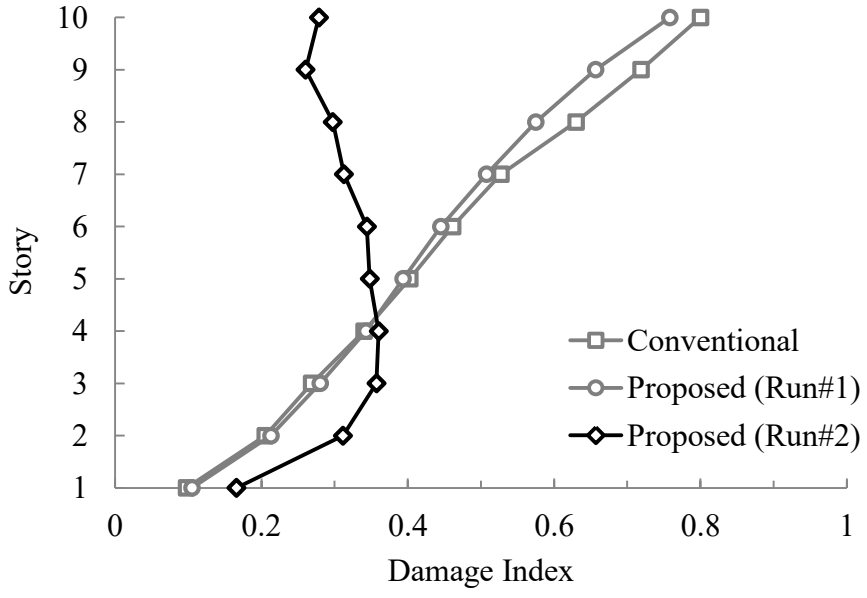

Figure 179. Comparison of story damage indices for all designs

Figure 180 shows the mean overall damage indices for all designs. The mean overall damage was reduced by 33% in the revised design by both increasing the strength of the members and shifting the demands to the stories with more energy dissipation capacity.

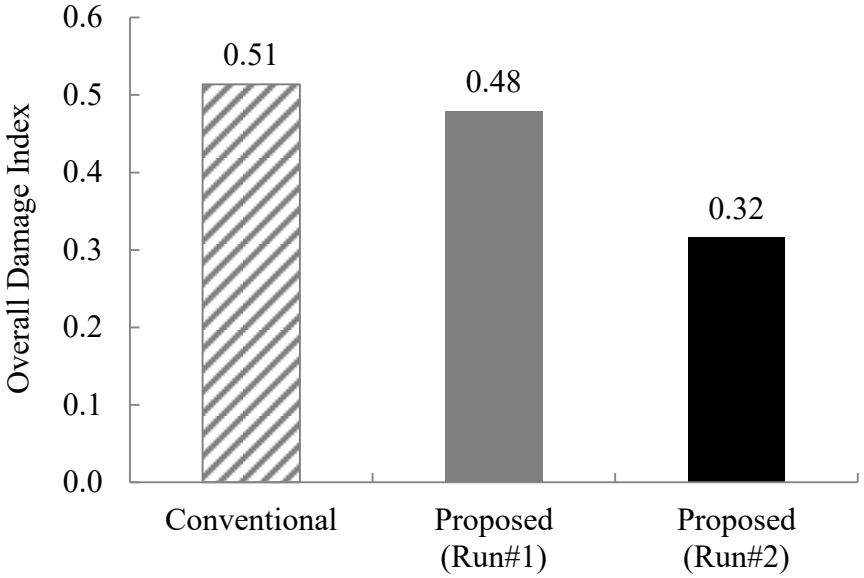

Figure 180. Mean overall damage indices for all designs

The means of the maximum plastic rotations attained at the end-sections of the beams and columns are given in Figure 181 for all designs. As it can be observed from the figure, the mean maximum plastic rotations at the beam-ends are close to the target maximum plastic rotation (0.01 rad) for the final design. The excessive plastic rotations at the upper story beams were successfully reduced in the revised design.

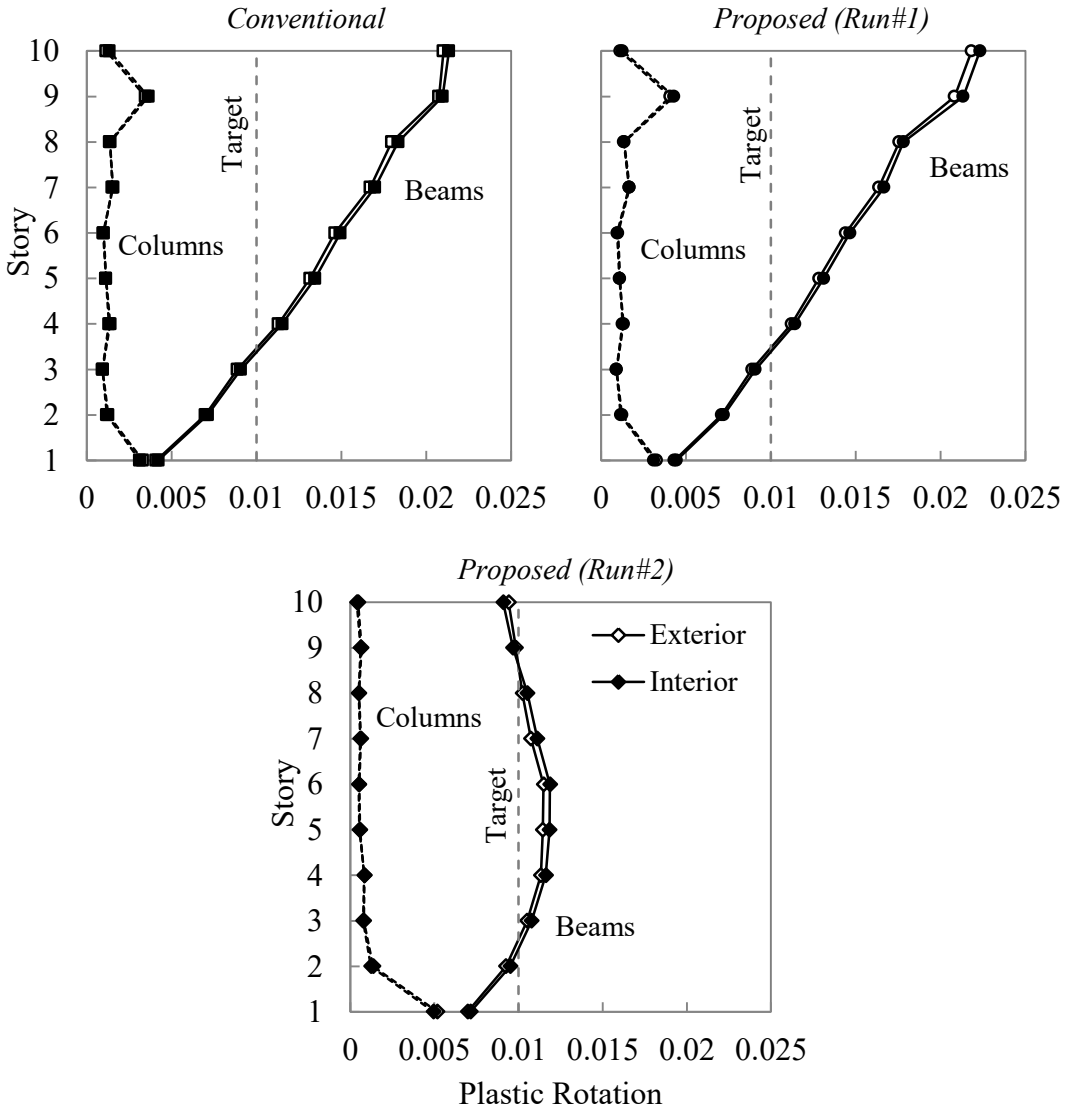

Figure 181. Mean maximum plastic rotations at columns and beams for all designs

All results are summarized from Figure 182 to Figure 184 for each design, respectively. These figures help show the relationship between the distribution of the plastic rotations, interstory drifts, and the story damage throughout the building height.

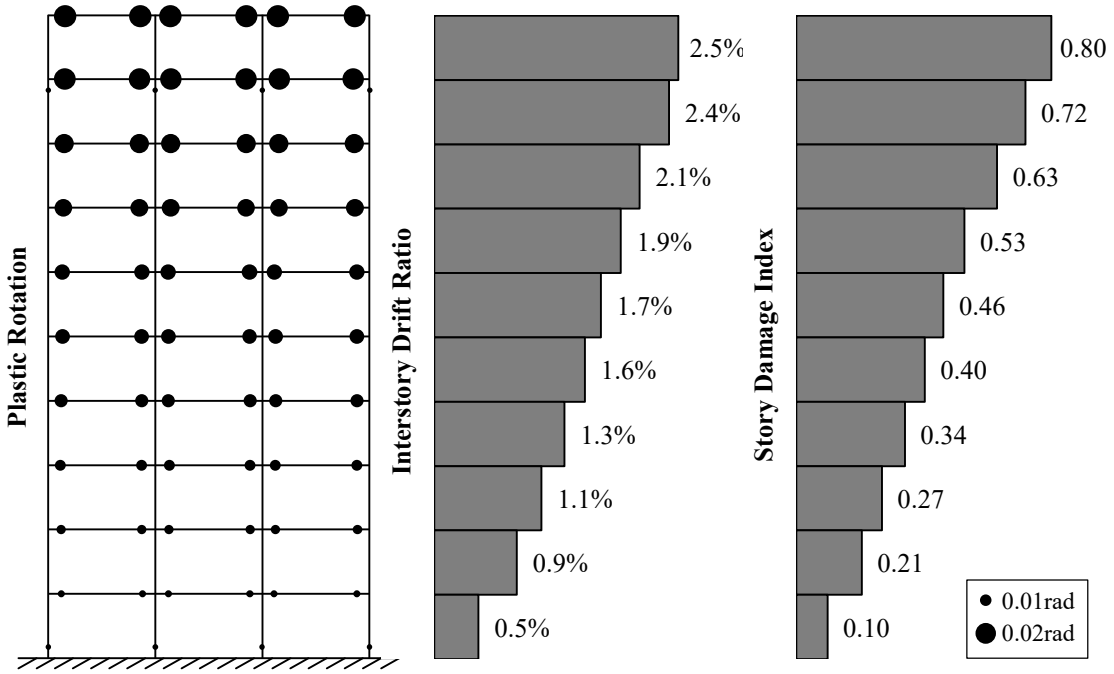

Figure 182. Summary of results for conventional frame

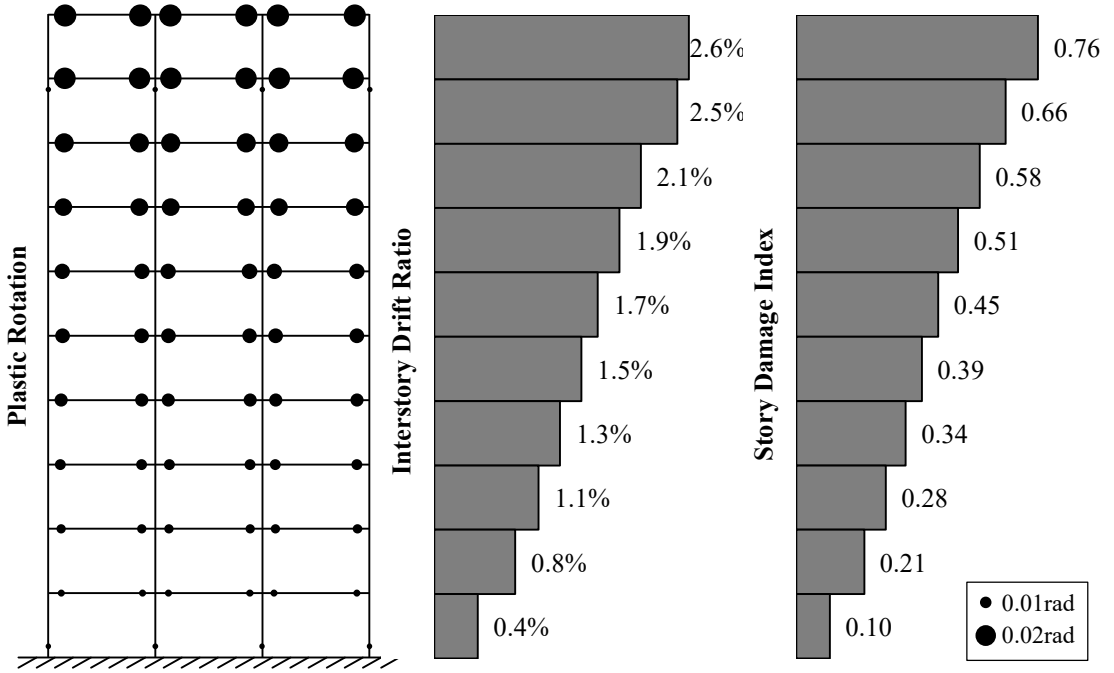

Figure 183. Summary of results for proposed frame (Run #1)

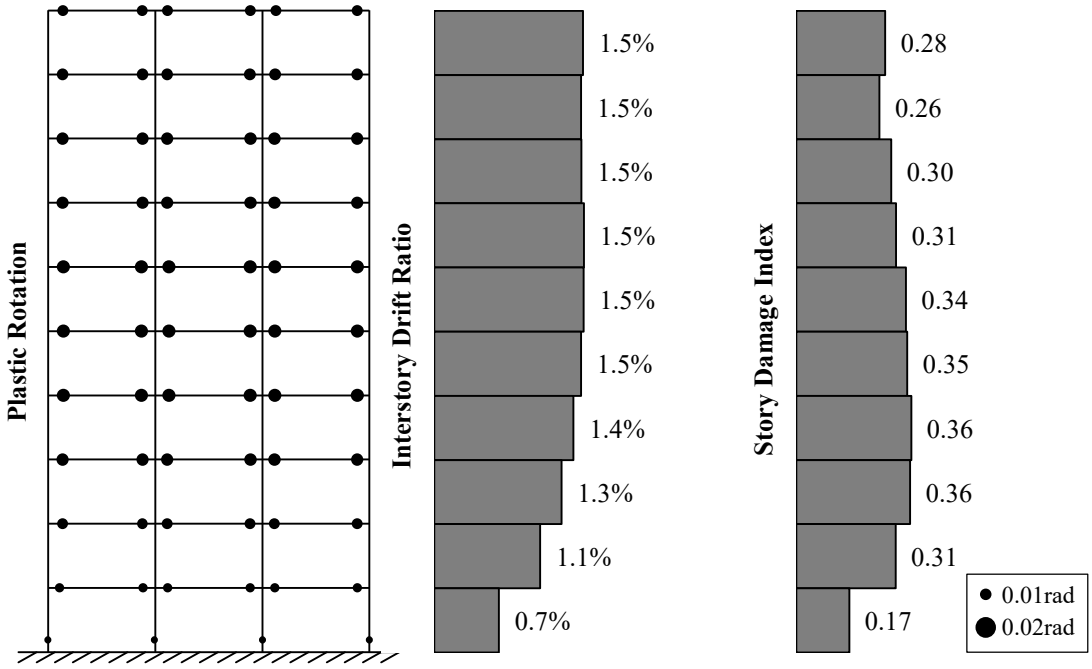

Figure 184. Summary of results for proposed frame (Run #2)

Figure 185 shows the beam moment capacities for all designs. It can be seen that the moment capacities, which satisfy the code demands, are not sufficient to control the interstory drift and the damage distribution. The beam moment capacities for the final design of the long-period frame are also shown in the figure. The beam strengths at the short-period frame are lower compared to the long-period frame except the top three stories.

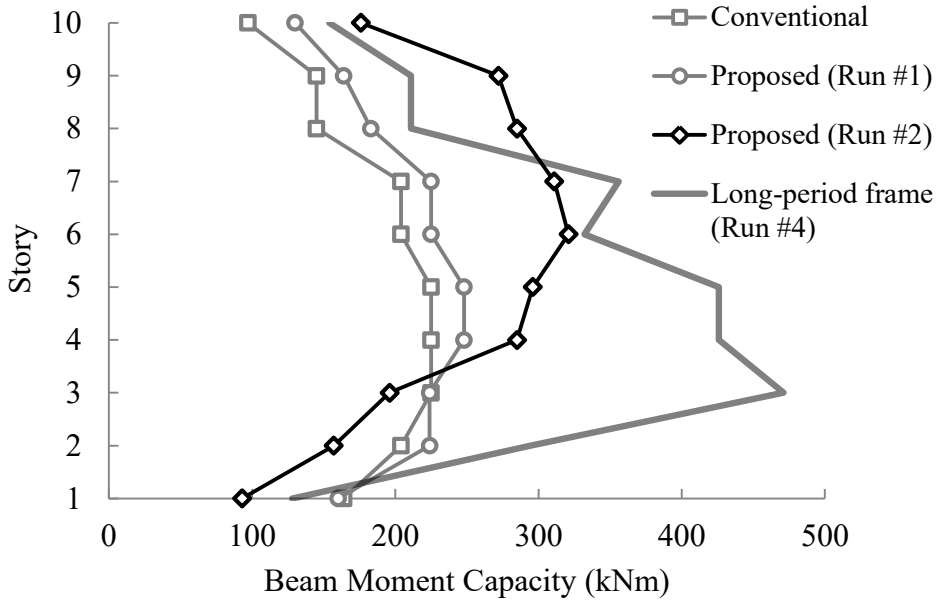

Figure 185. Beam moment capacities for all designs

7.2.6.1. Response at Various Levels of Ground Motions

In addition to the design-basis earthquake (DD2-level earthquake in TEC2018 − 10% probability of exceedance in 50 years), the initial designs and the final design were subjected to two additional levels of ground motions to observe the behavior under earthquakes of different intensities. For this purpose, the same ground motion set used in the previous case studies was separately scaled so as to satisfy the requirements of DD3- and DD4-level ground motions in TEC2018 for the selected location. These ground motion levels correspond to earthquakes with 72-year and 43-year return periods, respectively (i.e. 50% probability of exceedance in 50 years and 68% probability of exceedance in 50 years). The scale factors used to obtain the ground motion sets that satisfy the requirements for DD2-, DD3- and DD4-level acceleration response spectra are given in Table 41.

Table 41. Scale factors used to obtain ground motion sets for earthquakes of different levels

RSN	Earthquake Name	Station Name	DD-2 Scale Factor	DD-3 Scale Factor	DD-4 Scale Factor
169	Imperial Valley-06	Delta	1.90	0.94	0.75
178	Imperial Valley-06	El Centro Array #3	1.90	0.94	0.75
265	Victoria_ Mexico	Cerro Prieto	1.25	0.63	0.50
316	Westmorland	Parachute Test Site	1.50	0.75	0.60
549	Chalfant Valley-02	Bishop - LADWP South St	2.63	1.31	1.05
721	Superstition Hills-02	El Centro Imp. Co. Cent	1.44	0.72	0.58
848	Landers	Coolwater	2.00	1.00	0.80
1115	Kobe_ Japan	Sakai	2.75	1.38	1.10
1762	Hector Mine	Amboy	2.63	1.31	1.05
5990	El Mayor-Cucapah_ Mexico	El Centro Array #7	2.80	1.40	1.12
6060	Big Bear-01	North Palm Springs Fire Sta #36	2.75	1.38	1.10

The linear acceleration response spectra of the scaled ground motions, as well as the target mean spectra, are given in Figure 186 and Figure 187 for DD3 and DD4-level, respectively. Refer to Section 5.4.3 for further information about the ground motion records and the DD2-level spectra.

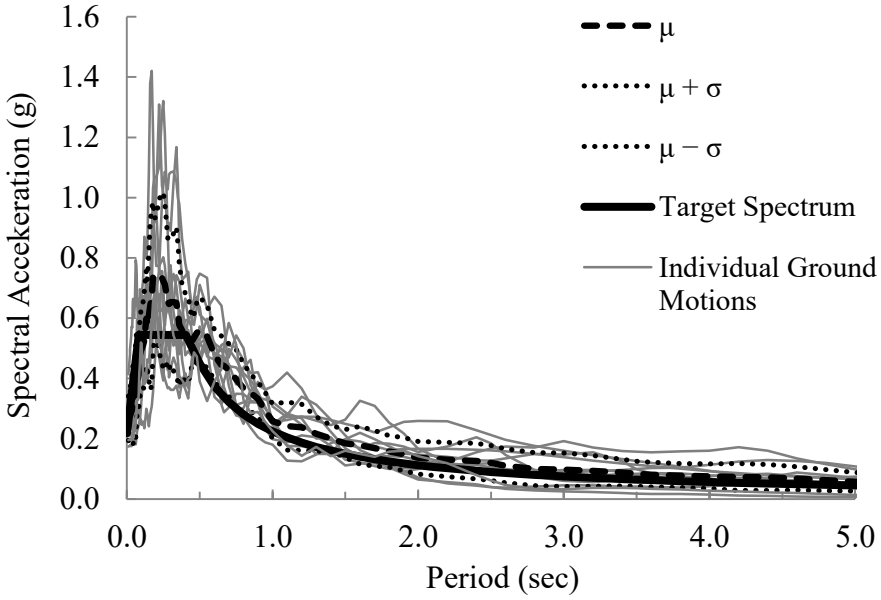

Figure 186. Linear acceleration response spectra for DD3-level earthquake

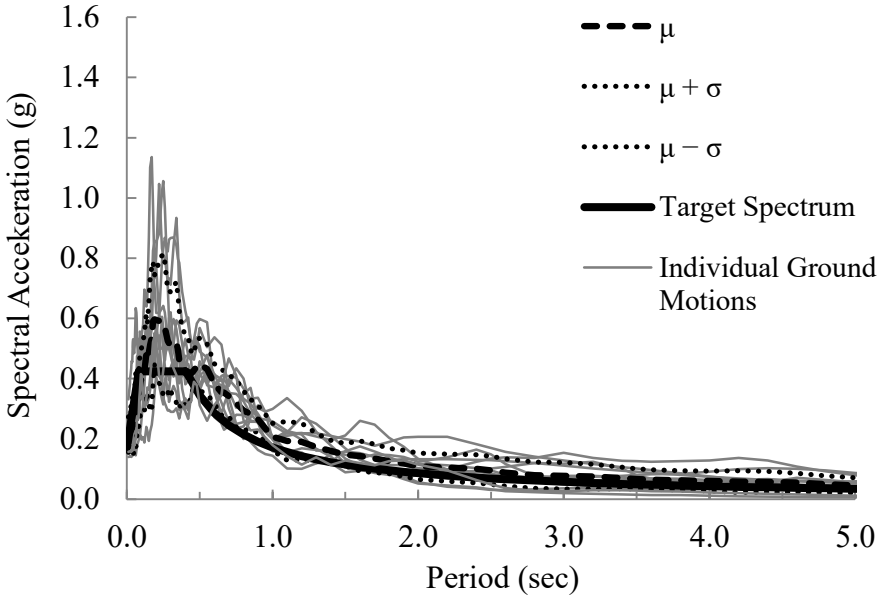

Figure 187. Linear acceleration response spectra for DD4-level earthquake

The mean envelope interstory drift ratios of the initial conventional and proposed designs, as well as those of the final design, are shown in Figure 188.

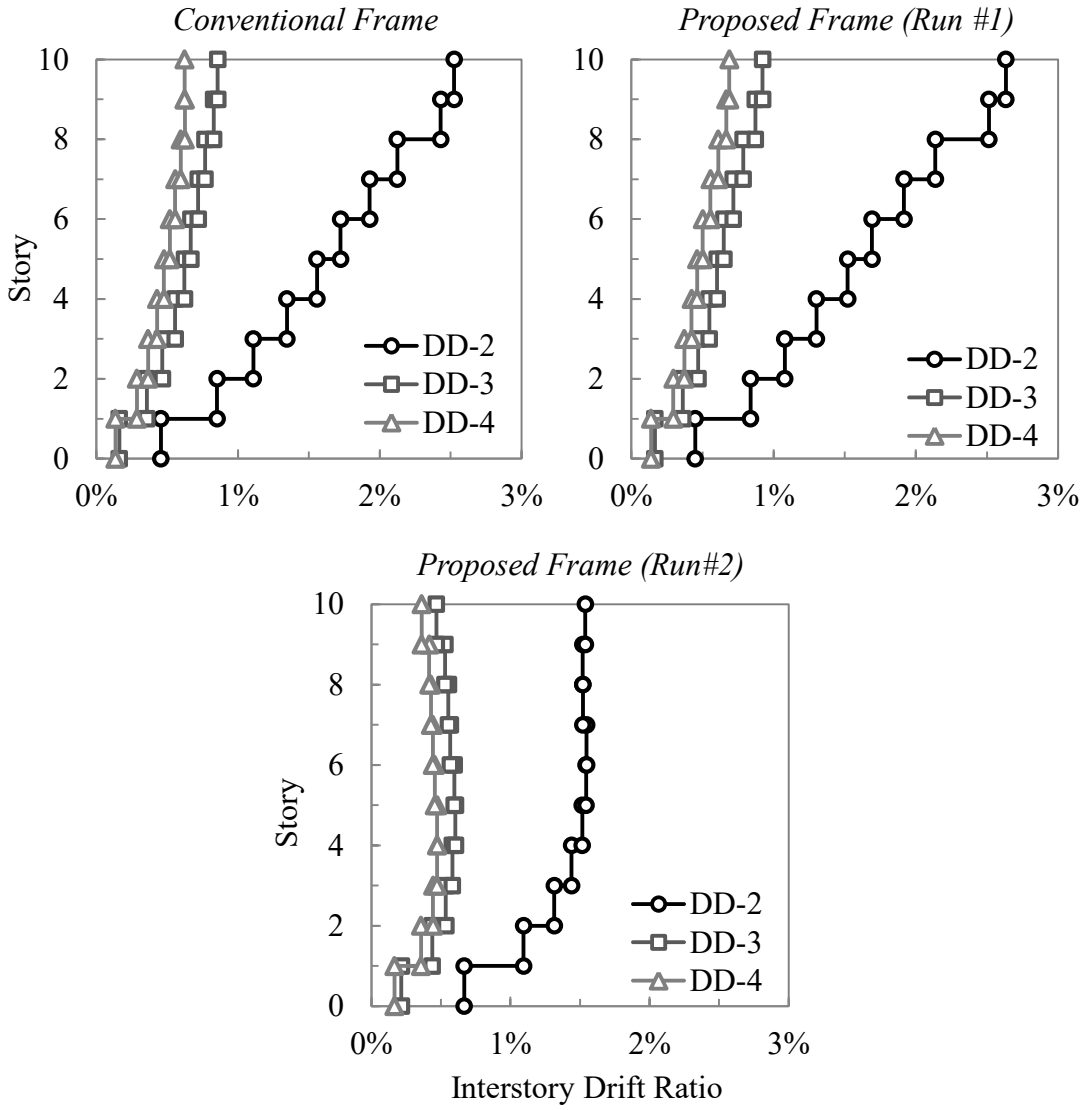

Figure 188. Mean envelope interstory drift ratios of all designs for DD2, DD3 and DD4-level earthquakes

The results show that the envelope interstory drifts of the final design are lower and more balanced for all levels of ground motions when compared to the initial designs. This result indicates that both the non-structural and the structural damage are lower and well-distributed in the final design. Furthermore, it can be seen that the envelope interstory drift distributions for all levels of ground motions are different from the linear case. It was observed that the yield rotation was exceeded at almost all beams for all levels due to high column-to-beam strength ratios. However, for DD2- and DD3-level ground motions, the plastic rotations were very limited and negligible.

Figure 189 shows the story damage indices of the initial conventional and proposed designs, as well as those of the final design. It can be seen that some damage

was observed during DD3- and DD4-level ground motions due to the limited plastic action in the beam-ends. However, these damage indices correspond to very slight damage levels according to the Park-Ang damage index. The final design has significantly balanced damage distribution in all cases.

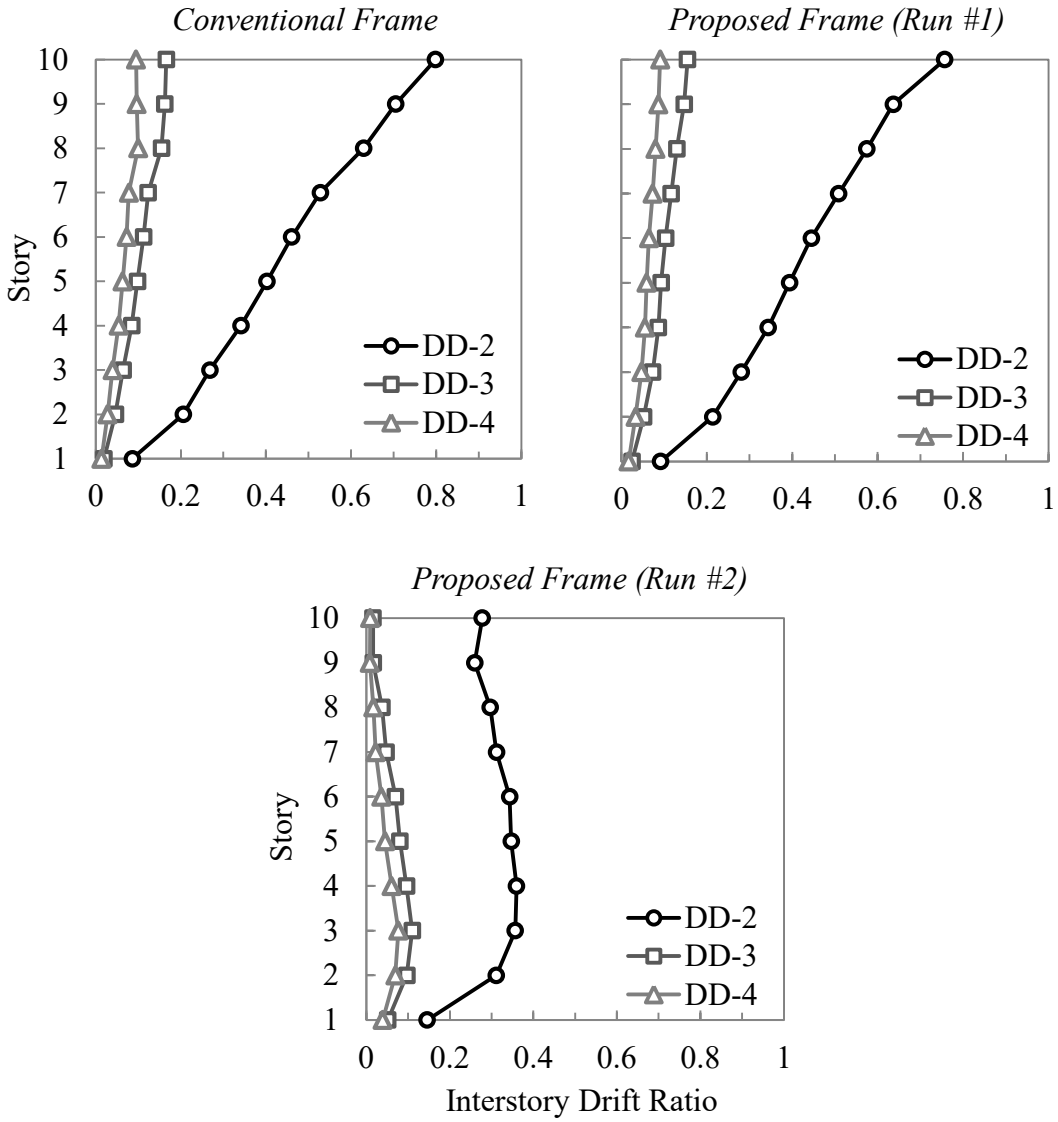

Figure 189. Story damage indices of all designs for DD2, DD3 and DD4-level earthquakes

7.2.7. Pushover Analyses

All designs were subjected to nonlinear pushover analyses to observe the change in the base shear coefficient and the effective stiffness after the design revision. The frames were “pushed” to the mean maximum roof drift ratios obtained from the

nonlinear time-history analyses (i.e. 1.44%, 1.44%, and 1.55% for the conventional frame, the proposed frame after Run #1 and Run #2, respectively). Figure 190 shows the pushover curves and the effective stiffnesses of all frames.

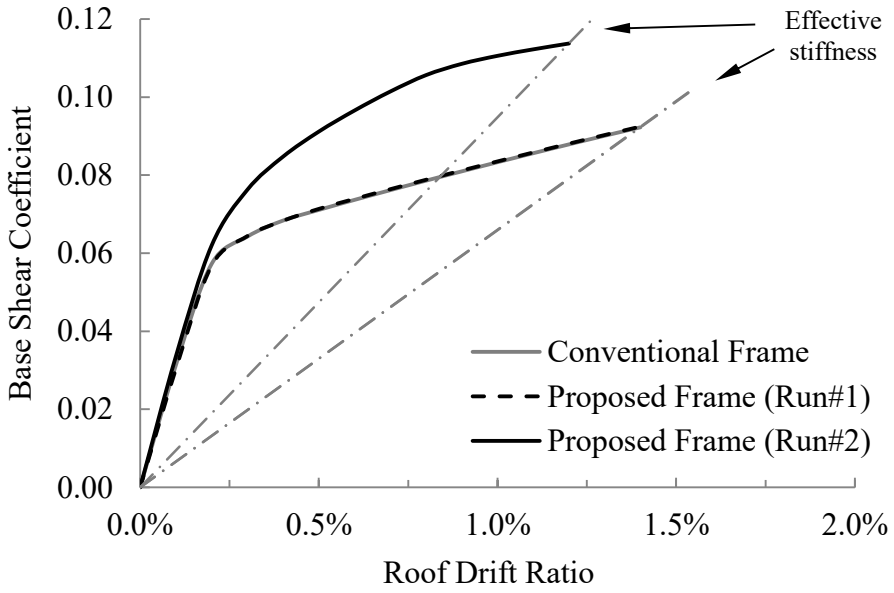

Figure 190. Pushover curves and effective stiffnesses for all designs

It can be observed from the figure that the pushover curves of the initial designs are identical. The base shear coefficient at the maximum roof drift is 0.09 for the initial designs. For the final design, the base shear coefficient increased by 23%, and the effective stiffness increased by 45%. Therefore, the global ductility demand decreased after the revision, which also leads to reduced overall damage throughout the frame.

Furthermore, it is observed that the square root of the ratio of the final effective stiffness ($K_{eff,2}$) to the initial effective stiffness ($K_{eff,1}$) approximates the ratio of the maximum roof drifts of the initial and the final designs, MRD_1 and MRD_2. Figure 191 compares the two parameters for individual ground motions, as well as for the mean results.

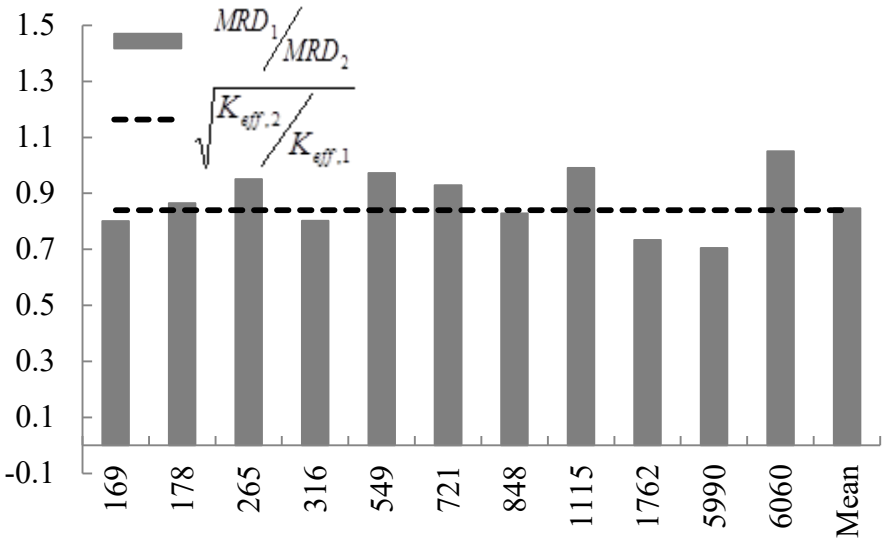

Figure 191. Relationship between the change in the maximum roof drift and the change in the effective stiffness

It can be seen that the mean maximum roof drift of Run #2 decreased to 85% of the mean maximum roof drift of Run #1. Similarly, the square root of the ratio of the initial effective stiffness to the final effective stiffness is 0.88. Therefore, this parameter can be used to estimate the average change in the peak roof displacement during ground motions between design revisions.

7.2.8. Iterative Procedure Applied to the Conventional Frame

The proposed iterative procedure was also applied to the conventional frame to investigate if the results are dependent on the performed manipulation of the modal vectors of the elastic structure as defined in Chapter 3. The reinforcement ratios and the moment capacities provided after the design revision are presented in Table 42 together with those of the initial designs and the final proposed design.

The reinforcement ratios of the columns and the β values are approximately the same as those of the Run #2 of the proposed frame. Figure 192 compares the mean envelope interstory drift distribution of all designs.

Table 42. Provided reinforcement ratios and moment capacities of the beams for all designs

Story	Run #1				Run #2			
	Conventional Frame		Proposed Frame		Conventional Frame		Proposed Frame	
	ρ (%)	M_r (kN·m)	ρ (%)	M_r (kN·m)	ρ (%)	M_r (kN·m)	ρ (%)	M_r (kN·m)
10	0.3	97	0.9	89	0.7	204	1.5	176
9	0.5	145	0.9	130	1.1	296	1.9	272
8	0.5	145	0.8	164	1.0	271	1.5	285
7	0.7	204	0.8	183	1.3	347	1.4	311
6	0.7	204	0.8	225	1.1	296	1.2	321
5	0.8	225	0.7	225	1.1	296	1.1	296
4	0.8	225	0.7	248	0.9	248	0.9	285
3	0.8	225	0.7	224	0.7	204	0.6	196
2	0.7	204	0.7	224	0.5	145	0.5	157
1	0.6	164	0.5	160	0.3	83	0.3	93

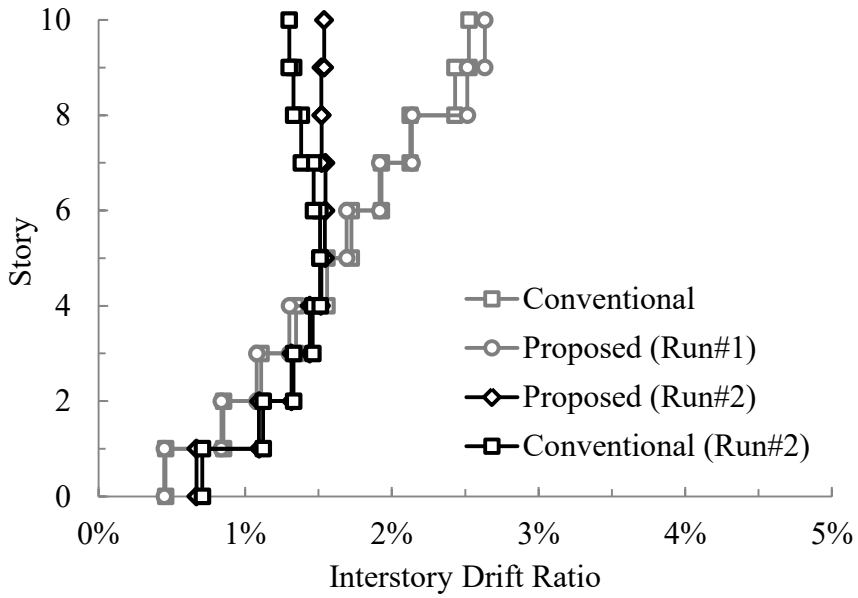

Figure 192. Comparison of mean envelope interstory drifts for all designs

From the figure, it can be observed that the results of the second runs for both designs are quite similar in terms of the envelope interstory drift ratios. Figure 193

shows the maximum roof drift ratios at all ground motions for all designs. It can be seen from the figure that the maximum roof drifts are approximately the same for both final designs.

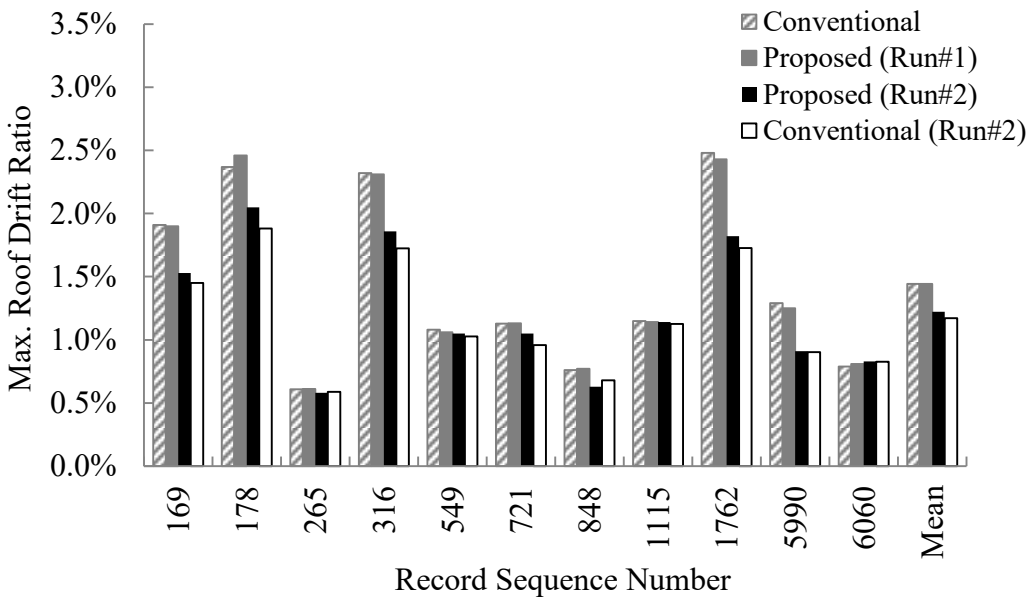

Figure 193. Maximum roof drift ratios at individual ground motions for all designs

The total amounts of dissipated hysteretic energy for each design are shown in Figure 194. Similarly, the hysteretic energy dissipation is almost the same for both final designs.

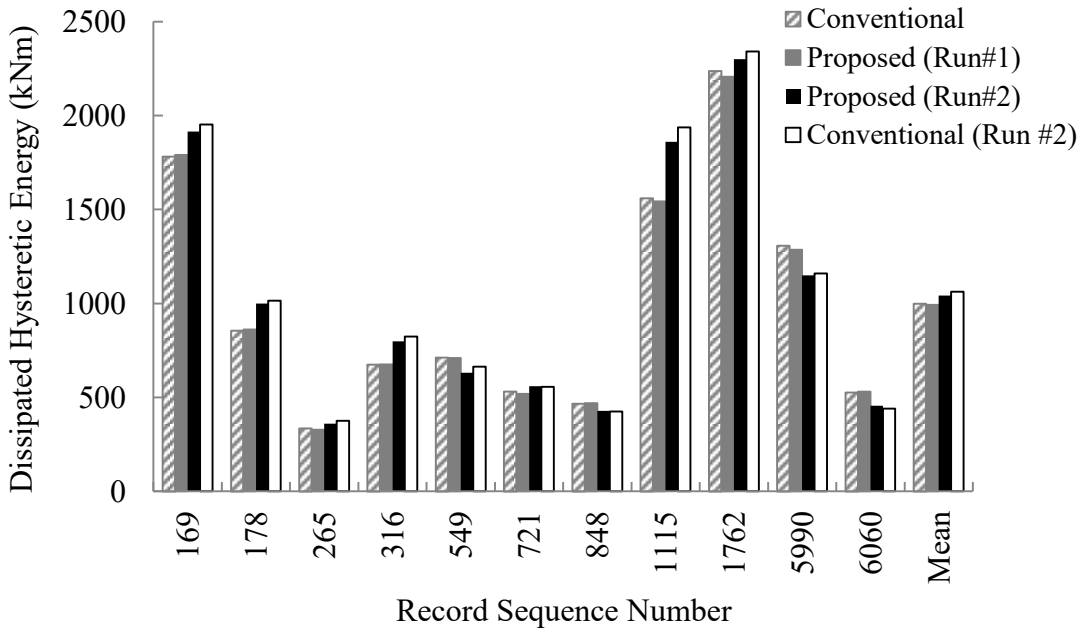

Figure 194. Total dissipated hysteretic energy at individual ground motions for all designs

The mean story damage indices of all designs are compared in Figure 195. In addition, Figure 196 shows the overall damage indices for all designs.

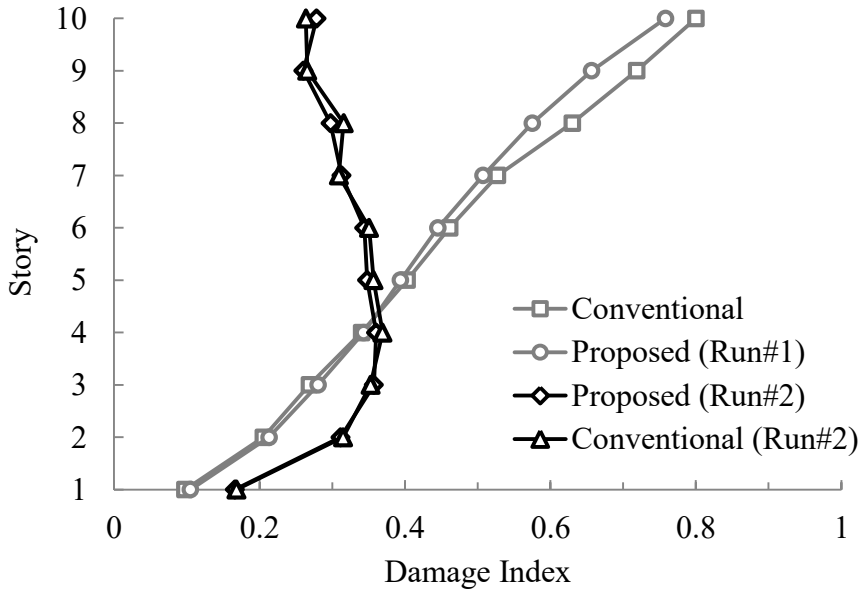

Figure 195. Comparison of story damage indices for all designs

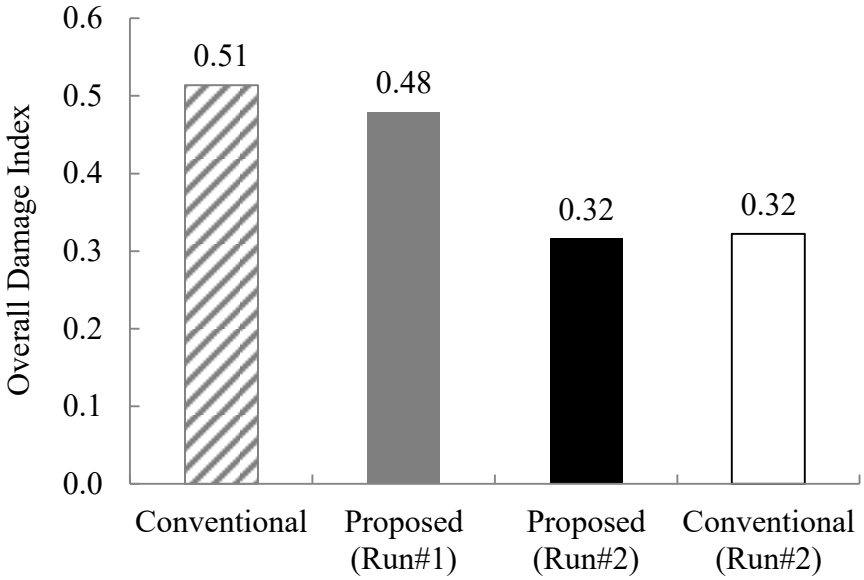

Figure 196. Mean overall damage indices for all designs

It can be seen that the damage indices for both final designs are almost identical both at the story level and at the global level. Figure 197 shows the beam moment capacities for all designs. It can be seen that the beam strength distribution for both final designs are very similar to each other.

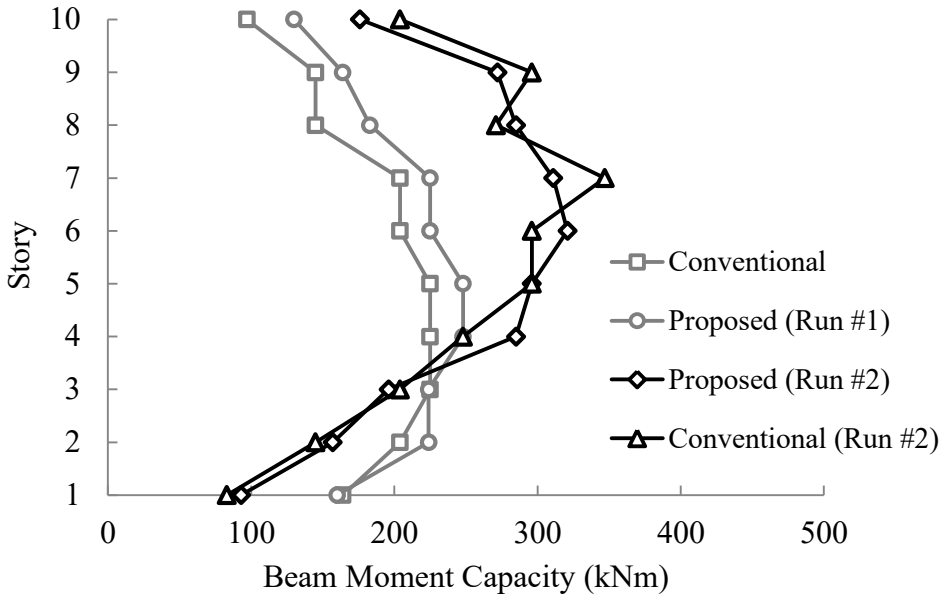

Figure 197. Beam moment capacities for all designs

7.3. Discussion of the Results

The results indicate that selecting the fundamental period of the frame based on the predefined maximum drift may be used to limit the maximum roof drift of the frames whether they are designed using the conventional or the proposed method. However, the envelope interstory drifts at particular stories may be excessive during the seismic response. This may lead to story mechanisms and severe damage in the frames. The proposed seismic design procedure mitigates the excessive interstory drifts and ensures a uniform distribution of the drift demand among the stories. Consequently, the story damage is mitigated, and the overall damage is reduced significantly.

Although the envelope interstory drifts and the maximum roof drift of the final design are lower than those of the long-period frame, the story damage indices and the overall damage are larger. This outcome is associated with the relatively higher column-to-beam strength ratios (β) described in Section 7.2.3. The beams of the short-period frame required less strength in order to preserve the initial β values, which are higher than those of the long-period frame. As a result, the energy dissipation capacities of these beams are lower than the ones of the long-period frame. This leads to slightly higher damage indices in the beams.

The result of the last section showed that the proposed iterative procedure can be applied successfully independent of the primary design. The damage levels of both final designs are almost identical to each other. Depending on this outcome, it can be implied that the strength distribution governs the extent and the distribution of the damage and the interstory drifts rather than the initial stiffness distribution, provided that the beam-failure mechanism is assured.

The proposed iterative procedure was shown to be very effective at optimizing the drift behavior of the considered frames. Only one revision was sufficient to reach a uniform interstory drift distribution.

7.4. Summary and Concluding Remarks

In this chapter, the seismic design of a pair of 10-story frames was performed according to a predefined target drift. The fundamental periods of the frames were determined using a correlation with the maximum drift response. Each pair consists of

frame designs using a conventional seismic design approach, and the proposed approach. The proposed iterative procedure was applied to both frames and shown to be effective at mitigating the interstory drift concentrations for both cases. Furthermore, the maximum mean envelope interstory drift ratio was decreased by 40%, while the overall damage was decreased by 33% after applying the proposed iterative procedure.

It was observed that the amount and the distribution of column-to-beam strength ratios are also significantly important in addition to the yield strength distribution of the members at controlling the drift and the damage. The short-period frames considered in this chapter sustained slightly higher damage compared to the long-period frames due to their relatively high column-to-beam strength ratios.

CHAPTER 8

SUMMARY AND CONCLUSIONS

8.1. Summary

The thesis study addresses the concentration of interstory drifts in reinforced concrete frame structures during seismic response. The aim is to develop a practical design method so as to avoid these concentrations by manipulating the design parameters. Interstory drift ratio is used as a tool for controlling the extent and the distribution of damage since there is a satisfactory correlation between drift and damage. A uniform interstory drift distribution is targeted to avoid damage concentrations at certain regions of the frames.

Initially, an elastic design procedure that aims to obtain a well-organized stiffness distribution along the height of the frames was proposed. The organized stiffness distribution is calculated such that it results in prescribed modal vector properties and fundamental period using an iterative procedure. The proposed procedure is based on the observation that the modal vectors govern the drift response of the frames within the linear response range. Thus, the distribution of the interstory drifts is aimed to be controlled by manipulating the modal vectors by the stiffness distribution. Then, the columns and the beams of the frames are proportioned separately for each story to obtain the required story stiffness. The effectiveness of the method was evaluated using both shear-beam models and linear reinforced concrete frames of various heights. Results showed that the proposed procedure is effective at low- to mid-rise frames.

In the following chapter, adequate material and element models to be used for modeling the reinforced concrete frames for the study are determined. The effect of different numerical material and element modeling methods on the seismic response of reinforced concrete members was investigated by a parametric study.

Subsequently, a design methodology for inelastic seismic response of low- to mid-rise reinforced concrete moment frame structures was developed. It is an iterative methodology that is based on the relationship between the plastic rotations and interstory drift ratios. In each iterative step, reinforcement ratios of the members are

revised to obtain a uniform plastic rotation distribution. The effectiveness of the proposed method was evaluated using five- and ten-story frames. These frames were designed using both a conventional method and the proposed method. Moreover, these frames had longer periods than expected for well-designed frames of the same type. The aim is to have a high drift demand and observe the performance of the proposed seismic design method at relatively higher displacement demands. Then, the seismic response of both types of frames was compared in terms of interstory drift and story damage distributions. The results showed that the frames designed using the proposed procedure had lower damage, as well as well-distributed interstory drifts and story damage.

In the following chapter, ten-story frames were designed by aiming at a prescribed drift target. The target period was determined based on the prescribed drift level using a correlation between the two. One of the frames was designed using conventional methods as per TEC2018. The other frame was designed using the proposed seismic design procedure described in Chapters 3 and 5. Then, the seismic response of both frames was compared in terms of interstory drift and story damage distributions. The results showed that the drift target was satisfied at both frames. However, the frame designed using the proposed methodology had significantly lower overall damage and well-distributed interstory drifts and story damage. Furthermore, the iterative reinforcement allocation method was also applied to the conventionally designed frame. This part showed that the proposed iterative procedure could be applied successfully independent of the primary design.

8.2. Conclusions

According to the results obtained throughout the study, the following conclusions can be drawn:

- Chapter 3 showed that the elastic design procedure is very effective at avoiding interstory drift distributions at low- to mid-rise frames in the linear response range. However, the effectiveness of the proposed stiffness distribution decreases as the height of the frames increase since the higher modes become effective. It was also seen that the interstory drift concentration may not be a major issue at tall frames. Therefore, the proposed elastic design procedure can be used to control the interstory drift distribution at low- to mid-rise frames

which respond in the linear range or whose modal properties do not change significantly in the nonlinear range.

- In Chapter 4, it was seen that BWH is the most appropriate element model in OpenSees for modeling the seismic response of the reinforced concrete members. Its advantages include the option to modify the gross flexural stiffness, reduced numerical issues, and lower computational demand. It was also observed that the effective stiffness had significant effects on the energy dissipation of the numerical model. A relationship between the calculated yield drift and the effective stiffness was observed. However, further research is required to establish a strong correlation between the yield drift and effective stiffness. The comparison of different concrete material models indicated that the results are not influenced notably from the concrete model used. However, Concrete01 model showed up as the most practical one with the least numerical issues.
- Chapter 5 showed that the extent of the plastic rotations at member-ends could be controlled by modifying the yield strengths using the plastic strain energy of the monotonic moment-curvature response of the end-sections. Depending on this observation and the correlation between the plastic rotation and interstory drift distribution, it was demonstrated that the interstory drift distribution could be controlled by adjusting the yield strength distribution of the members. It should be noted that the applicability of the procedure is limited to the frame structures where strong column - weak beam condition is assured.
- The modification of the member yield strengths does not introduce a major change in the seismic displacement demand of the frames. On the other side, it is observed that the changes are well correlated with the change in the effective stiffnesses of the frames.
- The case studies showed that the proposed design methodology is very effective at reducing the interstory drift concentrations and the overall damage. It was observed that the yield strength of the members and their distribution over the height play a crucial role in controlling the distribution of the story drifts and the damage throughout the frame during strong ground motions. Furthermore, it was seen that the amount and the distribution of column-to-beam strength ratios are also significantly important in addition to the yield strength distribution of the

members at controlling the drift and the damage. The short-period frames sustained slightly higher damage compared to the long-period frames due to their relatively high column-to-beam strength ratios. Another observation is that the iterative reinforcement allocation procedure can be applied regardless of the primary design to modify the yield strengths of the members.

8.3. Recommendations for Future Research

The proposed seismic design methodology was developed using planar reinforced concrete frame structures. However, it is not restricted to reinforced concrete structures. Further case studies could be performed using steel moment frames to investigate the applicability of the proposed methodology in this type of structures.

It was observed that the amount and the distribution of column-to-beam strength ratios are significantly effective on the distribution of the interstory drift ratios. The column-to-beam strength ratios are governed by the initial design demands and the minimum reinforcement ratio requirements. Therefore, the effect of column-to-beam strength ratios on the interstory drift distribution could be an investigation topic for future studies.

The parametric study which aims to investigate the effects of different element modeling approaches and material models (Chapter 4) revealed that the effective stiffness had significant effects on the energy dissipation of the numerical model. A relationship between the calculated yield drift and the effective stiffness was observed. However, to draw a generalized conclusion, it is necessary to perform a comprehensive parametric study on the subject.

REFERENCES

Algan, B. B. Drift and Damage Considerations in Earthquake Resistant Design of Reinforced Concrete Buildings. Ph.D. Dissertation, University of Illinois at Urbana-Champaign, Urbana, IL, 1982.

American Society of Civil Engineers. *Seismic Evaluation and Retrofit of Existing Buildings (ASCE/SEI 41-13)*; 2013.

Ancheta, T. D.; Darragh, R. B.; Stewart, J. P.; Seyhan, E.; Silva, W. J.; Chiou, B. S. J.; Wooddell, K. E.; Graves, R. W.; Kottke, A. R.; Boore, D. M.; Kishida, T.; Donahue, J. L. *PEER NGA-West2 Database*; PEER Report 2013/03, Pacific Earthquake Research Center: University of California, Berkeley, CA, 2013.

Bai, J.; Jin, S.; Ou, J. An Efficient Method for Optimizing the Seismic Resistance of Reinforced Concrete Frame Structures. *Adv. Struct. Eng.* **2020**, *23* (4), 670–686.

Bai, J.; Jin, S.; Zhang, C.; Ou, J. Seismic Optimization Design for Uniform Damage of Reinforced Concrete Moment-Resisting Frames Using Consecutive Modal Pushover Analysis. *Adv. Struct. Eng.* **2016**, *19* (8), 1313–1327.

Berry, M.; Parrish, M.; Eberhard, M. *PEER Structural Performance Database User's Manual (Version 1.0)*. Pacific Earthquake Engineering Research Center, University of California, Berkeley, CA, 2004.

Bertero, R. D.; Bertero, V. V. Performance-Based Seismic Engineering: Development and Application of a Comprehensive Conceptual Approach to the Design of Buildings. In *Earthquake Engineering: From Engineering Seismology to Performance-Based Engineering*, Bozorgnia Y., Bertero V. V., Eds.; CRC Press: 2004; 452–558.

Broderick, B. M. Seismic Testing, Analysis and Design of Composite Frames. Ph.D. Dissertation, University of London, London, England, 1994.

Calabrese, A.; Almeida, J. P.; Pinho, R. Numerical Issues in Distributed Inelasticity Modeling of RC Frame Elements for Seismic Analysis. *J. Earthq. Eng.* **2010**, *14* (1), 38–68.

Chang, G. A.; Mander, J. B. *Seismic Energy Based Fatigue Damage Analysis of Bridge Columns: Part I-Evaluation of Seismic Capacity*; NCEER-94-0006; National Center for Earthquake Engineering Research, Buffalo, NY, 1994.

Clough, R. W.; Benuska, K. L. *Earthquake Performance of High-Rise Buildings: A Digital Computer Investigation of the Seismic Response of a Wide Range of High-Rise Structural Systems*; TY Lin Associates, 1965.

Coleman, J.; Spacone, E. Localization Issues in Force-Based Frame Elements. *J. Struct. Eng.* **2001**, *127* (11), 1257–1265.

CSI. *SAP2000 v15*. Computers and Structures Inc., Berkeley, CA, 2016.

Elwood, K. J.; Eberhard, M. O. Effective Stiffness of Reinforced Concrete Columns. *ACI Struct. J.* **2009**, *106* (4), 476–484.

Estes, K. R. An Energy Method for Seismic Design. Ph.D. Dissertation, University of Southern California, Los Angeles, CA, 2003.

Fardis, M. N. Seismic Design Issues for Masonry-Infilled RC Frames. In *Proceedings of the First European Conference on Earthquake Engineering and Seismology*, Geneva, Switzerland, September 3-8, 2006.

French, A. P. *Vibrations and Waves*; MIT Introductory Physics Series, 1971.

Gharakhanloo, A. Distributed and Concentrated Inelasticity Beam-Column Elements Used in Earthquake Engineering. M.Sc. Dissertation, Norwegian University of Science and Technology, Trondheim, Norway, 2014.

Giuffrè, A. Il Comportamento Del Cemento Armato per Sollecitazioni Cicliche Di Forte Intensità. *G. del Genio Civ.* **1970**, *5*, 391-408.

Goel, S. C. Inelastic Behavior of Multistory Building Frames Subjected to Earthquake Motion. Ph.D. Dissertation, University of Michigan, Ann Arbor, MI, 1967.

Hajirasouliha, I.; Asadi, P.; Pilakoutas, K. An Efficient Performance-Based Seismic Design Method for Reinforced Concrete Frames. *Earthq. Eng. Struct. Dyn.* **2012**, *41* (4), 663–679.

Hajirasouliha, I.; Moghaddam, H. New Lateral Force Distribution for Seismic Design of Structures. *J. Struct. Eng.* **2009**, *135* (8), 906–915.

Haselton, C. B.; Liel, A. B.; Deierlein, G. G.; Dean, B. S.; Chou, J. H. Seismic Collapse Safety of Reinforced Concrete Buildings. I: Assessment of Ductile Moment Frames. *J. Struct. Eng.* **2011**, *137* (4), 481–491.

Huang, X.; Kwon, O. S. Numerical Models of RC Elements and Their Impacts on Seismic Performance Assessment. *Earthq. Eng. Struct. Dyn.* **2015**, *44* (2), 283–298.

Karsan, D. I.; Jirsa, J. O. Behavior of Concrete Under Compressive Loadings. *J. Struct. Div.* **1969**, *95* (12), 2543–2564.

Kent, D. C.; Park, R. Flexural Members with Confined Concrete. *J. Struct. Div.* **1971**, *97*, 1969–1990.

Kunnath, S. K.; Reinhorn, A. M.; Lobo, R. F. *IDARC Version 3.0: A Program for the Inelastic Damage Analysis of Reinforced Concrete Structures*; NCEER-92-0022; National Center for Earthquake Engineering Research, Buffalo, NY, 1992.

Lee, C. L.; Filippou, F. C. Efficient Beam-Column Element with Variable Inelastic End Zones. *J. Struct. Eng.* **2009**, *135* (11), 1310–1319.

Leelataviwat, S.; Goel, S. C.; Stojadinović, B. Energy-Based Seismic Design of Structures Using Yield Mechanism and Target Drift. *J. Struct. Eng.* **2002**, *128* (8), 1046–1054.

Lepage, A. A Method for Drift-Control in Earthquake-Resistant Design of RC Building Structures. Ph.D. Dissertation. Purdue University, West Lafayette, IN, 1997.

Mander, J. B.; Priestley, M. J.; Park, R. Theoretical Stress-Strain Model for Confined Concrete. *J. Struct. Eng. (United States)* **1988**, *114* (8), 1804–1826.

Mayengbam, S. S.; Choudhury, S. Determination of Column Size for Displacement-Based Design of Reinforced Concrete Frame Buildings. *Earthq. Eng. Struct. Dyn.* **2014**, *43* (8), 1149–1172.

Mazzoni, S.; Mckenna, F.; Scott, M. H.; Fenves, G. L. *Open System for Earthquake Engineering Simulation User Command-Language Manual*. Pacific Earthquake Engineering Research Center, University of California, Berkeley, CA, 2003.

McKenna, F.; Scott, M. H.; Fenves, G. L. Nonlinear Finite-Element Analysis Software Architecture Using Object Composition. *J. Comput. Civ. Eng.* **2010**, *24* (1), 95–107.

Medina, R. A. Story Shear Strength Patterns for the Performance-Based Seismic Design of Regular Frames. *ISET J. Earthq. Technol.* **2004**, *41* (442), 101–125.

Menegotto, M.; Pinto, P. E. Method of Analysis for Cyclically Loaded Reinforced Concrete Frames Including Changes in Geometry and Non-Elastic Behavior of Elements under Combined Normal Forces and Bending Moment. In *IASBE Proc.*, 1973.

Miranda, E. Approximate Seismic Lateral Deformation Demands in Multistory Buildings. *J. Struct. Eng.* **1999**, *125* (4), 417–425.

Miranda, E.; Bertero, V. V. Evaluation of Strength Reduction Factors for Earthquake-Resistant Design. *Earthq. Spectra* **1994**, *10* (2), 357–379.

Moehle, J. P. Displacement-Based Design of RC Structures Subjected to Earthquakes. *Earthq. Spectra* **1992**, *8* (3), 403–428.

Moghaddam, H.; Hajirasouliha, I. A New Approach for Optimum Design of Structures Under Dynamic Exciation. *Asian J. Civ. Eng.* **2004**, *5*, 69–84.

Moghaddam, H.; Hajirasouliha, I. Toward More Rational Criteria for Determination of Design Earthquake Forces. *Int. J. Solids Struct.* **2006**, *43* (9), 2631–2645.

Mohammadi, R. K.; El Naggar, M. H.; Moghaddam, H. Optimum Strength Distribution for Seismic Resistant Shear Buildings. *Int. J. Solids Struct.* **2004**, *41* (22–23), 6597–6612.

Naeim, F. *The Seismic Design Handbook*; Springer, 2001.

Neuenhofer, A.; Filippou, F. C. Evaluation of Nonlinear Frame Finite-Element Models. *J. Struct. Eng.* **1997**, *123* (7), 958–966.

Newmark, N. M.; Blume, J. A.; Kapur, K. K. *Seismic Design Spectra for Nuclear Power Plants*; Consulting Engineering Services, Urbana, IL, 1973.

Park, K.; Medina, R. A. Conceptual Seismic Design of Regular Frames Based on the Concept of Uniform Damage. *J. Struct. Eng.* **2007**, *133* (7), 945–955.

Park, Y. J.; Reinhorn, A. M.; Kunnath, S. K. *IDARC: Inelastic Damage Analysis of Frame Shear-Wall Structures*; NCEER-94-0006; National Center for Earthquake Engineering Research, Buffalo, NY, 1994.

Park, Y. J.; Ang, A. H.-S. Mechanistic Seismic Damage Model for Reinforced Concrete. *J. Struct. Eng. (United States)* **1985**, *111* (4), 722–739.

Popovics, S. A Numerical Approach to the Complete Stress-Strain Curve of Concrete. *Cem. Concr. Res.* **1973**, *3* (5), 583–599.

Priestley, M. J. N. Performance Based Seismic Design. *Bull. New Zeal. Soc. Earthq. Eng.* **2000**, *33* (3), 325–346.

Rodrigues, H.; Varum, H.; Arêde, A.; Costa, A. Comparative Efficiency Analysis of Different Nonlinear Modelling Strategies to Simulate the Biaxial Response of RC Columns. *Earthq. Eng. Eng. Vib.* **2012**, *11* (4), 553–566.

Schultz, A. E. Approximating Lateral Stiffness of Stories in Elastic Frames. *J. Struct. Eng. (United States)* **1992**, *118* (1), 243–263.

Scott, B. D. Stress : strain relationships for confined concrete: rectangular sections. M.Sc. Dissertation, University of Canterbury, Christchurch, New Zealand, 1980.

Scott, M. H.; Fenves, G. L. Plastic Hinge Integration Methods for Force-Based Beam-Column Elements. *J. Struct. Eng.* **2006**, *132* (2), 244–252.

Scott, M. H.; Hamutçuoğlu, O. M. Numerically Consistent Regularization of Force-based Frame Elements. *Int. J. Numer. Methods Eng.* **2008**, *76* (10), 1612–1631.

Shibata, A.; Sozen, M. A. Substitute-Structure Method for Seismic Design in R/C. *ASCE J Struct Div* **1976**, *102*, 1–18.

Shimazaki, K.; Sozen, M. A. *Seismic drift of reinforced concrete structures*; Tech. Res. Rep. of Hazama-Gumi, 1984, 145–166.

Sozen, M. A. The Velocity of Displacement. In *Seismic Assessment and Rehabilitation of Existing Buildings*; Kluwer Academic Publishers: Dordrecht, The Netherlands, 2003; Vol. 29; 11–28.

Spacone, E.; Filippou, F. C.; Taucer, F. F. Fibre Beam-Column Model for Non-Linear Analysis of R/C Frames: Part I. Formulation. *Earthq. Eng. Struct. Dyn.* **1996**, *25* (7), 711–725.

TEC2018. *Turkish Earthquake Code for Building Structures: Specifications for Design of Buildings under Earthquake Forces*; Presidency of Disaster and Emergency Management, 2018.

Terapathana, S. An Energy Method for Earthquake Resistant Design of RC Structures. Ph.D. Dissertation, University of Southern California, Los Angeles, CA, 2012.

MATLAB (R2015a); The Mathworks Inc., 2015.

Veletsos, A.; Newmark, N. M. Effect of Inelastic Behavior on the Response of Simple Systems to Earthquake Motions. In *Proceedings of the 2nd World Conference on Earthquake Engineering*, Tokyo and Kyoto, Japan, July 11-18, 1960.

Waugh, J. D. Nonlinear Analysis of T-Shaped Concrete Walls Subjected to Multi-Directional Displacements. Ph.D. Dissertation, Iowa State University, Ames, IA, 2009.

Yakut, A. Reinforced Concrete Frame Construction. *World Hous. Encycl. – Summary Publication* **2004**, 1–8.

Yassin, M. H. M. Nonlinear Analysis of Prestressed Concrete Structures under Monotonic and Cyclic Loads, Ph.D. Dissertation, University of California, Berkeley, CA, 1994.

Zhao, J.; Bin, D.; Yuilin, Z.; Kai, Z. Comparison of constitutive material models in OpenSees for hysteretic behavior of structures. Journal of Yuilin University of Technology **2017**, 37 (1), 58-67.

Zou, X. K.; Chan, C. M. Optimal Seismic Performance-Based Design of Reinforced Concrete Buildings Using Nonlinear Pushover Analysis. *Eng. Struct.* **2005**, *27* (8), 1289–1302.

Zou, X. Optimal Seismic Performance-Based Design of Reinforced Concrete Buildings. Ph.D. Dissertation, The Hong Kong University of Science and Technology, Kowloon, Hong Kong, 2002.

APPENDIX A

ACCELERATION TIME-HISTORIES OF THE GROUND MOTION RECORDS

A.1. Ground Motion Records Used in Chapter 3

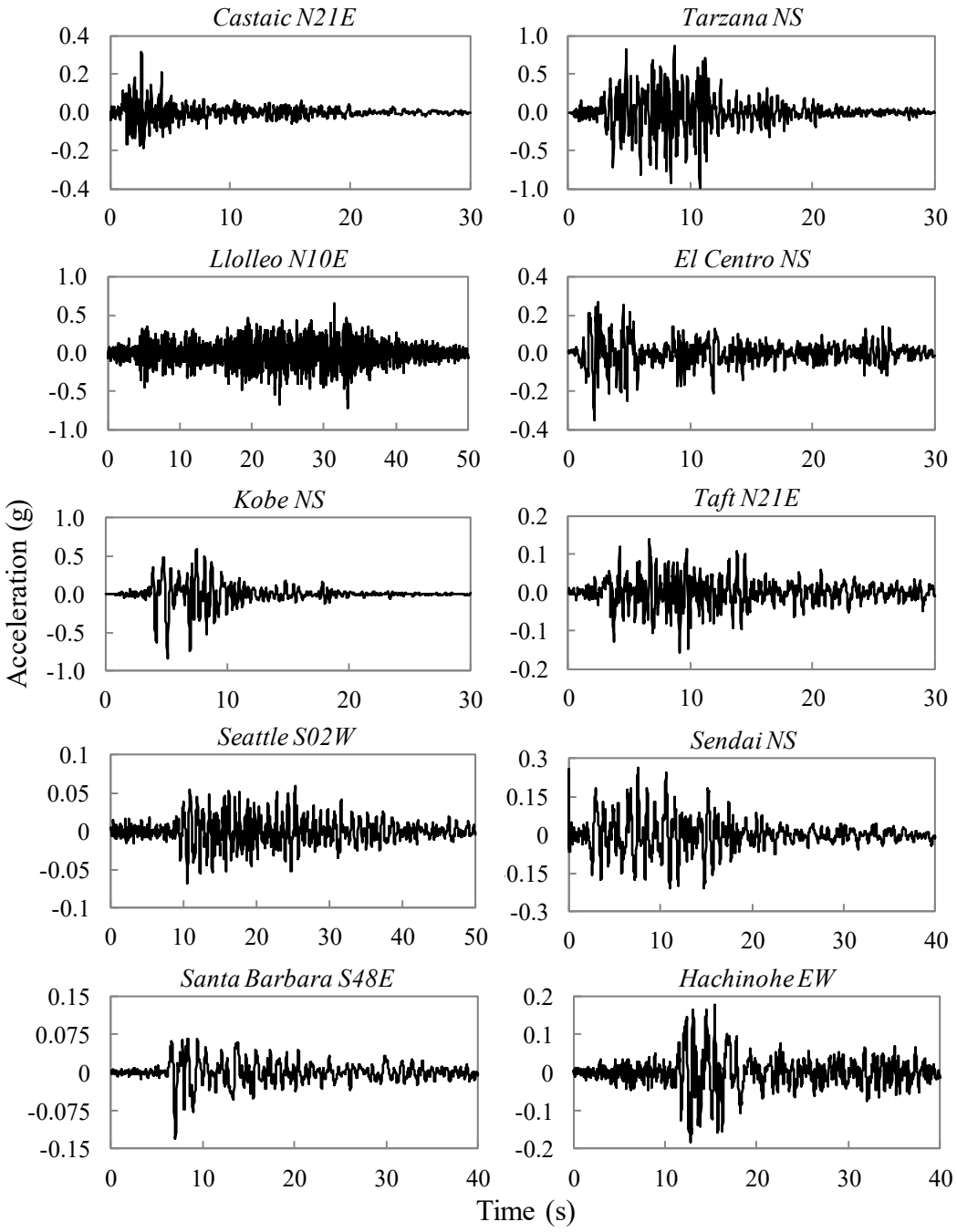

A.2. Ground Motion Records Used in Chapter 5, 6 and 7

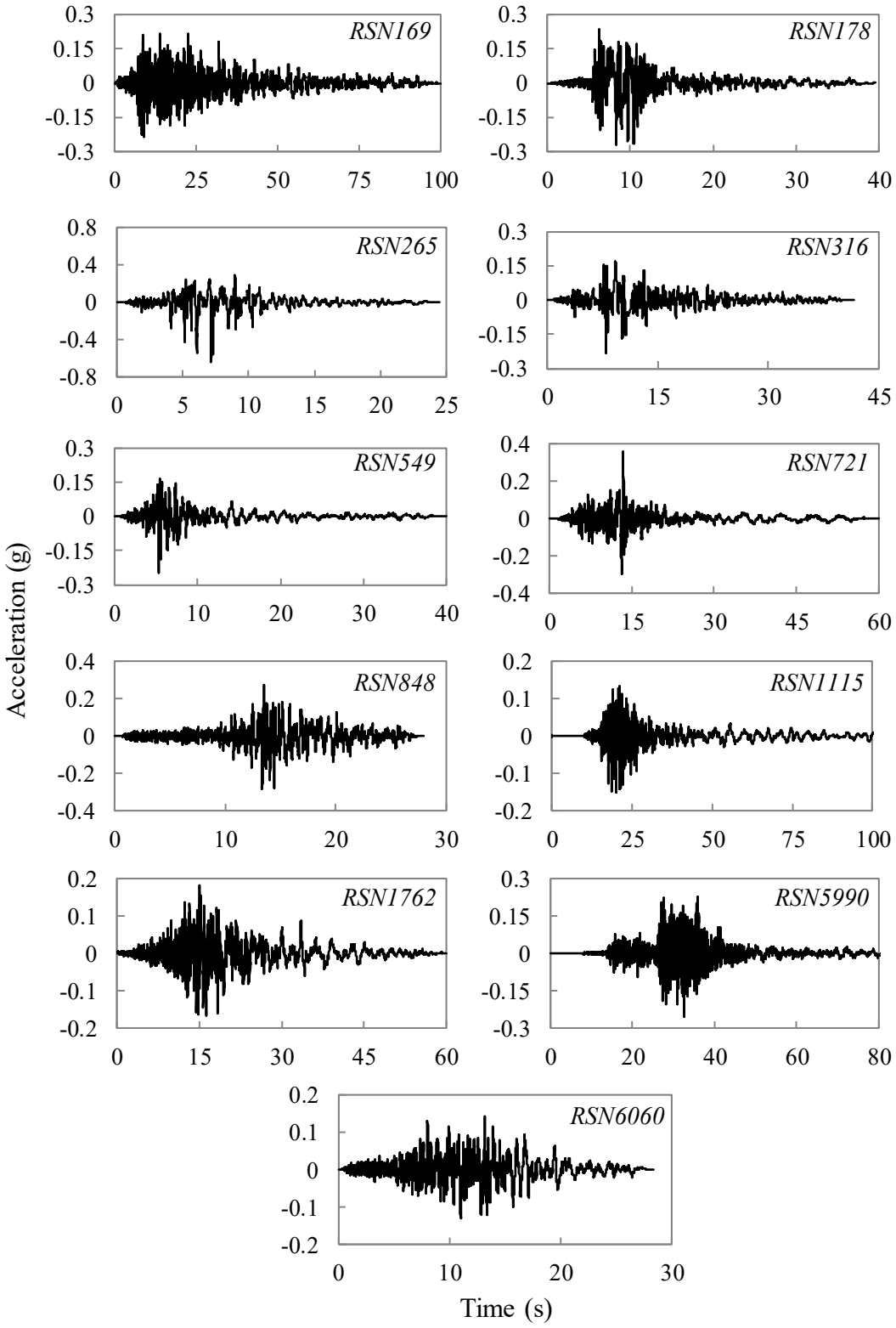

APPENDIX B

SCRIPT FLOWCHART OF THE INELASTIC DESIGN PROCEDURE

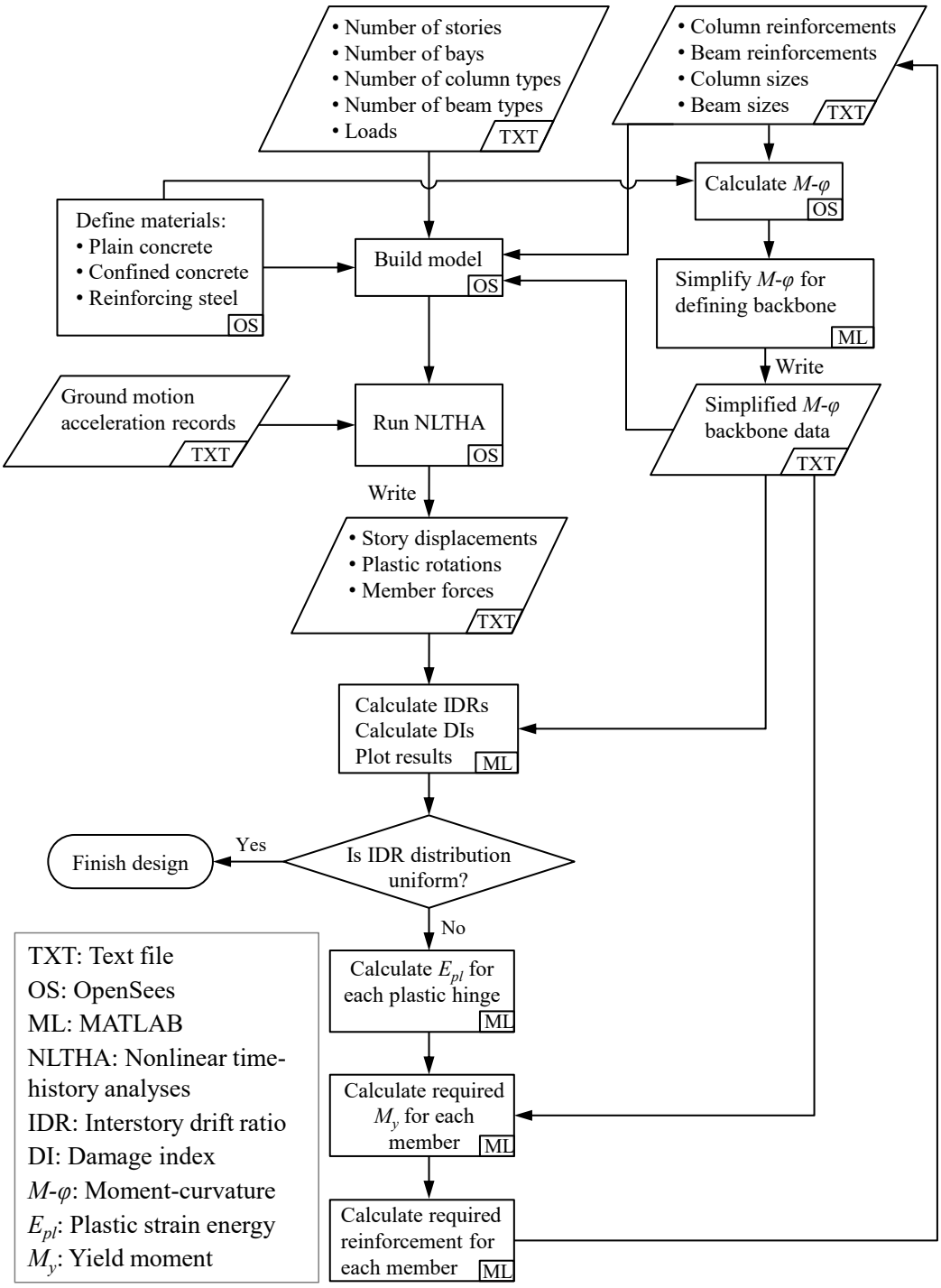

VITA

Egemen Sönmez

EDUCATION

M.Sc. in Civil Engineering **2013**
İzmir Institute of Technology, İzmir, Turkey
Title: Effect of Infill Wall Stiffness Variations on the Behavior of Reinforced Concrete Frames under Earthquake Demands
Advisor: Assoc. Prof. Cemalettin Dönmez

B.Sc. in Civil Engineering **2010**
Celal Bayar University, Manisa, Turkey

ACADEMIC EMPLOYMENT

Part-time Lecturer **2020 - Present**
Department of Construction Technology
İzmir University of Economics

Research Assistant **2010 - 2019**
Civil Engineering Department
Izmir Institute of Technology

PUBLICATIONS

MANUSCRIPTS SUBMITTED FOR REVIEW

Sönmez, E., Dönmez, C. (2019). A study on the mitigation of drift concentrations in RC frames under earthquake demands. *Ingegneria Sismica*. (Under review)

Sönmez, E., Dönmez, C. (2019). Variation of Reinforced Concrete Member Behavior in Seismic Simulation for the Selected Element and Material Models. *Journal of Earthquake Engineering.* (Under review)

CONFERENCE PRESENTATIONS

Sönmez, E., Dönmez, C. (2019). Malzeme ve Sayısal Modelleme Parametrelerinin Betonarme Elemanların Deprem Simülasyonları Üzerindeki Etkilerinin Araştırılması. *5th International Conference on Earthquake Engineering and Seismology,* Ankara, Turkey. (in Turkish)

Sönmez, E., Dönmez, C. (2015). Betonarme çerçevelerde dolgu duvarlar vasıtasıyla rijitlik dağılımının değiştirilmesinin deprem talepleri altındaki ötelenme dağılımına etkisi. *3rd Turkish Conference on Earthquake Engineering and Seismology*, Izmir, Turkey. (in Turkish)

Sönmez, E., Dönmez, C. (2014). Effect of infill wall stiffness variations on the behavior of reinforced concrete frames under earthquake demands. *2nd European Conference on Earthquake Engineering and Seismology.*